Modelling airlift photobioreactors for algal bioenergy, using *Scenedesmus* sp. as the model species

by

Murray Fraser

A thesis submitted to the University of Cape Town as fulfilment of the requirement for the degree of **Master of Science in Engineering**

Center for Bioprocess Engineering Research

Department of Chemical Engineering

University of Cape Town

29 May 2011

Synopsis

Rising global energy demands and global warming concerns from fossil derived fuels are two major problems affecting future generations. Bioenergy from algae offers a part solution that is both attractive and sustainable, by supplementing energy demands from a renewable energy source (the sun) and consuming carbon dioxide in the process.

Bioenergy from algae is a proven concept (e.g algal biodiesel), yet the low productivities and high costs of existing processes limit their ability to make a significant contribution. Algae production occurs in specially designed photobioreactors, which are typically light limited. Hence, optimization of light supply to algae is key. A mathematical model of a photobioreactor is useful to aid in the design and optimization process. A model enables the prediction of productivities as a function of changing model inputs and hence allows optima to be predicted. While these are typically validated experimentally, this greatly reduces the number of experiments required, thereby saving cost and time.

For this work, the production of algal biodiesel using airlift photobioreactors was used as the case study for the model development. *Scenedesmus* sp. was chosen as the model species owing to its comparatively high lipid productivity, a desirable trait for the production of biofuels. Although many parameters affect algal growth and lipid productivity, this project focused on one critical parameter, that of light provision. External illumination of the reactor, when combined with light attenuation by the fluid and the fluid dynamics in the reactor, causes algae cells to experience fluctuating light regimes inside photobioreactors which influence their growth characteristics. In this dissertation, experimental studies are presented to investigate the response of *Scenedesmus* sp. to the characteristics of the fluctuating light regimes, or light/dark cycling. Further, the development of a mathematical model for the airlift photobioreactor is presented. This required the development of three independent sub-models for light distribution, kinetic growth and hydrodynamics, and their subsequent integration. The integrated model informs reactor optimisation

Absorbance of light as it penetrates an algal suspension causes an exponential decrease in light intensity with increasing depth of the light path. The light distribution model was developed to model this light distribution in a cylindrical airlift reactor as a function of the distance from the reactor surface. The inaccuracies associated with using traditional Beer-Lambert law were highlighted. Model simulations showed how scale-up to larger reactor diameters resulted in large dark zones near the centre of the reactor that would be unable to support photosynthetic growth. This suggested the need for modular design of multiple smaller reactors to achieve a large productivity.

The kinetic growth model was developed to describe how algae grow as a function of available light and in response to changing light conditions. The model builds on previous work performed by Wu & Merchuk (2001) for a different species of algae, *Porphyridium* sp.. Experiments conducted in custom designed tubular loop reactors enabled light intensity, cycle time and fractional exposure to light to be varied independently, with the specific growth rate measured as a response parameter. Cycle times of 21,33 and 45 seconds were investigated, each at light intensities of 363 and 939 $\mu\text{mol}\cdot\text{m}^{-2}\cdot\text{s}^{-1}$;

and at light fractions of 0.40, 0.575, 0.75, 0.875 and 1.00. The model was fitted to these growth data and the results from the experiment formed part of an investigation into the effects of light provision on algal growth. Photoinhibition, which is commonly attributed to high light intensity and fractional exposure to light, was found to be influenced by cycle time. In the 45 second case, the longer light exposure time and insufficient dark recovery time resulted in inhibition whereas the shorter cycle times, having short light exposure time and frequent dark recovery, did not exhibit photoinhibition.

Using the kinetic model for simulations gave additional insight into a broad range of relationships that exist between light fraction and light intensity that influence algal growth. Furthermore, the model's ability to simulate growth contours as a function of light intensity and light fraction showed the potential of using the model to aid in design and optimization of airlift reactors in the presence of photoinhibition.

The hydrodynamic model was developed to give a description of a cell's movement inside an airlift reactor. To avoid the need for CFD simulation or particle tracking to predict cell trajectories, an approximate compartmentalized approach was used for modelling the airlift reactor which gave the advantage of a rapid solution. This approach built on previous work by Wu & Merchuk (2004) and this project introduced many refinements. To describe fluid movement through the model compartments, liquid circulation and gas hold-up models were used according to Chisti *et al.* (1988) and Miron *et al.* (2000), respectively. Best-fit parameters for these two models were obtained from laboratory airlift reactor data. The model was used to show the shortfalls of assuming a negligible downcomer hold-up. In addition, a model simulation showed how the model could be useful to aid in the design of photobioreactors with optimum A_r/A_d ratios to achieve optimum light/dark cycles and hence optimum growth.

Once independently defined, the three models were integrated into a global model in Chapter 6 to enable simulation of algal growth in an airlift reactor. This global model was successfully fitted to data from a laboratory airlift.

This work offers significant value in the field. A novel set of model parameters have been obtained for *Scenedesmus* sp. to describe light distribution in cylindrical (and rectangular) systems. The experiments for the kinetic model have created new knowledge about *Scenedesmus* sp. growth characteristics under light/dark cycles and have showed how cycle time plays a role in algal photoinhibition effects. A novel set of kinetic model parameters were determined for *Scenedesmus* sp.. To date, the only other single set of parameters in existence where determined for *Porphyridium* sp. by Wu & Merchuk (2001). Furthermore, the data over which this model applies has been expanded by investigating it's response over changing cycle times, which was not investigated by the previous authors Wu & Merchuk (2001). When defining the hydrodynamic mode, a novel set of liquid circulation model parameters were determined for a laboratory airlift reactor. The integration of all three models into a global model for an airlift reactor, while not based on a novel approach, incorporated superior sub-models for light distribution and hydrodynamics.

In general, this work comprises a refined approach to modelling airlift photobioreactors. The three

sub-models that were developed and tested represent the essential modelling components for any photobioreactor model. Alteration of the model to apply to other reactor types would entail adjustment of the hydrodynamic model to suit different flow characteristics and a redefinition of the light distribution model for different geometries, the kinetic model can be integrated as is. The results from this study are relevant to the design and optimization of algal photobioreactors in general, which is essential for making cost effective biodiesel and improving the feasibility of bioenergy processes.

Plagiarism declaration

I know the meaning of plagiarism and declare that all the work in the document, save for that which is properly acknowledged, is my own

Signed.....

Acknowledgments

First and foremost, I thank my supervisors Prof. Sue Harrison and A/Prof. Klaus Möller for their knowledge and guidance throughout this project.

Other people who deserve a big thank you and special mention are:

- Francis Pocock - her timeous help with *everything* lab-related has been invaluable.
- Clive Garcin - for advice, help in the lab, and technical knowledge on flow cells.
- Nicholas Langley - for knowledge, technical help, and advice on just about anything!
- Melinda Griffiths - for her knowledge and help with algae cultivation.
- Sue Jobson - for her swift attention and willingness to help with administration.
- Sarel Rautenbach - whose skilled work in the art of glass blowing made the reactor construction a success.
- Joachim Macke and Peter Dobias - for help and work on numerous workshop jobs.

I thank all the support staff at CeBER in general for their assistance. I also acknowledge friends and colleagues in the department for making my time here enjoyable.

I am grateful to the National Research Foundation (NRF) and to CeBER for funding as well as UCT's Postgraduate Funding Office and the Chemical Engineering Department for financial assistance during the duration of this programme.

Finally, I extend my utmost gratitude to my parents, who have supported me throughout my studies, financially and with guidance and love .

Contents

List of Figures

List of Tables

Glossary of terms and abbreviations

ALR - Airlift reactor.

ATP - Adenosine triphosphate, which are energy carrier molecules in cells.

CARPT - Computer automated radioactive particle tracking.

CFD - Computational fluid dynamics.

DB - Diffuse bidimensional.

NADPH - Nicotinamide adenine dinucleotide phosphate.

PAR - Photosynthetically active radiation, which represents the range of wavelengths of light that can be utilized by algae.

PE - Photosynthetic efficiency.

PFD - Photon flux density. PFD is the number of photons passing through a flat surface per unit of time, having units $\mu\text{mol}\cdot\text{m}^{-2}\cdot\text{s}^{-1}$.

PSF - Photosynthetic factory. The PSF is defined as the sum of the activity of the light trapping system, reaction centers and associated apparatus, which are activated by light energy to produce photoproduct.

PSI, PSII - Photosystem I and Photosystem II. (See Fig. 2.2).

Reynolds number - symbol *Re*, a dimensionless number that represents the ratio of inertial forces to viscous forces. It is used to quantifies flow characterstics as being either laminar, transition or turbulent.

RTE - Radiative transfer equation.

Turbidostat - A type of reactor in which the turbidity of the culture is kept constant and controlled via a feedback loop from the measured turbidity which varies the dilution rate

Nomenclature

$A(\lambda), A(z,\lambda)$	Absorbance (-)
$A'(C_x,\lambda), A'(C_x)$	Absorption coefficient (m^{-1})
A_r	Riser cross sectional area (m^2)
A_d	Downcomer cross sectional area (m^2)
a_t	Total concentration of PSFs ($mol \cdot cell^{-1}$)
a	Hydrodynamic model constant for calculating hold-up (-)
b	Hydrodynamic model constantfor calculating hold-up (-)
c	Velocity of light (3×10^8 $m \cdot s^{-1}$)
C_x	Biomass concentration ($g.L^{-1}$)
D	Diameter (m)
D_c	Outer column diameter (m)
D_d	Draft tube diameter (m)
E	Light intensity on an energy basis ($W \cdot m^{-2}$)
E_a	Specific absorption coefficient ($m^2.kg^{-1}$)
E_s	Specific scattering coefficient ($m^2.kg^{-1}$)
E_p	Energy of a photon (J)
$E_0(\lambda)$	Incident light intensity spectra ($W \cdot m^{-2} \cdot nm^{-1}$)
f	Light fraction, $f = t_l/t_C$ (-)
F	Radiant energy flux vector ($W\,m^{-2}$)
g	Gravitational acceleration (9.81 $m.s^{-2}$)
h	Planck's constant (6.63×10^{-34} $J \cdot s$)
h_D	Height of liquid dispersion (m)
H_0	Gas-free liquid height (m)
H_d	Draft tube height (m)
H_b	Bottom height (m)
H_s	Separator height (m)
I	Light intensity / PFD, cumulative over PAR range ($\mu mol \cdot m^{-2} \cdot s^{-1}$)
I_0	Light intensity at the surface ($\mu mol \cdot m^{-2} \cdot s^{-1}$)
$I(\lambda)$	PFD at wavelength λ ($\mu mol \cdot m^{-2} \cdot s^{-1}$)
$I_0(\lambda)$	Incident PFD at wavelength λ ($\mu mol \cdot m^{-2} \cdot s^{-1}$)
$K_a(\lambda)$	Specific extinction coefficient ($m^3 kg^{-1}$)
$K_{a,max}$	Maximal absorption coefficient (m^{-1})
K_a	Average specific extinction coefficient ($m^3 kg^{-1}$)
K_x	Constant for scattering by cells ($kg.m^{-3}$)
K_z	Constant for scattering by light path length (m)
k	Kinetic constant for biomass production rate (-)
k_c	Rate constant (s^{-1})
k_a	Absorption coefficient for photons ($m^2 \cdot mol^{-1}$)

L_r	Riser length (m)
L_d	Downcomer length (m)
Me	Maintenance constant (h^{-1})
N_{av}	Avogadro's number (6.022×10^{23} photons·mol^{-1})
$p(\theta, \theta')$	Phase function for scattered light
P_{O_2}	Rate of oxygen production ($g.g^{-1}h^{-1}$)
Q	Volumetric flow rate ($m^3.s^{-1}$)
Re	Reynolds number (-)
r, R	Radius (m)
R_c	Radius of outer column (m)
R_d	Radius of draft tube (m)
r_m^*	Maximum rate of energy consumption (mol·cells·s^{-1})
$s(z, \theta)$	Light path length for bidimensional model (m)
t_C	Cycle time (s)
t_l	Light time (s)
t_d	Dark time (s)
T	Residence time (s)
U_G	Superficial gas velocity ($m.s^{-1}$)
U_{Gr}	Superficial gas velocity in the riser ($m.s^{-1}$)
U_{Lr}	Superficial liquid velocity in the riser ($m.s^{-1}$)
U_{Ld}	Superficial liquid velocity in the downcomer ($m.s^{-1}$)
v	Circulation velocity ($m.s^{-1}$)
v_c	Mean circulation velocity for a cycle ($m.s^{-1}$)
V_{Lr}	Linear liquid velocity in the riser ($m.s^{-1}$)
V_{Ld}	Linear liquid velocity in the downcomer ($m.s^{-1}$)
w	Minimum angle of a light path that can reach z with opaque draft tube (rad.)
x_1	PSF fraction "active" (-)
x_2	PSF fraction "closed" (-)
x_3	PSF fraction "inhibited" (-)
$y(i)$	Fraction of cells in interval i (-)
z	Distance from illuminated surface (m)

Greek Letters

α	Kinetic rate constant of photon utilization for transfer $x_1 \rightarrow x_2$ $((\mu\text{mol.m}^{-2})^{-1})$
β	Kinetic rate constant of photon utilization for transfer $x_2 \rightarrow x_3$ $((\mu\text{mol.m}^{-2})^{-1})$
γ	Kinetic rate constant of transfer $x_2 \rightarrow x_1$ (s^{-1})
δ	Kinetic rate constant of transfer $x_3 \rightarrow x_1$ (s^{-1})
σ	Hydrodynamic model parameter (m.s^{-1})
ϕ	Hydrodynamic model parameter (-)
ε	Gas hold-up (-)
ε_r	Gas hold-up in riser (-)
ε_d	Gas hold-up in downcomer (-)
ς	Ratio of inhibition rate to recovery rate (-)
η	Fluid viscosity ($\text{kg.s}^{-1}\text{.m}^{-1}$)
ρ	Fluid density (kg.m^{-3})
θ	Angle (radians)
λ	Wavelength (nm)
μ	Specific growth rate (h^{-1})
μ_{max}	Maximum specific growth rate (h^{-1})
ω	Incident angle (radians)

Indices

d	Downcomer
r	Riser
s	Separator
c	Column

Chapter 1

Introduction

1.1 Context and scope for this study

Algal biotechnology is receiving increased attention, particularly in the areas of producing biodiesel from algae (Chisti, 2008, 2007), biohydrogen production (Berberoglu *et al.*, 2007), algal biomass for combustion (Bruhn *et al.*, 2011), anaerobic digestion to produce biogas energy (Schamphelaire & Verstraete, 2009) and CO_2 removal from flue gas (Chiu *et al.*, 2008; Vunjak-Novakovic *et al.*, 2005). Algae also have many other varied uses and are currently used in the production of foods and health foods, as aquaculture feeds, and for the production of pigments, polyunsaturated fatty acids and other fine chemicals (Eriksen, 2008).

The rising demand for energy from developing nations, towards the per capita use by developed nations, threatens the availability of sustainable energy for future generations (Kunjapur & Eldridge, 2010). Concurrently, impending global climate change concerns have manifested in a consciousness for developing processes with little or no carbon footprint. Algal bioenergy shows huge potential to alleviate both of these concerns, by simultaneously consuming CO_2 during photosynthetic growth and supplementing energy demands from a completely renewable energy source - the sun.

Improving the feasibility of algal bioenergy processes calls for the development of algae production stages that provide biomass with the highest potential for energy production at the lowest cost (Merchuk *et al.*, 2007). Subsequent to sourcing and selecting an optimal algae strain, the next step in the optimization, and the key focus of this project, is the design of optimal photobioreactors for producing biomass.

This project combines modelling with experimental investigation to simulate conditions experienced by cells inside a photobioreactor. By developing a mathematical model of a photobioreactor, one may predict the operation of a real reactor under any given set of conditions, as well as analyze the dynamics of a system to changing inputs. This allows the optimum design conditions to be proposed before performing validation experiments, thereby limiting cost and time.

For the model to achieve this, it has to represent the basic characteristic of algal growth kinetics and bioreactor behaviour. There are many controlling parameters in an algal photobioreactor that characterize growth, namely: nutrients supply, CO_2 mass transfer, the provision of light, mixing, pH and temperature control. The scope of this project focused on one of the most important of these effects: light provision. Light provision, when combined with fluid dynamics, causes algae cells to experience fluctuating light inside photobioreactors, which influences their growth characteristics.

While the impact of light supply and fluid dynamics on the production of microalgae is relevant across the range of applications for bioenergy, in this thesis its impact was considered in terms of the case study of the production of algal biodiesel. Algae are able to store large amounts of oil, which makes them an attractive source for biofuels. Fig.1.1 shows the key components of a generalized algae to biofuels process. The process starts with a biomass production step, requiring water, nutrients, light and CO_2. The second step recovers the biomass and concentrates it via dewatering, allowing a recycle of water and nutrients. Subsequently, the algal oil is extracted with a water-immiscible solvent. The oil is then be converted to biodiesel using existing methods, such as transesterification (Chisti, 2008, 2007). The remaining biomass after oil extraction can be utilized for high-protein animal feed, fertilizers or as a source for other high value microalgal products (Grima *et al.*, 1999). However, the majority of the biomass residue is envisaged to undergo anaerobic digestion to form biogas, which can serve as the source of energy for the process, with any surplus energy sold elsewhere to improve the economics of the process (Chisti, 2007).

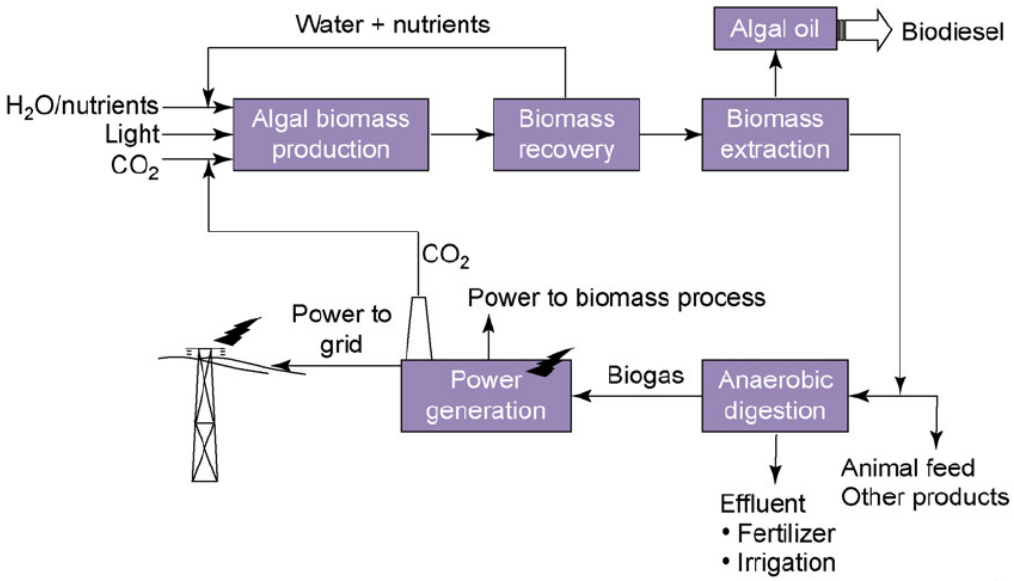

Figure 1.1 – A generalized process for producing microalgal oil for biodiesel. Image source: Chisti (2008)

For biodiesel production, a high oil or "lipid" content of the algae species is desirable. Recognizing this, Griffiths & Harrison (2009) collated 50 algae species according to their lipid productivities using literature data. This has been extended to experimentation using 10 species (Griffiths *et al.*, 2011b). From this data, which is given in Appendix A, the algae species *Scenedesmus* sp. showed a

comparatively high lipid productivity. As a result, it was chosen as the model species for use in this work.

Numerous photobioreactor types show potential for biofuel applications. In this study, the airlift photobioreactor was chosen as a case study for the model, owing to its many advantages over other reactor types. The background to this choice is presented in the Literature Review (Section 2.5.4). With the airlift reactor in mind, separate models were developed for light distribution, kinetic growth and fluid dynamics. These models were analyzed independently to investigate the effects of light availability on algal growth and to show the potential for using the models as tools for optimal airlift design. The three models were then integrated into a global model to enable simulation of algal growth in an airlift reactor. Since an airlift reactor can be used for any of the numerous algal to bioenergy applications listed above, the results of this study are not exclusively limited to the algal biofuels process.

1.2 Thesis structure

The literature review and theory is presented in Chapter 2. The first part concerns light, photosynthesis and algae cultivation in photobioreactors, the second part concerns the modelling of photobioreactors. The modelling of photobioreactors is decoupled into three components, or sub-models: light distribution, kinetic growth and fluid dynamics.

The three subsequent chapters (3,4 & 5) deal with each of the three modelling components separately showing the development for each model. Significant experimental work was performed for each model to obtain the necessary model parameters. Thus, each chapter contains its own experimental methods and experimental results. Each chapter then presents a discussion of these results along with model simulations, with the aim of optimization in mind.

Chapter 6 brings all three models together to develop a global model for an airlift reactor. The model development is outlined along with the method of simulation and comparison to experimental data. Finally, overall conclusions from this work are presented in Chapter 7.

Chapter 2

Literature review and theory

The literature review is divided into two parts. The first (Section 2.1 to 2.6) focuses on the system of algae and includes photosynthesis, provision of light, algae cultivation, photobioreactors and light/dark cycles. The second part (Section 2.7 to 2.10) concerns literature relevant to modelling photobioreactors and incorporates three main aspects, namely: light distribution, kinetic growth and hydrodynamics. The literature review forms the basis for the third section (Section 2.11) of the chapter, in which the objectives for the study presented are outlined.

2.1 The fundamentals of algal photosynthesis

Sunlight is the fundamental source of energy in the biosphere and photosynthesis is the process whereby this solar energy is converted into biologically usable energy. Algae are simple eukaryotic organisms which exploit photosynthesis to convert carbon dioxide and water into organic material. The net reaction mechanism can be generalized according to Eq. 2.1:

$$n\mathrm{CO_2} + n\mathrm{H_2O} + \text{light} \longrightarrow (\mathrm{CH_2O})_n + n\mathrm{O_2} \tag{2.1}$$

Light is composed of photons which, when absorbed by pigments within the algae cells (primarily *chlorophylls* and *carotenoids*), lead to the excitation of electrons and the potential to produce chemical work. Through a series of reaction steps, carbon is converted from its highest oxidized state $(\mathrm{CO_2})$ to strongly reduced compounds in the form of organic material or sugars $(\mathrm{CH_2O})_n$. This process liberates oxygen, whilst water is needed as an additional substrate.

Photosynthesis involves two types of reactions (Fig. 2.1) that work in unison: light dependent *light reactions*, and light independent *dark reactions*.

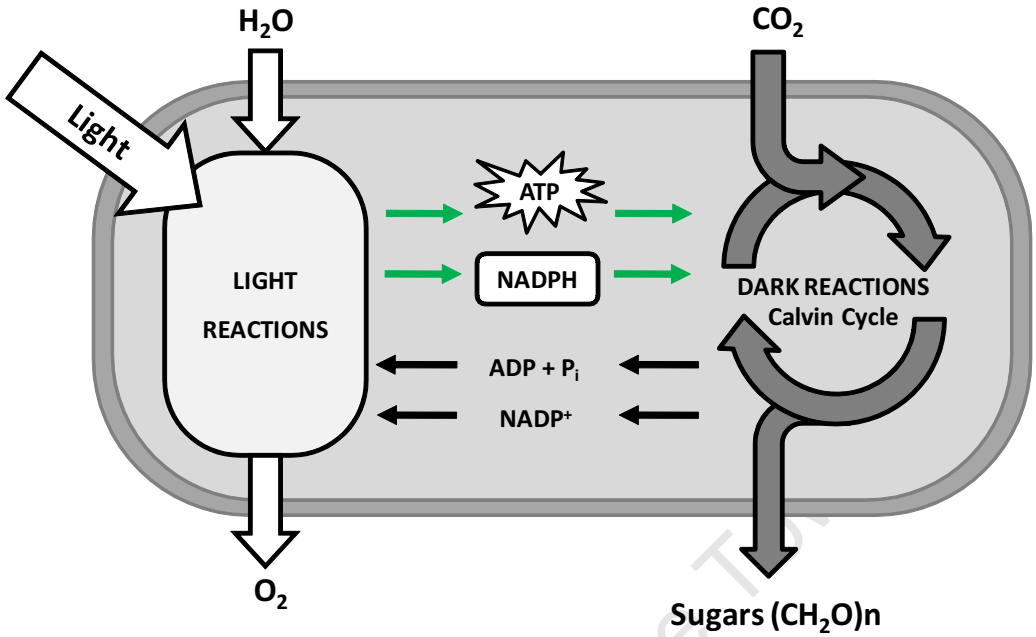

Figure 2.1 – Schematic of photosynthesis, showing light and dark reactions working in unison. Image source: this author.

Light reactions require the energy of light to make energy carrier molecules, ATP (adenosine triphosphate) and NADPH (nicotinamide adenine dinucleotide phosphate). The reactions take place within the thylakoid membranes (Fig. 2.2). The energy transforming units (electron transport) are two large protein complexes termed Photosystem I (PSI) and Photosystem II (PSII), which operate in series (Barsanti & Gualtieri, 2006).

The dark reactions utilize the reducing power and energy in the form of NADPH and ATP from the light reactions to implement a sequence of reactions to fix and reduce inorganic carbon via the Calvin Benson Bassham Cycle (Figure 2.3). The dark reactions do not necessarily occur in the dark; they occur simultaneously with the light reactions, without light being required. The critical rate limiting enzyme in this cycle is RuBisCo (Ribulose-1,5-bisphosphate carboxylase oxygenase), which catalyses the capture of CO_2 into the cycle, subsequently leading to the formation of sugars (Yoshimoto *et al.*, 2005).

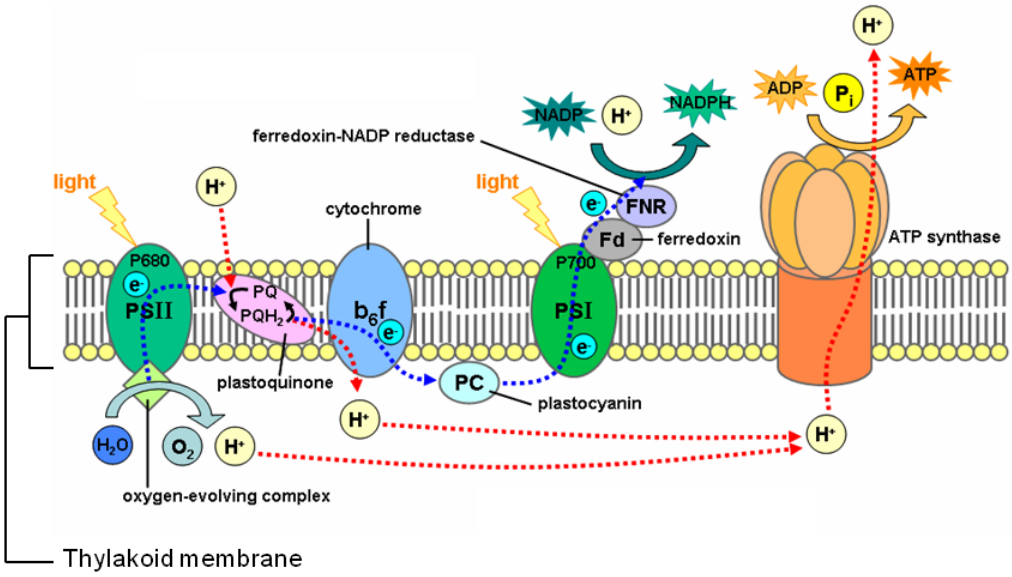

Figure 2.2 – Photosynthesis light dependent reactions (PSII and PSI). Image source: Wikimedia commons.

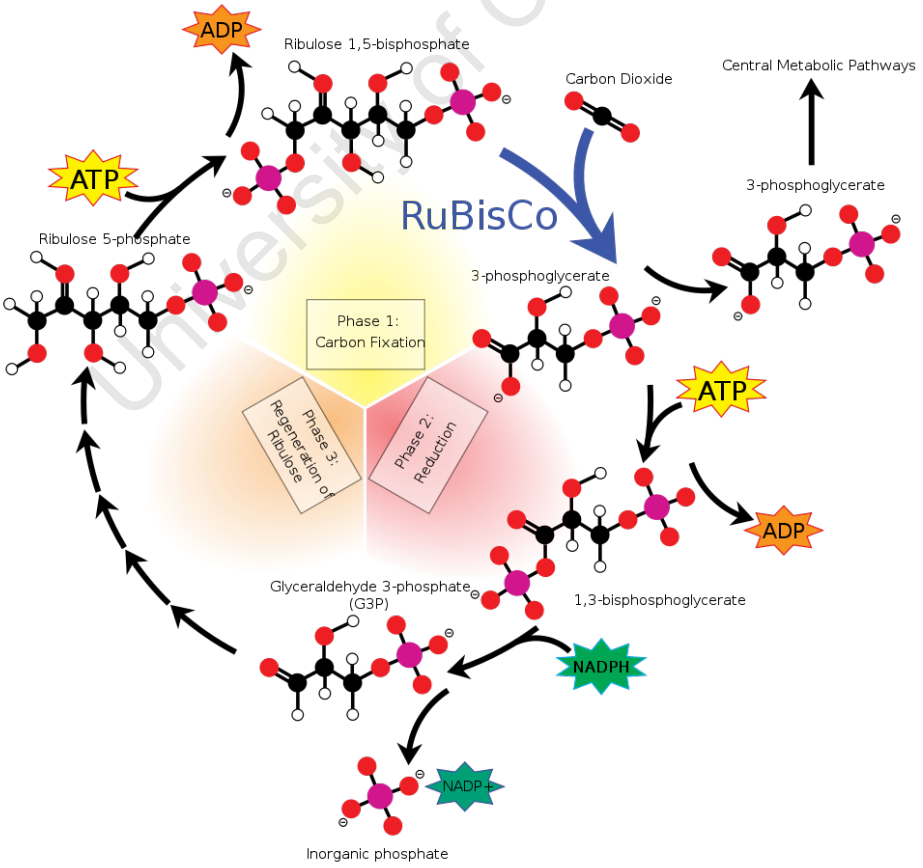

Figure 2.3 – The Calvin-Benson Bass Cycle of the dark reactions. Image source: Wikimedia commons.

2.2 The dependence of photosynthesis on light

2.2.1 Light intensity as irradiance

Photosynthetic rate shows a strong dependency on light intensity. Sunlight is composed of a broad range of electromagnetic radiation, shown in Fig. 2.4. Only light between 400 nm and 700 nm can be absorbed and utilized by algae. This part of the spectrum is termed Photosynthetic Active Radiation (PAR). On an energy basis, 43% of solar radiation lies within the PAR region (Janssen, 2002). Light intensity is most commonly expressed on an energy basis, as *irradiance (*or *radiant flux density),* with units of $\mathrm{W\,m^{-2}}$. Fig. 2.4 shows the *spectral irradiance* of sunlight, i.e. how the intensity of the light varies with wavelength. This can be described as the "energy composition" of light.

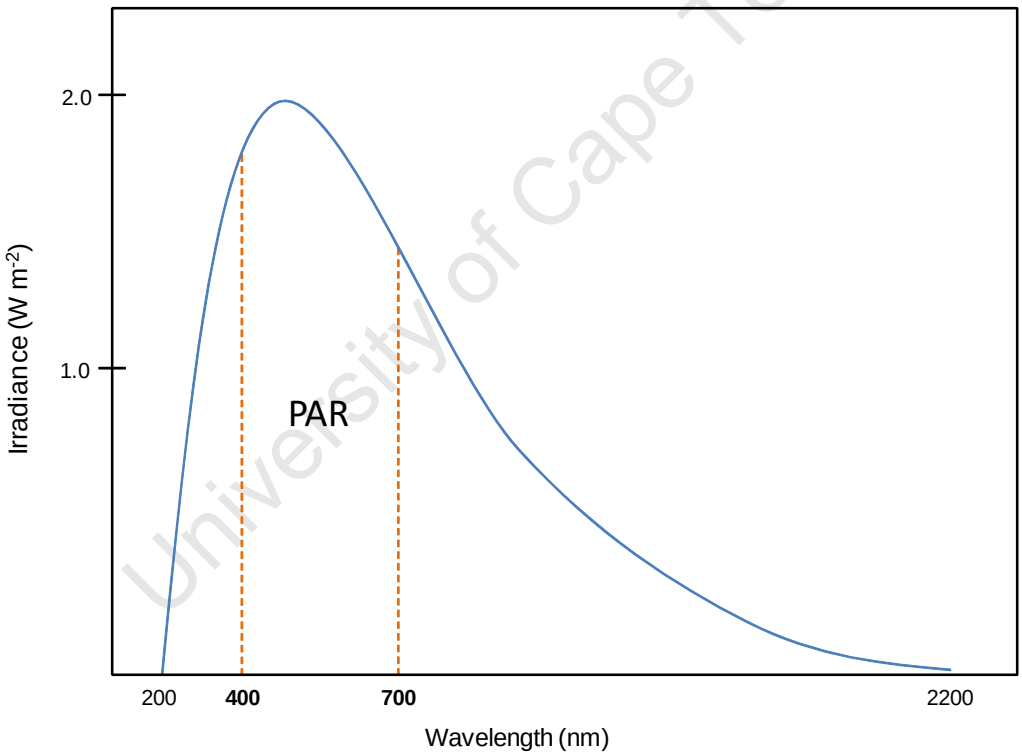

Figure 2.4 – Simplified schematic of typical spectral irradiance for sunlight $(\mathrm{W\,m^{-2}})$, showing the PAR range. Image source: this author

Algae can be grown in natural or artificial light. Since outdoor sunlight cannot be controlled, many studies investigating algal growth are performed under controlled conditions using artificial light sources. These have a different spectral irradiance to natural sunlight, as illustrated in Fig. 2.5.

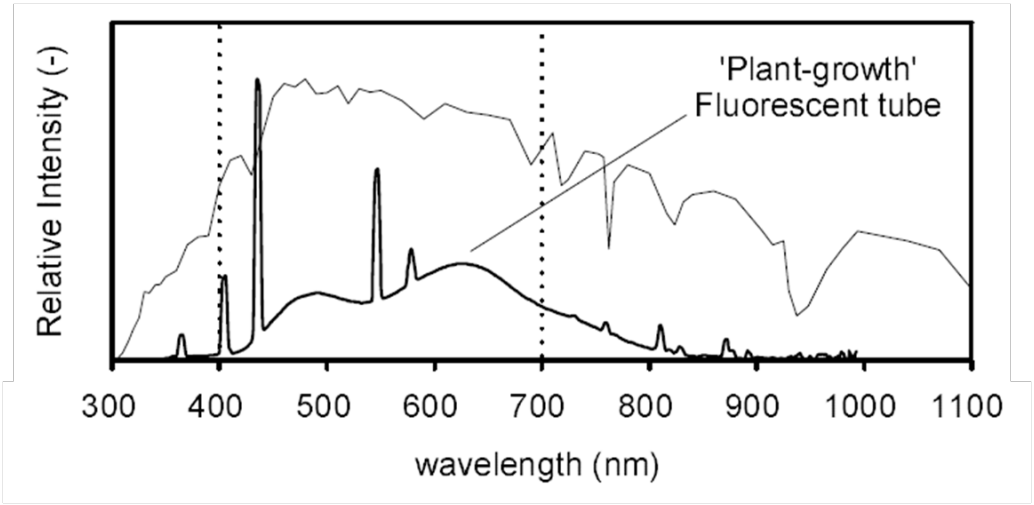

Figure 2.5 – The relative intensity (on an energy basis) of an artificial light source (bold line) to that of natural sunlight (thin line). The dotted lines show the PAR range. Image source: Janssen (2002).

2.2.2 Light intensity as photon flux density (PFD)

Photosynthesis is a quantum process, involving the direct absorption of photons. Thus, when relating light intensity to photosynthetic rate, it is more appropriate to express light intensity as a *photon flux density* or PFD rather than as an irradiance. PFD is the number of photons passing through a flat surface per unit of time, having units μmol·m^{-2}·s^{-1}. The number of photons in light at any given wavelength is directly related to the energy of light at that wavelength. Firstly, the energy of a single photon (E_p) is given by:

$$E_p = \frac{hc}{\lambda} \tag{2.2}$$

where h is Planck's constant (6.63×10^{-34} J·s), c is the velocity of light (3×10^8 m·s^{-1}) and λ is the wavelength of the photon in nanometers (nm). The shorter the photon wavelength, the higher its energy. Thus, photons contained within light of different wavelengths possess different energies. To convert from irradiance to PFD, the available light energy is divided by the energy of photons at each wavelength in the PAR range, the integral of which gives the overall PFD:

$$I = \int_{400}^{700} \frac{E_0(\lambda)d\lambda}{N_{av}\left(\frac{hc}{\lambda}\right)\cdot 10^9} \tag{2.3}$$

where I expresses the overall PFD for the PAR range (μmol·m^{-2}·s^{-1}) , $E_0(\lambda)$ is the incident light intensity on an energy basis for wavelength interval $[\lambda, \lambda + d\lambda]$ with units (W·m^{-2}·nm^{-1}) and N_{av} is Avogadro's number (6.022×10^{23} photons·mol^{-1}). In this thesis, light intensity (I) always refers to photon flux density (PFD).

2.2.3 Light absorbance by algae

When light travels through an algal culture, light waves are either scattered or absorbed (Barsanti & Gualtieri, 2006). Scattering is the process whereby cells cause light to be reflected and refracted in all directions, the extent of which is dependent on the optical properties and size of the cells. In scattering, no energy transformation occurs, there is only an altering in the spatial distribution of the radiation. Absorption, on the other hand, is the process whereby light is retained by algae and the free energy of the photons absorbed can be used to carry out work. Pigments embedded in special proteins constitute "light harvesting complexes" and are responsible for light absorption (Barsanti & Gualtieri, 2006). If excess energy is absorbed, it is either emitted as fluorescence or dissipated as heat.

Algae absorb varying amounts of light at each wavelength in the PAR range. Thus, each species of algae has a unique absorption spectrum. In spectroscopy, the mathematical definition of "absorbance" (symbol A) is defined as:

$$A(\lambda) = ln\frac{I_0(\lambda)}{I(\lambda)} \tag{2.4}$$

where $I_0(\lambda)$ is the intensity of light at a specific wavelength before passing through a sample, and $I(\lambda)$ is the light intensity after passing through the sample.

Absorption increases at higher algal concentrations, since a denser medium can absorb more light. Fig. 2.6 shows an example of an absorbance spectrum for *Chlorella vulgaris* at varying concentrations. The spectrum shows two peaks, one near 430 nm and the other near 675 nm, which is a typical characteristic of absorption spectra of a green algae containing *chlorophyll a* as the major light-harvesting pigment (Yun & Park, 2001). The absorbance peaks are clearly more distinct at higher concentrations.

It is well accepted that the absorbance of light as it penetrates an algal suspension causes an exponential decrease in light intensity with increasing depth of the light path, as illustrated in Fig. 2.7. Thus, algae cells within a photobioreactor experience varying amounts of light, which has an effect on their photosynthetic growth. For this reason, modelling of the light distribution profiles inside photobioreactors is a critical component of the overall model. This is discussed in more detail in Section 2.8 of the Literature Review.

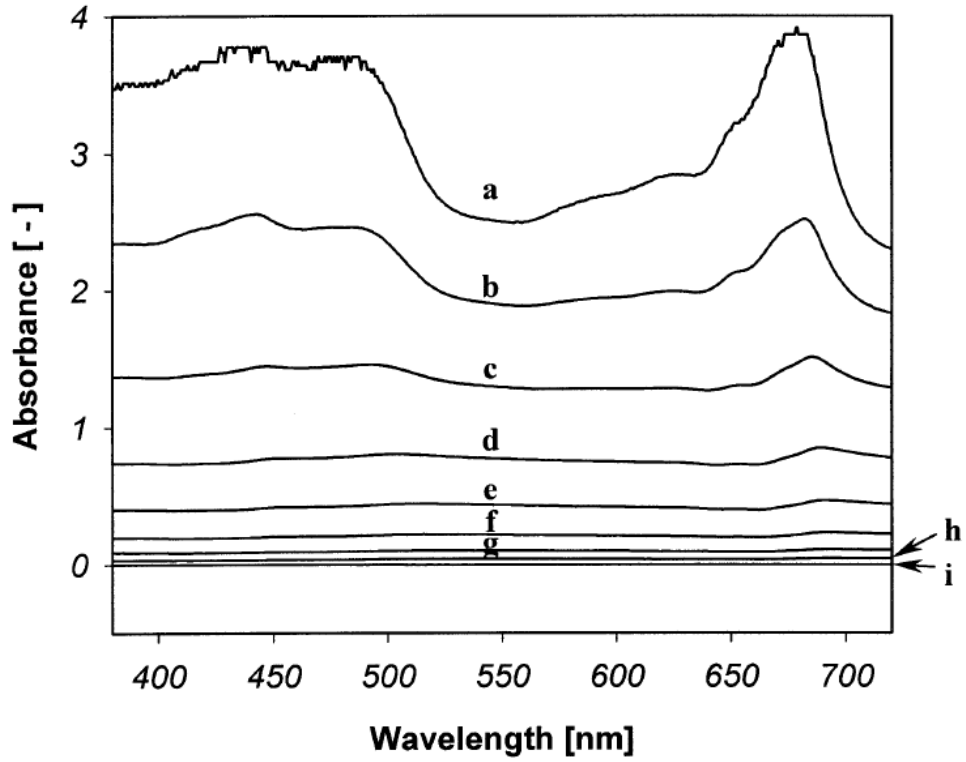

Figure 2.6 – Absorption spectra of *Chlorella vulgaris*. Cell concentrations (kg m^{-3}): *a* 1.71, *b* 0.855, *c* 0.427, *d* 0.217, *e* 0.107, *f* 0.054, *g* 0.027, *h* 0.013, *i* 0.00. Image source: Yun & Park (2001).

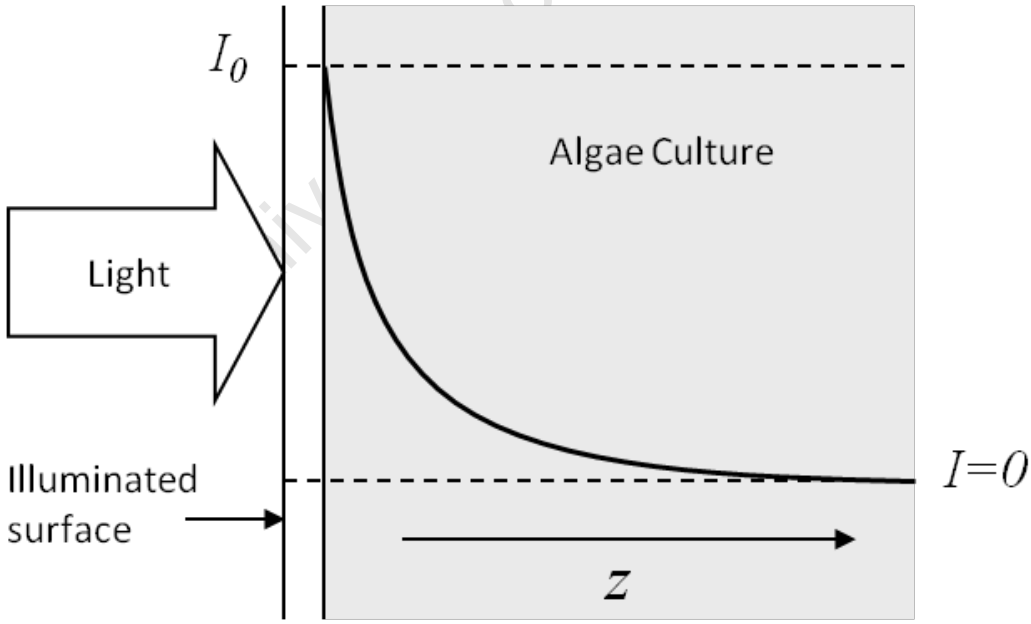

Figure 2.7 – Schematic of exponential light intensity decay when passing through an algal suspension. Image source: this author

2.2.4 The P versus I Curve

The relationship between available light and photosynthetic rate can be represented by the P-I curve, shown in Fig. 2.8. Since photosynthesis is a complicated process, involving many reaction pathways, overall photosynthetic rate is usually measured by measuring the rate of oxygen production P_{O_2} since it is directly related according to Eq. 2.1.

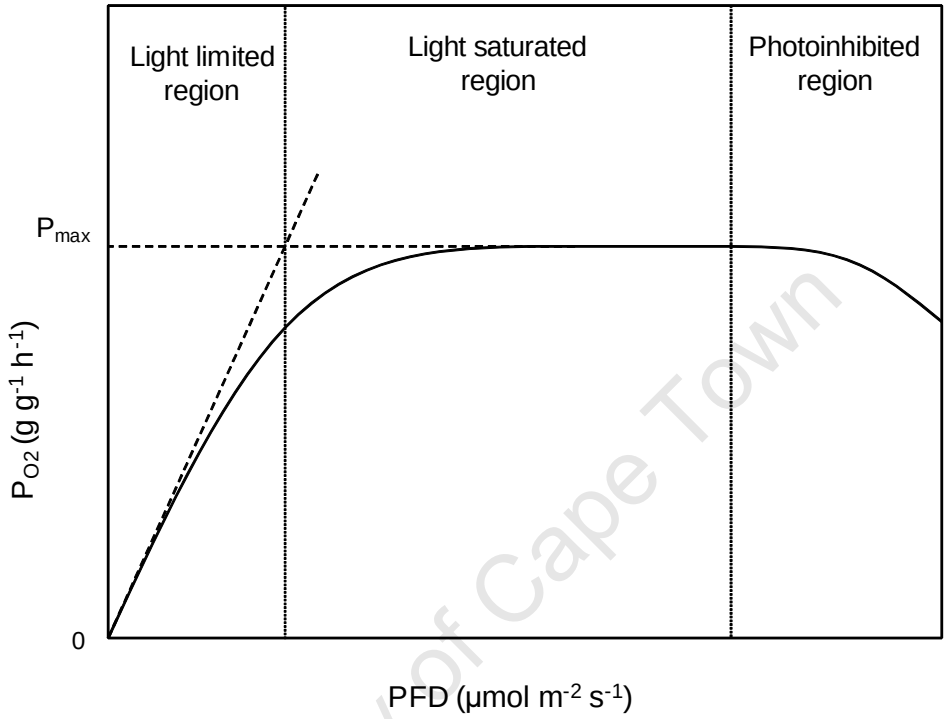

Figure 2.8 – Schematic of a typical P-I curve: photosynthetic rate, measured as oxygen production rate P_{O_2}, versus light intensity, measured as PFD. Image source: this author

The P-I curve has three characteristic regions: a light limited region, a light saturated region and a light-inhibited region:

- **Light limited photosynthesis**

  In the light limited region, oxygen production rate increases linearly with increasing PFD and the rate of photon absorption determines the rate of steady-state electron transport from H_2O to CO_2 (Barsanti & Gualtieri, 2006). The available light is insufficient to support the maximum rate of the light dependent reactions, and thus photosynthesis is limited.

- **Light saturated photosynthesis**

  At moderately high PFDs, the rate plateaus and the algal culture reaches its maximum oxygen production rate. This maximal region is the light saturated region. Any further increase in PFD cannot be utilized, since the rate of photon absorption exceeds the rate of steady-state electron transport from H_2O to CO_2 (Barsanti & Gualtieri, 2006). Any surplus energy not used for photosynthesis is dissipated as either heat or fluorescence.

- **Light-inhibited photosynthesis: photoinhibition**

  Further increases of light intensity beyond light saturation can lead to photoinhibition, a decrease in photosynthetic rate from the maximum at saturation. The decreased rate results from a reduction in the photochemical efficiency of PS II, via a reduction in the population of functional reaction centers. Barsanti & Gualtieri (2006) attributed photoinhibition to an over-absorption of photons per reaction center with increased PFD, i.e the absorption of two photons simultaneously, when the machinery is only "designed" to handle one. Merchuk *et al.* (2007) postulated that this causes temporary damage the chromophore's D1 proteins. Minor photoinhibition is reversible with time (Wu & Merchuk, 2001) whereby cells are able to recover however, excessive exposure to light can lead to cellular death. Since excess photons absorbed are dissipated as heat or fluorescence, a reduction in the rate of photosynthesis leads to an increase in the rate of fluorescence. For this reason, measurements of variable fluorescence emissions can be used to infer information about the extent of photoinhibition (Vonshak *et al.*, 1994).

2.2.5 Photoadaptation

Photoadaptation (also called *photoacclimation*) is the term used to describe the adaptation of algae to their light environment. This change can occur over time scales of hours to days, through changes in cellular pigmentation or structural characteristics, e.g the size and number of photosynthetic units. Increased concentrations of light absorbing pigments in cells is typically observed after having being exposed to low intensity light (Rubio *et al.*, 2003; Janssen *et al.*, 1999). In addition, algae cells are able to adjust photon utilization by changing the distribution of harvested energy between photosystems (Barsanti & Gualtieri, 2006). These changes are observable by factors such as chlorophylls per cell or per unit surface area, which can increase five to ten fold with increased PFD (Barsanti & Gualtieri, 2006). Photoadaptation often occurs when algae are exposed to fluctuating light. Janssen *et al.* (1999) reported the species *C. reinhardtii* doubling its *chlorophyll-a* content to increase its specific light absorbing surface under intermittent illumination [1] in comparison to continuous illumination.

[1] *chl-a* content increased from 10.3 to 20.2 mg.g^{-1}when changing from continuous to intermittent light/dark cycles of 13 s duration and a light fraction of 0.67 at PFD of 240 μmol $\cdot$ m^{-2}s^{-1}

2.3 Parameters affecting algal growth in photobioreactors

In all cultivation systems, algal growth is influenced by numerous factors, such as: light supply, mixing, water, dissolved CO_2 and O_2 concentration, nutrient supply, temperature and pH. A general understanding of these factor is required to compare reactor designs effectively.

2.3.1 Nutrient supply

Algae require more elements than those listed in Eq. 2.1 to grow and survive. The two essential elements are nitrogen and phosphorous. These have considerable influence on growth rate and lipid content. Other nutritional requirements include carbon, hydrogen, oxygen, sulphur, calcium, magnesium, sodium, potassium, and chlorine. Certain micro-elements, required in trace amounts, are iron (essential), boron, manganese, copper, molybdenum, vanadium, cobalt, nickel, silicon and selenium. The exact elemental requirements and ratios of these nutrients is species specific. Often certain nutrients are supplied in excess, such as phosphorous since it reacts with the metal irons present (Chisti, 2007). Nutrient limitation puts stress on the culture's growth ability. Under minor limitations the cells generally adapt their physiological characteristics. This phenomenon can be exploited in the case of N or P limitations, which increases the lipid content in the cell, but there is a trade-off between productivity and lipid content (Kunjapur & Eldridge, 2010).

2.3.2 Light supply

An optimum reactor type is one that maximises light intensity and light penetration, as well as the frequency of cellular exposure to light. Thus, as a general rule, maximization of the surface area to volume ratio is an important design consideration for all photobioreactors. The reactor geometry is the most important factor influencing light distribution. This is primarily determined by the variation in light path length from the external surface (e.g tube diameter in the case of a tubular reactor) but also the culture density. Since cells will experience varying light conditions, light/dark cycles are also highly influential in affecting algal growth, these are discussed in detail in Section 2.6.

2.3.3 Mixing and fluid dynamics

Mixing is critical for homogeneous distribution of cells, metabolites and heat; as well as to ensure adequate gas-liquid mass transfer (Eriksen, 2008; Richmond, 2004; Grobbelaar, 2000). Importantly, mixing causes cells to experience fluctuating light conditions when they move through regions of varied light intensity, this has a direct effect on photosynthetic rates. High levels of mixing can lead to high shear stress and potential cellular death. Shear stress is often used as an argument against

mechanical mixing in algal cultures. It has been recently suggested by both Eriksen (2008) and Kunjapur & Eldridge (2010) that bubbles may be the main cause of damage to algae by cellular adhesion to the bubble surfaces. As a result, shear damage could be as much of an issue in pneumatically mixed photobioreactors as their mechanically agitated counterparts.

2.3.4 Water consumption

Water supply is an increasing global concern and a key factor influencing reactor choice. Unlike conventional crops, many strains of algae do not require freshwater for cultivation. Instead, they can be grown using wastewater since it is often high in nitrogen and phosphorous concentrations. This provides two benefits: the algae receive an easily available and inexpensive medium rich in nutrients, and the wastewater is further treated resulting in reduced N and P levels. Marine algae can be grown using seawater supplemented with commercial nitrate and phosphate fertilizers (Grima *et al.*, 1999).

2.3.5 CO_2 consumption

Algae contain approximately 50% carbon by dry weight, which is almost completely derived from carbon dioxide. A minimum amount of carbon dioxide is essential for photosynthesis to occur, but excess CO_2 can hinder photosynthetic rates. Optimum CO_2 concentrations have been found to be in the range of 1-5 % by volume (Kunjapur & Eldridge, 2010). Flue-gas is a highly suitable an inexpensive (or free) source of CO_2 (up to 13 % by volume) and its consumption reduces green house gas emissions (Chisti, 2007).

2.3.6 Oxygen removal

Oxygen is a byproduct of photosynthesis (Eq. 2.1). Excess oxygen is undesirable and when combined with high light intensities it leads to photooxidative cellular damage (Chisti, 2007). An example of how this can impact on photobioreactor design is mentioned in more detail in the discussion of tubular photobioreactors (Section 2.5.2), where the effect of oxygen build up puts a constraint on tube length during scale-up.

2.3.7 Temperature control

Although algae can survive over a variable temperature range, optimal growth is often found within a narrow range specific to each strain. For example, Kunjapur & Eldridge (2010) mention the optimum temperature range for *Nannochloropsis*, *Tetraselmim*s and *Isochrysis* to be 19-21, 19-21 and 24-26 ºC, respectively. Since ambient temperature varies considerably, as a result of day/night, climatic and geographic factors, control of culture temperature is critical to ensure optimal productivity.

2.3.8 pH control

Each algae strain grows optimally in a narrow range of pH values. The pH of a culture medium is linked to the concentration of bicarbonates (dissolved CO_2). Cyclic pH variations are observed for outdoor photobioreactors, increasing during the daytime (photosynthesis consuming CO_2) and then decreasing during the night (Danquaha *et al.*, 2009). For this reason, pH control must be implemented in a commercial reactor for optimal productivity.

2.4 Open photobioreactors

Algae cultivation systems are generally classified into two groups: *open* (e.g raceway ponds) or *closed* systems (photobioreactors). Large-scale cultivation of algae in open ponds was conceived as early as the second World War in Europe, the purpose being to grow algae as a food supplement (Carvalho *et al.*, 2006). Since then, algae has been grown on an industrial scale in open systems all over the world for applications from food production to fertilizers. More recently, algae have attracted more attention, due to their potential as a feedstock for producing valuable chemicals and renewable bioenergy. The former requires cultivated in contaminant free closed photobioreactors (Ugwu *et al.*, 2008) while the latter is sensitive to optimized productivity.

Raceways ponds (Fig. 2.9) are the most common type of open system. They are relatively shallow (< 30cm), with water, nutrients and algae being continually circulated by means of a paddle wheel. CO_2 is supplied by one or more spargers. Open ponds, along with most closed photobioreactors, must be connected to a harvesting system, which periodically (or continuously) collects the biomass for downstream processing, and supplies fresh medium as a replacement (Chisti, 2007).

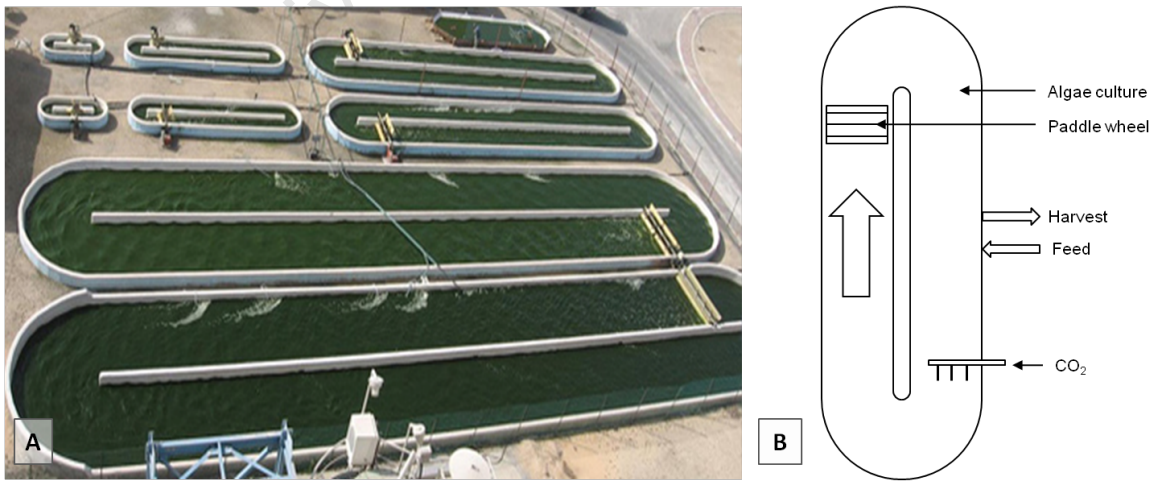

Figure 2.9 – (A): Commercial scale raceway ponds from Seambiotic, Ltd. (B): 150,000 liter raceways (B) Raceway schematic showing the basic elements of construction. Image sources: (A) http://www.seambiotic.com, (B) this author.

Raceways are more affordable, easier to construct, and simpler to operate than most closed photobioreactors. They are proven to be economical for applications such as growing algae for food products. For example, BioDELTA (Stellenbosch) grows pure *Spirulina* which is sold as a health supplement. Despite such successes, raceways have many disadvantages over closed systems. Raceway utilize light less efficiently and have large evaporation losses due to a large exposed surface area which also allows diffusion of CO_2 to the atmosphere. As a result of extremely poor mixing characteristics, they exhibit low mass transfer rates of CO_2 and nutrients. They require a larger land area use (Fig. 2.9) and achieve lower biomass concentrations than closed photobioreactors (Richmond & Cheng-Wu, 2001) making them inherently less productive .

A further technical challenge of open systems is contamination, as well as competition and predation by other fast growing heterotrophs (Ugwu *et al.*, 2008). As a result, it is very difficult to maintain a monoculture of a single desired strain in an outdoor open environment. Thus, only the most resilient algal species are able to be grown in open commercial systems. These species usually thrive in extreme environments that inhibit competition (Kunjapur & Eldridge, 2010), for example: *Dunaliella salina* at high salinity and *Spirulina platensis* at high alkalinity (Janssen, 2002). Many *other* algal species are promising for the production of valuable compounds and bioenergy, but require a contaminant free mono-culture to survive. In addition, raceways offer insufficient control of almost all growth conditions. Closed photobioreactors facilitate the need for stringent control and overcome many of the aforementioned limitations.

2.5 Closed photobioreactors

The industrial-scale production of single species algal biomass for highly valuable products (e.g., polyunsaturated fatty acids, vitamins, pharmaceuticals, etc.) is *only* feasible in closed photobioreactors (Carvalho *et al.*, 2006; Walter *et al.*, 2003; Grima *et al.*, 1999). According to Chisti (2007), algae for biofuel production can be produced in open systems, but there are many advantages of using closed systems, in particular, the substantially higher biomass concentrations achievable (30 times that obtainable in a raceway) and higher achievable volumetric productivities (10 times that obtained in a raceway). Closed photobioreactors are significantly more expensive than open systems, but it has been argued that as costs are reduced in the future they will become the reactors of choice for biofuel production (Kunjapur & Eldridge, 2010).

The most significant parameter of those mentioned in Section 2.3 that affects photobioreactor design, is the provision for efficient light utilization (Carvalho *et al.*, 2006). Many photobioreactor designs have been proposed, but only certain geometries are effective at utilizing light energy. These are generally classified as: *flat-plate*, *tubular*, or *vertical column* photobioreactors. Fig. 2.10 shows these three types conceptually.

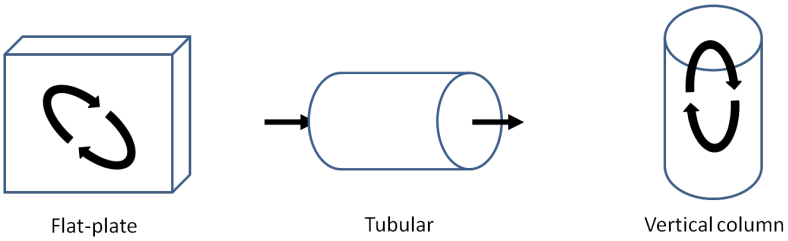

Figure 2.10 – Conceptual geometries of the three main photobioreactor types. Image source: this author

Numerous other reactor designs are found in literature that deviate from the three conventional types (e.g cone shaped, dome shaped, helical...), but have these shown limited promise, particularly for biofuel potential (Kunjapur & Eldridge, 2010).

2.5.1 Flat-plate photobioreactors

Flat-plate reactors provide the largest illuminated surface area, while insuring reasonable culture volume, mixing patterns and CO_2 levels (Richmond & Cheng-Wu, 2001). In some cases they comprise of two separate units: a light harvesting unit with short culture depth to maximise photosynthetic efficiency (PE); and a gas exchange unit, where CO_2 is supplied and biomass is harvested. The culture is circulated between these two units by a pump, which needs to be carefully designed so as to prevent shear forces from disrupting the cell integrity (Carvalho *et al.*, 2006). In other cases, the gas injection, harvesting and addition of water for cooling are achieved in a single chamber (Richmond, 2004), as illustrated in Fig. 2.11.

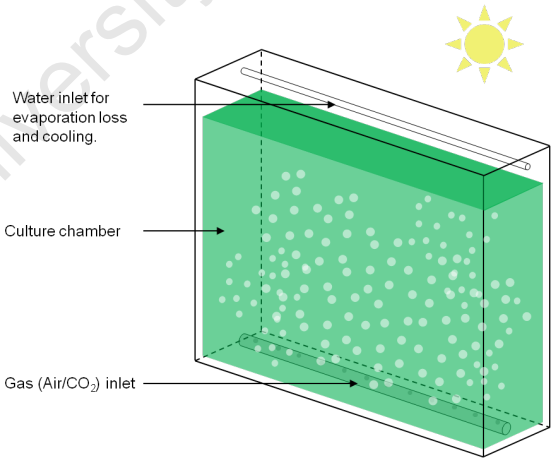

Figure 2.11 – Flat-plate photobioreactor. Image source: this author

Flat plate reactors exhibit a short oxygen path, which results in a lower accumulation of dissolved oxygen than horizontal tubular reactors (Ugwu *et al.*, 2008). Cell damage may occur as a result of the high stress from aeration, a problem that has not been reported in tubular reactors (Kunjapur & Eldridge, 2010). According to Eriksen (2008), flat plate photobioreactors support the highest densities of photoautotrophic cells, which can exceed 80 $g{\cdot}L^{-1}$in the most extreme case.

2.5.2 Horizontal tubular photobioreactors

Of all the closed photobioreactors developed, the design which is most widely accepted as being optimum is that which utilizes the circulation of fluid through a tubular system by the induced bubbling of gas (Fernandez *et al.*, 2001; Grobbelaar, 2000; Camacho *et al.*, 1999; Chisti, 1989). Both horizontal tubular and vertical column reactors are based on this principle.

Horizontal tubular photobioreactors (Fig. 2.12) comprise of an array of straight horizontal tubes (plastic or glass) through which the culture is circulated (Muller-Feuga *et al.*, 2003; Fernandez *et al.*, 2001; Molina *et al.*, 2001; Sobczuk *et al.*, 2000; Camacho *et al.*, 1999). They exist as the largest system for algae cultivation in a closed system, such as the 700 m^3 plant in Klötze, Germany, (Eriksen, 2008). They usually consist of a long tubed section or *solar array*, to maximise light exposure, and a separate gas exchange unit, as illustrated. Mechanical pumps, or ideally, an airlift system, creates the driving force for circulation.

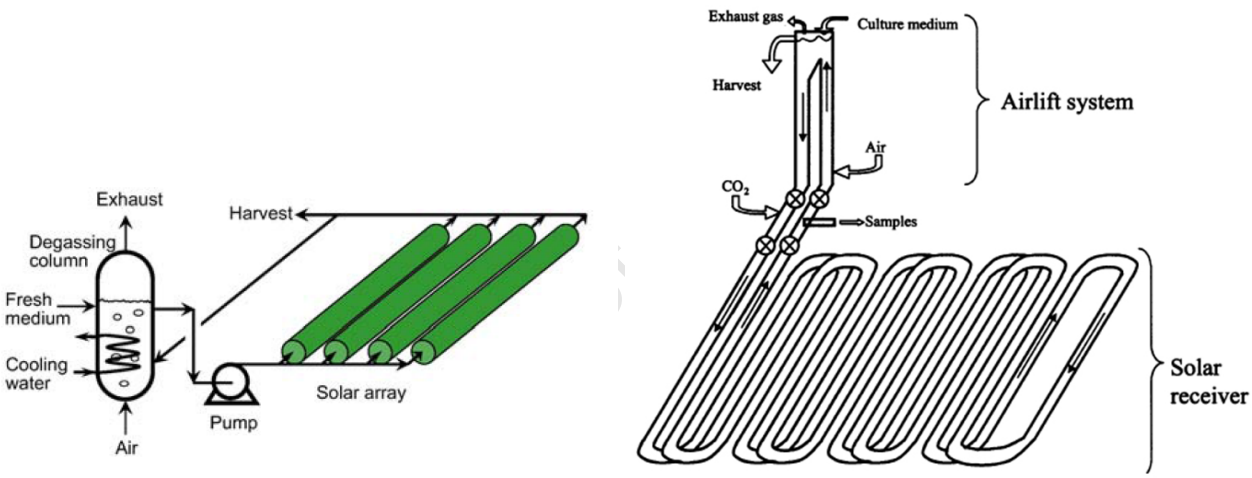

(a) Tubular photobioreactor with parallel run horizontal tubes. Image source: Chisti (2007).

(b) Tubular (horizontal) photobioreactor.Image source: Molina *et al.* (2001)

Figure 2.12 – Two designs of horizontal tubular photobioreactors.

Although these tubular photobioreactors have notable advantages compared to traditional systems (e.g open pond raceways) they still possess limitations:

- Photosynthesis produces a lot of oxygen (Eq. 2.1). High levels of dissolved oxygen inhibits photosynthesis (Chisti, 2007; Molina *et al.*, 2001) and when combined with high light intensities, produces photooxidative damage to cells. Studies have shown dissolved oxygen concentrations should not exceed 400% of air saturation (Chisti, 2007). Since oxygen cannot be removed from the tubes, this places a limit on total tube length with scale up (i.e the point to which the culture must return to the degassing unit to remove the accumulated oxygen).
- The illumination area to volume ratio decreases with scale-up, and without sufficient mixing the cells near the bottom half of the tubes receive insufficient light due to mutual shading effects.

This can be overcome by improving the mixing in the tubes so that cells do not stagnate in dark regions (Ugwu *et al.*, 2008)but at the risk of causing turbulence associated damage to the cells (Molina *et al.*, 2001).

- Adherence of the cells to the walls (fouling) calls for frequent cleaning, which is further enhanced by the long residence time spent in the tube section.
- The long tube length results in pH gradients caused by CO_2 consumption along the tubes which requires frequent and costly re-carbonation to lower the pH (Camacho *et al.*, 1999; Rubio *et al.*, 1999).

The aforementioned issues present serious challenges for commercial scale-up of horizontal tubular reactors. Their vertical column counterparts avoid some of the issues and thus show more potential.

2.5.3 Vertical column photobioreactors: bubble column and airlift reactors

Numerous designs and scales of vertical column reactors have been developed and tested (Miron *et al.*, 2002, 2000; Merchuk *et al.*, 2000) and can be categorized into two main types: *bubble column* and *airlift* reactors, both are illustrated in Fig. 2.13.

The bubble column reactor is the simplest of this form, utilizing a single cylinder filled with culture that is injected with gas near its base. The Airlift Reactor (ALR) evolved out of the bubble column design and contains a central draft tube. It has three distinct regions: the riser (inside the draft tube), the gas separator, and the downcomer. Gas is injected into the riser, creating a region with gas holdup. The gas holdup in the downcomer is always much lower than in the riser, which results in a difference in fluid density between the two regions that drives the liquid circulation. Fluid circulation takes place in a defined cyclic pattern, between the riser (inner tube) and downcomer (outer tube) with the majority of gas disengaging from the fluid in the separator. The flow characteristics in the riser and separator are usually bubbly and turbulent, whereas the downcomer is usually laminar (Wu & Merchuk, 2003). The type of configuration depicted in Fig. 2.13 is the most common and is called *internal loop.* This is characterized by the fact that the riser section sits concentrically inside the downcomer. Other configurations of airlift reactors exist, such as *external loop*, *split cylinder*, or *inclined*, having essentially the same regions.

Airlift reactors have overtaken bubble columns in popularity for algae cultivation since they allow a more efficient exposure of cells to light, better gas exchange, a more ordered liquid flow and occupy less land area (Camacho *et al.*, 1999). They are also simple to operate, since they contain no moving parts, and require minimal power input. Continuous oxygen removal is achieved by default, eliminating the possibility of inhibition by excessive dissolved oxygen levels.

The literature shows conflicting opinions as to whether airlift or bubble column reactors are better for algae cultivation. Both Merchuk *et al.* (2000) and Kaewpintong *et al.* (2007) found airlift reactors

to be superior to bubble columns as the result of direct experimental comparison, where higher productivities were achieved in the airlift reactors. Other authors (Barbosa *et al.*, 2003b; Janssen *et al.*, 2003; Miron *et al.*, 2002) found bubble columns to be more or less comparable to airlift reactors in productivities, but that bubble columns performed better at higher superficial gas velocities and taller column heights.

Camacho *et al.* (1999) compared an airlift to a horizontal tubular reactor and found that both yielded similar biomass productivities. Since the tubular reactor had higher light availability, it was concluded that the photosynthetic efficiency (PE) was higher in the airlift. The decreased photosynthetic efficiency in the tubular reactor was attributed to photoinhibition.

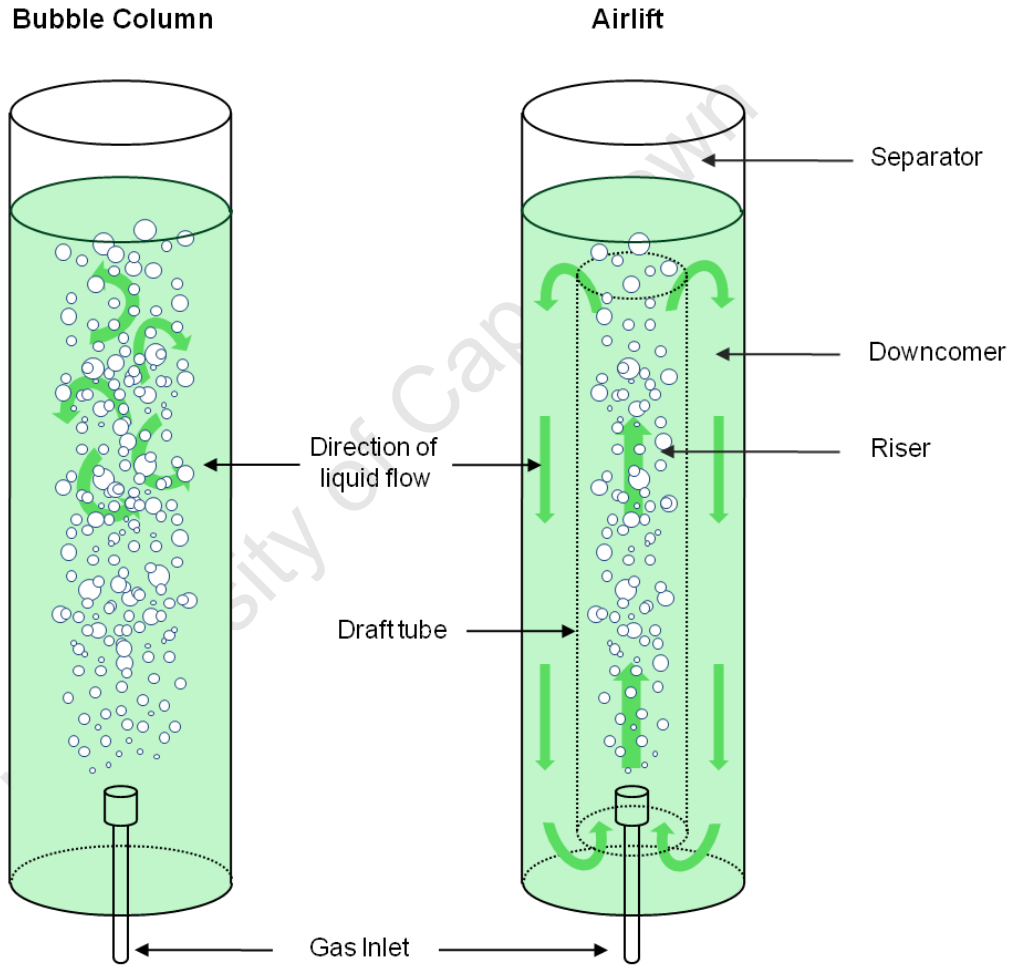

Figure 2.13 – Vertical column photobioreactors. Bubble column (Left) and Airlift (Right). Image source: author

Scale-up of vertical column reactors also results in a rapid decrease of surface area to volume ratio which results in a decrease in photosynthetic efficiency since light can only penetrate so far beyond the illuminated surface. This limitation can be overcome by implementing multiple smaller reactors as opposed to one large culture volume (Janssen, 2002). However, according to Carvalho *et al.* (2006), this method may become increasingly expensive since each unit requires a variety of expensive ma-

terials and control devices.

2.5.4 Choosing a suitable photobioreactor for this project: The airlift reactor

Table 2.1 summarizes the advantages and disadvantages of the closed photobioreactor types mentioned to illustrate how choosing a suitable photobioreactor involves a trade-off between key design considerations. Richmond (2004) proposed that the two basic factors affecting a reactor's efficiency and cost-effectiveness are: (i) the total illuminated surface required to produce a set quantity of product and (ii) the culture volume required to produce that quantity. As a general rule, the lower these values, the more efficient and cost-effective the reactor. This is in similar agreement to Kunjapur & Eldridge (2010), who propose that photosynthetic efficiency (PE) should be used in conjunction with volumetric productivity when comparing systems.

Table 2.2 (over page), taken from Eriksen (2008), summarises numerous operating variables for various photobioreactors taken from recent studies. Vertical tubular reactors (airlifts and bubble columns) generally feature the least land-use amongst all the closed reactor types and the highest PE.

Airlift photobioreactors have many advantages over other reactor types (Table 2.1) as well as the potential for high PE combined with low land area use (Table 2.2). Modular implementation could overcome the decreased surface area to volume ratio on scale-up (Janssen, 2002) and as a result, they have good potential as an optimum reactor type for bioenergy applications (Kunjapur & Eldridge, 2010). With these considerations in mind, the airlift reactor was chosen as the case study reactor type for this thesis.

Table 2.1 – Summary of advantages and disadvantages of photobioreactors. Adapted from Ugwu *et al.* (2008)

Reactor type	Advantages	Disadvantages
Flat-plate photobioreactors	large illuminated surface area, high biomass densities, short oxygen path (i.e low O_2 buildup), good biomass productivities, cheap construction,	scale-up requires many compartments and materials, poor temperature control, shear damage from aeration, low PE
Tubular photobioreactors	large illuminated surface area, suitable for outdoor cultivation, fairly good biomass productivities, relatively cheap, high volumetric biomass densities	pH, dissolved O_2 and CO_2 gradients along tubes, can lead to inhibition from oxygen accumulation, fouling, large land area, lowest PE
Vertical-column photobioreactors	greatest mass transfer, good mixing with low shear stress, low energy consumption, some potential for modular scalability, negligible oxygen build up, least land-use, high PE	high cost materials, decrease of illuminated surface area to volume ratio on scale-up

Table 2.2 – Performance measures of selected photoautotrophic cultures grown in different types of enclosed photobioreactors and under various photosynthetic photon flux densities. Source: Eriksen (2008).

Reactor type light source	PFFD $\mu mol\ m^{-2}\ s^{-1}$	E $MJ\ m^{-2}\ day^{-1}$	Light path cm	Volume l	Algal strain	x $g\ l^{-1}$	P_{volume} $g\ l^{-1}\ day^{-1}$	P_{area} $g\ m^{-2}\ day^{-1}$	PE %	Ref.
Tubular photobioreactors										
Artificial	80	–	1.2	5.5	*Spirulina*	–	0.42		8.1	A
Sun	–	13.5	10	*146*	*Arthrospira*	2.37	1.15	25.4	*4.7*[b]	B
Sun	1,126	*21.2*[a]	6	200	*Phaeodactylum*	2.29	1.15	19.1	*2.3*[b]	C
Sun	2,690	*50.5*[a]	6	200	*Phaeodactylum*	4.1	1.52	25.3	*1.3*[b]	C
Flat panel photobioreactors										
Sun[c]	–	*9.4*	0.6	400	*Chlorella*	–	*3.8*	22.8	5.6	D
Sun[c]	–	*6.4*	0.6	400	*Chlorella*	–	*3.2*	19.4	6.9	D
Column photobioreactors										
Sun	ca. 1,000	9.6	5	120	*Tetraselmis*	1.7	0.42	38.2	9.6	E
Alternative reactor designs										
Parabola/sun	–	–	–	70	*Chlorococcum*	1–2	0.09	14.9	–	F
Dome/sun	–	–	–	130	*Chlorococcum*	1–2	0.1	11.0	–	F

Values in italics are based on information in the references

References: A, Converti et al. (2006); B, Carlozzi (2000); C, Molina Grima et al. (2001); D, Doucha et al. (2005); E, Zitelli et al. (2006); F, Sato et al. (2006)

[a] Calculated from PFFD using a value of 18.78 kJ μmol^{-1} photons (Converti et al. 2006)

[b] Calculated using a specific energy content of biomass of 25 kJ g^{-1} (Degen et al. 2001)

[c] Open thin-layer culture

2.6 Light/dark cycles in photobioreactors

2.6.1 Definitions of a light/dark cycle

As a simplification, an airlift reactor can be thought to have two general regions: The *light volume* and the *dark volume*. The light volume exists near the surface of the reactor, where algae are exposed to sufficient light for cellular growth. As we move further away from the surface, depending on the biomass concentration, we reach a point at which the light intensity is too low to support photosynthesis, the dark volume. The dark volume will include the riser volume as well a portion of the downcomer that is closer to the center of the reactor. Due to the mixing characteristics in airlift reactors, cells constantly circulate between these two different regions inside the reactor experiencing a fluctuating light regime, called light/dark cycles.

In reality, the light and dark zones in an airlift photobioreactor have within themselves regions of varied light intensity, depending on the distance from the illuminated surface. Thus, cells moving within the reactor will experience a varied range of light intensities during each circulation through the reactor. Furthermore, the dark region is also not necessarily completely devoid of light. Fig. 2.16, which has more relevance later in this discussion, shows light/dark fluctuations from a real reactor.

However, as an approximation and to enable control and simulation of light/dark cycles experimentally, square wave cycles are employed, as illustrated in Fig. 2.14. The cells experience either full light or no light for controlled periods of time. In this manner, a light/dark cycle is defined by two parameters: (i) the duration of the cycle t_C, and (ii) the fraction of the total cycle that is exposed to light $f = t_l/t_C$. It is common to defined light/dark cycles in terms of a frequency, which is the reciprocal of the cycle time $\frac{1}{t_C}$ and has units of Hertz (s^{-1}) .

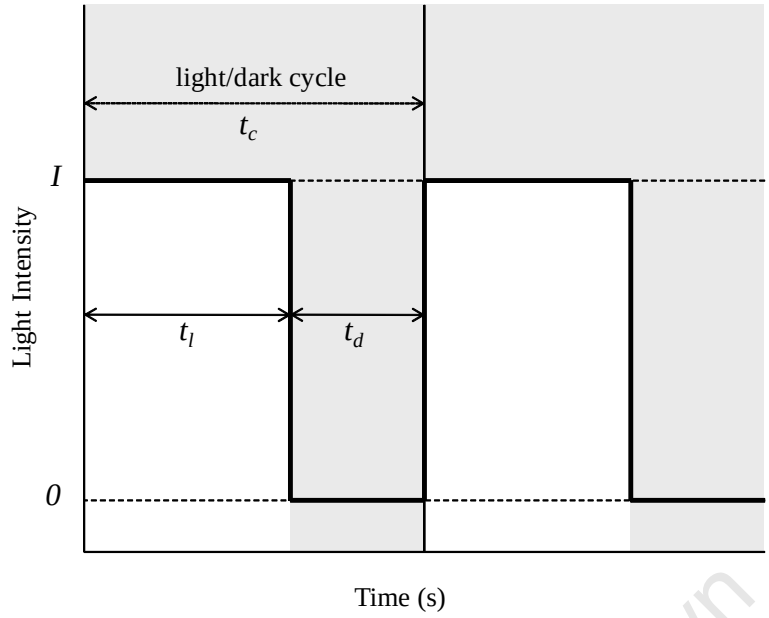

Figure 2.14 – Schematic of a square-wave light/dark cycle. t_C is the duration of the cycle, t_l is the duration of the light period and t_d the duration of the dark period. A "real" light/dark cycle pattern, which shows the scattered variance in the light experienced, is given in Fig. 2.16. Image source: this author

2.6.2 Experimental investigations into light/dark cycles

Algal growth is influenced by three ranges of light/dark cycles (Grobbelaar, 1994) as summarised here in Table 2.3 according to their relative frequencies.

Table 2.3 – Ranges of light/dark cycles experienced by algae in different systems

#	Frequency	Time scale
1	High Frequency	100 ms and less (>10 Hz)
2	Medium Frequency	seconds →minutes
3	Low Frequency	hours→days→months

Low Frequency light/dark cycles result from normal day/night cycles as well as seasonal and/or climate changes. These would affect overall solar irradiance experienced by an outdoor photobioreactor and their effects would be recognized in annual cultivation trends Jacob-Lopes *et al.* (2009). Since this was a controlled laboratory study, these effects did not need to be accounted for.

It is well documented that high frequency fluctuating light (< 100 ms) leads to increased rates of photosynthesis and growth rates in comparison to continuous light (Yoshimoto *et al.*, 2005; Janssen, 2002; Park & Lee, 2001, 2000; Nedbal *et al.*, 1996; Grobbelaar, 1994). These enhancements are greater under the shorter cycles in this range and this phenomenon has since been termed the *flashing light effect* (FLE). In a photobioreactor, such high frequency cycles can be induced with increased turbulence of a dense culture such that algal cells are only close to the illuminated surface for a fraction

of second, followed by a dark period. Numerous experimental studies using controlled flashing lights have proven the existence of and provided insight into the FLE phenomenon (Park & Lee, 2001, 2000; Nedbal *et al.*, 1996). As a case study, in Nedbal *et al.* (1996) the growth of *Scenedesmus quadricauda*, *Chlorella vulgaris* and *Synechoccus elongates* were studied over a range of light periods (0.1 ms to 10 s). Fig. 2.15 shows a result from their study for *Scenedesmus quadricauda*. Growth rate is presented as a function of intermittent light period, exhibiting a clear optimum.

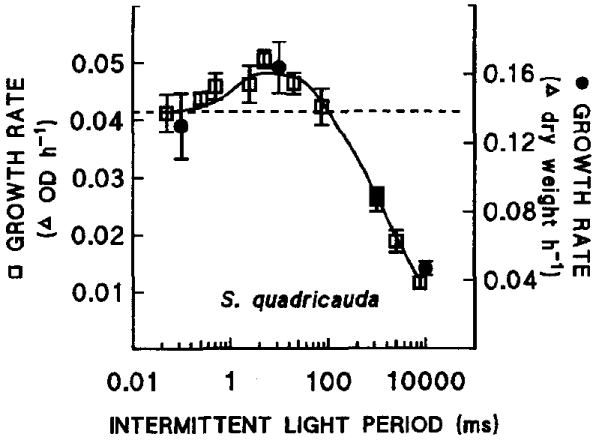

Figure 2.15 – Growth rate of *Scenedesmus quadricauda* as a function of intermittent light period. Image source: Nedbal *et al.* (1996)

Luo *et al.* (2003) employed particle tracking techniques to investigate flow dynamics in airlift photobioreactors and found three types of liquid-phase mixing mechanisms coexisting. Type I was in the order of 10 s due to bulk circulation between the riser and the downcomer and constitutes medium frequency cycles. Type II was in the order of 1 s due to the spiral movements. And type III was in the order of 0.1 s, or even smaller, due to radial fluctuations and turbulence, constituting high frequency cycles.

As shown in Fig. 2.16, increasing biomass concentration increases the magnitude of light fluctuation patterns (Luo *et al.*, 2003). At $C_x = 5000$ g.m^{-3}= 5 g.L^{-1} the light exposure becomes an alternation between light and completely dark periods, and can be appropriately modeled by a square wave cycle, as shown Fig. 2.14. Although Type III (high frequency) cycles exist in airlift reactors, Fig. 2.16 shows the predominance of Type I (medium frequency) light/dark cycles caused by circulation between the riser (dark region) and downcomer (light region). Thus, medium duration light/dark cycles and their effect on algal growth are of principle concern for modelling airlift photobioreactors.

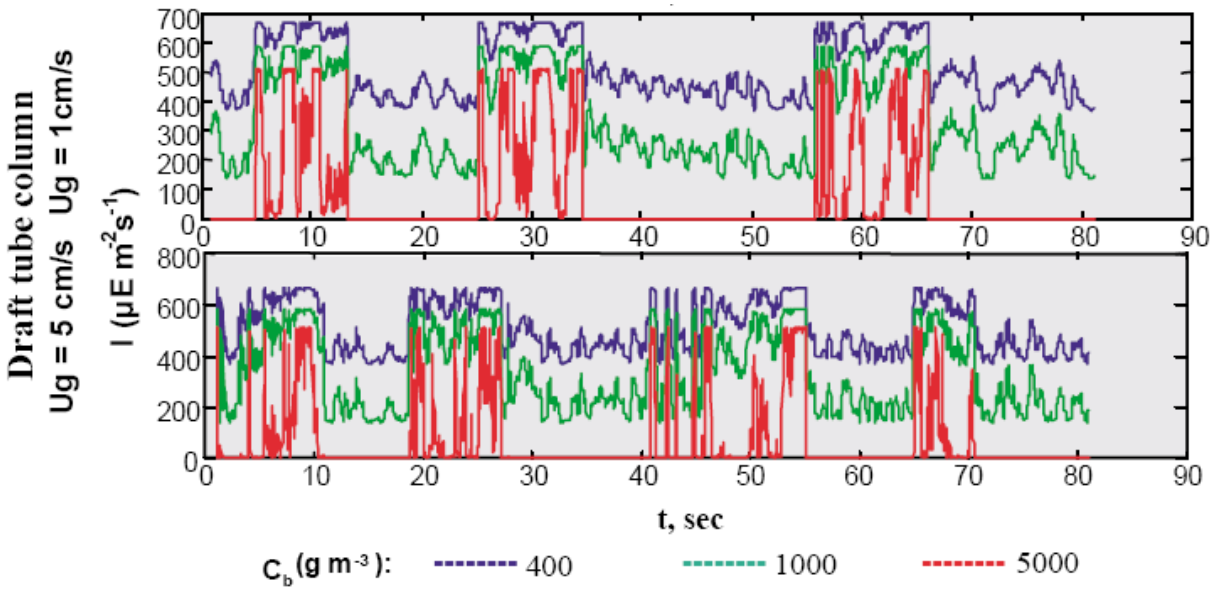

Figure 2.16 – Typical temporal irradiance pattern for an airlift photobioreactor at three different biomass concentrations and two different superficial gas velocities. Calculated by combing CARPT (Computer Automated Radioactive Particle Tracking) obtained trajectories and the irradiance distribution model proposed by Fernandez *et al.* (1997) with $K_a = 0.05$ m^{2}g^{-1}. Image source: Luo *et al.* (2003)

The influence of medium duration light/dark cycles on algal growth is not clear in literature.

Grobbelaar (1989, 1991) investigated short term oxygen evolution experiments and found no influences over a whole range of medium frequency light/dark cycles (1 – 263s / 1-0.0038 Hz) on photosynthetic rate and carbon fixation for the species *Chlorella* and *Scenedesmus*.

In other work, both Lee & Pirt (1981) and Merchuk *et al.* (1998a) investigated light dark cycles in thin tubular loop reactors for *Chlorella sorokiniana* and the red microalgae *Porphyridium* sp., respectively. The results of Merchuk *et al.* (1998a) are shown in Fig. 2.17. Straight lines have been drawn through the data for each cycle time to illustrate the apparent linear increase in growth with increasing light fraction. The arrows represent the points at which maximal growth was achieved, despite there being a dark period in the cycle. Merchuk *et al.* (1998a) found that a maximum dark period of 6 sec could still enable the same growth rates as under continuous light (for *Porphyridium* sp). Lee & Pirt (1981), who performed a similar experiment for *Chlorella sorokiniana*, observed a maximum dark period of 9.2 sec. For any dark periods longer than these maxima, the growth rate decreased with decreasing light fraction, as shown in Fig. 2.17. Both authors postulated that these algae could store energy (in the form of ATP) during the light period to be utilized during the dark period to maintain maximal growth, provided the dark period was not longer than 9.2 and 6 sec, for each respective species.

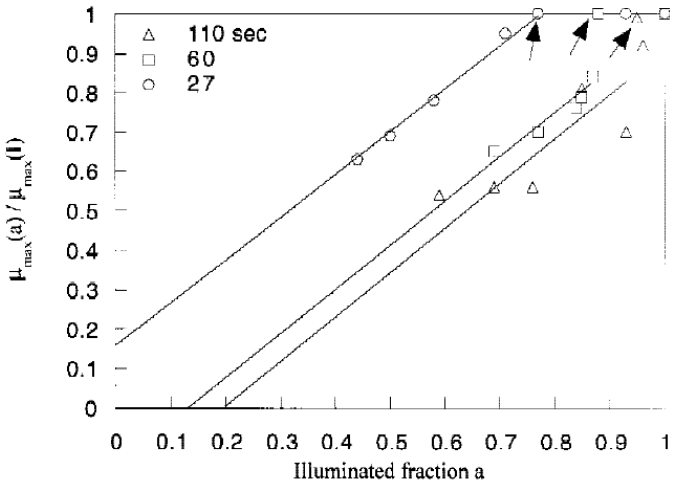

Figure 2.17 – Relative growth rate $[\mu_{max}(a)/\mu_{max}(I)]$ for *Porphyridium* sp. at 300 µmol.$m^2.s^{-1}$ for the three cycle times tested (27,60 & 110 sec), as a function of the illuminated fraction. Image source: Merchuk *et al.* (1998a)

In contrast to these findings, Janssen (2002) showed that the specific growth rate of *Chlamydomonas reinhardtii, Chlorella sorokiniana* and *D. Tertiolecta* strictly decreased under square-wave light:dark cycles of medium duration (6–100 sec) in comparison to continuous illumination. The results for *Chlorella sorokiniana,* shown in Fig. 2.18, are contradictory to those reported by Lee & Pirt (1981) for the same species. Janssen (2002) concluded that these algae are not able to store light energy during the light period to sustain growth in the dark period at the same level as under continuous light.

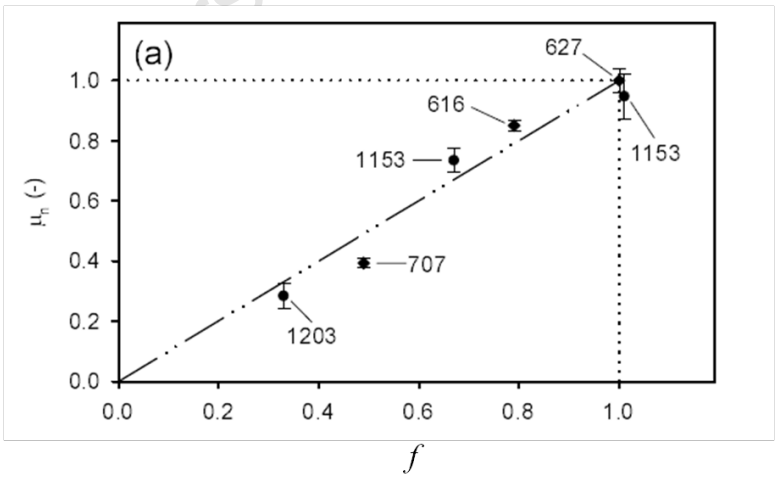

Figure 2.18 – Normalized specific growth rate $[\mu_{max}(a)/\mu_{max}(I)]$ of *Chlamydomonas reinhardtii.* 15 s light/dark cycles. The numbers give the PFD during the light period (μmol·m$^{-2}\cdot$s^{-1}) and the error bars show 95% confidence intervals. Image source: Janssen (2002)

As part of a further investigation by the same author (Janssen, 2002) and published in Barbosa *et al.* (2003b), the combined effect of total cycle time and light/dark fraction was investigated for *D. Terti-*

olecta under 10 - 100 second light/dark cycles. Fig. 2.19 shows the results. The left plot shows all the experimental points and the right plot shows a contour relationship obtained by fitting a statistical model to the experimental data. In the latter, the trend of decreasing growth rate under decreasing light fraction is easily observed. It is very difficult to see the relationships in the left hand 3D plot, however, it shows that under light fractions smaller than or equal to 0.55, short cycle times resulted in higher growth rates than longer cycles at the same light fraction. Specifically, growth rate increased 55%, when cycle time decreased from 55 to 10 s, and the light fraction was 0.55 (Barbosa *et al.*, 2003b). These results suggest that the total cycle time, in addition to the light/dark ratio, has an influence on growth characteristics.

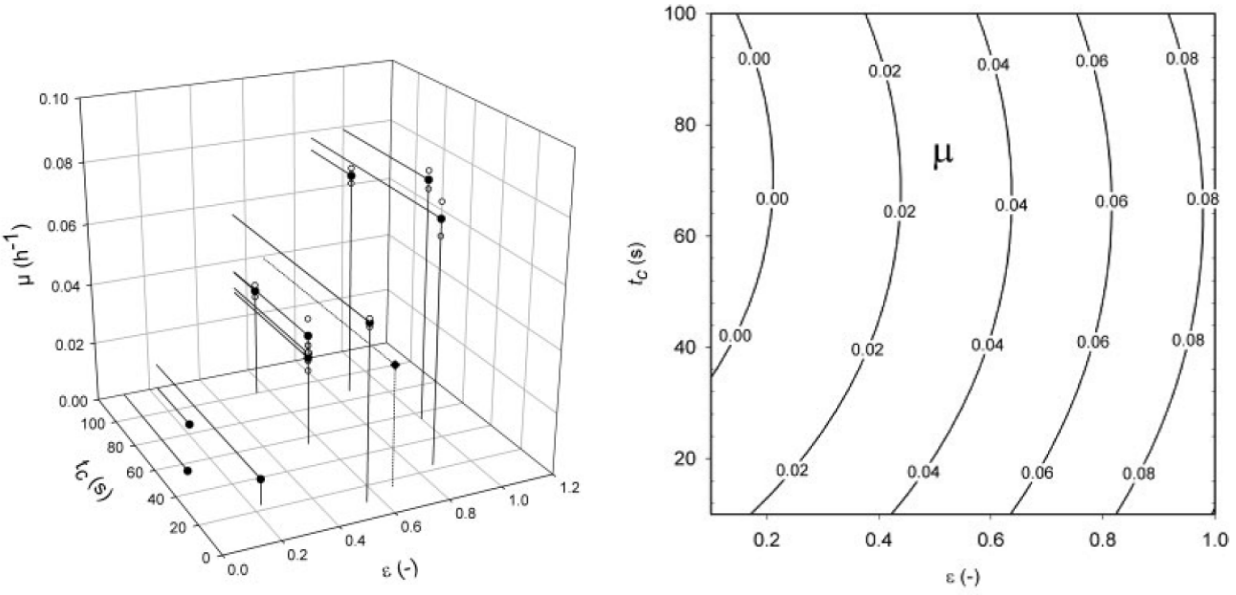

Figure 2.19 – (Left) Growth rate $\mu(h^{-1})$ of *Dunaliella tertiolecta* as a function of light fraction (ε) and cycle time (t_C). Non-filled circles represent 95% confidence intervals. (Right) Contour plot of light fraction (ε) and cycle time (t_C) on growth rate (μ). Image source: Barbosa *et al.* (2003b)

As a side thought, this author has noted considerable differences in the reactor types and modes of operation used in these investigations. For example, Janssen (2002) employed a 0.1 L turbidostat reactor whereas Lee & Pirt (1981), Merchuk *et al.* (1998a) and Grobbelaar (1991) utilized various designs of thin tubular loop reactors (to minimize light gradients). These differences raise questions about the validity of comparing results from these studies. The different reactors have clear differences in their method of light provision and were sure to have differences in mixing and flow characteristics as well CO_2 mass transfer effects - all of which could influence algal growth characteristics.

Other differences include the range of PFDs tested (Table 2.4) which no doubt have an influence on algal growth. Both Merchuk *et al.* (1998a) and Lee & Pirt (1981) were performed under considerably lower PFD to those of Janssen *et al.* (1999) and Grobbelaar (1994). Their conclusion that algae are able to store energy for use during a short dark period, may be valid under low PFDs where photoinhibition exists to a lesser extent.

Table 2.4 – Ranges of PFDs tested for light/dark cycles studies

Author	Range of PFD (μmol $\cdot$ m^{-2}s^{-1})
Janssen (2002)	$\sim 1000 - 1300$
Merchuk *et al.* (1998a)	$\sim 150 - 300$
Lee & Pirt (1981)	~ 320
Grobbelaar (1991)	~820

In summary, light/dark cycles are a complicated, confusing and unavoidable phenomenon in any photobioreactor. The effect they have on photosynthesis, which affects algal growth and bioreactor performance, is of critical importance and must be incorporated when developing a model.

2.7 Background to modelling photobioreactors

Assuming no micro-scale mass transfer limitations, nutrients can be supplied easily and in excess to algal cells inside a photobioreactor. Furthermore, assuming CO_2 is supplied optimally to ensure no CO_2 limitations, light becomes the major growth limiting substrate. In this regard, the scope of the modelling in this thesis is limited to light provision

To recap and summarize what has already been discussed: the existence of a large dark zone in the reactor center and a small highly illuminated zone near the illuminated surface results in regions of varied photosynthesis (see subsection 2.2.4) and thus varied regions of cellular growth. High light intensity may lead to photoinhibited growth (Luo & Al-Dahhan, 2004; Wu & Merchuk, 2001) while low light intensities in the dark zone may be insufficient to support growth. Hence, the major factor affecting photosynthetic growth is light availability (Merchuk *et al.*, 1998a).

In a well mixed reactor, cells move through regions of varying light intensity experiencing light/dark cycles. Hence, every point within the reactor is able to sustain a certain photosynthetic growth rate; which is a function of the light intensity at that point. In order to model growth, a quantitative description of both the light distribution profile and the movement of cells through these regions is needed. Knowledge of the cell's *light history* thus enables integration of a photosynthetic growth model and, prediction of biomass growth rates. In summary, overall modelling of a photobioreactor requires the coupling of three effects:

1. Light transfer inside the culture to predict the light regime - a *light distribution model*
2. Photosynthetic growth of the cells using the available light - a *kinetic growth model*
3. Description a cell's movement through this light regime - a *hydrodynamic model*

Literature pertaining to these three topics is reviewed in Section 2.8 to 2.10 to provide the basis for these three model components.

2.8 Modelling light distribution

Simplistic methods for modelling light transfer in photobioreactors use incident light intensity (the radiation on the surface of the bioreactor) or irradiating surface area per culture volume as a means to quantify light energy. These methods are only valid at very low cell densities and short light path lengths, and give no information about the local light distribution inside the photobioreactor (Suh & Lee, 2003). To overcome these limitations, mathematical models have been developed to describe light distribution profiles inside photobioreactors.

2.8.1 Beer-Lambert law and first principles

Beer Lambert law relates the absorbance of light to the properties of the material through which the light is travelling. From first principles, it is represented in differential form by Eq. 2.5, for the absorbance of light of wavelength λ though a medium of concentration C_x. The absorption coefficient $A'(C_x,\lambda)$ is a measure of how much light is lost due to absorption or scattering as a function of cell concentration.

$$\frac{dI(\lambda)}{dz} = A'(C_x,\lambda)\cdot I(\lambda) \tag{2.5}$$

Since $A'(C_x,\lambda)$ is constant and independent of z, integration yields:

$$\frac{I(\lambda)}{I_0(\lambda)} = e^{-A'(C_x,\lambda)\cdot z} \tag{2.6}$$

where $I_0(\lambda)$ is the incident light intensity (μmol·m$^{-2}\cdot$s^{-1}), $A'(C_x,\lambda)$ is the absorption coefficient (m^{-1}) and z is the distance from the illuminated surface (m^{-1}). In the Beer-Lambert law, the absorption coefficient is deemed linearly proportional to cell concentration:

$$A'(C_x,\lambda) = K_a(\lambda)\cdot C_x \tag{2.7}$$

The proportionality constant $K_a(\lambda)$ represents the specific extinction coefficient (m^3·kg^{-1}) for a specific species for each considered wavelength. $K_a(\lambda)$ can be determined experimentally using a spectrophotometer and Fig. 2.20 shows a typical $K_a(\lambda)$ vs. λ relationship taken from Pruvost *et al.* (2002). By substituting Eq. 2.7 into Eq. 2.6, the well known form of Beer-Lambert law results:

$$I(\lambda) = I_0(\lambda)\cdot e^{-K_a(\lambda)\cdot C_x\cdot z} \tag{2.8}$$

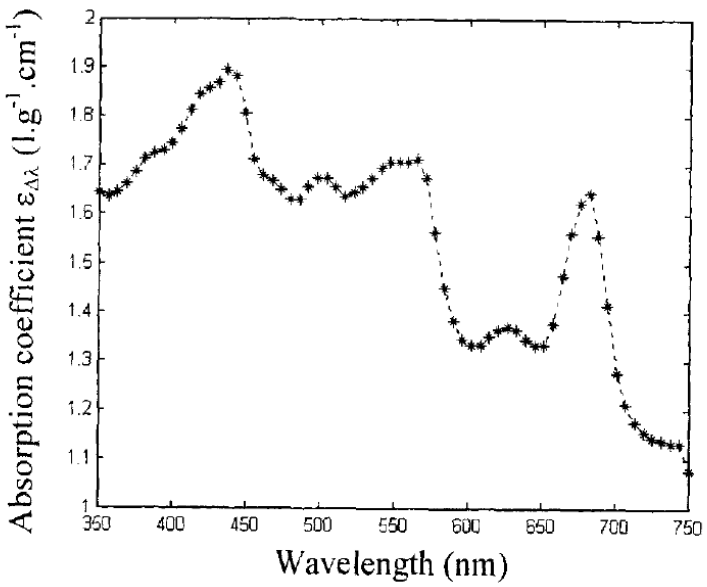

Figure 2.20 – Absorption coefficient variations with wavelength for *Porphyridium purpurem*, taken from Pruvost *et al.* (2002)

Up until this point, the development of Beer-Lambert law as been given as a function of wavelength, since the degree of absorption of light is not uniform over different wavelengths, as shown in Fig. 3.8. When dealing with polychromatic light (i.e multiple wavelengths), as encountered with sunlight or fluorescent light, it is more useful to express the total absorbance of light over all wavelengths, thus all contributions over the PAR range are integrated according to:

$$I = \int_{400}^{700} I_0(\lambda) \cdot e^{-K_a(\lambda) \cdot C_x \cdot z} d\lambda \tag{2.9}$$

However, this requires knowing $I_0(\lambda)$ for the light source in question. It is more common practice to simplify the law by assuming an average K_a that applies over all the wavelengths in question (Fernandez *et al.*, 1997).

$$K_a = \frac{1}{\triangle\lambda} \int_{400}^{700} K_a(\lambda) d\lambda \tag{2.10}$$

Thus, Eq. 2.9 is re-written according to Eq. 2.11, which is the simplest and most recognizable form of Beer-Lambert law.

$$I = I_0 \cdot e^{-K_a \cdot C_x \cdot z} \tag{2.11}$$

Due to its simplicity, Beer-Lambert law has been widely used to model light attenuation in photobioreactors (Marshall & Huang, 2010; Luo & Al-Dahhan, 2004; Wu & Merchuk, 2004, 2003; Muller-Feuga *et al.*, 2003; Wu & Merchuk, 2002; Molina *et al.*, 2001; Csogor *et al.*, 1999; Camacho *et al.*, 1999; Grima *et al.*, 1999, 1997). Beer-Lambert law is based on the assumptions that scattering effects are negligible compared to absorption. However, diverse scattering effects exist in algal suspensions, par-

ticularly at higher concentrations. Scattering effects depend on the optical properties and size of the cells which causes light to be reflected and refracted in all possible directions. Thus, Beer Lambert's linear prediction is only accurate for algal suspensions under low cell concentrations and short light path lengths (Suh & Lee, 2003). Beer-Lambert law has been shown to over-estimate the culture's real absorption (Pruvost *et al.*, 2002; Fernandez *et al.*, 1997) as depicted in Fig. 2.21. Hence, alternative approaches have been explored and are discussed in Sections 2.8.2 and 2.8.3.

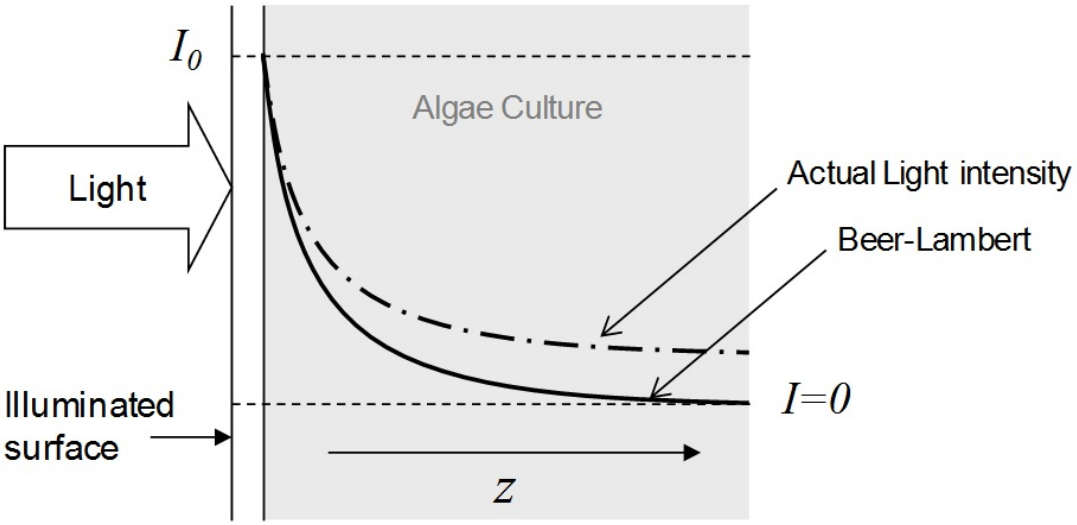

Figure 2.21 – Schematic showing how light intensity I varies with culture depth z in an illuminated algal culture; the real light intensity versus Beer-Lambert law model is shown. Image source: author

2.8.2 Structured models proposed to account for absorption and scattering effects separately

A far more sophisticated approach to modelling light distribution is one that incorporates light scattering effects (Berberoglu *et al.*, 2007; Cornet *et al.*, 1995, 1994, 1992b; Yokota *et al.*, 1991; Aiba, 1982). The disadvantages of such models are that they require rigorous mathematical treatment. These models are based on different formulations and solutions to the Radiative Transfer Equation (RTE). The RTE is a general mathematical description for the propagation of electromagnetic radiation through any medium. It attempts to describe how a beam of such radiation loses energy via absorption, gains energy by emissions and redistributes energy by scattering.

As a case study of one such model, Cornet *et al.* (1992a) proposed a model based on the RTE, which adapts the hypothesis of Schuster (1905), by assuming: (i) the light field remains isotropic throughout the whole culture; and (i) light absorption and scattering can be independently accounted for using the specific absorption coefficient E_a and the specific scattering coefficient E_s, respectively. The mathematical form of this model is given in Equation 2.12 and involves a time consuming solution of the RTE, formulated as:

$$-\nabla \cdot F = (E_a + E_s)C_x \int_{4\pi} E d\omega - E_a C_x \frac{1}{4\pi} \int_{4\pi} \int_{4\pi} p(\theta, \theta') E d\omega' d\omega \tag{2.12}$$

where F is the radiant energy flux vector $(\mathrm{W\,m^{-2}})$, E is the specific light intensity on an energy basis $(\mathrm{W\,m^{-2}})$, C_x is the algal concentration $(\mathrm{kg\,m^{-3}})$, and E_a and E_s are the specific absorption and scattering coefficients respectively $(\mathrm{m^2\ kg^{-1}})$; ω is a solid angle and $p(\theta, \theta')$ the phase function for scattered light, which is characteristic of the medium (both dimensionless).

Approximate monodimensional solutions to Eq. 2.12 have been proposed by both Cornet *et al.* (1995) and Pottier *et al.* (2005). For example, the simplified (and approximate) solution for the RTE, proposed by Cornet (1995) is given as:

$$\frac{I}{I_0} = \frac{4\Omega}{(1+\Omega)^2 e^{\Psi} - (1-\Omega)^2 e^{-\Psi}} \tag{2.13}$$

where Ω and Ψ are given by:

$$\Omega = \sqrt{\frac{E_a}{E_a + E_s}} \tag{2.14}$$

$$\Psi = (E_a + E_s) \cdot \Omega \cdot C_x \cdot z \tag{2.15}$$

Eq. 2.13 is derived for rectangular coordinates. Equivalent derivations for both cylindrical and spherical systems can be found in Cornet *et al.* (1995). Although the expression in Eq. 2.13 is far simpler to evaluate mathematically than Eq. 2.12, the determination of the necessary parameters (E_a and E_s) are difficult to measure experimentally (Pruvost *et al.*, 2002) and required to be determined at every wavelength of the light source (Aiba, 1982). In addition, the spectral composition of the light source used to measure these coefficients usually differs from the source used to illuminate the culture, particularly in the case of outdoor solar irradiation, since sunlight cannot be used in an analytical device. Therefore, the values obtained for E_a, and E_s could well be different from those in the actual culture (Fernandez *et al.*, 1997). The advantage of Cornet's model, is that it is a structured model established on a mechanistic basis. In other words, it attempts to model the real physical phenomena as realistically as possible. However, both Yun & Park (2001) and Fernandez *et al.* (1997) showed it unable to predict their experimental observations with any accuracy, as shown in Fig. 2.22. Furthermore, scattering and absorption are not the only factors affecting light distribution; the culture medium, bubbles, reactor surface, and other components of the reactor vessel all contribute to this effect. The complexity of the light distribution model has not yet been extended to account for all these effects.

2.8.3 Empirical modelling approaches

Empirical models proposed by Iehana (1983) and Fernandez *et al.* (1997) offer an alternative approach to such sophisticated methods. Fernandez *et al.* (1997) proposed that the absorption coefficient $A'(C_x)$ tends towards an asymptotic relationship with increasing concentration. At low cell concentrations there is a linear relationship (Beer-Lambert law), whilst at high concentrations $A'(C_x)$ has an asymptotic dependency towards a maximum absorbance. The model is formulated as:

$$A'(C_x) = \frac{K_{a,max} \cdot C_x}{C_x + K_x} \tag{2.16}$$

where $K_{a,max}$ is the maximal absorption coefficient (m^{-1}) and K_x is a constant accounting for scattering by cells ($kg.m^{-3}$). Substitution of Eq. 2.16 into Eq. 2.6 and assuming an average absorption coefficient for all wavelengths results in:

$$I(C_x, z) = I_0 \cdot exp\left[\frac{-K_{a,max} \cdot C_x \cdot z}{C_x + K_x}\right] \tag{2.17}$$

Although such models do not arise from any mechanistic understanding of light absorption, they are able to describe light attenuation accurately when fitted to experimental data, as shown in Fernandez *et al.* (1997) and Yun & Park (2001). Furthermore, Yun & Park (2001) compared the ability of all three types of models to predict experimental data, as shown in Fig. 2.22. Their comparison showed that although Cornet's model is able to predict the tendency of non-linearity, which Beer-Lambert law cannot, it is still inaccurate with regard to real data. This could be as a result of in the inherent error in the parameters used (E_a and E_s), as mentioned previously.

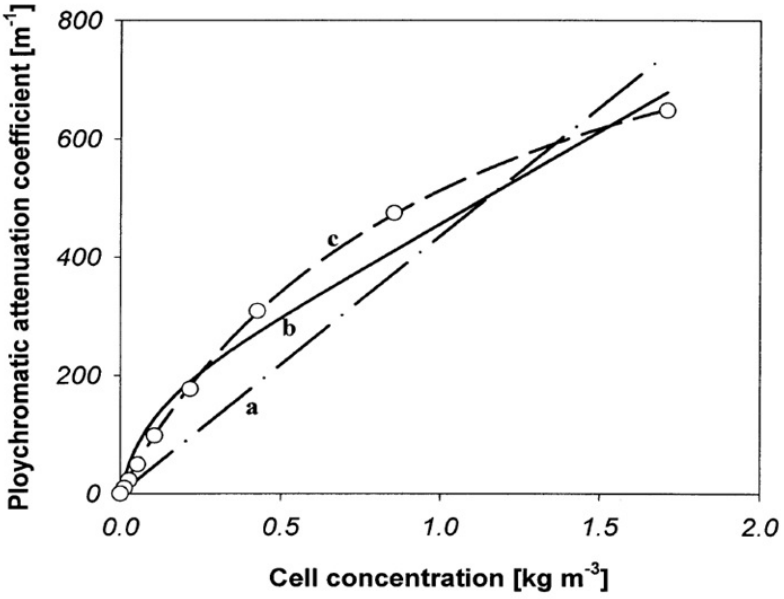

Figure 2.22 – A comparison between actual attenuation coefficients (o) of daylight in algal suspension and those predicted by various models: (a) Beer-Lambert law, (b) Cornet, and (c) asymptotic. Image source: Yun & Park (2001).

The asymptotic model in Eq. 2.16 was only tested at a single path length (center of a 0.05m ID tubular reactor) by Fernandez *et al.* (1997) and thus the model's response to nonlinear changes in cell concentration was good. However, no observations were made as to how well the model was able to respond to changing light path lengths, either closer or further away from the light source. Taking the asymptotic model one step further, Suh & Lee (2003) suggested that both light path *and* cell concentration had an effect on the absorption coefficient. They simply added another term into Eq. 2.17 to account for the effects of z, which resulted the the following model:

$$I(C_x, z) = I_0 \cdot exp\left[\frac{-K_{a,max} \cdot C_x \cdot z}{(C_x + K_x)(z + K_z)}\right] \tag{2.18}$$

where the additional constant K_z (m) accounts for light scattering by light path length. At low cell concentrations and short path lengths, $C_x \ll K_x$ and $z \ll K_z$ and the function takes the form of Beer-Lambert law, with the absorption co-efficient simply given by:

$$K_a \approx \frac{K_{a,max}}{K_x \cdot K_z} \tag{2.19}$$

Suh & Lee (2003) found excellent agreement between their dual-asymptotic model and experimental data over a range of cell concentrations ($0-4\,\mathrm{g.L^{-1}}$) and light path lengths ($0-5\,\mathrm{cm}$) for the algal species *Synechococcus,* as illustrated in Fig. 2.23.

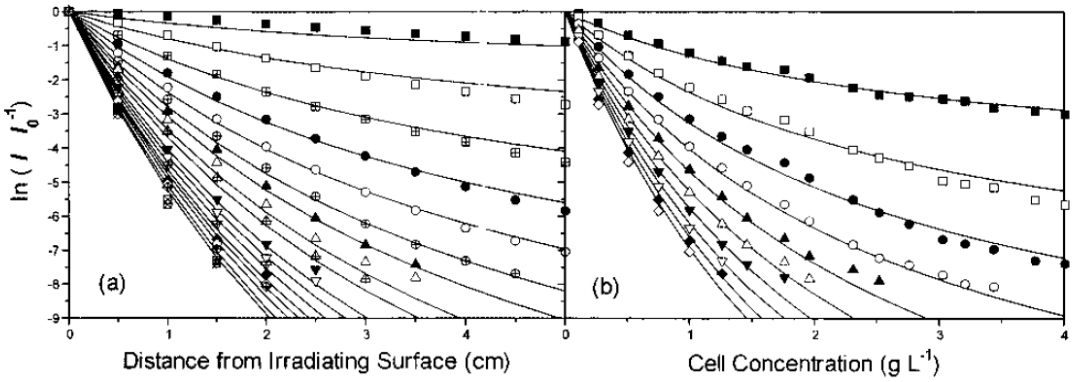

Figure 3. Change of light attenuation by (a) light path-length and (b) cells. Symbols in (a) are 0.11 (■), 0.27 (□), 0.51 (⊞), 0.75 (●), 1.00 (○), 1.26 (⊕), 1.46 (▲), 1.76 (△), 1.96 (⟑), 2.31 (▼), 2.52 (▽), 2.76 (⧩), 3.03 (◆), 3.21 (◇), 3.44 (⟠), 3.77 (⋈), 4.01 (⊗) $\mathrm{gL^{-1}}$ cell concentration. Symbols in (b) are 0.5 (■), 1.0 (□), 1.5 (●), 2.0 (○), 2.5 (▲), 3.0 (△), 3.5 (▼), 4.0 (▽), 4.5 (◆), 5.0 (◇) cm light path-length.

Figure 2.23 – Agreement between the dual asymptotic model and real data. Image source: Suh & Lee (2003)

2.9 Modelling algal growth kinetics

modelling photosynthetic growth as a function of light is the next critical model component. The relationship between light intensity and photosynthetic rate has been explained in some detail in Section 2.2.4 . This relationship is extremely complex, involving many reaction pathways and biological phenomena. Thus, the complete system is far too complicated to model in its entirety and all modelling attempts found in literature are based on lumping large amounts of biochemical reactions into simpler steps or hypothetical concepts (Merchuk *et al.*, 2007). Two general modelling approaches can be identified: (i) static light curves and (ii) dynamic physiological models.

2.9.1 Static light curve models

The simplest and most widely used approach to modelling biomass growth is based on the P-I curve (Section 2.2.4), since algal growth rate μ follows the same characteristics. μ increases with increasing PFD, reaching a maximum μ_{max} at an optimal light intensity I_{max}, thereafter further increases in PFD may lead to photoinhibition and inhibited growth. As a result of this trend, empirical models have been developed to fit curves obtained from experimental data. A schematic of a typical static growth curve is shown in Fig. 2.24.

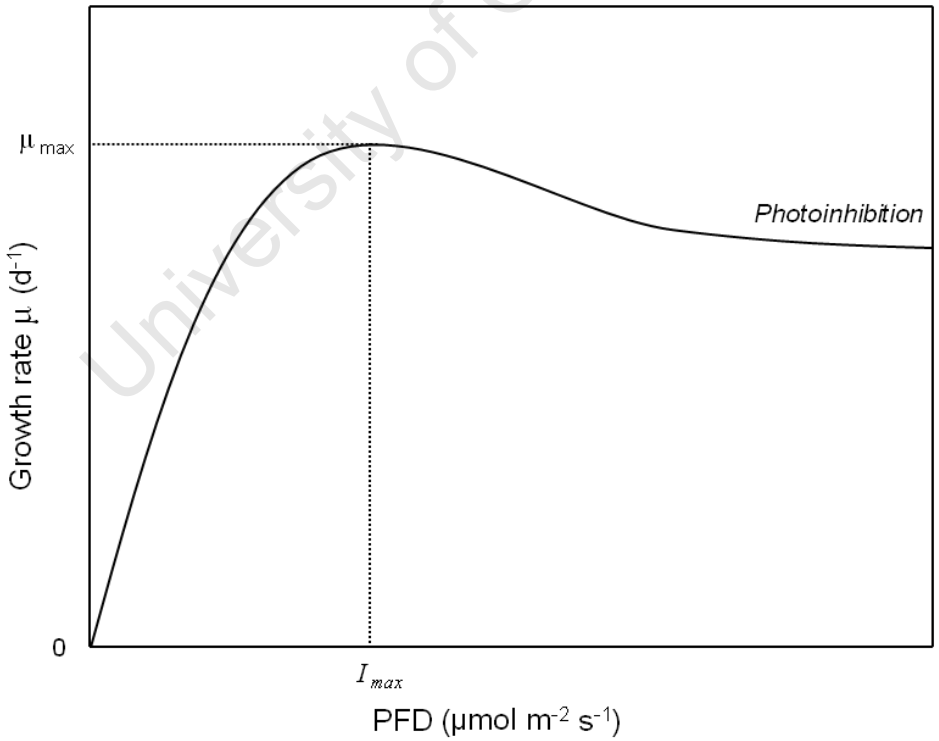

Figure 2.24 – Typical characteristics of light-dependent algal growth. Image source: this author.

Table 2.5 summarizes examples of static light curve models. Numerous models have been established for specific cases and cultures and the method is widely used in the algal biotechnology field (Richmond, 2004; Yun & Park, 2003; Pruvost *et al.*, 2002). One of the earliest approaches is the Aiba equation (Table 2.5), which adopts the form of a substrate inhibited enzymatic rate law to account for photoinhibition. Numerous other well known and more recent models found in literature (also shown in Table 2.5) are based on the form of the Aiba equation but incorporate additional empirical parameters.

Table 2.5 – Models for light–dependent specific growth rate.

Model #	Equation	Reference
1	$\mu = \frac{\mu_{max} I}{K_s + I + \frac{I^2}{K_i}}$	Aiba (1987)[1]
2	$\mu = \frac{\mu_{max} I^n}{I_k^n + I^n}$	Molina Grima et al. (1994)[1]
3	$\mu = \frac{2\mu_{max}\left(1-\frac{I_e}{I_{max}}\right)\left(\frac{I}{I_{max}}-\frac{I_e}{I_{max}}\right)}{\left(1-\frac{I_e}{I_{max}}\right)^2+\left(\frac{I}{I_{max}}-\frac{I_e}{I_{max}}\right)}$	Muller-Feuga (1998)[2]
4	$\mu = \frac{\mu_{max} I_{av}^{\left(b+\frac{c}{I}\right)}}{\left[I_k\left(1+\left(\frac{I}{K_i}\right)^a\right)\right]^{\left(b+\frac{c}{I}\right)}+I_{av}^{\left(b+\frac{c}{I}\right)}}$	Grima *et al.* (1999)

In Table 2.5, I is the local PFD experienced by cells, I_{max} is the PFD experienced at light saturation, I_{ave} is the average PFD over an extended period of time; μ the growth rate, μ_{max} the maximum specific growth rate at saturation and K_i,K_s, I_k, a, b, c are fitted parameters. I_e in Model 3 is the minimum PFD required for positive growth, in other words this model, unlike all the others can account for negative growth in extremely light inhibited conditions.

[1] cited in Grima *et al.* (1999)

[2] cited in Pruvost *et al.* (2002)

Owing to their empirically derived parameters, these models fit well with experimental observations (Richmond, 2004). Their main disadvantage is that they are not able to account for physiological changes that come about from changing light conditions, which the cells experience when moving through different light zones inside the reactor (Luo *et al.*, 2003). Growth rate is not only influenced by light intensity, but also by periodic changes in light availability which causes physiological changes in the cells. Thus, static models are not sufficient to represent the real response of photosynthetic growth, since they do not consider the underlying biochemistry and physiology of the photosynthetic process (Pruvost *et al.*, 2002). As a result, more fundamental models have been developed that attempt to represent photosynthesis dynamics.

2.9.2 Structured modelling approaches

By definition, a structural model considers the internal structure and physiological state of the cell. The most recent of these has been developed by Fleck-Schneider *et al.* (2007) to model the growth of *Porphyridium purpurem.* Since thousands of enzymatically catalyzed reactions take place within an algal cell, simplification was a necessity. The authors reduced the complex metabolic network to the most relevant key steps and metabolites to formulate stoichometric balances in an 11x16 matrix. A detailed description of the model and formulation of the underlying equations would be too laborious for this discussion. Instead, Fig. 2.25 shows a simplified schematic of their model taken from their paper.

Referring to the figure, the flow of "energy" through the cellular system can be traced visually: starting in the form of photons from light absorption, leaving PSI and PSII as electrons via either cyclic or non-cyclic electron transport, transferred to usable work in the form of ATP and NADPH, and ultimately producing CH_2O via the Calvin cycle. The model then infers a net growth rate from the sum of the specific growth rates of all intracellular metabolic products.

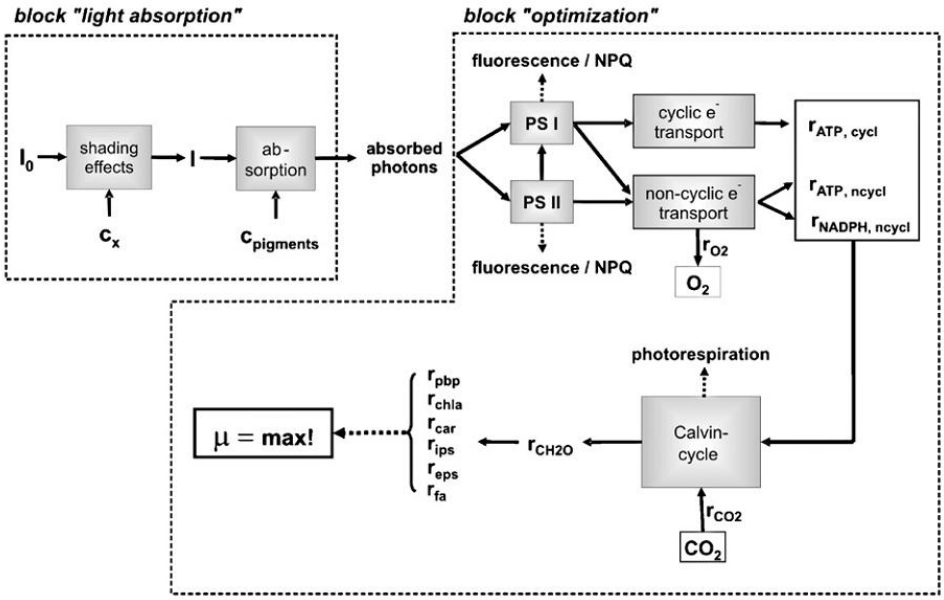

Figure 2.25 – Simplified schematic of the basic functionality of the Fleck-Schneider *et al.*, 2007 cell model. Image source: Fleck-Schneider *et al.* (2007).

The authors admitted their model to be incomplete. It does not contain enough known equations to enable an independent solution and thus can't directly predict growth rate as a function of model inputs. To overcome this limitation they assumed the principle of "maximization of specific growth" by hypothesizing that the unknown variables in their model would be appropriately varied by the cell in a manner that would allow it to optimally adapt to its changing environment. The idea is based on the basic principle that organisms adapt their metabolic behaviour depending on their environmental conditions. Thus, to make their model solvable, the unknown parameters were varied within the

model constraints through a process of linear optimization that maximised the growth rate for any given set of conditions.

The validation of their model required all extra and intracellular functional macrommolecules (e.g polysaccharides or different pigments) to be measured in both a batch and continuous cultivation. Although most of the model parameters could be derived from experimental conditions (e.g. light intensity, initial concentrations of biomass, pigments, polysaccharides etc.) many parameters - namely those describing intracellular control - had to be estimated from other sources and in some cases assumed.

The advantages of this type of model is that it can improve our physiological understanding of the fundamentals of photosynthetic growth. The disadvantages include, but are not limited to, the extensive experimental analysis required for validation and its incompleteness to be able to predict growth rates without a forced optimization.

Yoshimoto *et al.* (2005) used a different structured approach in their model, which was designed specifically to predict represent the flashing light effect (FLE). Their physiological approach focused on the RuBP particles (ribulose-1,5- bisphosphate) that circulate and react in the Calvin Cycle. The model requires no differential or integral equations. It was fitted and validated for batch cultures of *Caetoceros calcitrans* under conditions of inducing the FLE (*freq.* from 0 to 10 s^{-1}) and under constant illumination ~ 180 $\mu mol \cdot m^{-2} \cdot s^{-1}$. The model fitted well in the case of representing a P-I curve and was able to simulate the FLE as a function of frequency. As the authors admit, the model parameters were chosen so as to fit the data, and thus the model's true mechanistic abilities were not necessarily validated.

2.9.3 Dynamic physiological models utilizing the concept of photosynthetic factories (PSF)

Sitting somewhere between the two extremes of static light curve models and fully structured models are models that employ the concept of Photosynthetic Factories (PSF), also called the Photosynthetic Unit (PSU). These models break down photosynthesis into its simplest individual steps to include at least one photochemical energy capture step and a metabolic consumption step. It was Eilers & Peeters (1988) who first proposed this type of dynamic model for photosynthesis and it has since been adapted and extended by other authors (Rubio *et al.*, 2003; Wu & Merchuk, 2001; Han, 2002, 2001; Eilers & Peeters, 1993).

The PSF is defined as the sum of the activity of the light trapping system, reaction centers and associated apparatus, which are activated by light energy to produce photoproduct. Despite this lumping together, the definition allows the possibility of representing many of the characteristics of actual photosynthesis (Merchuk *et al.*, 2007).

The PSF is assumed to have three possible states and x_i is defined as the fraction of all PSFs in state i.

The three states are: the open state (indicating that photons can enter the PSF) called x_1, the closed or activated state x_2, and the inhibited or nonfunctional state x_3. Interchange between these three states represent different enzymatic reactions, e.g. light and dark reactions and inhibition. The possible transitions in the model are shown schematically in Fig. 2.26 and a description follows:

• The PSFs in resting state x_1 can be stimulated and transfer to active state x_2 by absorbing sufficient photons for excitation.

• The PSFs in active state x_2 have two possible paths: either absorbing additional photons and becoming inhibited to state x_3, or alternatively, releasing the energy gained from the photons to initiate the dark reactions of photosynthesis, which returns it back to the open state x_1.

• The inhibited PSF state x_3 can recover slowly over time and return to the open state x_1.

The total number of PSFs per cell can be assumed to remain constant, and if x_i is thought of as the fraction of PSFs in that respective state then: $x_1 + x_2 + x_3 = 1$. The model assumes nutrient saturation, leaving the available light I as the only variable having an effect on the kinetics.

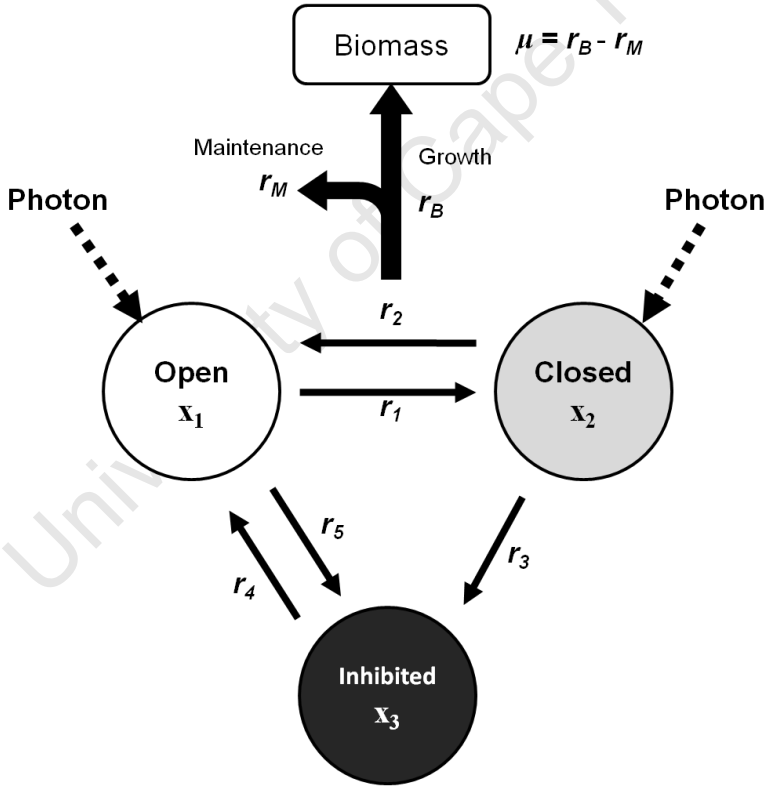

Figure 2.26 – The three possible states of the PSF are shown (x_1, x_2, x_3) together with the possible rates and directions of transition between each. r_1 is the rate of light energy absorption, r_2 the rate of release of photochemical energy for metabolic consumption, r_3 and r_5 the rate of PSF inhibition, r_4 the rate of inhibited PSF recovery, r_M the rate of energy use for cell maintenance, and r_B the rate of biomass production. The specific biomass growth rate is given by μ. Image source: this author.

The kinetics describing the rates of transition between the three states depicted in Fig. 2.26, have been formulated differently by different researchers and are summarized in Table 2.7.

Table 2.7 – Kinetic expressions proposed for the transitional steps of different PSF models

Step	Eilers & Peeters (1988)	Wu & Merchuk (2001)	Rubio *et al.* (2003)
r_1	$\alpha I x_1$	$\alpha I x_1$	$\alpha I x_1$
r_2	γx_2	γx_2	$\frac{r_{max} I x_2}{x_2 + K_s}$
r_3	$\beta I x_2$	$\beta I x_2$	$\beta \sqrt{I} x_2$
r_4	δx_3	δx_3	δx_3
r_5	-	-	$\beta \sqrt{I} x_1$
r_B	$k\gamma x_2$	$k\gamma x_2$	$k\gamma x_2$
r_M	-	$-Me$	-

Starting with the original formulation of Eilers & Peeters (1988), the probabilities of the state transfers after photon capture (r_1 and r_3) are assumed to have a first order proportionality to light intensity I with rate constants α and β . The other state transitions (r_2 and r_4) are light independent and their rates of transfer are assumed constant: γ for metabolic consumption, and δ for the zero order recovery from photoinhibition. It must be understood that I is not a fixed constant but a function of time, i.e. $I(t)$, which is the *light history* experienced by the cells. The PSF fractions are also constantly changing with time. Thus, the model can be represented by a set of linear differential equations to represent the rates of transitions between the three states:

$$\frac{dx_1}{dt} = -\alpha I x_1 + \gamma x_2 + \delta x_3 \tag{2.20}$$

$$\frac{dx_2}{dt} = \alpha I x_1 - \gamma x_2 - \beta I x_2 \tag{2.21}$$

with

$$x_1 + x_2 + x_3 = 1 \tag{2.22}$$

This original model of Eilers & Peeters (1988) was adapted by Wu & Merchuk (2001) to model biomass growth for the red marine algae *Porphyridium* sp. The specific biomass growth rate μ was assumed proportional to the release of energy for metabolic consumption r_2. In order for the model to to be able to predict a negative growth rate, a maintenance term Me was introduced to account

for energy used for cellular maintenance as well as cellular damage in adverse environments (e.g. high shear stress or extreme low light intensity) with k as a yield constant and x representing biomass concentration. Eq. 2.24 shows the resulting biomass production rate:

$$\mu = k\gamma x_2 - Me \tag{2.23}$$

$$\frac{dx}{dt} = \mu x \tag{2.24}$$

Parameters for this kinetic model were determined for *Porphyridium sp.* by conducting experiments in a thin tubular loop reactor under different light/dark cycles and over a range of light intensities (Wu & Merchuk, 2001). To date, this is the only species for which the model has been fitted, with results shown in Fig. 2.27 and the associated parameters given in Table 2.8. The fit is adequate at best and although 95% confidence intervals are given in Table 2.8, they are meaningless given their extreme range.

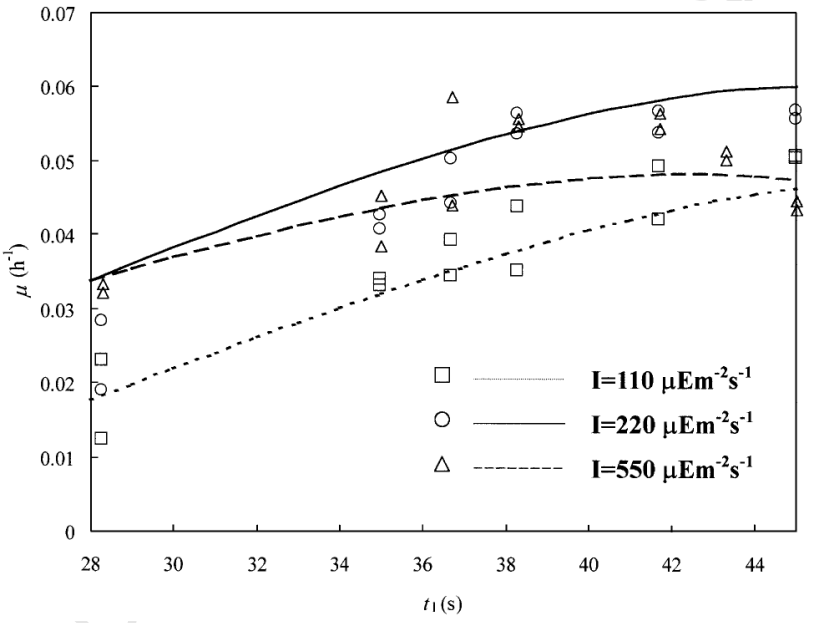

Figure 2.27 – Experimental data for specific growth rate μ of *Porphyridium* sp. , vs. light time t_l for three different light intensities, and the curves corresponding to the fitted model. Image source: Wu & Merchuk (2001)

Table 2.8 – Values of parameters for PSF model, determined by Wu & Merchuk (2001) for algal species *Porphyridium.* The parameter f' was used for fitting the model to *chlorophyll* fluorescence data and is not part of the PSF model. Source: Wu & Merchuk (2001)

Parameter	Value	95% confidence interval
α	0.001935 μE m^{-2}	−0.00189–0.00576
β	5.7848×10^{-7} μE m^{-2}	−0.000343–0.000344
γ	0.1460 s^{-1}	−0.133–0.425
δ	0.0004796 s^{-1}	−0.284–0.285
k	0.0003647 (dimensionless)	−0.000531–0.00126
Me	0.05908 h^{-1}	−0.0126–0.131
f'	0.5110 (dimensionless)	0.494–0.528

Owing to the simplifications made in the Wu & Merchuk (2001) model, not all of the physiological occurrences of photosynthesis are accounted for, namely photoadaptation. However, the advantage of the model is that the differential equations are easy to solve by fast analytical or numerical means and with a minimum number of parameters.

Rubio *et al.* (2003) proposed different equations to describe the rates of transitions between PSF states, as presented in Table 2.7. Their model can account for photoadaption, photoinhibition and flashing light effect. It as two distinguishing features:

1. Rubio *et al.* (2003) propose that r_2, the release of stored photochemical energy for carbon fixation and biomass production, is an enzyme mediated process which obeys a rate law. Eilers & Peeters (1988) and Wu & Merchuk (2001) assumed this transition to occur at a constant rate in proportion to the available light energy. Rubio *et al.* (2003) assumed a Michaelis-Menten type relation for this step, i.e:

$$r_2 = \frac{r_{max} x_2}{K_s + x_2} \tag{2.25}$$

where K_s is a constant. Therefore, in the presence of a high concentration of active states x_2 (light-saturated growth), the consumption rate approaches a maximum given by r_{max} , whilst the rate shows a linear dependence to x_2 when the fraction of active PSFs is low ($x_2 \approx K_s$) i.e light-limited growth.

2. Photoinhibition is assumed to have a square root dependence on PFD (rather than a first order dependence) which the authors based on results of experimental studies done by Nedbal *et al.* (1996):

$$r_3 = \beta \sqrt{I} x_2 \tag{2.26}$$

Photoadaptation was incorporated into the model by varying the total "amount" of PSFs in response to changing light intensity. The higher the PFD, the less PSFs were required, and the converse was assumed true under low irradiances, for which the concentration of PSFs increased. This was modeled according to the asymptotic function of Zonnenveld (1998) (cited in Rubio *et al.* (2003)):

$$a_t = \frac{r_m^*}{k_c + \frac{k_a \sqrt{I}}{\varsigma}} \tag{2.27}$$

where a_t is the total concentration of PSFs (mol·cell^{-1}), k_c is a rate constant (s^{-1}), k_a is the absorption coefficient for photons (m^2·mol^{-1}), ς is the ratio of inhibition rate to recovery rate, r_m^* is the maximum rate of energy consumption (mol·cells·s^{-1}). As a result of the Michaelis-Mention modification, shown in Eq. 2.25, the system of ordinary differential equations representing the model are non-linear and an analytical solution is nontrivial, leaving only numerical techniques to obtain a solution. The model has been used to explain previously published data, as shown in Fig. 2.28a, and has been able explain trends and predict growth rates for the high-frequency light/dark cycles data of Nedbal *et al.* (1996), shown in Fig. 2.28b.

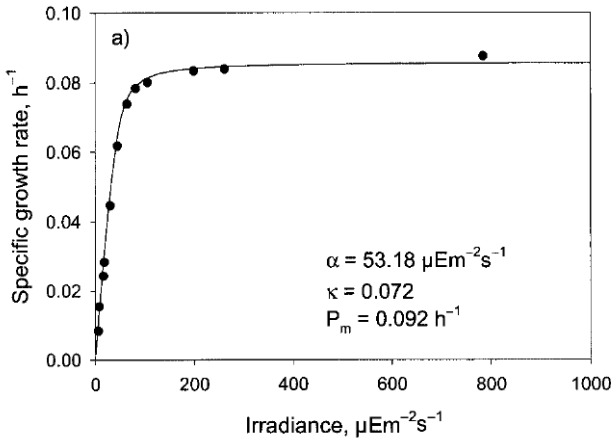

(a) Fit of the model to steady state growth data of Phillips and Myers (1954), emulating P/I growth curve.

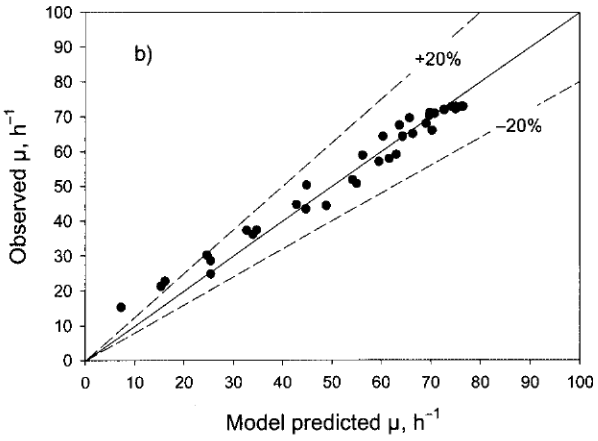

(b) Observed specific growth rate vs. model-predicted specific growth rate: data of Nedbal et al. (1996) for cultures of *Scenedesmus quadricauda*, *Chlorella vulgaris* and *Synechococcus Elongates*. The solid lines indicates exact agreement.

Figure 2.28 – Model predictions versus real experimental data. Both figures taken from Rubio *et al.* (2003).

Although three such PSF models have been proposed (Table 2.7), thorough model validation and parameter estimation is scarce. Despite the fact that the model of Rubio *et al.* (2003) has been used to predict many results found in literature, a thorough experimental investigation on a single species to obtain species specific parameters is lacking. In addition, many of the predicted literature results were for steady-state conditions (Rubio *et al.*, 2003). Although the model can predict dynamic light/dark cycling characteristics satisfactorily, it was not tested against any such experiments. To the best of the authors knowledge, only the Wu & Merchuk (2001) model has been properly investigated experimentally and the model and model parameters (Table 2.8) have since been used for other modelling investigations for airlift photobioreactors (Marshall & Huang, 2010; Vunjak-Novakovic *et al.*, 2005; Wu & Merchuk, 2004; Luo & Al-Dahhan, 2004).

2.10 Modelling fluid dynamics to generate light history

The *light history* experienced by a cell can be approximated by knowledge of a cell's trajectory through a photobioreactor's light regime, which is defined by a light distribution model. The conventional description of flow in a reactor, using residence time distribution (RTD), does not provide sufficient information for photosynthetic model integration. This is because fluid elements that spend the same time in the reactor will move through regions of differing light intensity, and thus have different kinetic behaviour. As such, a hydrodynamic model is required to predict fluid trajectories and approximate a cell's light history by combining the hydrodynamic model with the light distribution model.

2.10.1 Advanced hydrodynamic measurement techniques

One such method of predicting cellular trajectories relies entirely on experimental data generated by particle tracking. Luo & Al-Dahhan (2004) developed and utilized CARPT (Computer Automated Radioactive Particle Tracking) to track and calculate the variable light intensities experienced by cells circulating inside an airlift reactor. This was done by combining the Lagrangian information $(x(t), y(t), z(t))$, as shown in Fig. 2.29a, with a light distribution model (in their case, Beer-Lambert law). This enabled the generation of a light history function $I(t)$ as shown in Fig. 2.29b.

To predict biomass growth in an airlift reactor, the light history was combined with the dynamic photosynthetic growth model and parameters of Wu & Merchuk (2001). The authors noted that such Lagrangian information could be unattainable experimentally, especially for large reactors where particle tracking would be impractical by the CARPT technique. This would create difficulties associated with scaling-up the model for design of a commercial sized reactor, since CARPT data from a lab scale reactor could not be scaled-up to a commercial size. However, the same Lagrangian information could be obtained by CFD modelling that could enable appropriate scale-up.

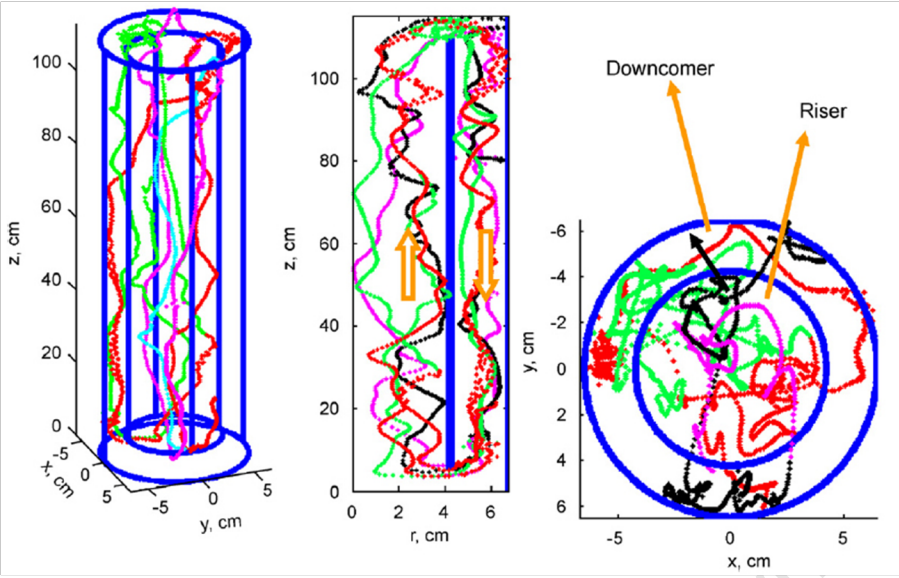

(a) Visualization of typical trajectories of the tracer particle in ALR draft tube. (a) 3-D visualization; (b) projected on the r-z plane; and (c) on the cross-sectional plane. Image source: Luo & Al-Dahhan (2008a)

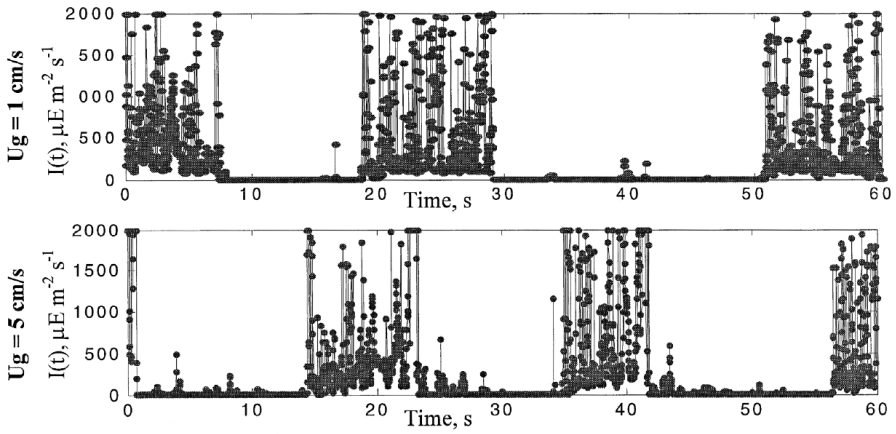

(b) Time series of irradiance a cell experienced in the bioreactors. Image source: Luo & Al-Dahhan (2004).

Figure 2.29 – Generating light history using CARPT: Experimental results from the work of Luo & Al-Dahhan (2004, 2008a)

2.10.2 Computational fluid dynamics (CFD)

The use of CFD modelling enables the prediction and visualization of complex movements of individual cells through light gradients inside the reactor. Various approaches have been developed in literature (Perner-Nochta & Posten, 2007; Sastre *et al.*, 2007; Pruvost *et al.*, 2002) using either either commercial code (FLUENT) or Lagrangian formulation from first principles. The methods combine CFD simulations of three-dimensional turbulent single-phase fluid flow with statistical particle tracking and signal analysis. Particle trajectories are then analyzed and combined with an independent light

distribution model to obtain light fluctuations experienced by single cells. The method shows huge potential for scale-up. To date, only Pruvost *et al.* (2008) has avoided an independent solution, by simultaneous solution of the RTE and their Lagrangian model (extremely complex!). More recently, Sato *et al.* (2010) developed a 2-fluid model (accounting for gas and liquid separately) to predict the fluid trajectories more accurately and account for mass transfer effects. Other successful CFD models for airlift reactors, but not for photobioreactor applications, have also been developed by Feng *et al.* (2007) and Talvy *et al.* (2005).

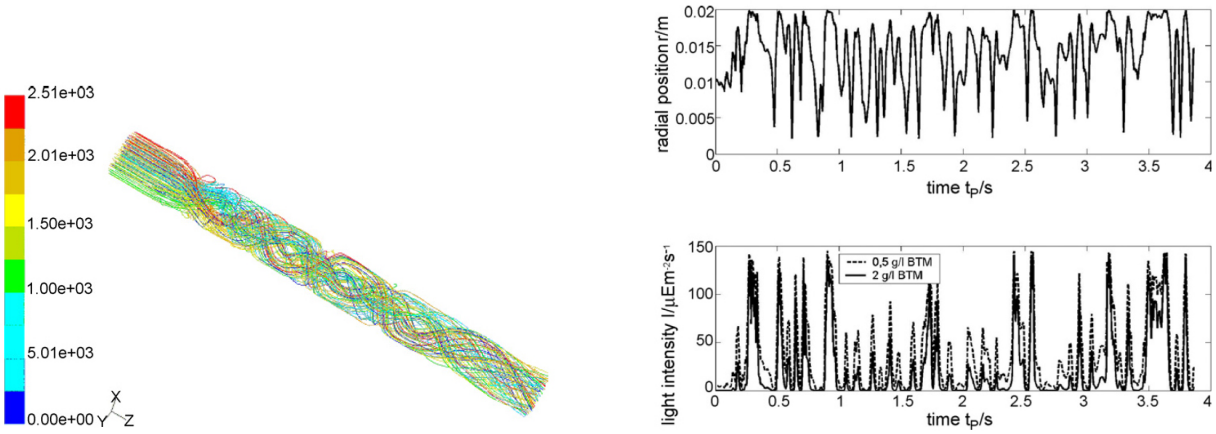

(a) Cell trajectories predicted by CFD for a tubular photobioreactor with static mixer.

(b) Simulations of radial light distribution (top) and light history (bottom) for two different biomass concentrations.

Figure 2.30 – Examples of CFD modelling results. Both images sourced from Perner-Nochta & Posten (2007).

Fig. 2.30 shows typical results from CFD simulations by Perner-Nochta & Posten (2007). Fig. 2.30a shows a single cell's trajectories trajectory and Fig. 2.30b translates this trajectory in to a light history by using the light absorption model of Yun & Park (2001). It is clear to see the similarity in the results for the light histories simulated by CFD code (Figure 2.30b) and those found experimentally for an airlift via particle tracking (Figure 2.29b). The main difference between these results comes about from the difference in the reactor geometries tested. In the Perner-Nochta & Posten (2007) simulation, the reactor was tubular with flow in a single direction, hence one does not see periodic regions of light and dark, as seen in the results for an airlift reactor (Figure 2.29b).

CFD simulations are promising for scale-up of hydrodynamic behaviour to commercial sized reactors since they are based on fundamental principles. Their main disadvantage lies in their complexity and extremely long computation time. Other more general techniques have been developed which can obtain rapid approximations of hydrodynamic behaviour.

2.10.3 Approximate compartmental method to generate light history

Wu & Merchuk (2004) developed an approximate method for modelling an airlift reactor based on dividing the reactor into regions of varied flow (Fig. 2.31 (a)). The region of the riser was regarded as a dark zone and the rest of the ALR as a light zone with variable light intensity. In the riser (dark zone) the cell kinetics do not depend on the light absorbed, and hence the flow characteristics (in this case turbulent) have no influence on light utilization. In the gas separator, the flow rates are high, such that perfect mixing can be assumed (Wu & Merchuk, 2004). Because of the short residence time and mixing in this region, the light history of cells can be approximated as one of constant light intensity. In the downcomer of an airlift, the cells have the longest residence time and they experience variable light intensity depending on their position relative to the reactor surface. Thus, the flow patterns in an ALR downcomer are of particular importance.

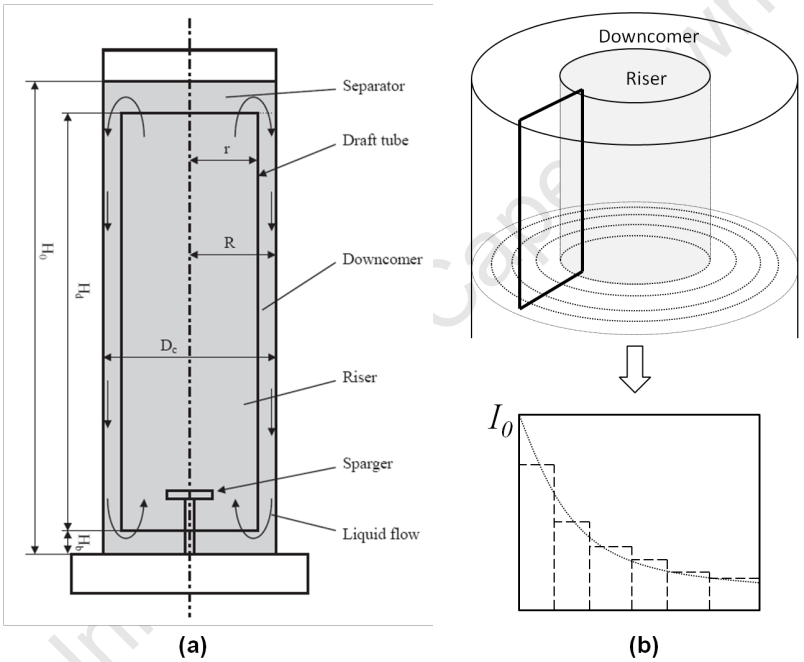

Figure 2.31 – Schematic of Wu and Merchuk (2004) compartmental approach: (a) dividing the ALR in to regions (b) distribution of light zones in the downcomer of the ALR. Image sources: (a) Wu & Merchuk (2001) (b) author

Wu & Merchuk (2003) proposed that under reasonably low gas flow rates (U_{Gr} 0.005 - 0.025 m.s^{-1}), the downcomer experiences plug flow characteristics, with essentially no gas entrainment. This conclusion was based on previous work done by the same authors using an optical tracking technique (OTTS) to accurately monitor fluid trajectories in an airlift downcomer. Luo & Al-Dahhan (2008b) confirmed the same plug flow hypothesis using the CARPT technique when investigate macro-mixing in airlift draft tubes over a range of U_{Gr} from 0.0029 to 0.05 m.s^{-1}. Results from both studies are shown graphically in Fig. 2.32.

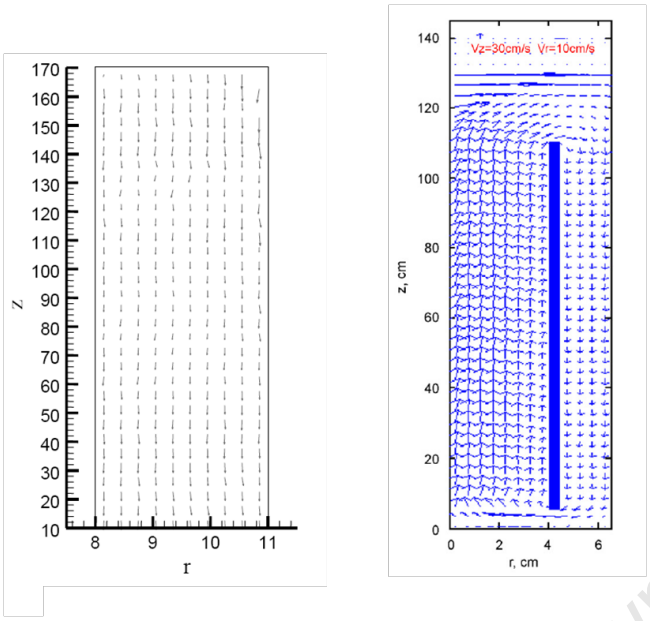

Figure 2.32 – **Left**: Flow map of the downcomer (Wu & Merchuk, 2003) for $U_{Gr} = 0.025$ m.s^{-1}. **Right**: Visualization of liquid velocity vectors in the r-z and cross-sectional planes (the solid area shows the draft tube) from Luo & Al- Dahhan (2008) for $U_{Gr} = 0.05$m.s^{-1}

Using this result, Wu & Merchuk (2004) assumed that individual cells entering the downcomer experience more or less the same light intensity for the duration of the time spent traveling down the downcomer, i.e there is minimal lateral movement. The downcomer was divided into radial regions representing light zones of the same averaged illuminance. The fraction of cells in each zone could be calculated based on the assumption that the cells are homogeneously distributed. The fluid dynamics in each region were then defined using hydrodynamic models for liquid circulation and gas hold-up. Using all this information, a light history of cells could be approximated and used to integrate the kinetic model (Wu & Merchuk, 2001) to estimate growth rates. Wu & Merchuk (2004) found good agreement with between their simulated growth curves for an airlift reactor and experimental data (Fig. 2.33) over a range of superficial gas velocities (0.00113 - 0.0171 m.s^{-1}).

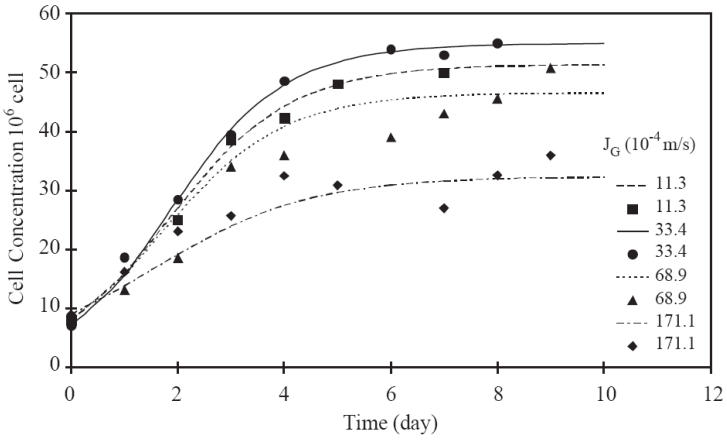

Figure 2.33 – Simulations of biomass growth in and airlift reactor over a range of superficial gas velocities, with comparison to the experimental data . Image source: Wu & Merchuk (2004)

2.11 Aim and objectives of research

The aims this research involved developing a model of an airlift photobioreactor. Three separate models were required in unison to describe the overall system:

1. A light distribution model to describe the light regime inside the photobioreactor
2. A kinetic growth model to describe cellular growth under changing light conditions
3. A fluid dynamic model to describe cellular movement through the light regime

Each of these sub-models was developed separately, requiring separate experiments to obtain parameters and validate results. The results of each model were then analyzed independently with key questions that center on investigating the effects of light provision on algal growth and showing the potential of using the models as tools to achieve optimal algal growth and airlift design. The final objective of this work was to couple the three models together to produce a global model for an airlift reactor.

Chapter 3

Light distribution: model development, results, simulations and discussion

This chapter deals with the development of a light distribution model for a cylindrical system. Experiments were performed to obtain model parameters for the algal species *Scenedesmus* sp. The model, once fully defined, is integrated into an overall model for an airlift reactor in Chapter 6.

3.1 Geometric considerations

The dual asymptotic model proposed by Suh & Lee (2003) was chosen and adapted for modelling the light distribution for this work, as given in Eq. 3.1. It enables a more realistic representation of light distribution in algal suspensions than traditional linear Beer-Lambert law. This is because scattering effects in algal suspensions cause a non-linear relationship between absorbance and cell concentration (Fig. 3.10). Furthermore, the fully structured modelling approaches based on the RTE were deemed unnecessarily complex. The background to these models has been covered in Section 2.8.

$$I(C_x, z) = I_0 \cdot exp\left[\frac{-K_{a,max} \cdot C_x \cdot z}{(C_x + K_x)(z + K_z)}\right] \tag{3.1}$$

The model parameters $K_{a,max}$(-), K_x (g.L^{-1}) and K_z(m) are species specific. K_x is a function of the scattering effects of the species (which is directly related to the optical properties of the species) and K_z accounts for increased non-linearity at increased path lengths.

Fig. 3.1 shows a graphical representation of the cylindrical system for which the model applies. Eq. 3.1 is strictly valid for a rectangular system, where each point at a depth z receives light from a single direction, i.e one dimensional light propagation. For an airlift reactor, i.e a cylindrical system, the outer surface is curved and a one dimensional light model does not suffice.

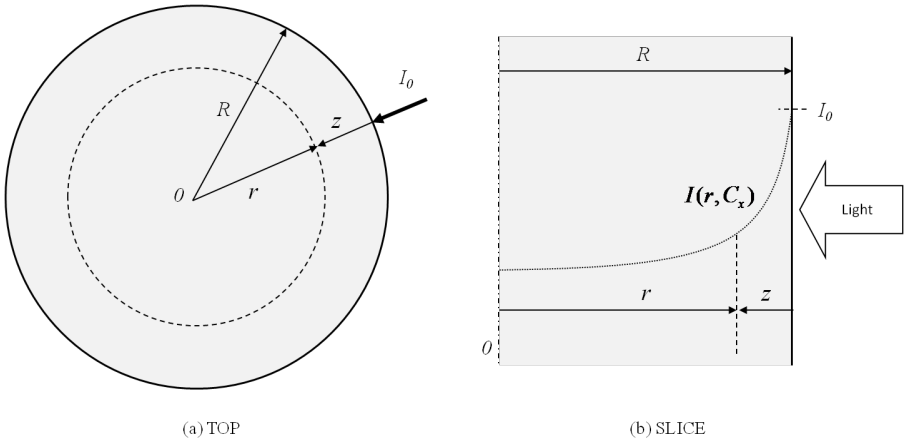

Figure 3.1 – Graphical depiction of cylindrical system for light model. (a) Top view. (b) Showing a thin slice. Image source: this author.

3.1.1 Radial versus bidimensional versus tridimensional modelling approaches

The starting point for extending the light model to a cylindrical system is assuming the radial model (Roger & Villermaux, 1983) which assumes that all incident rays intersect at the reactor central axis, as depicted in Fig. 3.2 (a). In the radial model, every point in the reactor only receives light in the direction that is perpendicular to the tangent at the outer surface *and* passing through to the center point. An obvious mathematical problem with the radial model is that it predicts an infinite light intensity as $r \to 0$.

In reality, every point within a cylindrical transparent reactor experiences light from every point on external surface, assuming that the entire surface is illuminated. The diffuse bidimensional model can account for this (Roger & Villermaux, 1983; Matsuura & Smith, 1970; Evers, 1991) and assumes that light passes through the reactor from all directions with equal probability, such that any single point experiences light according to the scheme shown in Fig 3.2 (b). Light travel is assumed to only occur in the plane normal to the cylindrical axis. This assumption is valid provided one has long enough light sources to assume a constant PFD in the vertical direction (Suh & Lee, 2003).

Models have been formulated to account for light traveling in *all* spatial directions - i.e tridimensional. Fernandez *et al.* (1997) used a tridimensional formulation for their photobioreactor light model (Fig. 3.3). A tridimensional model can account for variations in the direction of incident radiation, particularly for outdoor photobioreactors, as well as reflected radiation from the surroundings and diffuse radiation due to particulate matter in the atmosphere (Grima *et al.*, 1999; Camacho *et al.*, 1999; Fernandez *et al.*, 1997). For the scope of this study (artificial light sources and laboratory reactors) these complications were deemed unnecessary and neglected. Furthermore, Roger & Villermaux (1983) showed light absorbance data could be equally well represented by both radial, bidimensional and tridimensional models, with only slight differences between them. This suggests that the accuracy gained by using more sophisticated model may not be worth the added complexity and are not a necessity for design and scale-up purposes.

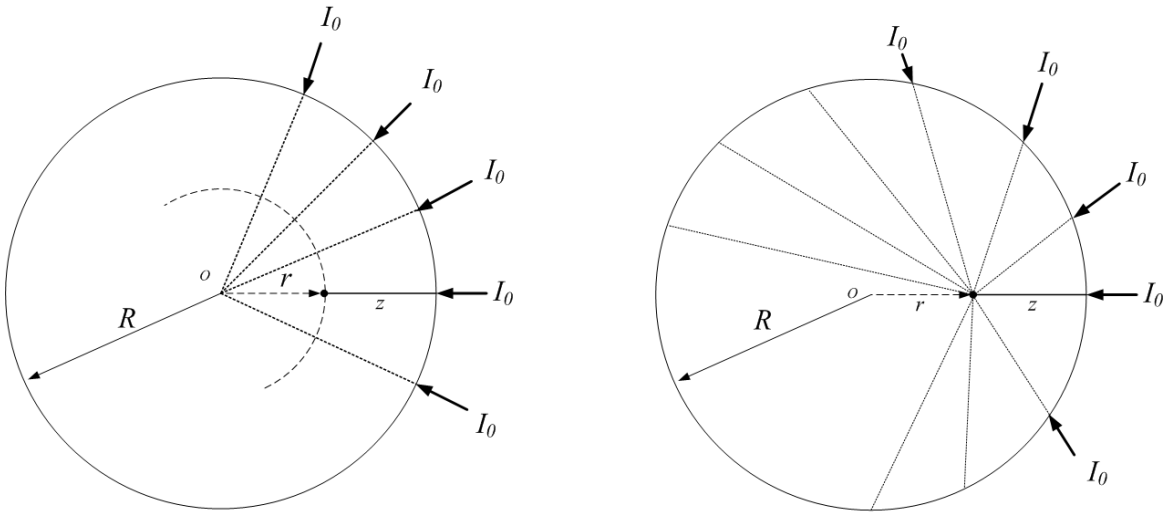

Figure 3.2 – Schematic of radial (a) and bidimensional (b) models for cylindrical systems. Image source: this author.

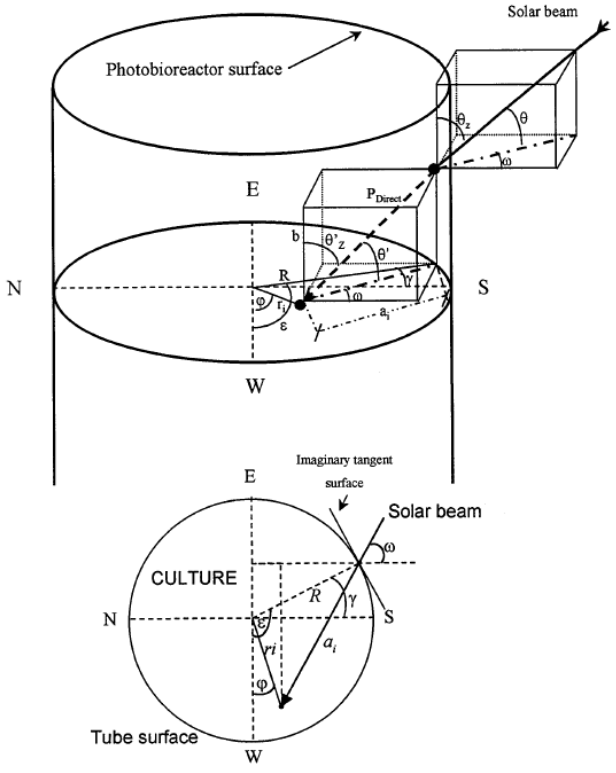

Figure 3.3 – Schematic of tridimensional light distribution model that can account for direct sunlight at changing angles, reflected radiation from the surroundings and diffuse radiation due to particulate matter in the atmosphere. Image source: Grima *et al.* (1999).

3.1.2 Light distribution model using a bidimensional (2D) approach

For the present work, a radial model was deemed too simplistic and the three dimensional analysis shown to lead to an unnecessarily complex mathematical solution (Suh & Lee, 2003). The bidimensional approach was used, which assumes that light intensity does not vary vertically in the reactor. Other important assumptions for the model include:

1. Light attenuation depends *only* on cell concentration and light path length.
2. The cells are homogeneously suspended in the medium, such that all properties that depends on cell concentration can be assumed constant throughout the reactor volume.
3. The external light source is constant at every external point around the reactor surface.

The model requires that absorption along every possible light path must be accounted for. This was done according to the analysis of Evers (1991) and illustrated in Fig. 3.4.

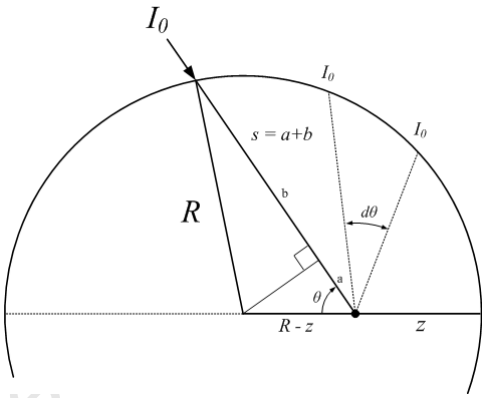

Figure 3.4 – Cross section through a cylindrical photobioreactor. All possible light paths that can reach a point at z are represented by s, where $s = a + b$. R is the outer radius and z the distance from the outer surface (i.e $r = R - z$). θ is the angle of the light path. Image source: this author after Evers (1991).

First, let the light path length from any source I_0 defined by an angle θ be $s(z,\theta)$. In Fig. 3.4, $s = a+b$ and thus:

$$s(z,\theta) = a+b = (R-z)\cdot cos\theta + \sqrt{R^2-(R-z)^2 sin^2\theta} \tag{3.2}$$

The light absorption along this path is therefore:

$$I(C_x, s(z,\theta)) = I_0 \cdot exp\left[\frac{-K_{a,max}\cdot C_x \cdot s(z,\theta))}{(C_x+K_x)\,(s(z,\theta)+K_z)}\right] \tag{3.3}$$

Light coming from all directions $(0 \leq \theta \leq 2\pi)$ has be to accounted for to calculate light intensity at any single point z. For reasons of symmetry, it is simpler to consider doubling the effects from

$0 \leq \theta \leq \pi$, thus:

$$\begin{aligned} I(z,C_x) &= \frac{2}{\pi}\int_0^{\pi} I(z,C_x,s(z,\theta))d\theta \\ &= \frac{2I_0}{\pi}\int_0^{\pi} exp\left[\frac{-K_{a,max}\cdot C_x \cdot s(z,\theta))}{(C_x+K_x)\,(s(z,\theta)+K_z)}\right]d\theta \end{aligned} \tag{3.4}$$

The light intensity experienced at the center of the reactor is minimal (Fig. 3.14) and the riser is essentially a dark zone for much of the cultivation. Thus, it is common practice to employ an opaque draft tube since it unnecessary to use a more expensive transparent material (glass or perspex) when a cheaper opaque material could be used with minimal difference in performance. Eq. 3.4 can be adjusted to account for only light *not* blocked by an opaque draft tube by using the analysis previously done by Wu & Merchuk (2004). If one lets ω be the the *minimum* angle of a light path that can reach z, then according to Fig. 3.5, ω is defined by:

$$\omega = arcsin\left(\frac{R_d}{R-z}\right) \tag{3.5}$$

Eq. 3.4, now with integration limits on θ, becomes:

$$I(z,C_x) = \frac{2I_0}{\pi}\int_{\omega(z)}^{\pi} exp\left[\frac{-K_{a,max}\cdot C_x \cdot s(z,\theta))}{(C_x+K_x)\,(s(z,\theta)+K_z)}\right]d\theta \tag{3.6}$$

In the case of Wu & Merchuk (2004), the experimental airlift reactor used had an opaque draft tube. In our laboratories, the draft tubes were made of glass and thus Eq. 3.4 is more applicable. However, it is worth showing the development of both models for completeness.

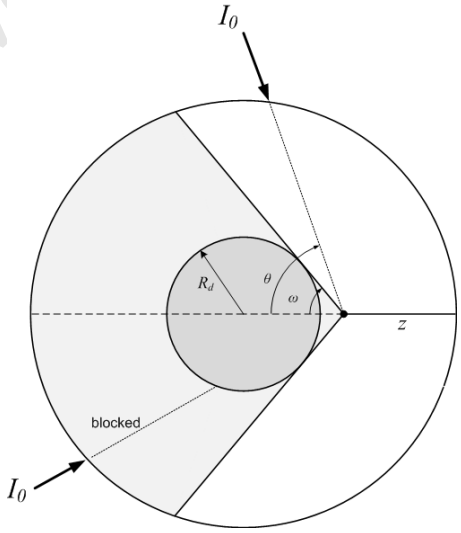

Figure 3.5 – Schematic of analysis according to Wu & Merchuk (2004) after Evers (1991). Every point in the downcomer receives light from every point on the external surface, except for those blocked by an opaque draft tube. Image source: this author, after Wu & Merchuk (2004).

3.2 Materials and experimental methods

The model is a function of two variables: (i) the distance from the illuminated surface and (ii) the algal concentration. Thus, parameter estimation was performed by measuring light intensity changes at increasing depths over a range of algal concentrations.

Using the same methodology of Suh & Lee (2003), a rectangular system was utilized so that it could be assumed that light travelling in one direction was being measured. The model parameters obtained from a rectangular system could then used for the cylindrical system (Suh & Lee, 2003). A container was constructed (Fig. 3.6) comprising of 6 opaque non-reflective perspex sides with a single side made from fully transparent perspex. The clear side was illuminated uni-directionally at a fixed distance by a light source comprising three 40W fluorescent lights (Osram). This yielded a surface PFD of 180 μmol $\cdot$ m^{-2}s^{-1}.

Light intensity changes were measured at increasing distances from the light-source surface from 0 to 5 cm. This was repeated over a range of cell concentrations, from 0.1 to 3.83 g$\cdot$L^{-1}. *Scenedesmus* sp. (the algal species used) cultivated according to the methods outlined in Appendix B.

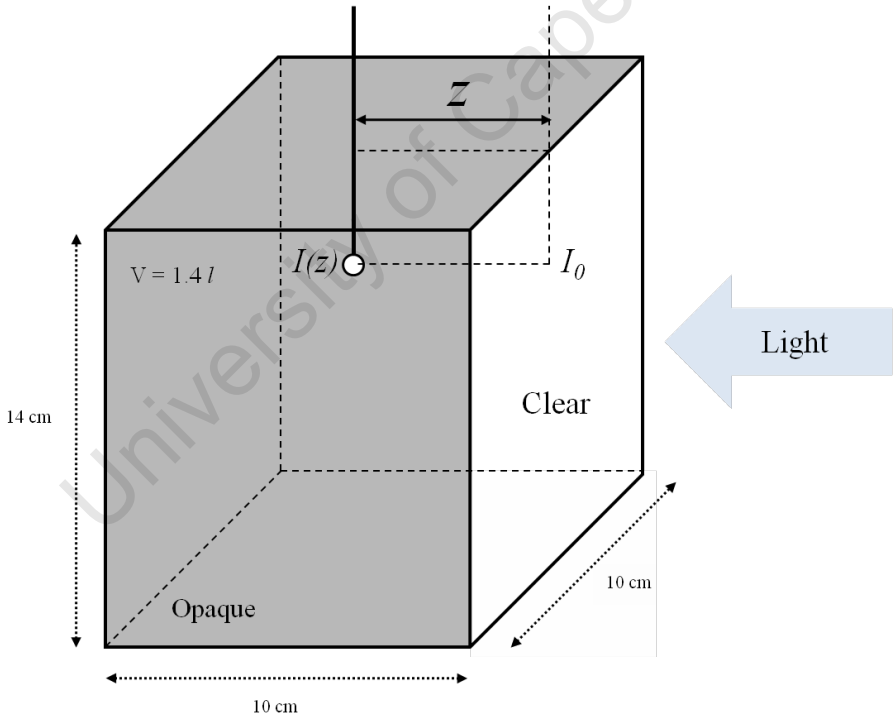

Figure 3.6 – Schematic of the rectangular chamber constructed for controlled light measurements: Dimensions were 10x10x14 cm. The chamber held a maximum of 1.4 liters of algal culture, kept in homogeneous suspension by frequent mixing. A narrow slit on the lid of the chamber allowed the sensor to be submerged and moved to various distances from the illuminated surface. Image source: this author.

(a) (b)

Figure 3.7 – (a) Submersible spherical micro quantum sensor (US-SQS/L, Walz). Image source: http://www.walz.com/ (b) flat-plane quantum sensor (Li-190, Li-COR). Image source: http://www.licor.com/

Light intensity was measured using a submersible micro quantum sensor (US-SQS/L, Walz), shown in Fig. 3.7. This was connected to a light meter and datalogger (Li-250, LI-COR) . This type of quantum sensor measures total PFD in the PAR range (400 – 700 nm). Its spherical shape allows it to measure light absorbed from all directions. This enables it to account for light absorbed from scattering effects. More specifically, the micro sensor measures the photosynthetic photon fluence rate (PPFR). This is defined as the amount of PAR hitting a point or small sphere from all directions weighted equally and divided by the cross-sectional area of the sphere and time-interval. The units for PPFR are μmol.m^{-2}s^{-1}, which are the same as PFD. PPFR quantifies exactly the same thing as PFD but is based on a spherical rather than planar geometry.

3.3 Results and discussion for light distribution model

3.3.1 Beer-Lambert law parameters

For comparison purposes, Beer-Lambert law parameters were obtained for *Scenedesmus* sp. from spectrophotometer data. Absorbance was measured over the PAR range for a range of different concentrations, as shown in Fig. 3.8. The data obtained is very similar to the data from Yun & Park (2001) for *Chlorella vulgaris*, given in Section 2.2.3. *Scenedesmus* sp. shows the same two peaks, one near 430 nm and the other near 675 nm, both typical characteristic of absorption spectra of a green algae containing *chlorophyll-a* as the major light-harvesting pigment (Yun & Park, 2001).

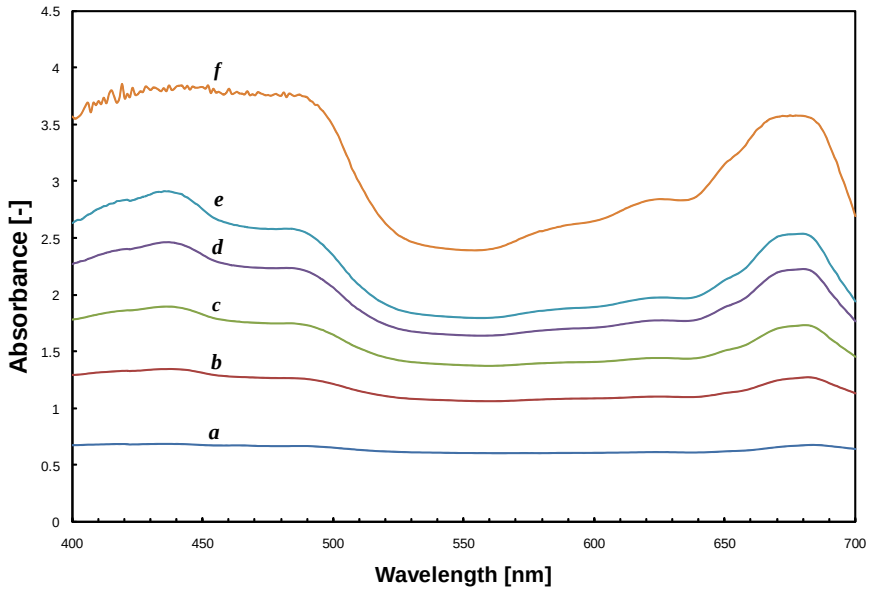

Figure 3.8 – Absorbance spectra for *Scenedesmus* sp. in the PAR range. Algal concentrations (g.L^{-1}) are: ***a*** 0.227, ***b*** 0.454, ***c*** 0.681, ***d*** 0.901, ***e*** 1.135, and ***f*** 2.27 . These spectra were obtained using standard 1 cm cuvettes in a spectrophotometer (Helios Gamma UV-Vis, Thermo Scientific).

The Beer-Lambert law $K_a(\lambda)$ was obtained for each wavelength by least squares linear regression of Eq. 3.7 over all concentrations in Fig. 3.8 and at every integer wavelength in the PAR range, according to the methods outlined in Pruvost *et al.* (2002).

$$A'(C_x,\lambda) = K_a(\lambda)\cdot C_x \tag{3.7}$$

Fig. 3.9 shows the result for the absorption coefficient $K_a(\lambda)$ varying with wavelength. From this data, an average absorption coefficient of $K_a = 2.3\text{L}.g^{-1}.cm^{-1}$ was calculated according to Eq. 2.10 and this value is represented by the dotted line.

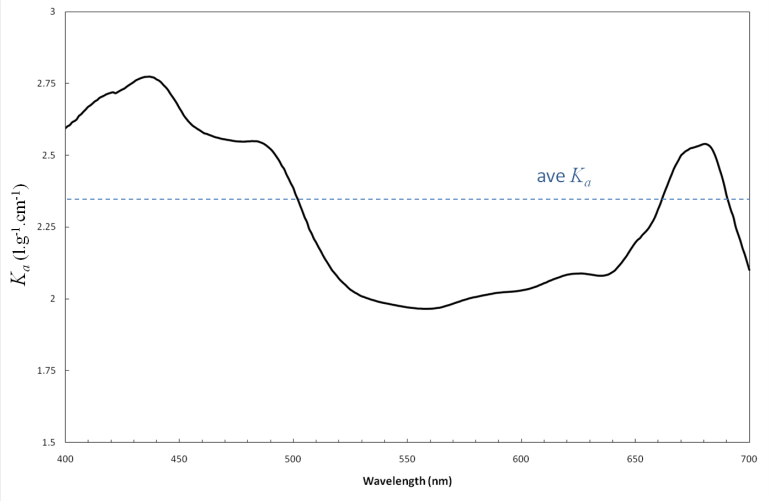

Figure 3.9 – Absorption coefficient K_a as a function of wavelength obtained from the data depicted in Fig. 3.8, by linear regression of the function $A'(C_x, \lambda) = K_a(\lambda) \cdot C_x$ for the concentrations tested.

3.3.2 Parameter estimation from rectangular system

With re-arrangement of Eq. 3.1, the model is derived for a rectangular system:

$$ln\frac{I}{I_0} = \frac{-K_{a,max} \cdot C_x \cdot z}{(C_x + K_x)(z + K_z)} \tag{3.8}$$

where z (cm) is the light path length from the irradiated surface, I_0 (μmol $\cdot$ m^{-2}s^{-1}) is the light intensity at $z = 0$ and I is the light intensity at any path length and concentration C_x (g.L^{-1}).

Best-fit model parameters (Table 3.1) were obtained by non-linear regression of the model over the experimental data. The regression was performed in MATLAB according to the methods shown in Appendix G.1.

Table 3.1 – Light distribution model parameters determined from nonlinear regression along with 95% confidence intervals.

Parameter	Value	95% Confidence	Unit
$K_{a,max}$	83.9	$\pm$9.64	(-)
K_x	7.51	$\pm$0.85	g.L^{-1}
K_z	9.53	$\pm$1.06	cm

The results show light absorption deviating from Beer-Lambert law linearity as the light path length (Fig. 3.10) and cell concentration increased (Figure 3.11). The smooth dashed lines show the model's good fit with the experimentally observed light absorption patterns.

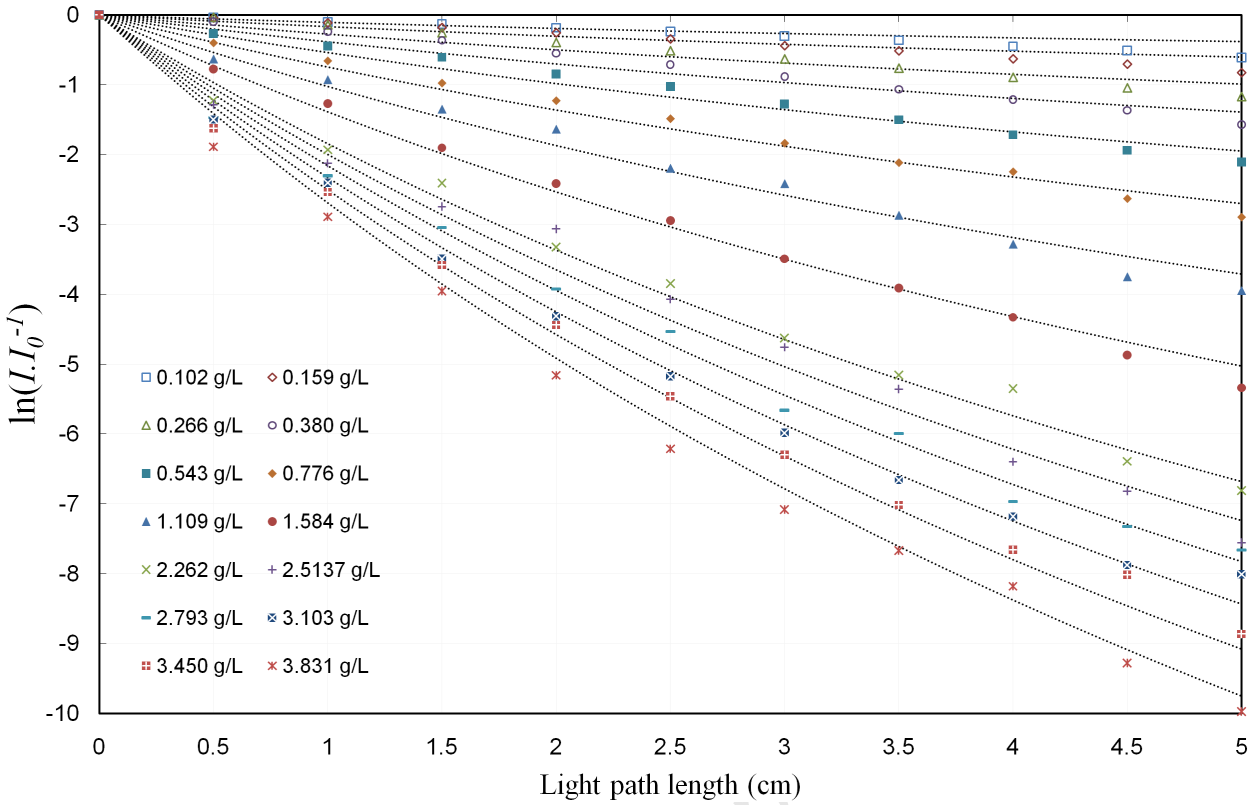

Figure 3.10 – Light absorption versus path length. Discrete points are experimental data and lines are model fits.

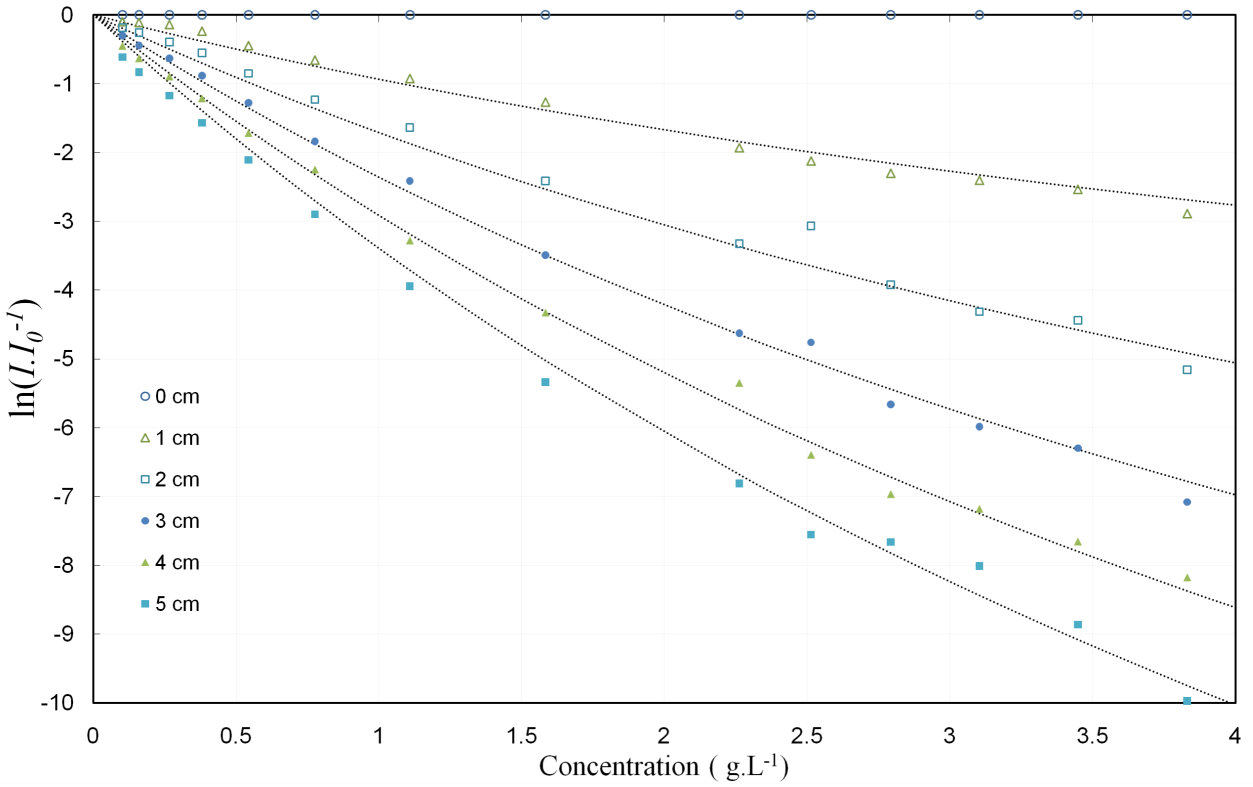

Figure 3.11 – Change of light absorption versus cell concentration. Discrete points are experimental data and lines are model fits.

3.3.3 Model simulations

Fig. 3.12 shows a comparison between the fitted model (Eq. 3.8) and Beer-Lambert law for the rectangular system. In order to illustrate the characteristic exponential decay, I/I_0 has been plotted instead of $ln\,(I/I_0)$ and the comparison is shown for one of the concentrations tested (0.775 g.L^{-1}).

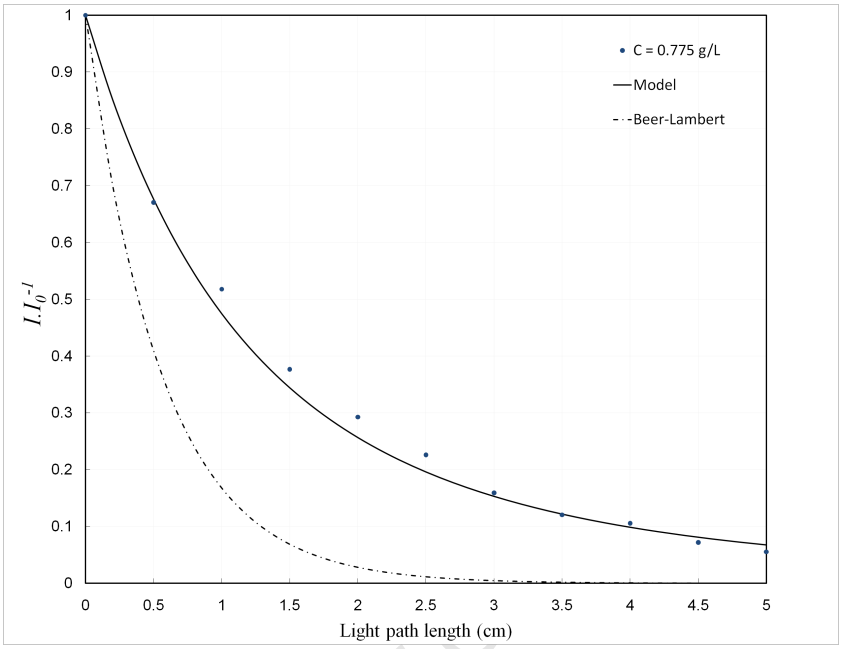

Figure 3.12 – Comparison between dual-asymptotic model and Beer-Lambert law for changes with light path length at a concentration of C_x= 0.775 g.L^{-1}. Data and model for rectangular system.

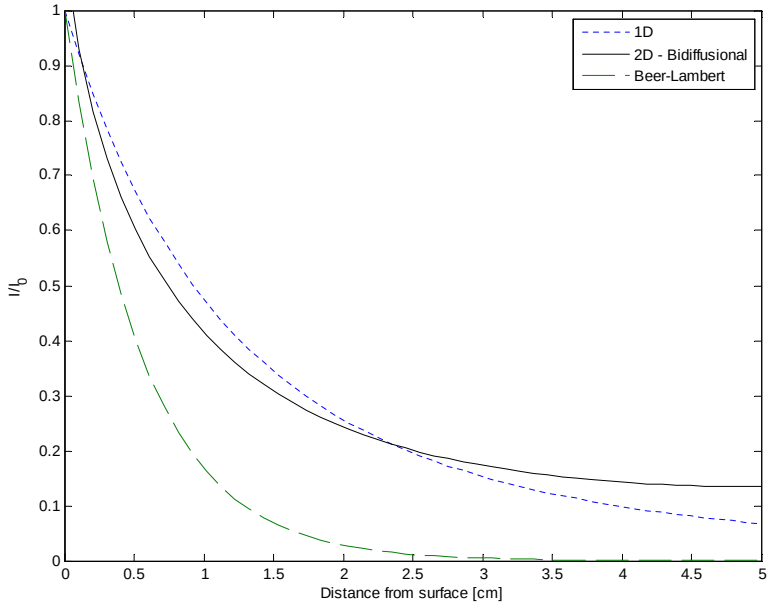

Figure 3.13 – Comparison between 1D light model (Eq. 3.1) and 2D light model (Eq. 3.4) for a 5cm radius cylinder, species *Scenedesmus* sp. at C_x = 0.775 g.L^{-1}. Model simulated for cylindrical system.

Beer-Lambert law's overestimation of light absorption is clear in Fig. 3.12 and the dual-asymptotic model is able to predict the characteristic decay with greater accuracy. The importance of accurately modelling the light distribution becomes hugely significant when integrating the light distribution model into the overall airlift model. An underestimation in available light intensity will result in an underestimation of growth in the kinetic model. It could also lead to an underestimation in inhibition experienced by cells near the surface, depending on the level of the light intensity. By proving an adequate model fit independently (Fig.3.10) one can predict light intensity in the overall photobioreactor model with more confidence.

The model for a cylindrical system (Eq. 3.4) was solved in MATLAB, using simple numerical means[1] to perform the integration, and using model parameters given in Table 3.1. Fig. 3.13 compares the 2D bidimensional model (Eq. 3.4), the simple 1D light model (Eq. 3.1), and Beer-Lambert law, for a cylindrical simulation. The differences between the 1D and 2D models are not too significant, compared to the inaccuracy of Beer-Lambert law. The 2D model is more computationally intensive than the 1D model, and should it be required to save processing time, the 1D model could be used as a first estimate. This judgment could be improved by comparison of both methods to real experimental data for a cylindrical system, which would enable the error to be quantified explicitly, but such experimental means were not available in this work[2].

Fig. 3.14a shows the light distribution profile for a hypothetical 10 cm OD cylindrical reactor simulated over a typical range of algal concentrations. Supposing a hypothetical transparent draft tube of 5 cm diameter (shown by the dotted line), one can clearly see how, with the exception of the low concentration line ($1 g.L^{-1}$), the light intensity is almost negligible in the riser region. For an even larger reactor, as simulated in Fig 3.14b, the riser could be assumed almost completely dark for the duration of cultivation. Furthermore, Fig. 3.14 shows how the light volume is affected by scale-up. In Fig. 3.14b the majority of the reactor is essentially a dark volume and would be unable to support photosynthetic growth. This illustrates how scale-up of airlift reactors to larger diameters would be impractical, instead multiple smaller airlift reactors should be utilized to achieve a certain volumetric production.

Because the light intensity at any depth z is assumed to be the same for every depth z moving angularly around the reactor, the light model can be simulated using a surface plot. Fig. 3.15a shows a solution of Eq. 3.4 in three dimensions for $C_x = 1$ g.L^{-1}, assuming a nonexistent or perfectly transparent draft tube. In reality, a transparent draft tube would cause its own reflection and scattering of light, which would cause the real profile to deviate from the model prediction near the center of the reactor. Since this region of the reactor has such a low light intensity and is essentially a *dark zone* (Fig. 3.14), the inaccuracies of the model in this region are not critical. Fig. 3.15b simulates the model assuming an *opaque* draft tube through which light cannot penetrate and was solved according to Eq. 3.6.

[1] ode45 solver based on an explicit Runge-Kutta formula

[2] Such a comparison is recommended for future work.

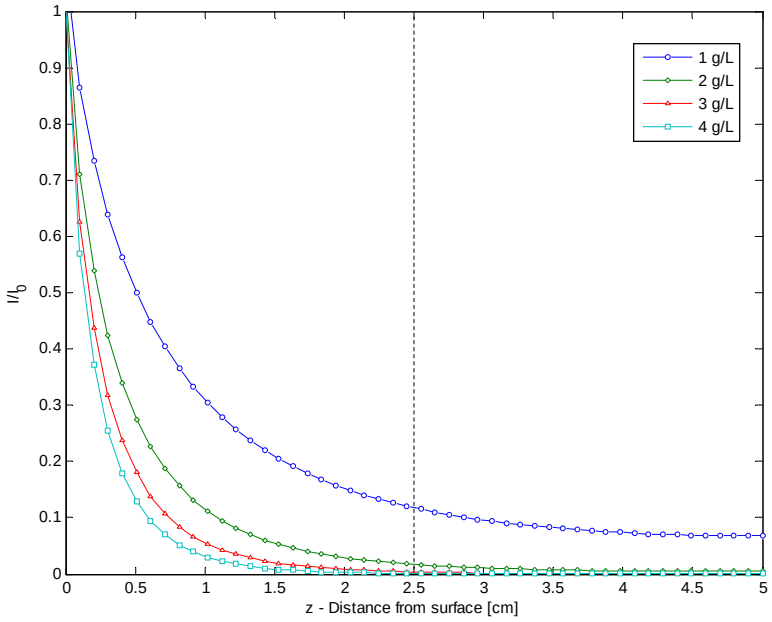

(a) Simulated for 10 cm diameter reactor

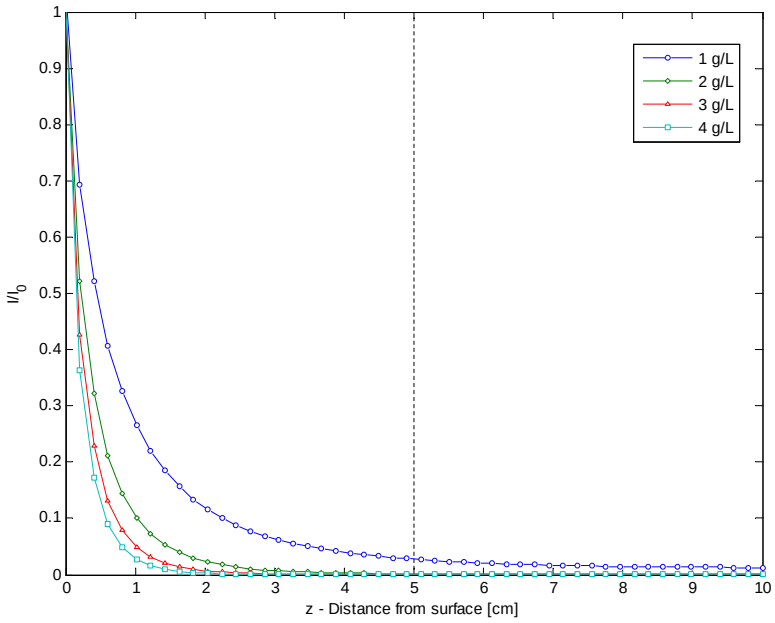

(b) Simulated for 20 cm diameter reactor.

Figure 3.14 – Simulated light intensity variation with increasing depth z in cylindrical photobioreactors, at varying algal concentrations (1,2,3 and 4 g.L^{-1}). Dotted line shows location of possible draft tube outer wall and hence the division between the riser (light) and downcomer (dark) regions.

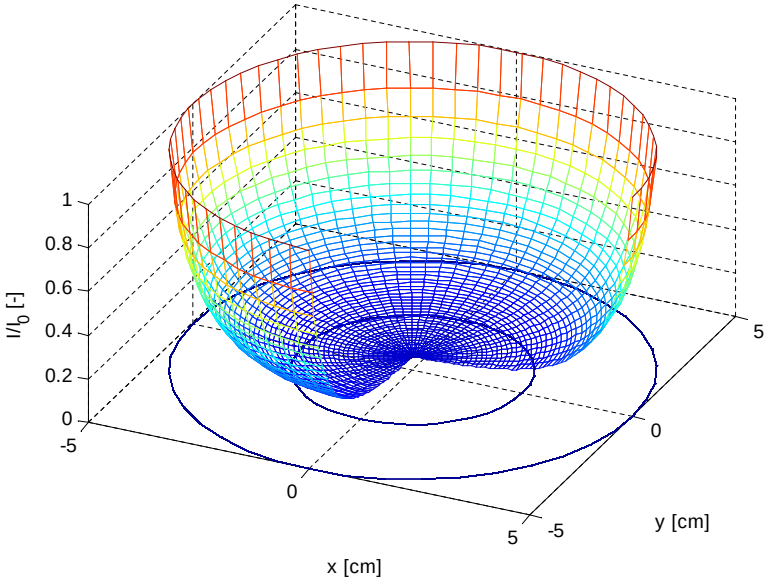

(a) Profile assuming a clear draft tube (i.e no draft tube), Eq. 3.4.

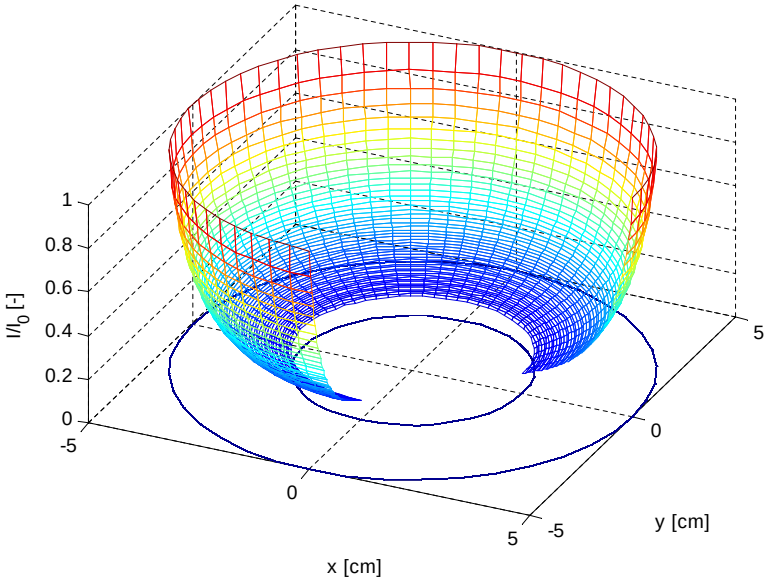

(b) Profile assuming an opaque draft tube, Eq. 3.6.

Figure 3.15 – Visualization (using 2D approach) of light distribution profiles inside a hypothetical 10 cm diameter photobioreactor with a 5 cm diameter draft tube. C_x = 1 g.L^{-1}.

3.4 Summary and conclusions for light model

- Beer-Lambert law, although widely used to model algal suspension in photobioreactors, predicts an inaccurate light distribution profile owing to nonlinearities caused by scattering effects.
- The dual-asymptotic model (Eq. 3.1), a superior model to the Beer-Lambert law, was fitted to data comprising a range of cell concentrations and path lengths and could accurately represent the light profile, as illustrated in Figures 3.10 and 3.11.
- Subsequent comparisons between the data, the fitted model, and Beer-Lambert law for a rectangular system showed the inaccuracy of Beer-Lambert law prediction more clearly (Fig 3.12).
- The dual asymptotic model could be used to simulate light distribution in a cylindrical system as a function of the distance from the reactor surface using either a simple 1D or a more accurate 2D approach (bidimensional). The difference between these approaches was not too significant (Fig. 3.13) but could not be quantified by comparison to experimental data. Should the computational intensity of the 2D model be undesirable, the 1D model could be used as an approximation.
- Simulation of the light distribution model for a cylindrical airlift system over a range of cell concentrations showed how the riser region is essentially a dark zone, which the assumption being more valid in larger reactors. The rapid increase in the dark volume with scale-up suggests the need for implementing a farm of smaller airlift reactors to achieve a large volumetric productivity.
- The light distribution model was developed independently with the aim of integrating it into a global model for an airlift photobioreactor. This is done in Chapter 6.

3.5 Recommendations

- Apparatus can be designed to test the validity of the 2D bidimensional light model for a cylindrical system. This could be achieved by construction of a transparent cylinder surrounded by multiple light sources to achieve a homogeneous incident PFD. A similar experiment to that conducted in Section 3.2 could then be performed on this cylindrical system. The 2D form of the model could then be regressed on to this new data and the results compared to those in Section 3.3.2 for the rectangular system.
- Similar experiments, using either the rectangular approach used in this work or the proposed cylindrical approach, could be performed for other algal species to build a database of model parameters as well as characterize the differences in absorbance characteristics between species.

Chapter 4

Photosynthetic growth: model development, results, discussion and simulations

The dynamic PSF model of Wu & Merchuk (2001) was chosen to simulate photosynthetic kinetic growth. The background to this model has been covered in Section 2.9.3. The model has been fitted to experimental data for the algal species *Porphyridium* sp. successfully and was integrated into a global airlift model (Wu & Merchuk, 2004). In this part of the study, the author feels that he is making a relevant contribution to the field by:

1. Testing the model, improving aspects of its formulation and developing different methods for a model solution.
2. Coding it into an "easy to use" format in MATLAB.
3. Fitting the model to an additional species, *Scenedesmus* sp., which demonstrates the model's generic value.
4. Investigating the model's applicability to variations in cycle time, since this was not previously investigated by Wu & Merchuk (2001).

This chapter presents the model development, analysis, method of solution and the experimental means to obtain new model parameters. The results from the experiment, as well as model simulations, are then analyzed and discussed.

4.1 Model development

A detailed description of the model and the concept of photosynthetic factories (PSF) has been given in Section 2.9.3. The model equations that express the PSF dynamics and rate of biomass production are given as follows:

$$\frac{dx_1}{dt} = -\alpha I x_1 + \gamma x_2 + \delta x_3 \tag{4.1}$$

$$\frac{dx_2}{dt} = \alpha I x_1 - \gamma x_2 - \beta I x_2 \tag{4.2}$$

$$\sum_{i=1}^{3} x_i = 1 \tag{4.3}$$

$$\mu = k\gamma x_2 - Me \tag{4.4}$$

Where x_1, x_2, x_3 are the fractions of PSFs in open, closed and inhibited states, respectively; I is the instantaneous light intensity experienced by cells; $\alpha, \beta, \gamma, \delta, k, Me$ are reaction constants, and μ is the specific growth rate. The physical significance of each parameter is summarized in Table 4.1.

Table 4.1 – Physical significance of kinetic model parameters (Wu & Merchuk, 2001)

Parameter	Physical significance	Units
α	Kinetic rate constant of photon utilization for transfer $x_1 \rightarrow x_2$	$(\mu\text{mol.m}^{-2})^{-1}$
β	Kinetic rate constant of photon utilization for transfer $x_2 \rightarrow x_3$	$(\mu\text{mol.m}^{-2})^{-1}$
γ	Kinetic rate constant of transfer $x_2 \rightarrow x_1$	s^{-1}
δ	Kinetic rate constant of transfer $x_3 \rightarrow x_1$	s^{-1}
k	Biomass growth yield on x_2 activity in 4.4	(-)
Me	Constant for cellular maintenance and cellular damage	s^{-1}

The set of ordinary differential equations (Eq.4.1 to 4.3) are a linear initial value problem and can be solved for explicitly by classical methods. Three methods were developed and tested in this work: (i) an analytical solution (ii) numerical integration and (iii) an eigen vector method. The analytical solution was based on the solution of Wu & Merchuk (2001) and found most applicable to be used for the final model solution. However, the numerical method was shown to be useful, should the kinetic model be of a nonlinear form. These methods are outlined in Appendix F.2, with comparison of their respective computational efficiency.

4.1.1 Integrating the model over a single light dark cycle

The model is to be used to simulate growth for continuous light dark cycles. The starting point for the solution is to consider only a single cycle. Fig. 4.2 shows a single light/dark cycle, having a light period from $t = 0$ to $t = t_l$ with light intensity I ($I > 0$) and a dark period from $t = t_l$ to $t = t_c$ with $I = 0$.

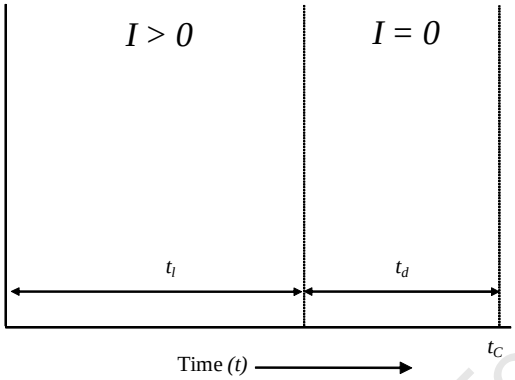

Figure 4.1 – Schematic of a single light/dark cycle of the square-wave form (see Section 2.6.1). Image source: this author.

Analytical integration of the model equations was done according to the method of Wu & Merchuk (2001, 2004). First, we re-write the set of ODEs, leaving only two independent equations, since $x_3 = 1 - x_1 - x_2$:

$$\frac{dx_1}{dt} = -\alpha I x_1 + \gamma x_2 + \delta(1 - x_1 - x_2) \tag{4.5}$$

$$\frac{dx_2}{dt} = \alpha I x_1 - \gamma x_2 - \beta I x_2 \tag{4.6}$$

Considering the *light period* first. Rearrangement of Eq. 4.6 yields:

$$\alpha I x_1 = \frac{dx_2}{dt} + \gamma x_2 + \beta I x_2 \tag{4.7}$$

Substituting Eq. 4.7 and the derivative of Eq. 4.7 into Eq. 4.5 yields:

$$\frac{d^2x_2}{dt^2} + (\alpha I + \beta I + \gamma + \delta)\frac{dx_2}{dt} + (\alpha\beta I^2 + \alpha I\delta + \beta I\delta + \delta\gamma)x_2 = \alpha I\delta \tag{4.8}$$

The general solution of Eq. 4.8 for the light period is:

$$x_{1,l}(t) = \frac{c(\beta I + \gamma) + bC_1(A + \beta I + \gamma)e^{At} + bC_2(B + \beta I + \gamma)e^{Bt}}{\alpha I b} \tag{4.9}$$

$$x_{2,l}(t) = \frac{c}{b} + C_1 e^{At} + C_2 e^{Bt} \tag{4.10}$$

Where $x_{1,l}(t)$ and $x_{2,l}(t)$ are the time variant values of x_1 and x_2 during the light period, with constants

represented by:

$$a = \alpha I + \beta I + \gamma + \delta$$

$$b = \alpha\beta I^2 + \delta\gamma + \alpha I\delta + \beta I\delta$$

$$c = \alpha I\delta$$

and

$$A = -\frac{a + \sqrt{a^2 - 4b}}{2}$$

$$B = -\frac{a - \sqrt{a^2 - 4b}}{2}$$

At the start of the light period, $t = 0$ and thus:

$$x_1(0) = \frac{c(\beta I + \gamma) + bC_1(A + \beta I + \gamma) + bC_2(B + \beta I + \gamma)}{\alpha I b} \tag{4.11}$$

$$x_2(0) = \frac{c}{b} + C_1 + C_2 \tag{4.12}$$

Thus, the integration constants C_1 and C_2 are:

$$C_1 = -\frac{Bc - \alpha I b x_1(0) + b x_2(0)(A + \beta I + \gamma)}{b(A - B)} \tag{4.13}$$

$$C_2 = -\frac{Ac - \alpha I b x_1(0) - b x_2(0)(A + \beta I + \gamma)}{b(A - B)} \tag{4.14}$$

The final value of the PSFs at the end of the light period, $t = t_l$ are:

$$x_{1,l}(t_l) = \frac{c(\beta I + \gamma) + bC_1(A + \beta I + \gamma)e^{At_l} + bC_2(B + \beta I + \gamma)e^{Bt_l}}{\alpha I b} \tag{4.15}$$

$$x_{2,l}(t_l) = \frac{c}{b} + C_1 e^{At_l} + C_2 e^{Bt_l} \tag{4.16}$$

Considering the *dark period* of the cycle: $I = 0$ and the initial conditions are set by the final conditions of the light period. Classical integration yields a solution for the PSFs during the dark period:

$$x_{1,d}(t) = 1 - e^{-\gamma(t_t - t_l)} - (1 - x_2(t_l) - x_1(t_l))e^{-\delta(t - t_l)} \tag{4.17}$$

$$x_{2,d}(t) = x_2(t_l)e^{-\gamma(t - t_l)} \tag{4.18}$$

At the end of the dark period $t = t_c$, therefore:

$$x_{1,d}(t_c) = 1 - x_2(t_l)e^{-\gamma(t_c - t_l)} - (1 - x_2(t_l) - x_1(t_l))e^{-\delta(t_c - t_l)} \tag{4.19}$$

$$x_{2,d}(t_c) = x_2(t_l)e^{-\gamma(t_c - t_l)} \tag{4.20}$$

The PSF model is now fully defined over a single light/dark cycle. A schematic of a typical PSF profile (x_1 and x_2) for a single light/dark cycle is given in Fig. 4.2. The profile shows the active state x_2 increasing during light exposure and decreasing in the dark period.

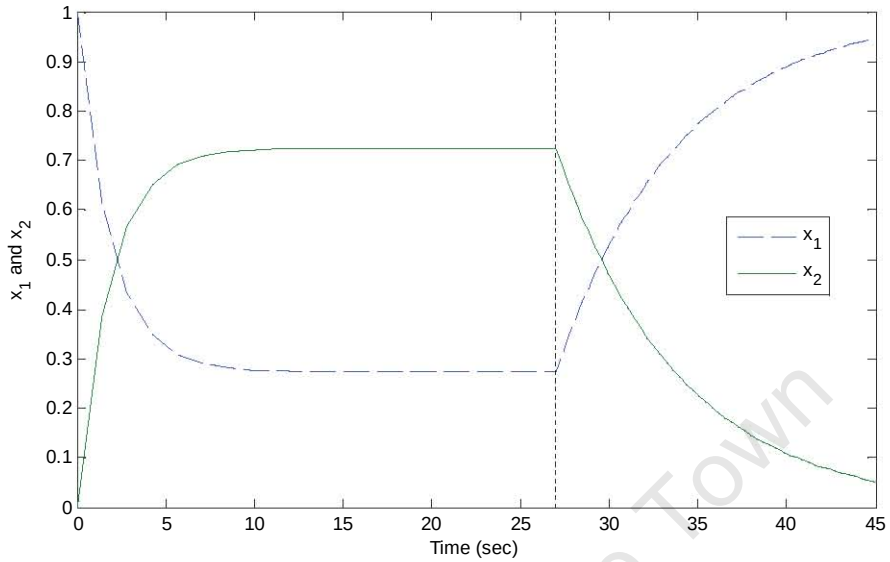

Figure 4.2 – Example of model solution showing typical PSF profiles for a single light/dark cycle. $t_C = 45$ seconds with light fraction $t_l/t_C = 0.6$. Dotted line shows start of the dark period. Simulated conditions: $I = 200\ \mu\text{mol}\cdot\text{m}^{-2}\cdot\text{s}^{-1}$and parameters α, β, γ, δ are those of Wu & Merchuk (2001) and can be found in Table 2.8.

The growth rate from a single cycle is calculated using Eq. 4.4:

$$\mu = k\gamma x_2(t) - Me \tag{4.21}$$

$$\text{where } x_2(t) = \begin{cases} x_{2,l}(t) & 0 \le t \le t_l \\ x_{2,d}(t) & t_l \le t \le t_c \end{cases}$$

Eq. 4.21 yields growth rate as a function of time. The model is to be used to simulate many continuous cycles repeated for time periods of hours to days. A single cycle is in the of order of magnitude seconds, whereas the doubling time of algae is of order of magnitude hours, thus it is only necessary to calculate a mean growth rate per cycle for evaluating growth (Wu & Merchuk, 2001). The mean specific growth rate for a single cycle can be calculated using Eq. 4.22, which was evaluated numerically via a simple Euler method.

$$\begin{aligned} \overline{\mu} &= \frac{k\gamma}{t_c}\int_0^{t_c} x_2(t)dt - Me \\ &= \frac{k\gamma}{t_c}\left[\int_0^{t_l} x_{2,l}(t)dt + \int_{t_l}^{t_c} x_{2,d}(t)dt\right] - Me \end{aligned} \tag{4.22}$$

4.1.2 Integrating the model over continuous cycles to predict experimental results

Algae experience continuous cycles in an airlift reactor. A the thin loop tubular reactor was designed to simulate these cycles according to the experimental methods outlined in Section 4.2.

For continuous cycles, the initial values of the PSFs for each subsequent cycle are equal to final values of the PSFs from the previous cycle. Periodic exposure to PFD will finally lead to a cyclic growth rate, eventually reaching a cyclic steady state (Wu & Merchuk, 2001) in which successive cycles are identical, as depicted in Fig. 4.3. Since the circulation time is of the time scale seconds, whereas an experimental run take 2-3 days, this cyclic-steady state is the prevailing situation (Wu & Merchuk, 2001).

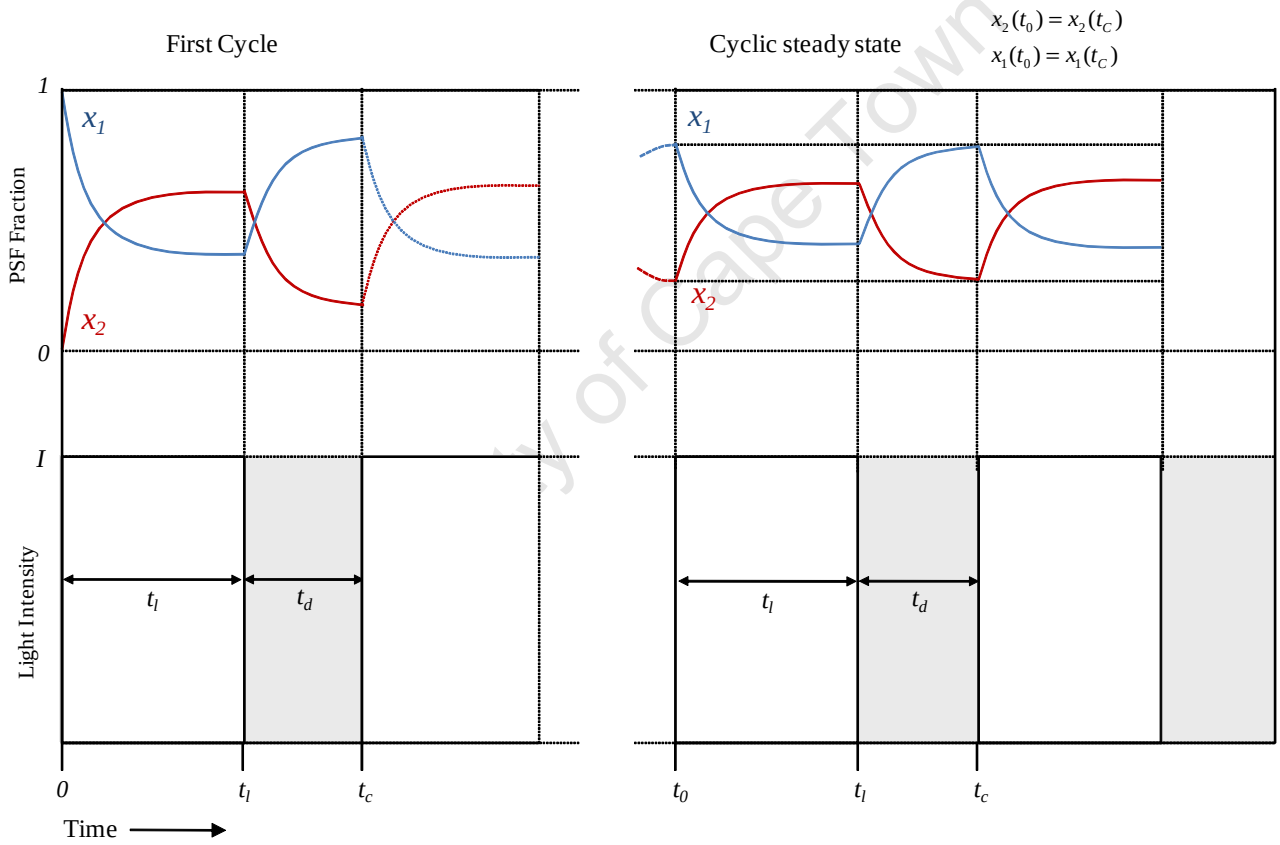

Figure 4.3 – Schematic of the variation of the PSF fractions (x_1 and x_2) during dark and light periods, at cyclic steady state.

The experiment outlined in Section 4.2 was designed to simulate cyclic steady state conditions by allowing algae to continuously circulate around a loop reactor under controlled light/dark cycles. Using the model to simulate cyclic steady state and predict experimental results ultimately enabled parameter estimation. A cyclic steady state cycle is defined in a similar way to a single cycle, having a light period from $t = 0$ to $t = t_l$ with light intensity I ($I > 0$) and a dark period from $t = t_l$ to $t = t_c$ with $I = 0$. Each cycle is integrated according to the methods outlined previously (Section 4.1.1).

However, for cyclic steady state to exist:

$$x_1(0) = x_1(t_c) \tag{4.23}$$

$$x_2(0) = x_2(t_c) \tag{4.24}$$

In other words, at the end of each cycle the PSF fractions return to the same values that they had at the start of that cycle. This is illustrated visually in Fig. 4.3.

A simple way to simulate cyclic steady state is to integrate successive cycles repeatedly until the system converges and there is no change between the final and starting PSF fractions. To achieve this, the initial conditions for the beginning of the first cycle ($n = 1$ and $t = 0$) are set as:

$$x_1 = 1 \tag{4.25}$$

$$x_2 = 0 \tag{4.26}$$

For each subsequent cycle $n+1$, the initial conditions for the PSF fractions are equal the final conditions of the PSFs from the previous cycle, thus:

$$x_1(t_{n+1} = 0) = x_1(t_n = t_c) \tag{4.27}$$

$$x_2(t_{n+1} = 0) = x_2(t_n = t_c) \tag{4.28}$$

Cyclic steady state can easily be simulated by running the simulation to the point where the system converges and there is no change in the final PSF values from the initial values. Using this method, the model could simulate cyclic steady state, as illustrated in Fig. 4.4.

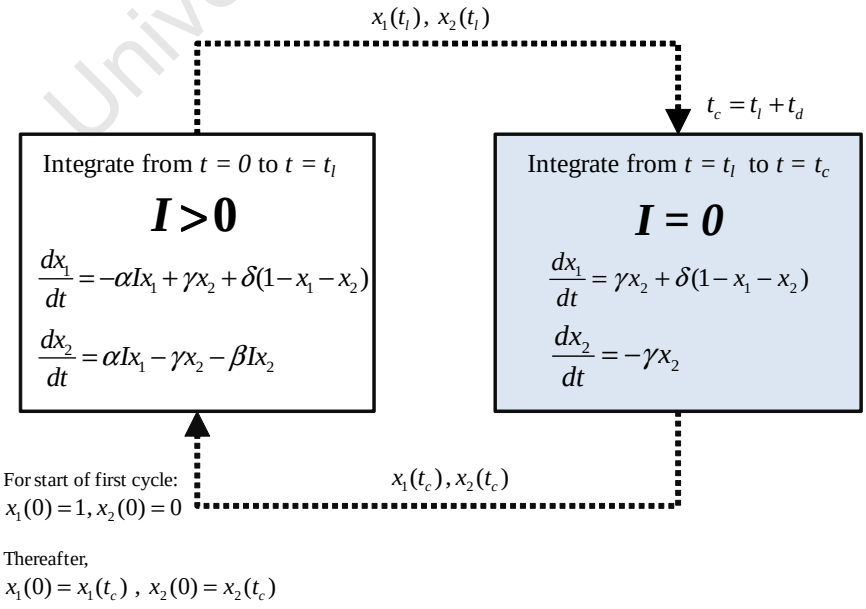

Figure 4.4 – Method of simulating cyclic steady state

To prove and illustrate the existence of cyclic steady state in the model, Fig. 4.5 shows overlapping curves for the x_2 profile as the system approaches steady state. Furthermore, the least squares error between each cycle for the given simulation was calculated, with the value arriving at 2.1366e-011 at convergence from a starting value of 0.0035.

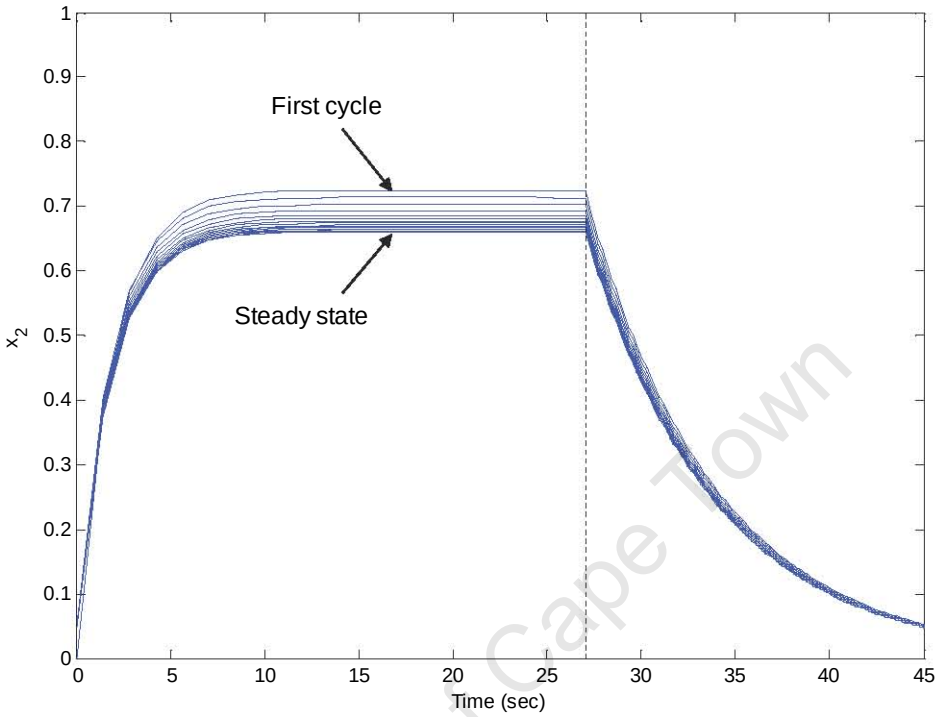

Figure 4.5 – Overlapping curves for x_2 PSF profile to show convergence to cyclic steady state. $t_C = 45$ seconds with light fraction $t_l/t_C = 0.6$. Dotted line shows start of the dark period. Simulated conditions: $I = 200\ \mu\text{mol}\cdot\text{m}^{-2}\cdot\text{s}^{-1}$and parameters α, β, γ, δ are those of Wu & Merchuk (2001) and can be found in Table 2.8.

For any given combination of cycle time, light intensity and light/dark fraction a unique cyclic steady state profile exists. This profile defines an average growth rate for those specific conditions since $\overline{\mu} = f(I, t_C, t_l/t_C)$ from Eq. 4.22. Thus, by fitting the model to data of varying cycle time, light intensity and light/dark fractions, best-fit model parameters can be obtained for any algal species tested.

4.2 Experimental Methods

The aim of the experiments was to simulate algal growth under periodic light/dark cycles to produce data from which "best-fit" kinetic model parameters could be determined. Variations in light intensity I, cycle time t_C and the ratio of illuminated time to overall cycle time or "light fraction" $f = t_l/t_C$ were investigated. In addition to producing data that enabled parameter fitting, the data was also relevant as part of an experimental investigation into to the effects of medium frequency light/dark cycles on algal growth.

4.2.1 Analysis of experimental plans from previous studies

Two previous studies reporting similar work (Table 4.2) were analyzed in order to formulate an appropriate experimental plan for this work.

The aim of Wu & Merchuk (2001)'s experimental plan was to fit their kinetic model for the species *Porphyridium* sp. They tested several light fractions ranging from 0.628 to 1.00, repeated at three PFDs of 100, 200 and 550 $\mu\text{mol}\cdot\text{m}^{-2}\cdot\text{s}^{-1}$. A thin tubular loop reactor was used with a fixed cycle time of 45 seconds. Sections of the reactor were covered to simulate light/dark cycles. The main results of their study have been presented already in the Literature Review (Fig. 2.27 in Section 2.9.3).

In Barbosa *et al.* (2003b), the aim was to study the effects of cycle time (10–100 s) and light fraction (0.1–1) on biomass yield on light energy and specific growth rate. The species tested was *Dunaliella tertiolecta* and the experiments were performed using a turbidostat reactor with a controlled light gradient of 1066–1331 $\mu\text{mol}\cdot\text{m}^{-2}\cdot\text{s}^{-1}$. A turbidostat is a continuous culturing method where the turbidity of the culture is kept constant by controlling the dilution rate. The light/dark cycles were simulated by a shutter that blocked the light source at controlled times. A central composite experimental design was used which enabled the fitting of a statistical model for growth rate as a function of cycle time and light fraction, via surface response topology. The results of their study were also presented previously in the Literature Review (Fig. 2.19 in Section 2.6.2).

Table 4.2 – Summary of experimental methods from literature for fitting a PSF kinetic model (Wu & Merchuk, 2001) and for investigating light/dark cycles (Barbosa *et al.*, 2003b).

Factor Tested:	**Units**	**Wu and Merchuk (2001)**	**Barbosa et al. (2003)**
Species		*Phorphyridium* sp.	*Dunaliella tertiolecta*
Cycle time - t_C	sec	45	10 - 23.1 - 55 - 86.9 - 100
Light fractions - f	(-)	0.628 - 0.778 - 0.816 0.851 - 0.927 - 1.000	0.100 - 0.231 - 0.55 0.869 - 1.000
PFD - I	μ mol. $m^{-2}.s^{-1}$	100, 200, 550	gradient from 1066–1331
Total runs		19 + 19 repeats = 38	9 + 2 repeats at center point = 11

Wu & Merchuk (2001) gave no direct justification for choosing a circulation time of 45 seconds. Furthermore, since their model was only fitted to this single cycle time it may not be able to simulate changes in growth that occur across varying cycle times. In Barbosa *et al.* (2003b), different cycle times were tested and were found to have a definite effect on growth, with shorter cycle times yielding higher growth rates at light fractions less than 0.55. For light fractions over 0.55, longer cycle times yielding higher biomass yields on light energy than shorter cycle times. As a side note, the two smallest light fractions tested (0.1 and 0.231) were found to be too low to sustain algal growth. Whereas Wu & Merchuk (2001) tested a rang of PFDs, Barbosa *et al.* (2003b) neglected testing this effect.

Although Wu & Merchuk (2001)'s experimental plan enabled fitting model parameters over a range of light fractions and PFDs, it excluded the impact of cycle time on the dynamics of the system, which Barbosa *et al.* (2003b)'s experimental plan accounted for. The aim of developing this model is to predict growth rate as a function of changing conditions inside a photobioreactor, and this includes variations in cycle time. Thus, for the present work, an experimental plan was formulated that incorporated elements from both previous studies. The aim of the experiments was to fit the kinetic model and, to a lesser extent, to investigate the effects of light/dark cycles on algal growth.

4.2.2 Experimental plan for the present work

A trade off had to be found between investigating the effects thoroughly and ensuring a reasonable number of experiments. The experimental plan used is shown in Table 4.3. For two values of light intensity (I_1 and I_2 of 363 and 939 μmol·m$^{-2}\cdot$s^{-1} respectively) a series of experiments were run at three cycle times (21, 33 and 45 sec) across 3 to 5 light fractions (0.40, 0.575, 0.750, 0.875, 1.00). For the 45 sec cycle times, more variations in light fractions were tested. The runs were numbered 1 through 24 as shown in Table 4.3. Runs 21 and 22 were repeats of Run 5, to test reproducibility and error in the data.

Table 4.3 – Experimental plan to determine kinetic model parameters and investigate light/dark cycles. The runs performed are numbered 1 through 24.

I_1 = 363 µmol. m^{-2}.s^{-1}				I_2 = 939 µmol. m^{-2}.s^{-1}			
$f = t_I/t_C$	t_C (sec)			$f = t_I/t_C$	t_C (sec)		
	21	**33**	**45**		**21**	**33**	**45**
0.400	1	2	3	**0.400**	10	11	12
0.575			19	0.575			23
0.750	4	5,21,22	6	**0.750**	13	14	15
0.875			20	0.875			24
1.000	7	8	9	**1.000**	16	17	18

To select appropriate cycle times for this investigation, tracer experiments were performed on a laboratory-scale airlift reactor. These experiments were done as part of the hydrodynamic model parameter determination and are presented later in Section 5.3 with the results given in Fig. 5.4. Importantly, this provided an estimate of the range of mean circulation times that cells experience in our laboratory airlift reactors, which was found to be between 6 and 20 seconds. However, it was desired to fit the model at circulation times that could be achievable in much larger airlift reactors, thus cycle times of up to 45 seconds were investigated. What follows is a discussion of how the cycle times and PFD values in Table 4.3 were arrived at, as well as specific details regarding the reactor systems used. The choice of these exact cycle times are explained in Section 4.2.4.2, with relevance to the design of the tubular reactors.

Apart from the three variables tested (I, t_C,f), all other factors that affect growth needed to be kept constant across all experiments. To achieve this, a tubular loop reactor was designed and built to enable easy control of the variables and limited variation.

4.2.3 Design of the tubular-loop photobioreactors

The photobioreactor, shown schematically in Fig. 4.6 and photographed in Figures 4.7 and 4.8, was constructed using a series of angled (5°) glass tubes (7 mm ID) connected via glass U-bends and closed via an airlift pump. This type of system was first constructed by Lee & Pirt (1981) for their light/dark cycles study. Their design used a mechanical pump to create circulation and a separate gas injection section, in addition, the reactor was horizontally oriented. The same type of reactor was used in Merchuk *et al.* (1998a) for a light/dark cycle study. Wu & Merchuk (2001) redesigned a similar loop reactor for their kinetic model simulation by incorporating an an airlift pump to create circulation and facilitate gas transfer, which meant that the reactor was oriented vertically.

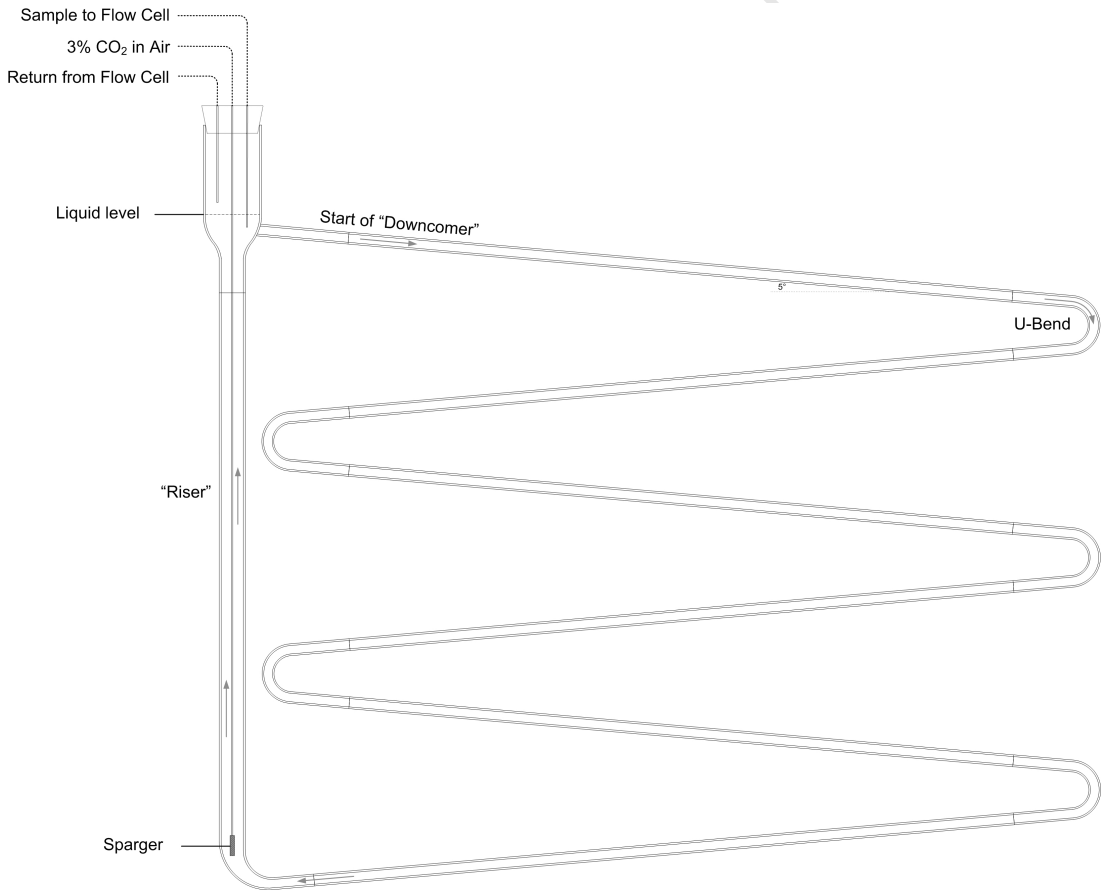

Figure 4.6 – Schematic of thin tube loop reactor (6 tube version). Downcomer comprised of straight 7 mm ID glass tubing at 5° angles joined by 7 mm ID glass U-bends.

The reactor was designed and built according to the design used by Wu & Merchuk (2001). The reactor was first designed conceptually using Microsoft Excel^{TM} to simulate the dimensions, angles,

volume, velocities and mass transfer via a number of literature correlations. Once the general design was established, prototypes were constructed and tested with minor modifications being made before the working design was finalized. A more detailed presentation of the reactor design, including precise dimensions, can be found in Appendix E. Three versions of the reactor were made, an 8-tube, 6-tube and 4-tube version, the reason for this is discussed in Section 4.2.4.2.

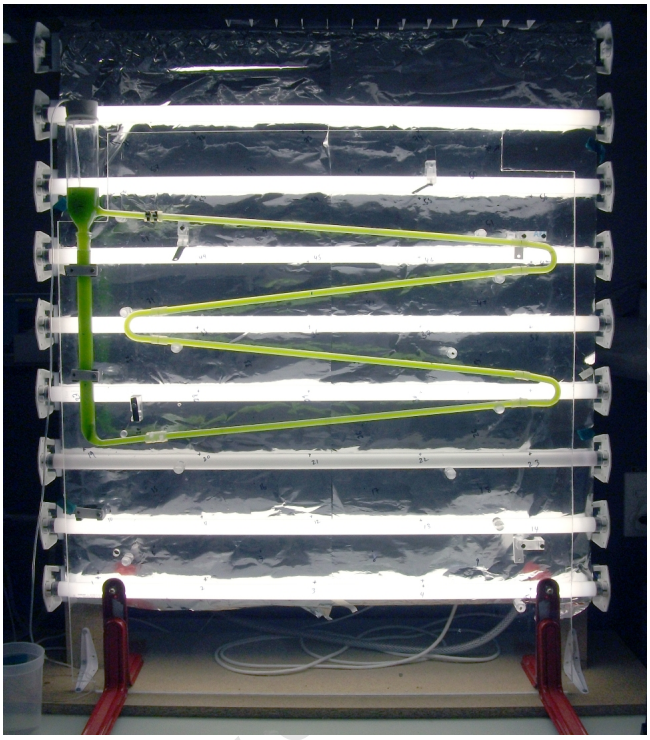

Figure 4.7 – Photograph of tubular loop reactor (4 tube version) with a single light bank.

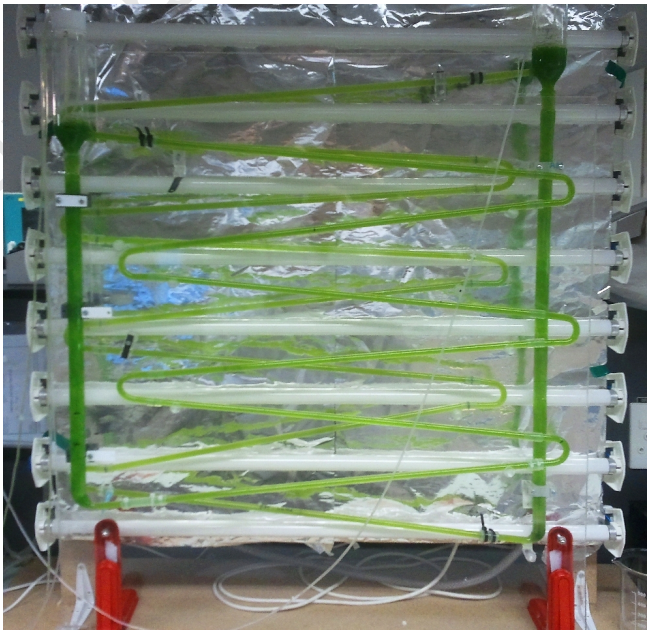

Figure 4.8 – Photograph of tubular loop reactors (8 tube and 6 tube versions) with a single light bank. A perspex stand was build to hold two reactors simultaneously.

4.2.4 Tubular reactor design considerations

Important design factors were considered in order to meet the requirements to fit the model and to ensure that all untested variables remained constant, or within acceptable tolerances.

4.2.4.1 Requisite thin film culture assumption

Ideally, growth needed to be simulated at a constant light intensity. Narrow tubes were selected to ensure a short light path and allow minimal light gradients caused by mutual cell shading (Wu & Merchuk, 2001; Lee & Pirt, 1981). A standard 7 mm ID tubing was used for the downcomer section.

In the case of the lower light intensity tested (363 μmol·m$^{-2}\cdot$s^{-1}), light was provided from one side of the tubes and in the case of the higher light intensity tested (939 μmol·m$^{-2}\cdot$s^{-1}), light was provided from both sides of the tubes. Fig. 4.9 shows a simulation for monodimensional light transfer in a single direction using the light distribution model (Chapter 3). The simulation shows the potential for light gradients to exist, even in such narrow tubes (7 mm), becoming more pronounced at higher concentrations. However, Fig. 4.9 does not simulate the *real* light profile inside the tubes owing to the fact that they receive light from multiple directions in a non-uniform distribution. Thus, since they receive more light than what could be simulated in Fig. 4.9, particularly in the case of receiving light from both light banks, Fig. 4.9 represents a worst case scenario. The real light gradients inside the tubes were likely to be less dramatic. The riser section required a larger diameter of 18 mm to avoid gas slugging and to ensure sufficient gas mass transfer, using a smaller diameter would have been impractical. As a result of this larger diameter there was more potential for light gradients in the riser. Furthermore, all the experiments were performed under low cell concentrations ($C_x < 1$ g.L^{-1}), since a high cell density would aggravate light gradients (Fig. 4.9). All these factors ensured that the PFD inside the reactor could be assumed close to homogeneous.

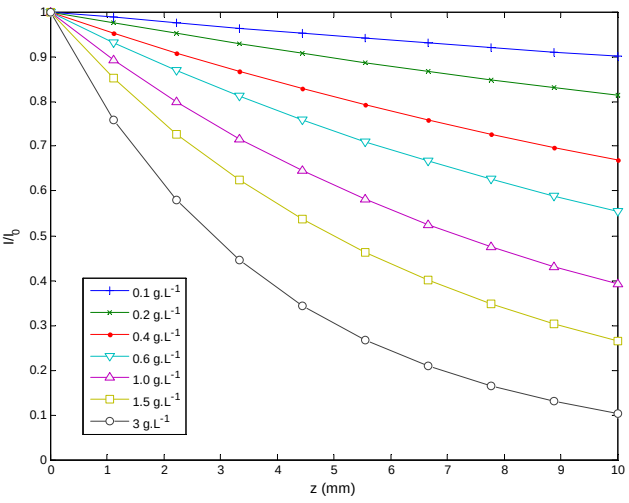

Figure 4.9 – Light model simulation of one dimensional light attenuation through *Scenedesmus* sp. at varied concentrations (0.1 to 3 g.L^{-1}). Represents *worst case scenario* of light transfer in tubes.

4.2.4.2 Controlling and choosing cycle times

The cycle time was controlled by varying the gas flow rate. Using the same length of reactor to simulate a shorter cycle time required increasing the circulation velocity, by increasing the gas flow rate. Increasing the fluid velocity beyond a certain point could cause transition or turbulent flow in the narrow tubes of the downcomer section. Such undefined flow conditions would lose an element of control over all the experiments performed. Degrees of turbulence are known to affect algal growth by varying the rate of transfer of nutrients and metabolites between cells and their growth medium (Grobbelaar, 1994). Thus, it was desired to simulate laminar flow to ensure control.

A reactor was first designed comprising 8 straight tube sections to simulate the longest of the three cycle times to be tested (45 seconds). Preliminary calculations during the conceptual design phase predicted that using the same 8-tube version to simulate a cycle time of 20 seconds would result in transition or turbulent flow. For this reason, shorter versions of the reactor had to be designed and built to simulate shorter cycle times of 20 - 30 seconds. Table 4.4 gives brief details for each of the three reactors. Detailed specifications can be found in the Appendix E.1. Once the reactors were made, experiments were performed to characterize the fluid dynamics in the downcomer tubes as a function of gas velocity. This enabled exact cycle times to be chosen for each system that would ensure (i) that the flow was laminar and (ii) that the flow conditions for all three systems would be kept similar.

Table 4.4 – Basic details of the three reactor systems used.

Reactor	Volume	Riser Height	Downcomer Length	U-bends	Cycle time range
	(ml)	(m)	(m)	#	(sec)
8 tubes	450	0.66	5.63	7	30 - 70
6 tubes	330	0.50	4.24	5	25 - 53
4 tubes	209	0.28	2.86	3	17 - 38

Calibrations of gas flow rate versus cycle time were performed using small (< 2 mm) Ca-alginate tracer beads traveling between a known distance in the loop. Fixed intervals of gas flow rate were set and the velocity of the fluid in the downcomer was measured and converted to a circulation time. Appendix E.2 outlines the method and results of calibration. By calculating Reynolds numbers in the tubes, according to to Eq. 4.29, the flow conditions for various cycle times in each reactor type could be estimated.

$$Re = \frac{\rho D v}{\eta} \tag{4.29}$$

where ρ is the fluid density (kg.m^{-3}), D is the tube diameter (m), v is the velocity in the tube (ms^{-1}) and η the fluid viscosity (kg.s^{-1}.m^{-1}).

Generally, tube flow is considered laminar if $Re < 2300$. For $Re > 4000$ the flow is considered turbulent. In the interval between 2300 and 4000, laminar and turbulent flows are possible depending on pipe roughness and flow uniformity, this is called the transition flow region.

Table 4.5 shows the calculated Reynolds numbers for each gas flow rate F, with the corresponding velocity in the downcomer v and estimated circulation time t_C. Analysis of the Reynolds numbers in Table 4.5 confirmed the predictions of the preliminary calculations during the design phase. Attempting to simulate short cycle times of between 23 and 25 seconds in the long reactor (8 tubes) would yield transition flow conditions in the downcomer, since $Re \geq 2406 > 2300$. Furthermore, the experiments found that the shorter reactors could not simulate long cycle times ($>$ 52 sec for 6 tube, $>$ 37 for 4 tube) since the low velocity in the tubes could allowed algae to settle[1].

Table 4.5 – Cycle times and Reynolds numbers estimated from calibration. See Appendix E.2 for data and calculation.

	8 Tubes			6 Tubes			4 Tubes		
F (ml/min)	v (m.s^{-1})	t_C (sec)	Re	v (m.s^{-1})	t_C (sec)	Re	v (m.s^{-1})	t_C (sec)	Re
100	0.13	70.2	897	x	x	x	x	x	x
200	0.17	52.5	1190	0.14	52.6	969	0.12	37.3	857
400	0.31	28.0	2188	0.23	30.3	1640	0.21	21.8	1457
500	0.34	25.4	2406	0.26	26.9	1845	0.25	18.4	1719
600	0.37	23.4	2590	0.30	23.8	2083	0.26	17.2	1840

x - circulation times could not be measured because fluid velocity was low enough to allow tracer particles to settle in downcomer

To maintain similar flow characteristics (Reynolds numbers) for all experiments, and ensure operation within the laminar regime ($Re < 2300$), the selected cycle times were chosen by interpolation of the data in Table 4.5 (dotted lines) to arrive at the values given in Table 4.6. Each cycle time was achieved by changing the gas flow rate. The Reynolds number maintained was at an average of 1525 with a maximum of 2.3% variance.

Table 4.6 – Chosen cycle times with corresponding Reynolds numbers and gas flow rates

	t_C (sec)	Re	F (ml/min)	System
Long	45	1495	261	8 tubes
Medium	33	1560	376	6 tubes
Short	21	1519	423	4 tubes

4.2.4.3 Airlift pump and mass transfer

The airlift pump utilized a sparger made from a 6 mm OD stainless steel sintered metal tube (SIKA R-10, GKN Metals). A simple CO_2 mass transfer model was utilized during the conceptual design phase to test for CO_2 limitations in the downcomer tubes. This limitation implies that the available

[1]This was assumed from the observation of the small tracer particles settling at these low velocities.

CO_2 would be depleted in the downcomer tubes (via biomass growth) before the cells returned to the riser section. The model and simulation results are presented in Appendix E.3. The model made use of many assumptions but was sufficient to test for worst case scenarios. The important result was that by providing excess CO_2 at 3% (in air) one could ensure that the possibility of CO_2 limitations could be neglected.

4.2.5 Light environment and light fractions

Light was provided by banks of 8 Osram 18 watt cool white fluorescent bulbs (photographed in Fig. 4.7 & 4.8) placed at a distance of 2 cm from the plane of the tubes surface. By using one or two light panels (one on either side of the reactor) it was possible to simulate two different light intensities, as shown in Fig. 4.10.

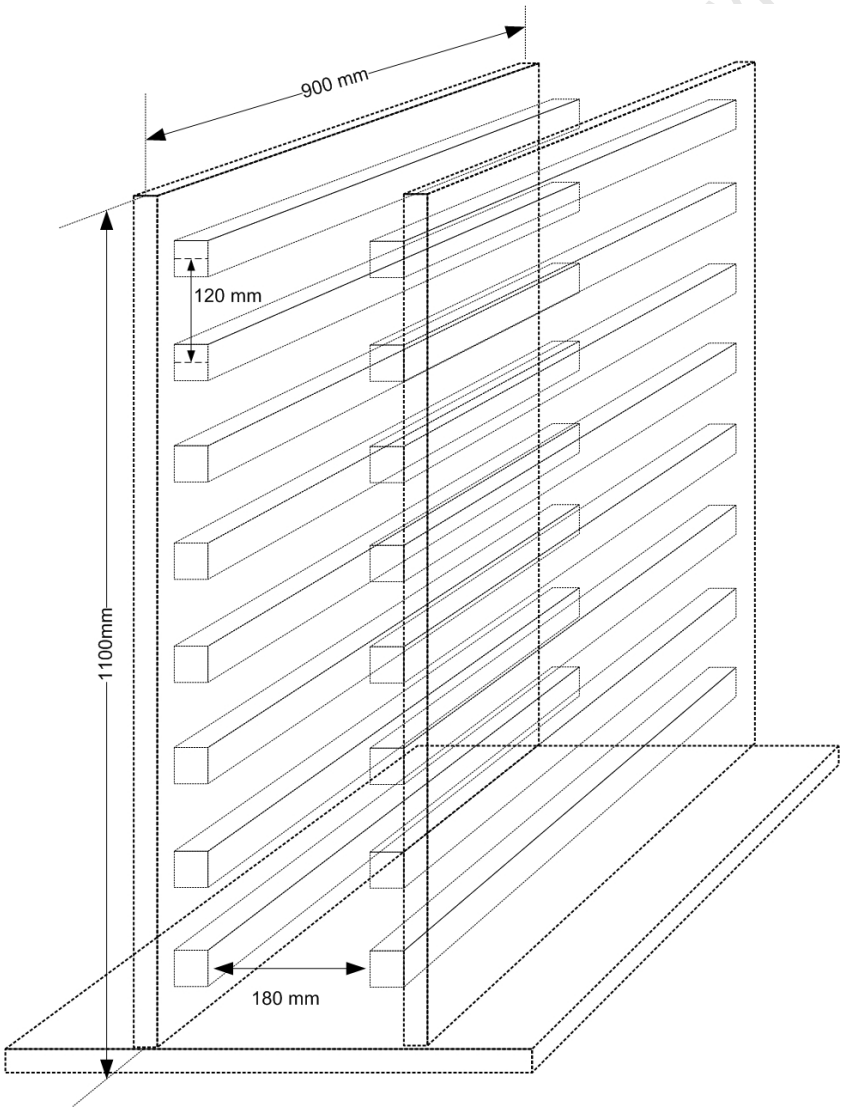

Figure 4.10 – Schematic showing how fluorescent light banks were used to create light environment. Reactor stand fitted in the center between both banks. (Drawing not to scale)

Light intensity was measured using a quantum sensor (US-SQS/L, Walz) calibrated for use in air, connected to light meter and data logger (LI-250, L-COR). The sensor measured light in the PAR range (400 – 700 nm) with a 2π solid angle. The same sensor was used for the light distribution model experiment (see Fig. 3.7 in Section 5.3).

Fluorescent bulbs do not emit a constant light intensity over their length, particularly near each end, where it is lower. The spacing of the bulbs caused regions of lower light, hence the light intensity varied at every point along the tubular reactor. The light environment was quantified by measuring light at 68 points on a defined grid (Fig. H.1 in Appendix H.3). Fig. 4.11 shows colour maps generated from the grid point measurements for both light environments and the regions of high and low light intensity can be clearly seen.

In reality, the PFD experienced for each cycle time was slightly different, since each reactor system was of different dimensions and this meant that the cells passed through different regions of the light environments, this is illustrated in Fig. 4.12. Thus, since it was impossible to achieve exactly the same PFD across different cycle times, a mean PFD was assumed from the 68 measured points for each of the two light environments. Table 4.7 shows the mean values determined and these were assumed for the model simulation.

Table 4.7 – Mean estimated values of PFD for the two light environments tested in μmol·m$^{-2}\cdot$s^{-1}.

	Mean PFD	Highest PFD	Lowest PFD
I_1	363	459	188
I_2	939	1262	447

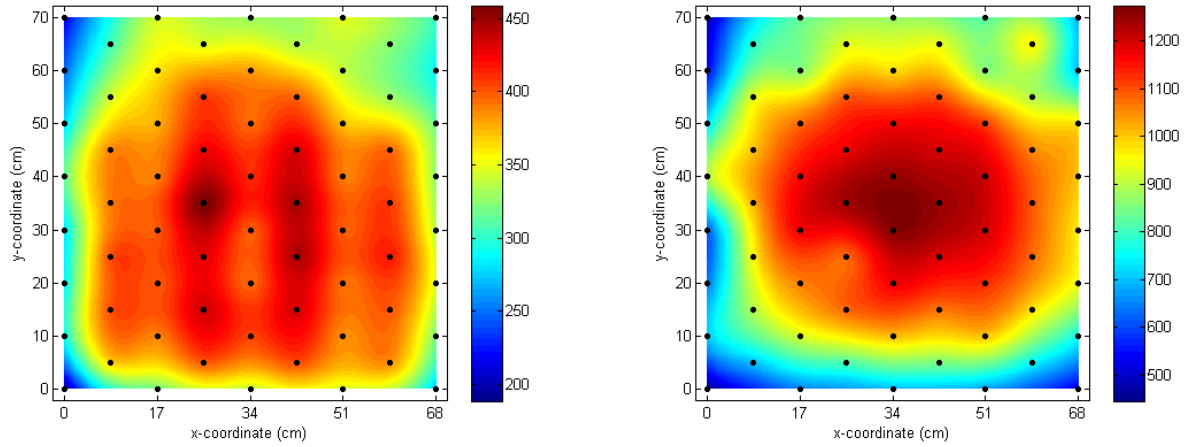

(a) Light map for I_1 **(b)** Light map for I_2

Figure 4.11 – Interpolation of light intensity data for the two different light inputs. Black dots show the points at which measurements were taken. I_1: I_{ave}= 363μmol·m$^{-2}\cdot$s^{-1} and I_2: I_{ave}= 939μmol·m$^{-2}\cdot$s^{-1}. Measurement data can be found in Table H.5 in Appendix H.3.

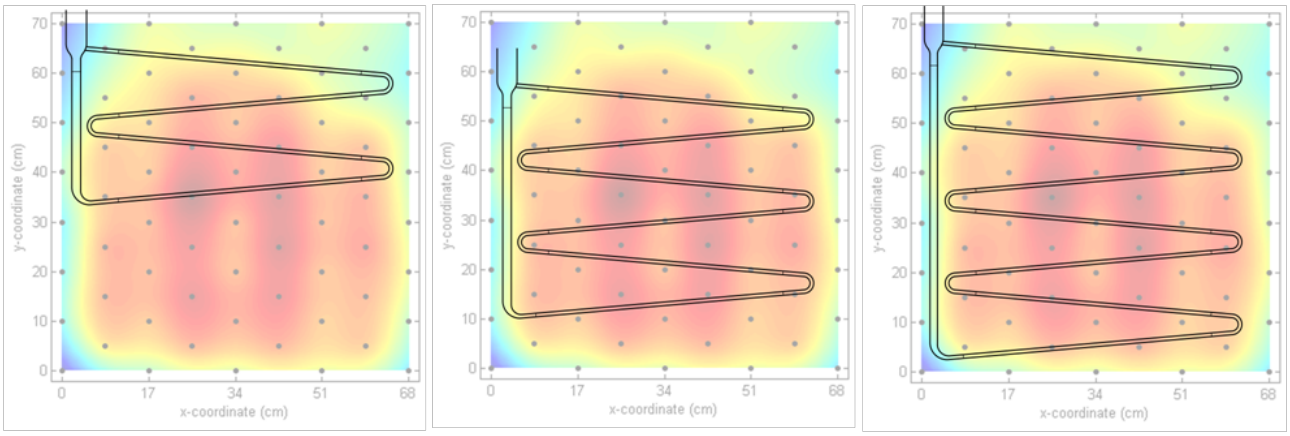

Figure 4.12 – Schematic to show how each system (4,6 and 8 tube) was located within the light environment. Example shown for I_1.

To simulate varying light/dark ratios, sections of the flow loop were covered with aluminum foil. An equal fraction of the riser and downcomer were covered in each case to ensure a constant light/dark ratio over the entire cycle. For $f = t_l/t_C = 1$ the reactor was left uncovered. The values used for each case are given in Table 4.8 and Fig. 4.13 shows a schematic of how this was achieved. In reality, f should be proportional to the actual exposure profiles in each case, since each case offered different light environments, according to Fig. 4.12. Making f proportional to covered area was a necessary assumption for the experiments.

Table 4.8 – Exact lengths of reactor tubing covered with foil to simulate controlled light/dark cycles.

	8 tube		**6 tube**		**4 tube**	
Riser length - L_r (cm)	66		50		28	
Downcomer length - L_d (cm)	563.6		424.3		286.4	
Light fraction	**RC**	**DC**	**RC**	**DC**	**RC**	**DC**
$f = t_l/t_c$	cm	cm	cm	cm	cm	cm
0.400	39.6	338.1	30.0	254.6	16.8	171.8
0.575	28.1	239.5	21.3	180.3	11.9	121.7
0.750	16.5	140.9	12.5	106.1	7.0	71.6
0.875	8.3	70.4	6.3	53.0	3.5	35.8

RC = Riser cover = L_r*(1-f)
DC = Downcomer cover = L_d*(1-f)

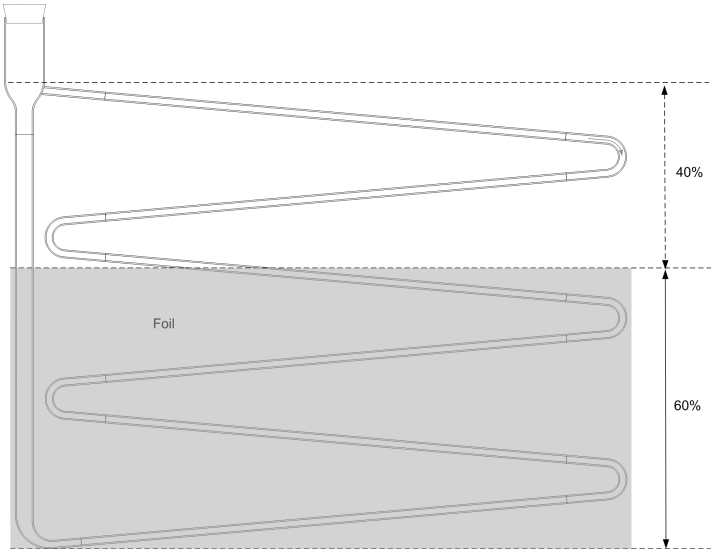

Figure 4.13 – Schematic showing 6-tube version of loop reactor covered to simulate a light/dark fraction of 0.4. In reality the tubes were wrapped in foil to completely block off the light.

4.2.6 Algal cultivation, growth conditions and cleaning

Scenedesmus sp. was stock-cultured in a modified Bold 3N media (see Appendix B) at ambient temperature in 500ml flasks, sparged with air and illuminated with fluorescent bulbs (~120 μmol.m^{-2}.s^{-1} at the surface). Inoculums for experimental runs were either taken from stock cultures or from the final biomass of the previous run. The starting algal concentrations for all experiments was controlled in the range of 0.08-0.25 g.L^{-1}.

The experiments were conducted in a temperature controlled laboratory of 22$\pm$2 °C. To counteract the heating effects of the fluorescent lights a fan was used to maintain the temperature in the reactor at 26$\pm$1 °C for all runs. Minimal adherence of the cells to the walls of the tubing was observed during runs. Between runs, the tubes were cleaned and water was run through the loop to wash out any minor adherences.

4.2.7 Sampling methods

Sampling was performed from the top of the riser as shown in Fig. 4.6. Two methods of sampling were used:

1. **Manual sampling:** Four mililitre samples were withdrawn 3 to 4 times daily and measured in duplicate or triplicate for absorbance at 750 nm. These absorbances were converted to concentration using a concentration-absorbance calibration curve given in Appendix C. A 750 nm wavelength was chosen to minimise the influence of changing chlorophyll concentrations (Griffiths *et al.*, 2011a).

2. **Automated sampling via a continuous flow cell system:** Algae were continuously pumped out of the top of the riser and sent through a flow cell before being recirculated back to the reactor. Continuous absorbance data from the flow cell enabled continuous logging of concentration. This author played a part in the development of the flow cell system for use with algae, and a large section is devoted to this in Appendix D. Owing to the current shortfalls of this system for algae use, manual sampling of data was predominantly used for calculating growth rates.

4.2.8 Calculation of exponential growth rates

Algal growth typically progresses through lag, exponential, linear, stationary and death phases, as shown in Fig. 4.14. The exponential phase characterizes balanced growth, whereas the linear phase results from limitation by a nutrient provided at a constant rate (e.g light, CO_2). These experiments focused on estimating the exponential growth rate μ. Exponential growth can be modeled using the well known Malthus equation:

$$C_x(t) = C_{x_0} e^{\mu t} \tag{4.30}$$

where $C_x(t)$ is the concentration ($g{\cdot}L^{-1}$) at time t (h), C_{x_0} is the concentration at $t = 0$ and μ the maximum specific growth rate (h^{-1}). Eq. 4.30 can be linearized as:

$$\ln(C_x) - \ln(C_{x_0}) = \mu \cdot t \tag{4.31}$$

Thus, $\ln(C_x)$ as a function of t is linear during true exponential growth. The maximum specific growth rate during *only* the exponential phase was calculated for model comparison.

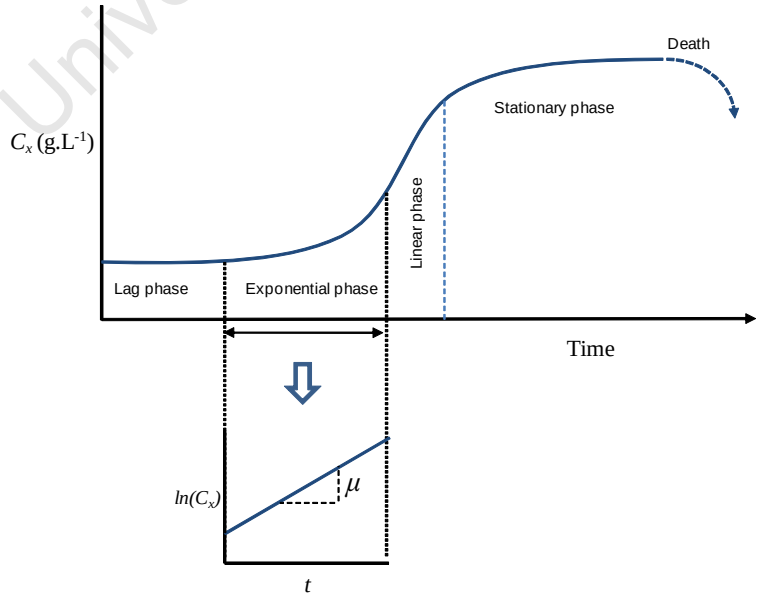

Figure 4.14 – Schematic of characteristic algal growth curve showing exponential phase and the manner in which μ was estimated from the data. Image source: this author.

4.3 Results and discussion from kinetic growth experiments

4.3.1 Growth curves and exponential growth rates

Fig. 4.15 shows the experimental growth curves as a function of time (hours). Appendix H.4 presents the raw data for each run. The runs lasted between 25 and 50 hours, depending on the time taken to pass from exponential to linear and/or stationary phase.

Runs 2 and 5 in Fig. 4.15b show flow cell data (see Section 4.2.7). Appendix D presents an additional chapter on this sampling method, including its development and the reasons for it not being more widely used in this project. Runs 11 and 12, in Figures 4.15e and 4.15f respectively, experienced some cellular death during the lag phase (indicated by $\ln(C_x/C_{x0}) < 0$).

The linear regions in the growth curves in Fig. 4.15 are indicative of the exponential growth phases. These regions enabled exponential growth rates to be calculated by performing linear regressions, with μ values estimated from the slope the best fit straight lines. The calculated exponential growth rates are presented in Table 4.9 as a function of light intensity, cycle time and light fraction.

Table 4.9 – Exponential growth rates, μ for each run, as a function of I, t_C and light fraction. Linear graphs used to obtain data for each run are given in Appendix H.4.. Runs 5,22,25 were repeats of the same conditions, yielding an error of 2.6%.

Run	I_1 (μmol. $m^{-2}.s^{-1}$)	t_C (s)	$f = t_l/t_C$ (s)	μ_{max} (h^{-1})	Run	I_2 (μmol. $m^{-2}.s^{-1}$)	t_C (s)	$f = t_l/t_C$ (s)	μ_{max} (h^{-1})
3	363	45	0.400	0.077	12	939	45	0.400	0.073
19	363	45	0.575	0.100	23	939	45	0.575	0.094
6	363	45	0.750	0.143	15	939	45	0.750	0.101
20	363	45	0.875	0.133	24	939	45	0.875	0.127
9	363	45	1.000	0.113	18	939	45	1.000	0.120
2	363	33	0.400	0.050	11	939	33	0.400	0.071
5	363	33	0.750	0.067	14	939	33	0.750	0.085
21	363	33	0.750	0.070	17	939	33	1.000	0.114
22	363	33	0.750	0.070	10	939	21	0.400	0.077
8	363	33	1.000	0.091	13	939	21	0.750	0.095
1	363	21	0.400	0.054	16	939	21	1.000	0.114
4	363	21	0.750	0.076					
7	363	21	1.000	0.096					

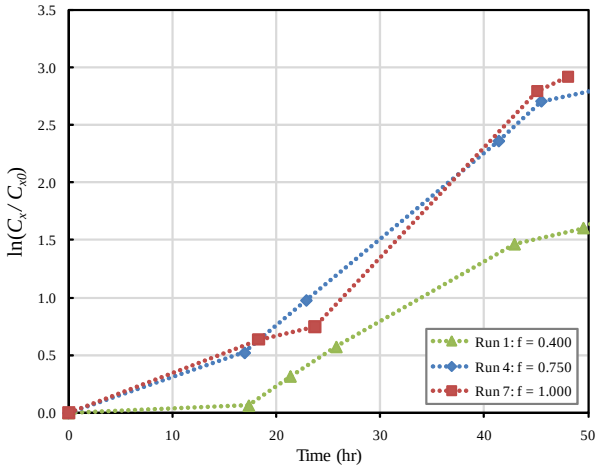

(a) Runs 1,4 & 7: $t_C = 21$ sec, $I_1 = 363\ \mu\text{mol}\cdot\text{m}^{-2}\cdot\text{s}^{-1}$

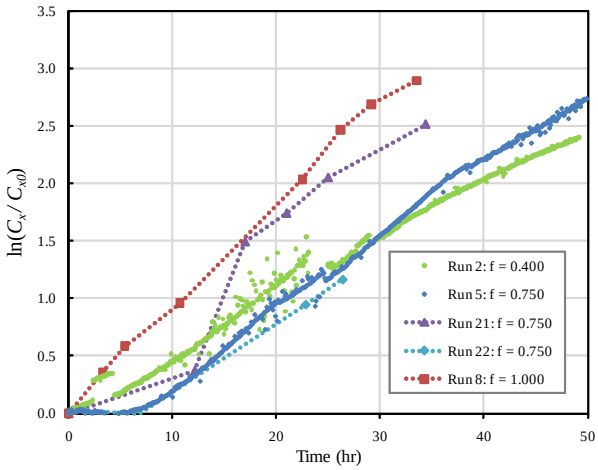

(b) Runs 2,5,21,22 & 8: $t_C = 33$ sec, $I_1 = 363\ \mu\text{mol}\cdot\text{m}^{-2}\cdot\text{s}^{-1}$

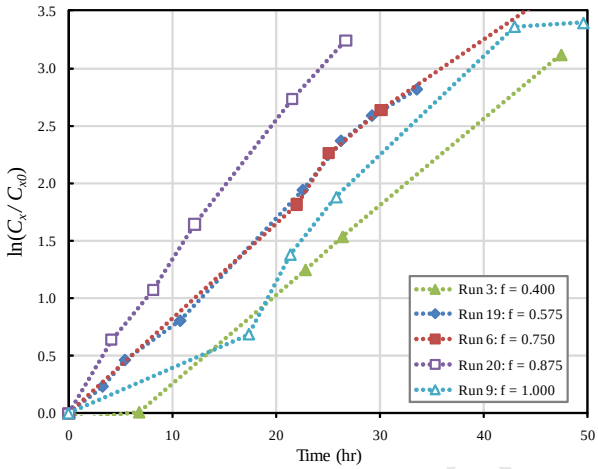

(c) Runs 3,19,6,20 & 9: $t_C = 45$ sec, $I_1 = 363\ \mu\text{mol}\cdot\text{m}^{-2}\cdot\text{s}^{-1}$

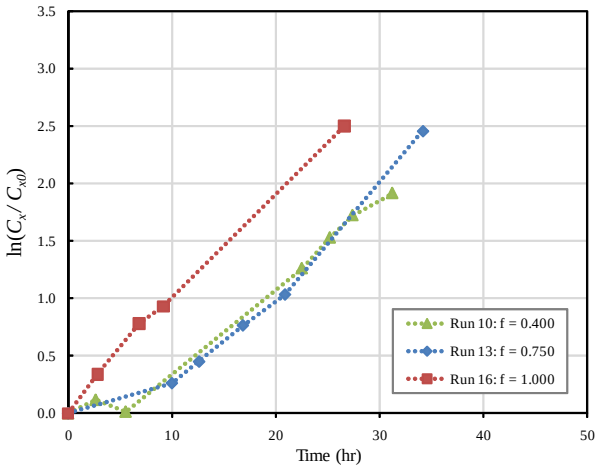

(d) Runs 10,13 & 16: $t_C = 21$ sec, $I_1 = 939\ \mu\text{mol}\cdot\text{m}^{-2}\cdot\text{s}^{-1}$

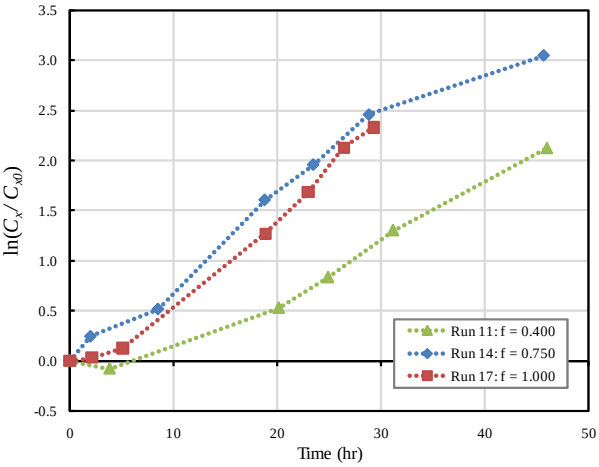

(e) Runs 11,14 & 17: $t_C = 33$ sec, $I_1 = 939\ \mu\text{mol}\cdot\text{m}^{-2}\cdot\text{s}^{-1}$

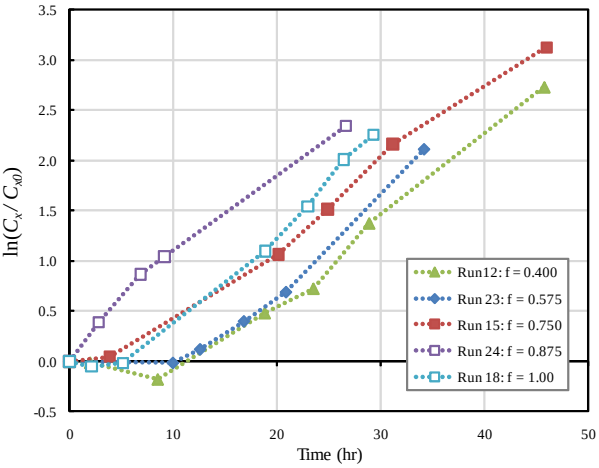

(f) Runs 12,23,15,24 & 16: $t_C = 45$ sec, $I_1 = 939\ \mu\text{mol}\cdot\text{m}^{-2}\cdot\text{s}^{-1}$

Figure 4.15 – $\ln(C_x/C_{x0})$ as a function of time grouped according to PFD and cycle time. In Fig. 4.15b, Runs 2 and 5 show flow cell data.

4.3.2 Growth rate as a function of PFD, light fraction and cycle time

The results and discussion that follows constitutes an investigation into the effects of medium duration light dark cycles for the species *Scenedesmus*. To analyze the effects of the three parameters (I, f and t_C) on growth rate, the data was represented in two ways, the first to highlight the effects of cycle time, and the second to highlight the effects of PFD. In both cases the effect of light fraction f was represented.

Decoupling the effects of cycle time

Fig. 4.16 shows growth rate as a function of light fraction and cycle time separated per PFD, to illustrate the effect of cycle time.

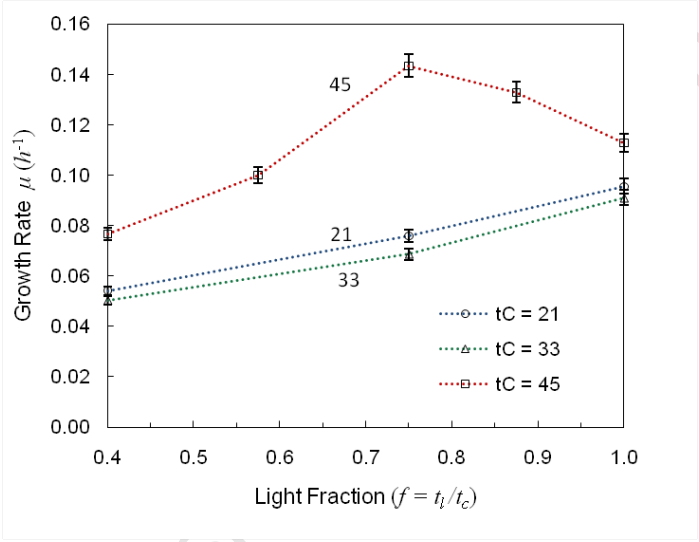

(a) PFD of 363 μmol·m^{-2}·s^{-1}

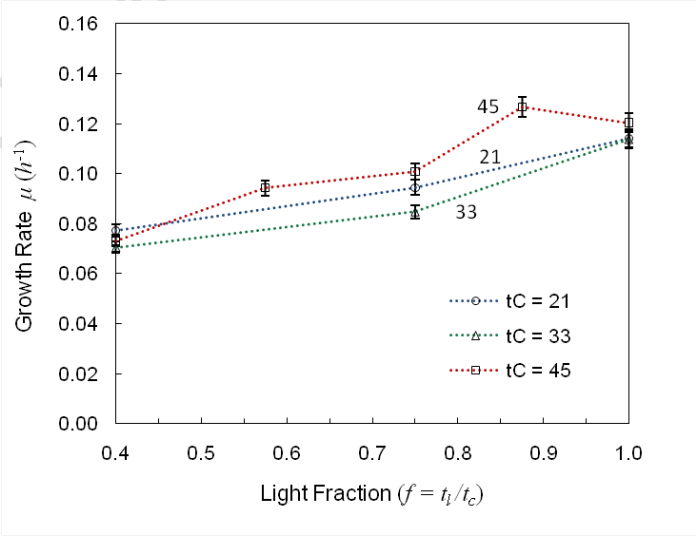

(b) PFD of 939 μmol·m^{-2}·s^{-1}

Figure 4.16 – Growth rate μ as a function of light fraction $(f = t_l/t_C)$ for each cycle time, separated for the two PFDs tested. Error bars represent experimental error of 2.6%, assumed from the repeated Run in Table 4.9.

Cells circulating around a fixed loop of *continuous* light ($f = 1$) of the same light intensity should experience similar growth conditions independent of the cycle time. Fig. 4.16b shows that for the higher PFD of 939 μmol·m$^{-2}\cdot$s^{-1}, growth rates were almost identical under constant light ($f = 1$) for all three cycle times. For the lower PFD of 363 μmol·m$^{-2}\cdot$s^{-1}, Fig. 4.16a shows that the longest cycle time of 45 seconds exhibited a higher growth rate under constant light than the two shorter cycles, which both show similar growth. This difference could be attributed to unaccounted differences between the 8-tube reactor, used to simulate the longer cycle time, and the 4 and 6-tube versions. The most notable difference between the systems used to achieve different cycle times is the length of riser required to join both ends of downcomer tubing, with the 8-tube version having the longest. The risers for each system experienced different light environments (see Fig. 4.12) and also had the most potential for light gradients (larger diameter). Thus, a longer riser section is more detrimental to the constant light assumption. In addition, a longer riser sections could provide more mixing for the cells and influence their growth. Both these factors could have influenced the discrepancy of this result at the 45 sec cycle time from the predicted result.

For the two shorter cycle times of 21 and 33 seconds, growth rate strictly increased with increasing light fraction, with the maximum experienced under continuous light (Figure 4.16a). This follows previous trends reported for the species *Chlamydomonas reinhardtii, Chlorella sorokiniana* and *D. tertiolecta* (Janssen, 2002), and for *Porphyridium* (Merchuk *et al.*, 1998a). In fact, growth rate increased almost in proportion to light fraction for both low and high PFDs. Fig. 4.17 shows the results for both 21 and 33 cycle times superimposed and normalized in terms of μ. Janssen (2002) observed similar linear trends for *Chlamydomonas reinhardtii,* as shown previously in Fig. 2.18.

For the longer cycle time (45 seconds) this linear trend was absent, owing to it having a maximum growth rate under intermittent light. Since a light fraction between 0.75 and 1.0 was not tested for either of the two shorter cycle times, it was not possible to know whether these data also exhibited maximums (or a plateau) under intermittent light. As a result, the postulation by Lee & Pirt (1981) and Merchuk *et al.* (1998a), who said that algae could maintain their maximum growth (experienced under continuous light) beyond a certain light fraction, could neither be confirmed nor denied by this data. Insufficient light fractions were tested, particularly between 0.6 and 1.0, which would be required to see if the growth plateaued towards a maximum.

In the case of the longer cycle time (45 seconds), growth rate increased with light fraction to a maximum after which it was lower under continuous exposure to light. This maximum was observed at light fractions of 0.750 and 0.875 for the lower and higher PFDs, respectively. This same trend was observed by Wu & Merchuk (2001) for *Porphyridium* sp. at their highest PFD tested (500 μmol·m$^{-2}\cdot$s^{-1}). The phenomenon is attributed to photoinhibition experienced by the cells exposed to high PFD. Both the higher and the lower PFDs tested in this work exhibited this characteristic for the long cycle time, with the growth rate under constant illumination being less than maximum. A minimal dark period is desirable to allow cells recovery time from photoinhibitory damage, as suggested by Merchuk *et al.* (1998a). Continuous light at high PFDs does not allow any cell recovery

time and as a result the growth rate is lower than maximal. Importantly, in this data this phenomenon *only* occurred under the longer cycle time in our experiments.

The longer cycle times exhibited generally higher growth rates than those of 21 and 33 seconds under conditions of intermittent light (Figures 4.16a and 4.16a). If one considers the same light fraction applied to a shorter or longer cycle time, it results in a physically longer dark period in the latter. e.g. for $f = 0.75$, cycle time of 21, 33 and 45 seconds would have dark periods of 5.25, 8.25 and 11.25 seconds, respectively. Thus, the enhanced growth experienced under the longest cycle time could be attributed to the longer dark period recovery time. However, if one was to assume this, then the shortest cycle time (having the shortest dark period) should exhibit the lowest growth. This assumption is definitely too simplistic, since for both PFDs tested, the shortest cycle time of 21 sec exhibited higher growth rates under intermittent light ($f < 1$) than the medium cycle time of 33 seconds. Barbosa *et al.* (2003b) observed this same trend for *D. tertiolecta,* but only at light fractions less than 0.550, beyond which the shortest cycle times exhibited the lowest growth rates.

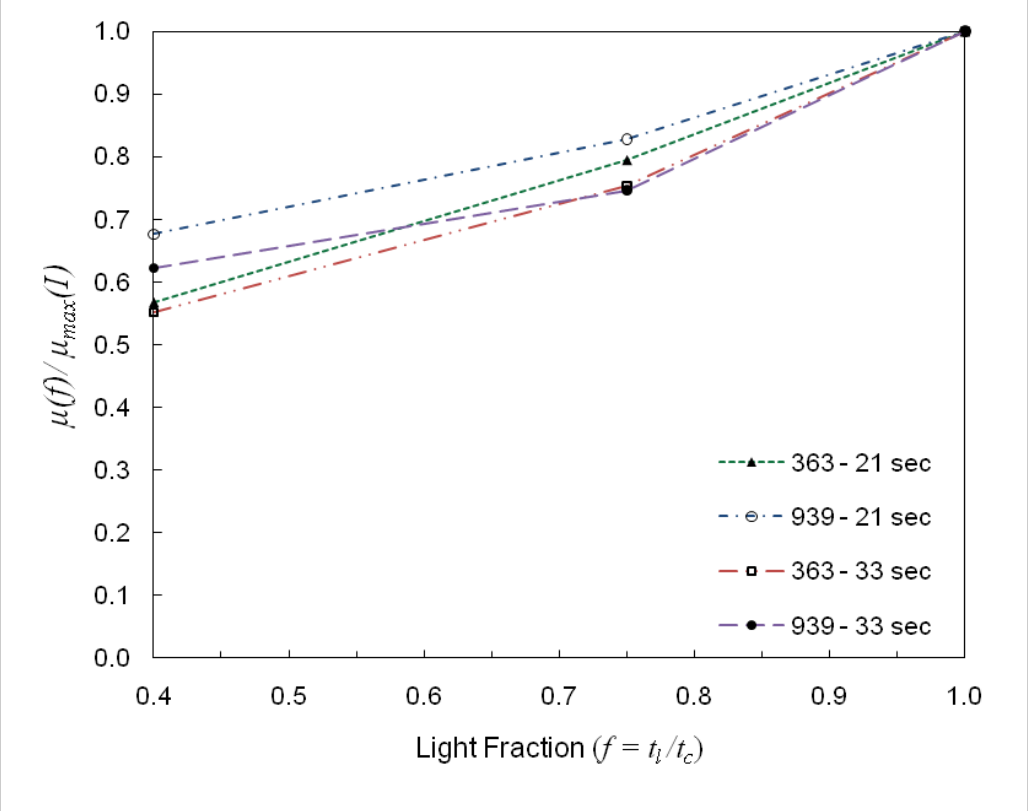

Figure 4.17 – Growth rates normalized relative to maximal growth rate, $\mu_{max}(I,t_C,f)/\max[\mu(I,t_C)]$ as a function of light fraction (t_l/t_C) for both PFDs tested (363 and 939 μmol·m$^{-2}\cdot$s^{-1}) and for cycle times 21 and 33 sec.

Decoupling the effects of PFD

Fig 4.18 shows growth rate as a function of light fraction for each PFD, separated by cycle time, to illustrate the effect of PFD on growth.

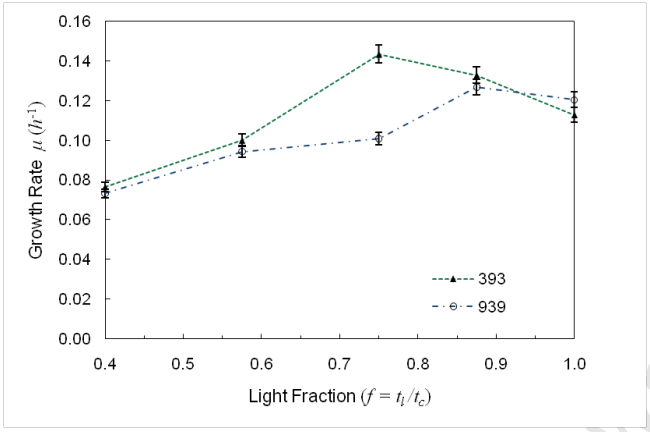

(a) $t_C = 45$sec

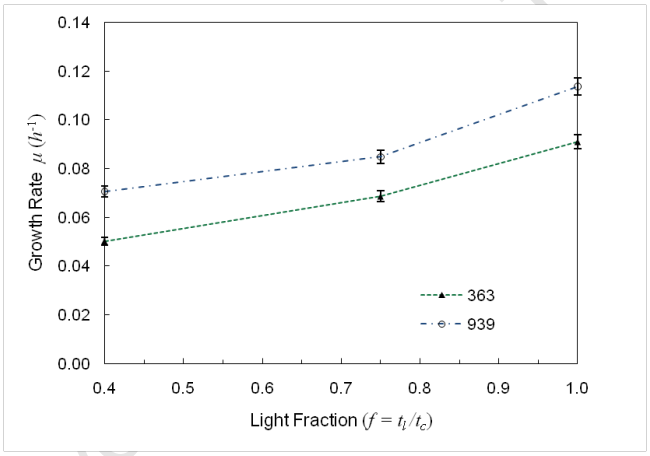

(b) $t_C = 33$sec

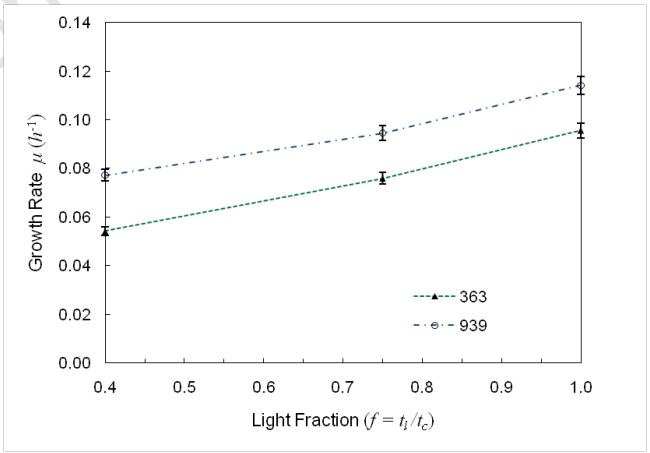

(c) $t_C = 21$sec

Figure 4.18 – Maximal growth rates μ versus Light fraction $(f = t_l/t_C)$ for two PFDs tested, I_1= 363 μmol·m$^{-2}\cdot$s^{-1} and I_2= 939 μmol·m$^{-2}\cdot$s^{-1}, shown for each fixed cycle time.

For the two shorter cycle times (22 and 33 sec) higher PFD yielded higher growth rates (Figures 4.18c and 4.18b). Interestingly, for the longest cycle time (45 sec), higher growth rates were observed for the lower of the two PFDs for all light fraction excluding unity (Fig. 4.18a). *Scenedesmus* sp. could therefore have experience photoinhibition at the higher PFD, with this effect could only be realized at the longer cycle time. For the shorter cycle times, the algae is exposed to light for less time before being allowed a dark period to recover from photoinhibitory damage. For the longer cycle time, although dark periods do exist, the longer length of exposure to light at high PFD could mean that recovery during the dark period is less effective than in the case of shorter exposure to light, thus growth rate is generally lower.

Under continuous light, the growth rate was *always* higher for the higher PFD, as seen by the cross-over point in Fig. 4.18a at $f = 1$. This is in accordance with what has already been discussed regarding the similar growth rates expected across all cycle times at $f = 1$ for the same PFD. The second expectation is that for increasing PFD at a fixed cycle time, under continuous light (i.e no light/dark cycle dynamics), the growth rate should increase. Table 4.10 shows the growth rates encountered for the low and high PFD for all cycles considering only continuous light. The trend of increased growth with increased PFD is clearly shown.

Table 4.10 – Growth rates (μ) as a function of cycle time (t_C) and PFD (I_1 and I_2) for continuous illumination ($f = 1$).

	μ (h^{-1})	
t_C (sec)	I_1	I_2
21	0.096	0.114
33	0.091	0.114
45	0.113	0.120

4.3.3 Fitting the model to the experimental data

The kinetic model was solved to simulate cyclic steady state using the method presented in Section 4.1.2. This enabled simulation of the experimental data for each combination of cycle time, light fraction and PFD. "Best-fit" kinetic parameters (α, β, γ, δ, k and Me) were then found via regression of the model to the experimental data.

Figures 4.19, 4.20 and 4.21 show the results of fitting the model to separate data from each cycle time. The parameters obtained are given in Table 4.11 and the methods used for the regression are outlined in Appendix G.2. For the 21 and 33 second cycle times, the model predicted the systematic increase in growth rate with light intensity (Figures 4.19 and 4.20). For the 45 second cycle time, the model was able to predict the maximum that occurs as a result of photoinhibition and the fact that the lower light intensity exhibited higher growth rates (Fig. 4.21).

Attempts were made to fit the model to combined data for all cycle times, but it was unable to represent the data with any accuracy. This was as a result of cross over points in the combined data. The data for the 21 and 33 second cycle times exhibited an increase in growth rate with PFD, whereas the data for the 45 second cycle time exhibited a reverse relationship. Thus, any attempts to fit the model to the combined data failed since the model was counteracting itself. The model was adequately fitted to the combined data for the 21 and 33 second cycle times (excluding 45 sec data) and this is shown in Fig. 4.22 and was able to provide a reasonable description of the data. For all the model fits, the model converged to $\mu = -Me$ at $f = 0$ and confirmation of this is illustrated in the simulations in Section 4.4.

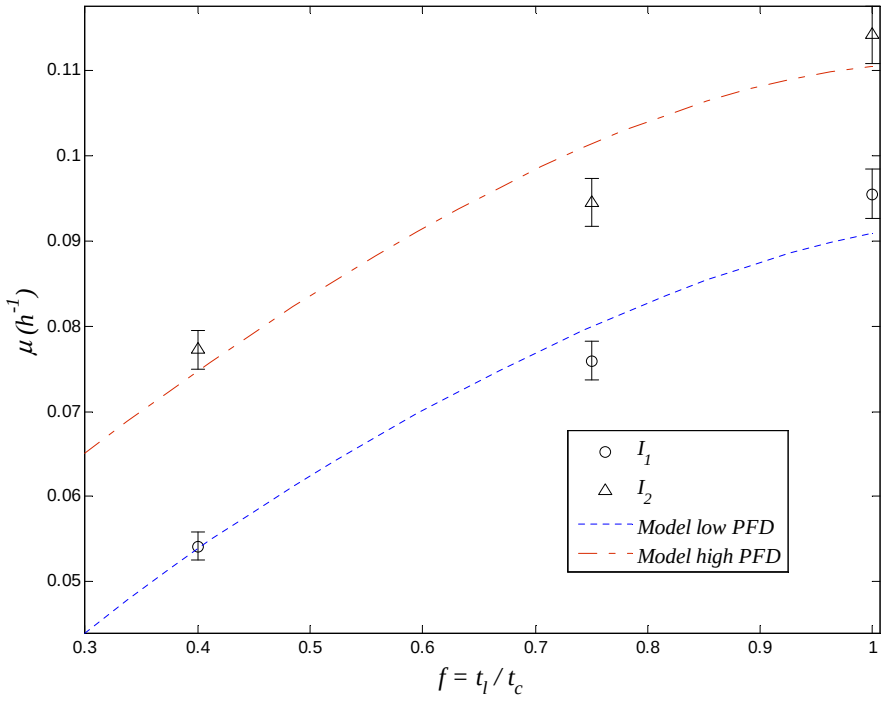

93

Figure 4.19 – Model fit for $t_C = 21$sec, showing growth rate as a function of light fraction for I_1 and I_2

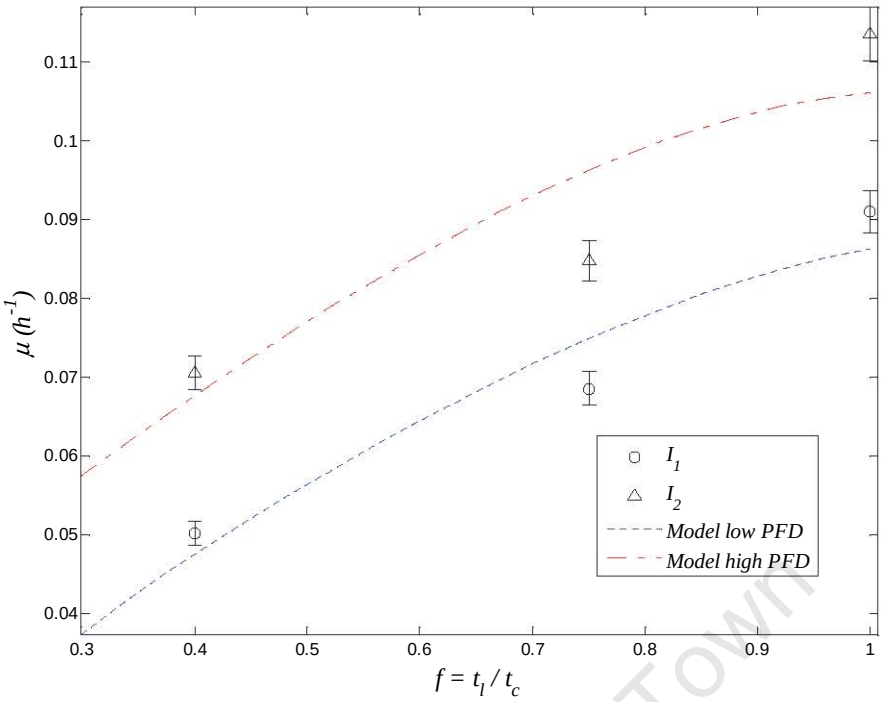

Figure 4.20 – Model fit for $t_C = 33$sec, showing growth rate as a function of light fraction for I_1 and I_2

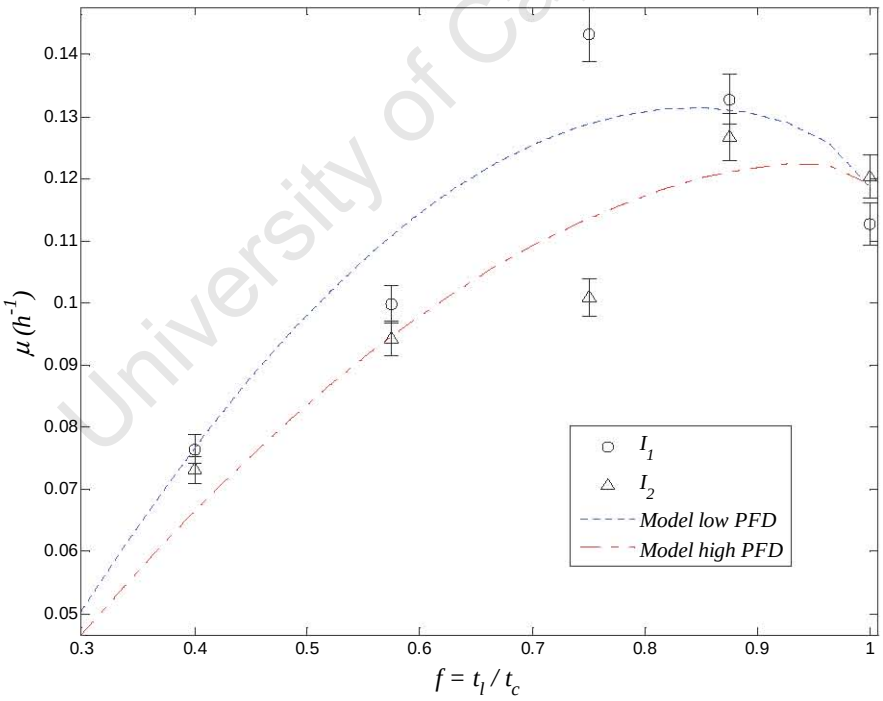

Figure 4.21 – Model fit for $t_C = 45$sec, showing growth rate as a function of light fraction for I_1 and I_2

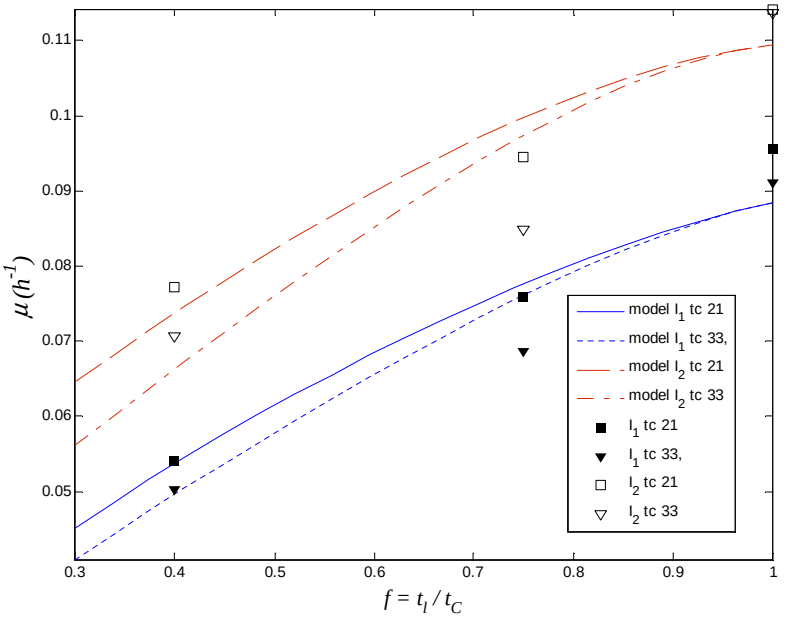

Figure 4.22 – Model fit for $t_C = 21$ and 33 sec, showing growth rate as a function of light fraction for I_1 and I_2

Table 4.11 – Best-fit parameters for *Scenedesmus* for the kinetic model regressed separately to data from the three cycle times (45, 33, 21 sec), and regressed to the the combined data from the 21 and 33 sec. Parameters of Wu & Merchuk (2001) for *Porphyridium* given for comparison.

Parameter	Units	45	33	21	21 and 33	Wu and Merchuck (2001)
α	$(\mu$ mol. m$^{-2})^{-1}$	6.56E-03	5.59E-04	7.19E-04	6.61E-04	1.94E-03
β	$(\mu$ mol. m$^{-2})^{-1}$	1.09E-03	2.43E-07	1.40E-07	3.45E-08	5.78E-07
γ	s^{-1}	0.015	0.067	0.097	0.113	0.146
δ	s^{-1}	8.42E-01	1.56E-02	5.63E-03	2.35E-03	4.80E+00
k	(-)	2.61E-02	6.01E-04	4.17E-04	3.21E-04	3.65E-04
Me	h^{-1}	0.461	0.021	0.013	6.92E-05	0.059

Confidence intervals are not shown for these parameters since they were arbitrarily large or non-existent. This suggests an over parameterization of the system for the range of data tested. In other words, the influence of certain model parameters on the output could be more significant at values that have not been accounted for, i.e. between light fractions of 0 and 0.4. Owing to the limited the number of data points used for each of these fits, the parameters obtained should be seen as first approximations, which could be improved by increasing the number of experimental data points.

For the combined fit in Fig. 4.22 the model converged at $f = 1$ for the same I values, which was expected. It was expected that the combined model fit would yield parameters that were similar to the values of the individual fits. The parameters were similar (Table 4.11) except for the Me value, which approached a value of zero for the combined fit. This could not be explained and further investigation of the model over different cycle times could be investigated with further experimentation.

4.4 Simulations

Despite the fact that the parameters found by regression are only valid over the range of variables used in these experiments, some insight can be gained from the mathematical simulation of the process over wider ranges. In this respect, a parametric study of the model can show how it could be useful as a tool to inform photobioreactor design.

Four sets of parameters were generated for *Scenedesmus* sp. from the four separate fits (Table 4.11). The 21 second cycle time parameters were chosen to be illustrative for the simulation. Variations in cycle time were not tested in these simulations, since the model ability account for such changes is questionable. In addition, for each simulation performed, a comparison is given using the parameters of Wu & Merchuk (2001) for *Porphyridium* sp. to illustrate how the model differs per species.

4.4.1 Growth rate as a function light fraction and PFD

Fig. 4.23 shows a simulation of specific growth rate, μ, as a function of light fraction, $f = t_l/t_C$, for various fixed light intensities. Cyclic steady state is assumed (see Section 4.1.2). Each curve predicts the change in μ as a function of the light fraction as it increases from 0 to 1. Two of the lines correspond to the PFDs used in these experiments and the others simulate lower and higher values of PFD. Although this experiment only covered light fractions of $t_l/t_C > 0.4$, the simulation allows a wider understanding of the system.

For *Scenedesmus sp.* (Fig. 4.23a), growth rate increases with light fraction for all values of PFD and higher PFDs yield higher growth rates. In contrast, for *Porphyridium* sp. (Fig. 4.23b), growth rate increases with light fraction for the lower PFD (100 μmol·m$^{-2}\cdot$s^{-1}), whereas for 363 & 500 μmol·m$^{-2}\cdot$s^{-1} the curve approaches a plateau as t_l/t_C approaches unity. For the higher values of PFD growth rate is generally lower than at lower PFDs (due to photoinhibition) and a clear maximum occurs at a light fraction less than unity. The simulation shows that the higher the value of the PFD, the further the maximum shifts towards a lower light fraction (Wu & Merchuk, 2001). In other words, the higher PFDs require longer dark periods for maximum growth. For higher values of I, a larger fraction of the PSFs reach the closed state x_3, and the dark period allows reparation of damaged PSFs returning them to active states as x_1 and thus allowing photoproduction to continue (Wu & Merchuk, 2001). The model prediction for *Scenedesmus* sp. does exhibit maximums, but only at PFDs > 2000, which are beyond the bound of what is possible in reality in terms of PFD from the sun.

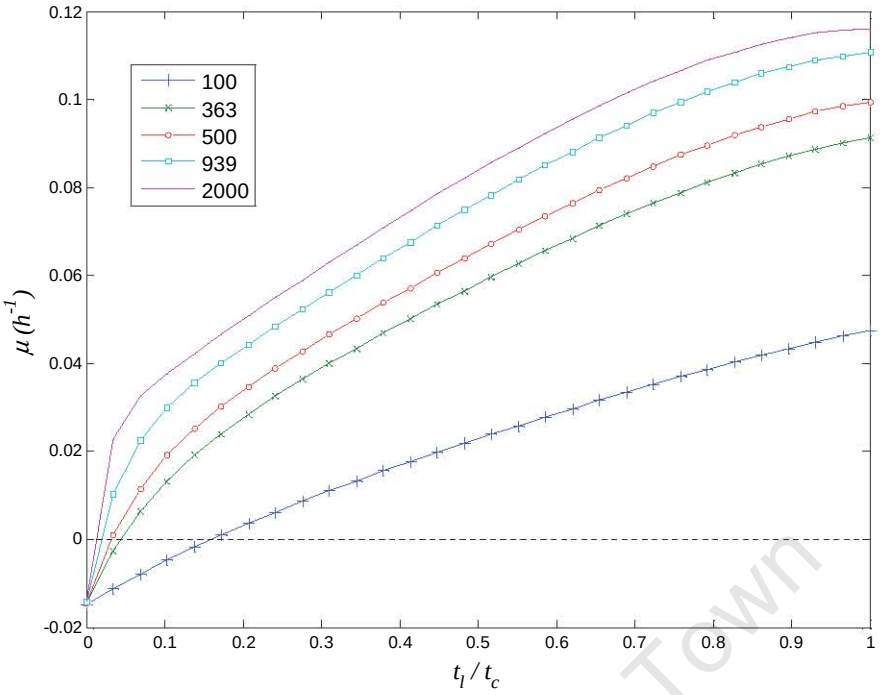

(a)

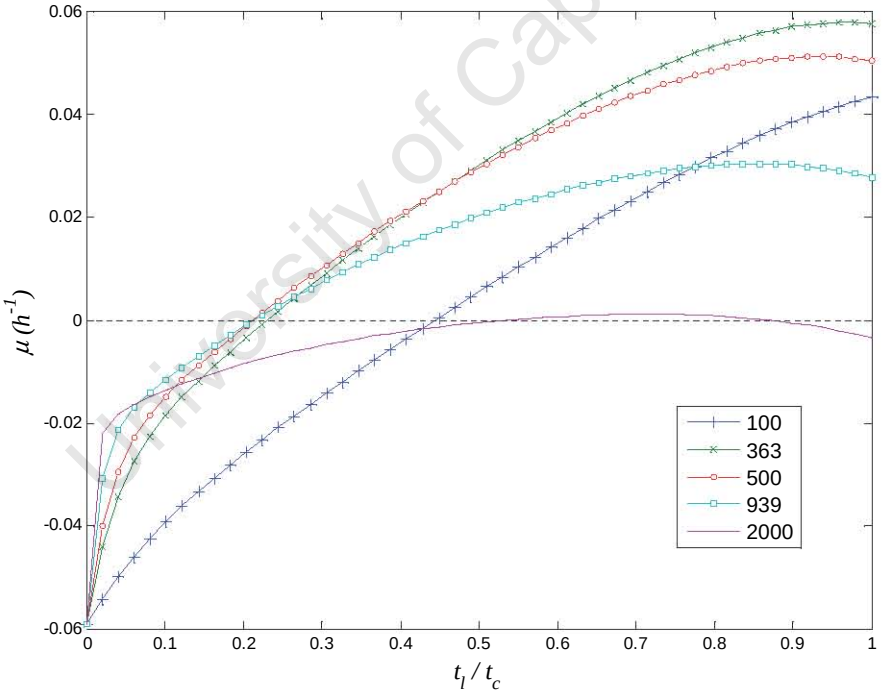

(b)

Figure 4.23 – Simulation of the effects of light fraction ($f = t_l/t_C$) on the specific growth rate μ over a range of light intensities. **(a)** Parameters used from the 21 second cycle time fit (Table 4.11) obtained for *Scenedesmus*. **(b)** Parameters of Wu & Merchuk (2001) for *Porphyridium* sp. The values in the figure indicate PFD in $\mu\text{mol}\cdot\text{m}^{-2}\cdot\text{s}^{-1}$.

The *Scenedesmus* trend in Fig. 4.23a shows almost no photoinhibition effects up to a PFD of 939 μmol·m$^{-2}\cdot$s^{-1}, whereas the *Porphyridium* sp. trend shows photoinhibition at 500 μmol·m$^{-2}\cdot$s^{-1} and beyond. This is most likely due to how the parameters were determined for each species and is not an indication of *Scenedesmus* being less sensitive to photoinhibition. The model clearly can account for photoinhibition in the case of the 45 second cycle data (Fig. 4.21). Use of the 45 second parameters in the simulations produced undefined results when extrapolated to light fractions below those fitted in the data ($f < 0$). The the parameters used for the simulation (from the 21 second cycle time fit) came from data that showed μ to be only strictly increasing with light fraction, hence the simulation doesn't represent photoinhibition well. The parameters obtained for *Porphyridium* sp. were obtained from data at a single cycle time that exhibited both strictly increasing μ at low PFDs (110 and 220 μmol·m$^{-2}\cdot$s^{-1}) and photoinhibition at the high PFD of 550 μmol·m$^{-2}\cdot$s^{-1}(Wu & Merchuk, 2001). One could therefore argue that the parameters for *Porphyridium* sp. are more representative of the algae's response to changing light whereas the parameters for *Scenedesmus* are limited.

Fig. 4.24 shows predictions of growth rate μ as a function of PFD for various values of light fraction. For *Scenedesmus* sp. (Fig. 4.24a) μ strictly increases with PFD, reaching higher values for higher light fractions. For *Porphyridium* sp. (Fig. 4.24b) μ reaches a maximum at a specific PFD, after which growth is inhibited. This maximum can be sustained at increasingly higher PFDs for decreasing light fractions. This suggests that with more dark time for recovery the cells can take better advantage of higher PFDs (Wu & Merchuk, 2001).

Fig. 4.25 shows light fractions (t_l/t_C) as a function of PFD with the transition point between positive and negative growth (i.e $\mu = 0$) represented by a solid line to show a "positive growth island". The purpose of such a simulation is to show that for every PFD, there is a distinct range of light fractions over which growth is possible, outside of which the cells would die. The contour defining this range shows the combination of PFD and light fraction that provide sufficient photons per cycle to overcome cellular maintenance (Wu & Merchuk, 2001). There are distinct differences between the prediction for *Scenedesmus* sp. (Fig. 4.25a) and for *Porphyridium* sp. (Fig. 4.25b). The maximum PFD for *Scenedesmus* sp. after which growth is not possible is beyond the regions of the simulation, whereas this region for *Porphyridium* sp. is clearly defined up until a critical PFD of approximately 2000 μmol·m$^{-2}\cdot$s^{-1}.

Fig. 4.26 is an extension of the positive growth island with contours of equivalent growth. Fig. 4.26a illustrates the relationship between PFD and light fraction where photoinhibition does not occur and Fig. 4.26b where it does occur. In both figures the trend in the predictions is the same at PFDs less than 400 μmol·m$^{-2}\cdot$s^{-1}. These results show the potential for using the model to realize the combination of PFD and light fraction that will optimize a photobioreactor. In the case where photoinhibition occurs, this would entail minimizing the exposure to PFD towards the optimum at ~300 μmol·m$^{-2}\cdot$s^{-1}(Fig. 4.26b). The growth contours then show the light fraction that achieves optimum growth at any given PFD. For example, given a fixed average PFD of 500 μmol·m$^{-2}\cdot$s^{-1}, this would entail designing for

maximum possible light fractions for *Scenedesmus* sp. (see Fig. 4.26a), assuming no photoinhibition, and for *Porphyridium* sp., this would entail light fractions of approximately 0.9 (from Fig. 4.26a).

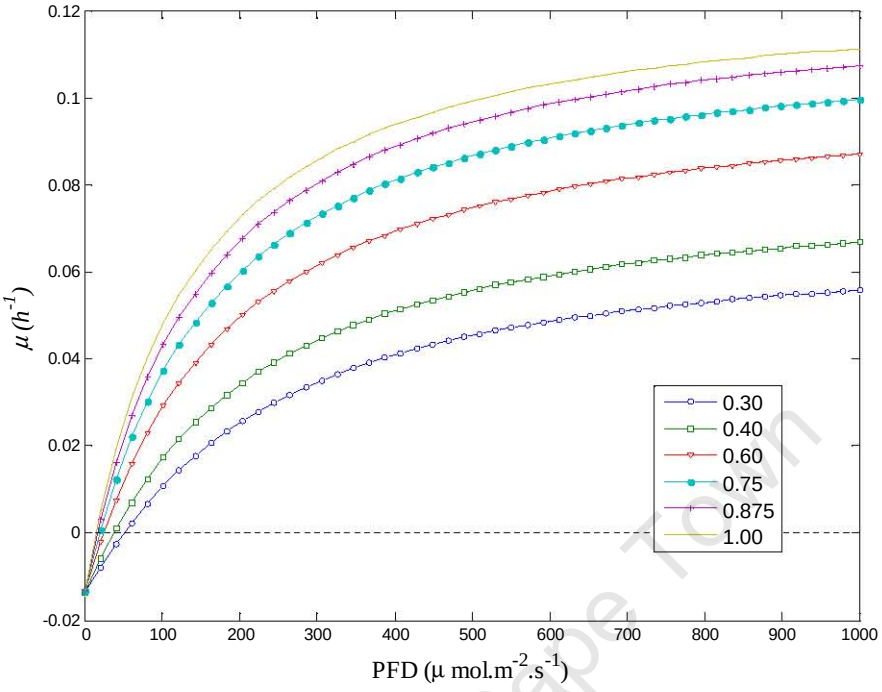

(a)

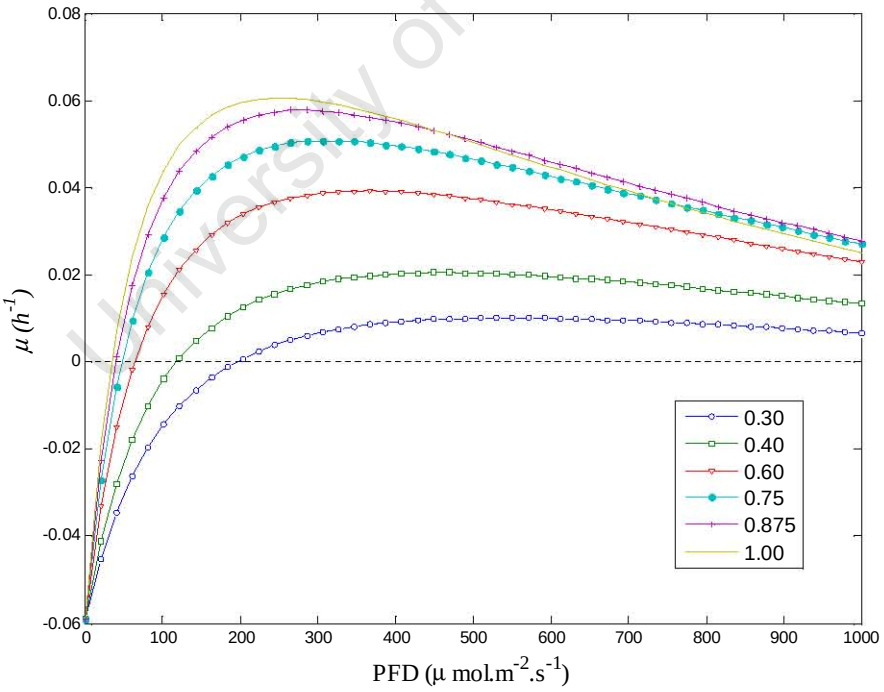

(b)

Figure 4.24 – Simulation for of the effects of PFD on the specific growth rate μ over a range of light fractions. **(a)** Parameters used from the 21 second cycle time fit (Table 4.11) obtained for *Scenedesmus*. **(b)** Parameters of Wu & Merchuk (2001) for *Porphyridium* sp. The values in the figure indicate light fractions $f = t_l/t_C$.

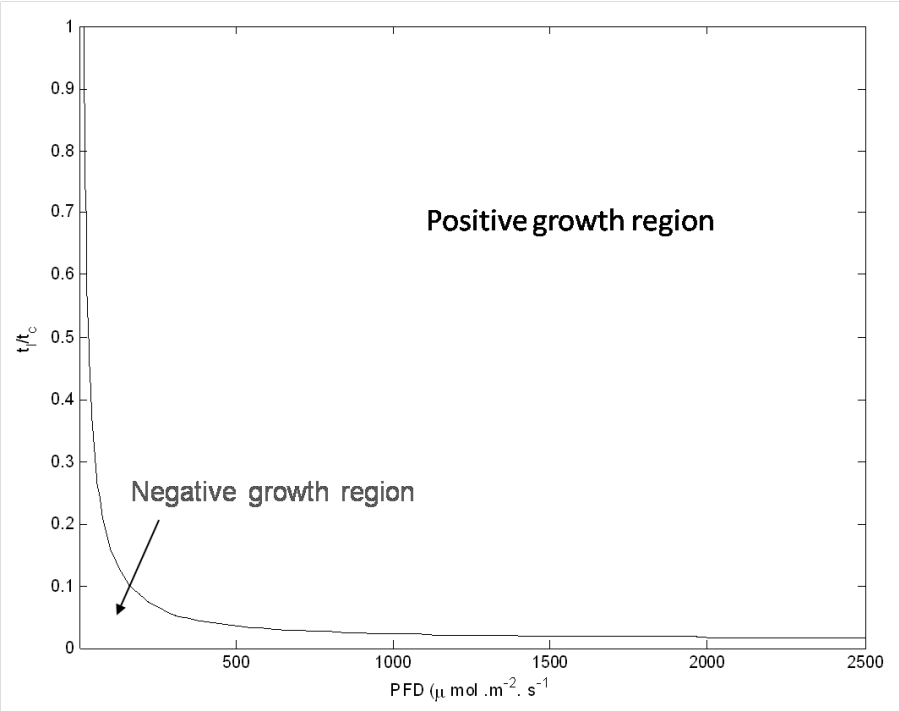

(a)

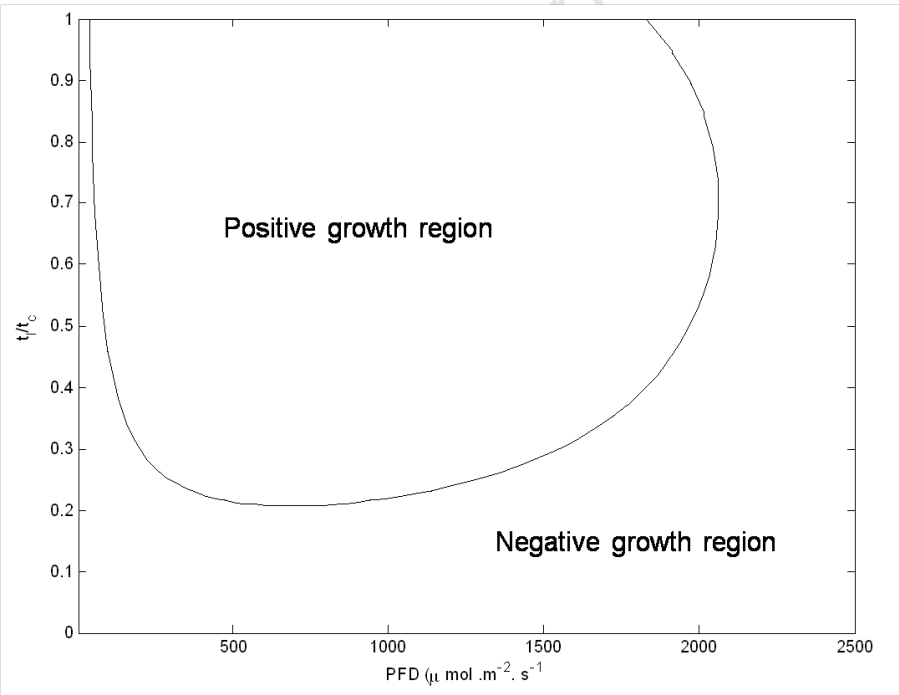

(b)

Figure 4.25 – Simulation of a positive growth islands on the plane t_l/t_C vs. PFD. The line dividing the two regions denotes $\mu = 0$. **(a)** Parameters used from the 21 second cycle time fit (Table 4.11) obtained for *Scenedesmus*. **(b)** Parameters of Wu & Merchuk (2001) for *Porphyridium* sp.

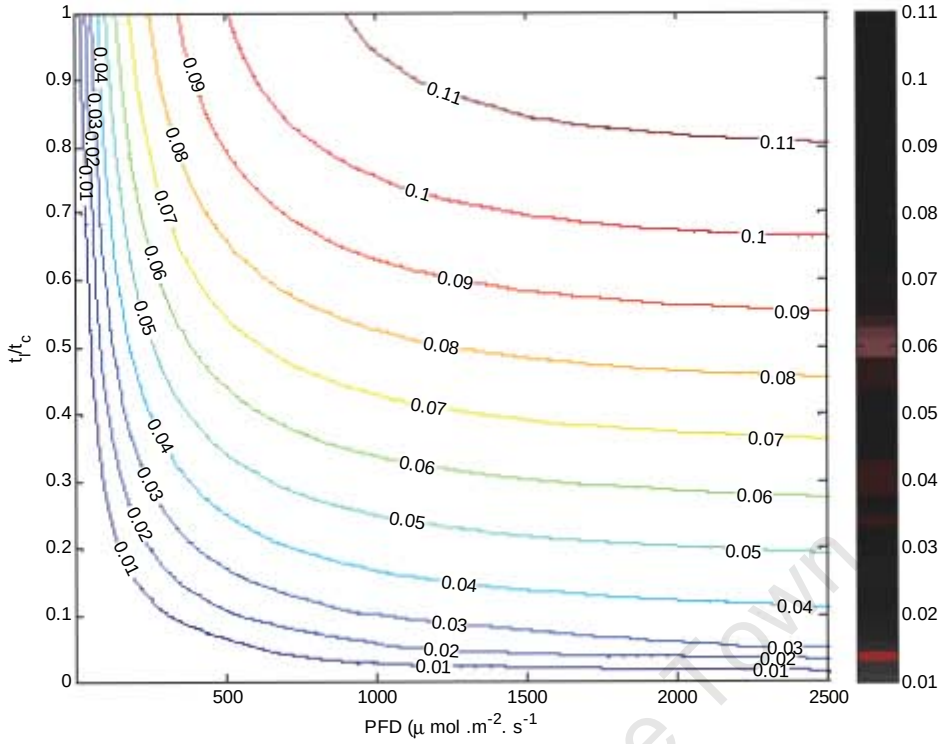

(a)

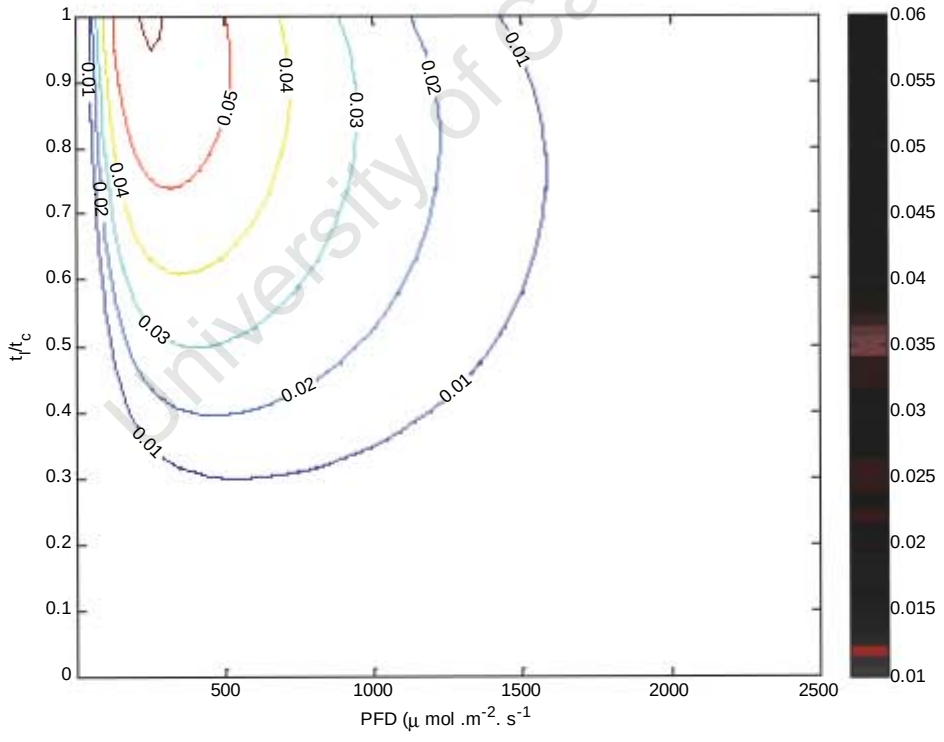

(b)

Figure 4.26 – Simulation of various growth contours normal to the plane of t_l/t_C vs. PFD. The lines denote lines of constant μ with their value given (h^{-1}). **(a)** Parameters used from the 21 second cycle time fit (Table 4.11) obtained for *Scenedesmus*. **(b)** Parameters of Wu & Merchuk (2001) for *Porphyridium* sp.

4.4.2 Model solution at steady state

Analysis of the model at steady state was performed to justify its consistency and check for expected behaviour and stability at its extreme point, i.e. as $t \to \infty$.

The analytical steady-state solution of the system of equations gives the steady state growth rate for any given light intensity (Eilers & Peeters, 1988). This is obtained by setting the LHS in Equations (4.1)–(4.3) to zero, and solving for the steady state PSF values $\overline{x_i}$:

$$\overline{x_1} = \frac{\delta(\beta I + \alpha)}{\alpha\beta I^2 + \delta I(\alpha + \beta) + \gamma\delta} \tag{4.32}$$

$$\overline{x_2} = \frac{\alpha\delta I}{\alpha\beta I^2 + \delta I(\alpha + \beta) + \gamma\delta} \tag{4.33}$$

$$\mu = k\gamma\overline{x_2} - Me \tag{4.34}$$

Plotting steady-state growth (Eq. 4.34) as a function of light intensity I produces a simulation of the well known P-I curve (see Section 2.2.4) as shown in Fig. 4.27. The steady-state profiles for the PSF fractions, x_1, x_2, x_3, are also shown. There are clear differences between the PSF profiles for the *Scenedesmus* and *Porphyridium* sp. parameters. As previously mentioned, the *Scenedesmus* parameters do not show the inhibition effects and hence x_3 remains small with increasing PFD. In contrast, for *Porphyridium* sp., the x_3 fraction rises considerably as PFD increases to model photoinhibition. In conjunction with this, the x_2 fraction for *Porphyridium* sp reaches a maximum at I_{opt} whereas the x_2 fraction for *Scenedesmus* strictly increases.

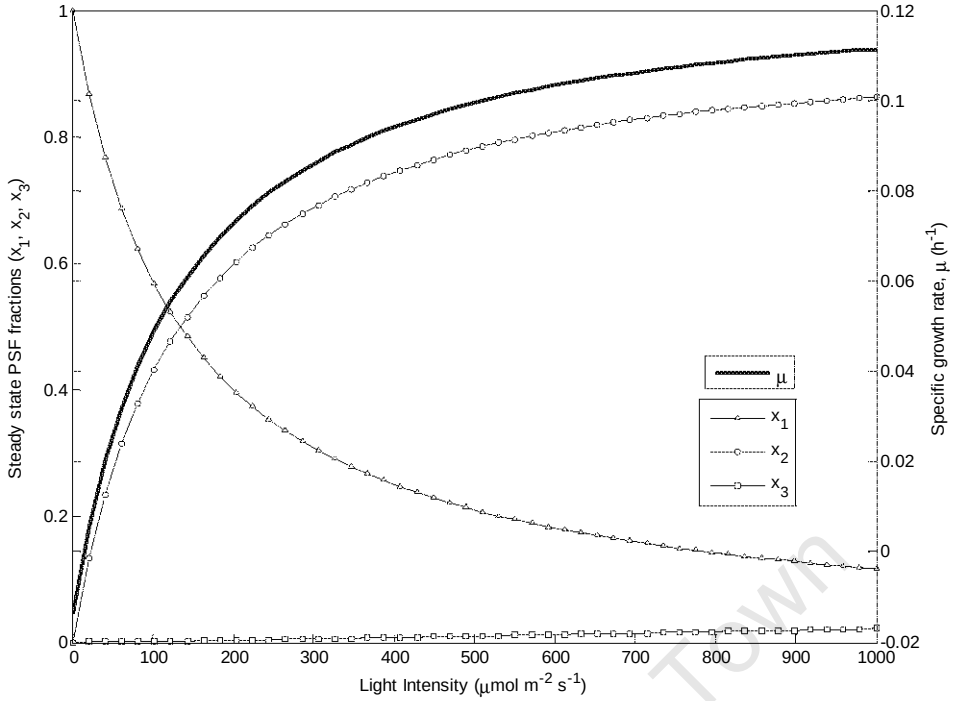

(a)

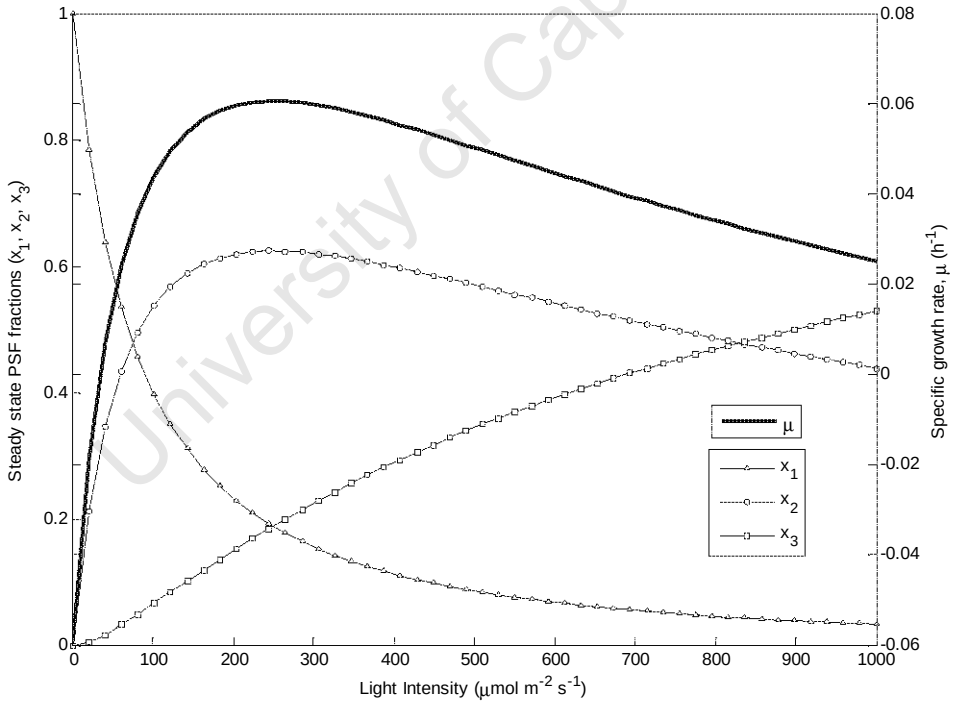

(b)

Figure 4.27 – Simulated P/I curve, together with profiles for PSF fractions. **(a)** Parameters used from the 21 second cycle time fit (Table 4.11) obtained for *Scenedesmus*. **(b)** Parameters of Wu & Merchuk (2001) for *Porphyridium* sp.

Fig. 4.27a shows that *Scenedesmus* approaches light saturated growth at high PFDs without decreases due to inhibition. Fig. 4.27b shows *Porphyridium* reaching a maximum at I_{opt} ~250 μmol·m$^{-2}\cdot$s^{-1}, after which growth is photoinhibited . The value for the optimal light intensity (I_{opt}) that gives maximum steady-state growth can be solved for explicitly by differentiating Eq. 4.34 with respect to I and equating to zero:

$$\frac{d\mu}{dI} = \frac{\alpha\delta\gamma k(\delta\gamma - I^2\alpha\beta)}{(\delta\gamma + I\alpha\delta + I\beta\delta + I^2\alpha\beta)} = 0 \tag{4.35}$$

Solving for I yields and expression for I_{opt} :

$$I_{opt} = \sqrt{\frac{\delta\gamma}{\alpha\beta}} \tag{4.36}$$

By substituting the parameters given for *Porphyridium* in Table 2.8, this yields an exact value of $I_{opt} =$ 250.1 μmol·m$^{-2}\cdot$s^{-1}. For *Scenedesmus,* the optimum calculated from this model is an unrealistically high value of 2320 μmol·m$^{-2}\cdot$s^{-1}. However, the fact the model *does* produce an optimum confirms the models underlying consistency.

Further analysis of the steady state solution reveals a relationship between the PSF kinetics model and monod-type substrate inhibition kinetics, previously noted by Eilers & Peeters (1988, 1993). Considering light to be the inhibiting substrate, Eq. 4.34 can be re-written in Monod form as:

$$\mu = \frac{\mu^* I}{K_S + I + \frac{I^2}{K_I}} - Me \tag{4.37}$$

$$\text{where, } \mu^* = \frac{k\gamma\alpha}{\alpha+\beta},\ K_s = \frac{\gamma}{\alpha+\beta} \text{ and } K_I = \frac{\delta(\alpha+\beta)}{\alpha\beta}$$

Eq. 4.37 is of exactly the same form as the static light curve model of Aiba (1987), shown previously in Table 2.5 in the literature review.

4.5 Summary and conclusions for kinetic growth model

- Methods of solving the kinetic model were developed and tested to allow for a non-linear form of the model equations and to be able to simulate algal growth under cyclic steady state conditions (Section 4.1).

- Simulation of algal growth under controlled light/dark cycles in specially designed tubular loop reactors enabled growth data to be generated at varying light fractions, cycle times and PFDs according to the experimental plan given in Section 4.2.2. The ranges for these variables were determined to represent the laboratory airlift reactor.

- The increase in growth rate with increasing light fraction approached linearity for the 21 and 33 cycle time data. This was similar to the trend reported by Janssen (2002). For the 45 sec cycle time data, the growth rate exhibited a maximum at a light fraction less than unity, which was indicative of photoinhibition effects. Wu & Merchuk (2001), who only tested a 45 second cycle time, observed similar photoinhibition trends for *Porphyridium* sp. The 21 and 33 second cycle times did not exhibit photoinhibition. Thus, photoinhibition was attributed to the longer light exposure time in the 45 second case, whereas the two shorter cases had shorter light exposure and more frequent dark recovery periods.

- The longest cycle time (45 seconds) exhibited generally higher growth rates than the two shorter cycle times under conditions of intermittent light. This effect was more pronounced at the lower light intensity than at the higher light intensity under which photoinhibition was observed.

- Solutions of the PSF kinetic model developed in Section 4.1 enabled best-fit kinetic parameters to be determined for the species in question, *Scenedesmus* sp. Importantly, the model was found to be unable to simulate the combined data for variations in cycle time. As a result, a different set of parameters were determined for each cycle time tested. The model was found to be able to reasonably simulate the subset of data for the combined 21 and 33 second cycle time. However, this produce an erroneous Me parameter and the models ability to describe variations in cycle should be investigated further.

- Despite the inconsistencies in the model parameters, a parametric study was performed in Section 4.4 (ignoring variations in cycle time). This produced simulations that gave meaningful insight into a broad range relationships between light fraction and PFD that influence algal growth. These results yielded interesting insight into culture conditions with and without photoinhibition and illustrated the potential to provide data that could be used to design photobioreactors that incorporate optimum light/dark cycles. Any photobioreactor with turbulent mixing falls in to the latter category

- Finally, the model was analyzed at steady-state to produce a P-I curve and test the model's consistency at its extreme. The similarity between the model's fundamental structure and the

well known substrate inhibition kinetic formulation was also highlighted.

- This kinetic model is targeted for integration into a global airlift model, which incorporates both the light distribution and hydrodynamic models. This development is done in Chapter 6.

4.6 Recommendations

- The influence of different riser lengths between the three tubular reactor systems should be investigated to ascertain whether this has a significant effect on growth differences. Should such a difference arise, then the tubular systems requires redesign to use the same length of riser tubing.

- The non-uniform light history experienced by the cells in the experiment (discussed in Section 4.2.5) should be accounted for in the model. This would require measurement of the light intensity at fixed distances along the tubes for each of three systems. Using this data it would be possible to model how the light changes with distance along the tubes: $I(z)$. Combined with the rate of circulation around the tubes, this could produce a quantitative description of light history $I(t)$, which could be used instead of an average PFD when integrating the kinetic model.

- Additional experimental data should be generated for *Scenedesmus* sp. at the same two PFDs and cycle times but over a larger range of light fractions. This would give a better description of the growth characteristics under light/dark cycles and give more confidence in fitted parameters. Owing to the limited data points tested, some of the trends and anomalies observed in Section 4.3.2 could not be explained.

- The relevance of the parameters should be tested across different algal species with consideration to their light uptake rates and tolerance to photoinhibition.

- It is suggested that the non-linear kinetic model of Rubio *et al.* (2003) be tested against this same data to test whether its different formulation is more or less effective at predicting the data.

Chapter 5

Fluid dynamics: model development, results, comparisons and discussion

The background to various approaches for modelling ALR hydrodynamics and generating light history is discussed in the main literature review (Section 2.10.3). In this section, the compartmentalized approach originally used by Wu & Merchuk (2004) was used to model the fluid flow in the ALR for use in the global model in Chapter 6. It is appropriate to model approximate hydrodynamic characteristics in an ALR and requires minimal computational power when compared to complex CFD models.

To recap the approach: the fluid flow is modeled to flow in a defined circulation pattern through regions that are defined by the geometry of the airlift. A description of this movement forms the underlying assumption for typical cell trajectories in the reactor. A liquid model is required to predict how long the cells are present in each region. Liquid circulation is defined by the rate of gas input to the bottom of the riser, the gas hold-up in the reactor and the geometry of the circulation path. In order to fully predict the hydrodynamics, a model for gas-holdup is required in combination with a liquid circulation model.

In this chapter, the necessary theory is presented first, thereafter a focused literature review on hydrodynamic modelling in airlift reactors is presented. This informs the formulation of the hydrodynamic model used in the present work. Once formulated, the experimental and mathematical methods used to obtain the necessary parameters are given. Furthermore, the model is used to simulate variations in the A_r/A_d ratios to illustrate the advantages of using the model to design for optimum light/dark cycles.

5.1 Focused literature review and theory on modelling gas hold-up and liquid circulation in airlift reactors

5.1.1 Gas hold-up: Definitions, measurement and modelling

The gas hold-up ε is defined as the gaseous fraction within the total reactor volume ($V = V_G + V_L$) where V_G and V_L are the total volumes of gas and liquid in the reactor at any local position:

$$\varepsilon = \frac{V_G}{V_L + V_G} \tag{5.1}$$

In an airlift reactor, the individual hold-ups of the riser ε_r and downcomer ε_d can be related to the overall hold-up ε by a simple mass balance:

$$\varepsilon = \frac{A_r\varepsilon_r + A_d\varepsilon_d}{A_r + A_d} \tag{5.2}$$

where A_r and A_d are the cross sectional areas of the riser and downcomer, respectively.

Gas hold-up determines the residence time of the gas in liquid, affects the bubble size and influences the gas interfacial area available for mass transfer (Merchuk *et al.*, 2000; Chisti, 1989). The difference in gas hold-up between the riser and downcomer creates the driving force for liquid circulation.

Gas hold-up most commonly measured by using manometers, placed in different parts of the reactor, to enable the measurement of "local" or "overall" hold-up inferred from pressure differences (Freitas *et al.*, 1999; Korpijarvi *et al.*, 1999; Merchuk *et al.*, 1998b; Chisti, 1989). More sophisticated techniques since been developed, such as Electrical Resistance Tomography (ERT), which was successfully employed for local gas hold-up measurements in bubble columns and airlift reactors by Jin *et al.* (2007). ERT measures the conductivity of the media and calculated gas hold-up via Maxwell equations. Most recently, Luo & Al-Dahhan (2010) employed gamma-ray Computer Tomography (CT), a well known medical imaging technique, to accurately measure and visualize local hold-ups.

Generally, gas hold-up shows a dependence on gas flow rate, the geometry of the vessel (i.e. A_d/A_r), type of sparger and the physical properties of fluid. Most of the correlations available for airlift reactors make empirical use of these parameters. Since the majority of the gas hold-up in an airlift reactor is present in the riser, almost all of the models developed are for correlating *riser* gas-holdup ε_r, with the downcomer holdup ε_d either assumed to be negligible or calculated from a separate model. Numerous gas hold-up models are available for airlift reactors (Table 5.1), many of which are inconsistent with each other (Miron *et al.*, 2000; Chisti, 1989).

Table 5.1 – Selected models for gas hold-up in airlift bioreactors. Table source: Gumery *et al.* (2009). Subscripts for ε: g = gas, d =downcomer, r = riser, s =solids.

Reference	Media	Conditions	Design	Equation
Hwang and Cheng, 1997	Air Water CMC	A_r/A_d= 0.69-3.22 H=2.5m D_d= 0.9-0.14m	Internal Loop	$\varepsilon_{gd} = 0.001U_g^{0.733}\left(\frac{A_d}{A_r}\right)^{-0.378} \cup_h H_d^{0.125}(1+\varepsilon_s)^{-2.060}$
Kemblowski *et al.*, 1993	Air Water Glycol Syrup CMC	A_d/A_r= 1-1.33 U_{gr} = 0.001-0.15m/s.	External Loop	$\varepsilon_{gr} = 0.203\frac{F_r^{0.31}}{M_o^{0.012}}\left(\frac{U_{gr}A_r}{U_{lr}A_d}\right)^{0.74}$
Popovic *et al.*, 2004	Air CMC	A_d/A_r= 0.11-0.44 H=1.88m D_d= 0.15m	Internal Loop	$\varepsilon_{gr} = 0.93U_{gr}^{0.65}(1-\varepsilon_s)^{0.74}\left(1+\frac{A_d}{A_r}\right)^{-1.05}$
Renzo, 2005	Air Water	N/A	External Loop	$\varepsilon_g = \frac{U_g/A_r}{0.25+1.1\left(U_g/A_r+U_l/A_r\right)}$

Wu & Merchuk (2004) used a correlation from Popovic and Robinson (1984) (cited in Wu & Merchuk (2004)) for their global airlift model, as given by:

$$\varepsilon_r = 0.465 \cdot U_{Gr}^{0.65}\left(1+\frac{A_d}{A_r}\right)^{-1.06}\eta^{-0.103} \tag{5.3}$$

where η is the apparent viscosity (Pa·s) and U_{Gr} is the superficial gas velocity in the riser (m.s^{-1})

A superior approach to correlating gas hold-up uses the drift flux model (Miron *et al.*, 2000; Rubio *et al.*, 1999; Chisti, 1989). For gas-liquid flow in the riser of an airlift, this is formulated as:

$$\varepsilon_r = \frac{U_{Gr}}{\sigma+\phi\left(U_{Gr}+U_{Lr}\right)} \tag{5.4}$$

Miron *et al.* (2000) found good agreement between this drift flux type model and experimental data for gas hold-ups in an airlift reactor over a range of superficial gas velocities (U_{Gr} 0.001-0.09 m.s^{-1}). Eq. 5.16 is a function of the superficial liquid circulation velocity U_{Lr} which is not always known *a priori*. With U_{Lr} unknown, Eq. 5.16 needs to be used in conjunction with a liquid circulation model that defines U_{Lr}.

It is well established that the relationship between the riser and downcomer gas hold-up can be expressed by Eq. 5.5 (Miron *et al.*, 2000; Contreras *et al.*, 1998):

$$\varepsilon_d = a\varepsilon_r - b \tag{5.5}$$

The parameters a and b are constants which have different values determined for different airlift systems. The parameter b accounts for the fact that the downcomer has zero hold-up until a critical finite hold-up has been achieved in the riser. Thus, the relationship is better expressed mathematically as follows:

$$\varepsilon_d \begin{cases} = 0 & for \quad \varepsilon_r \leq \frac{b}{a} \\ = a\varepsilon_r - b & for \quad \varepsilon_r \geq \frac{b}{a} \end{cases} \tag{5.6}$$

An alternative explanation for this behaviour, is that the liquid circulation flow needs to be fast enough to allow bubbles from the riser to be entrained in the fluid when passing from the riser to the downcomer. At low liquid circulation rates, the majority of the bubbles will disengage from the liquid in the top section of the airlift. Liquid circulation rate increases with increasing gas injection. Since ε_r also increases with increasing gas injection, there will be a critical ε_r at which entrainment occurs.

5.1.2 Liquid circulation: Definitions, measurement and modelling

Liquid circulation velocity is an important parameter in airlift reactors. It affects the residence time of gas, the mass transfer coefficient k_La and the mixing time. In an airlift reactor, the liquid circulation velocity is directly influenced by the inlet gas flow rate and the reactor geometry.

Since the volumetric flow rate through the riser and downcomer regions must be conserved, the velocity at which the liquid circulates per different region is usually different, owing to the different gas holdups present and the respective size of each region. To give a very simple analogy: imagine water flowing with volumetric flow rate Q through a large pipe with cross sectional area A_1 into a much smaller pipe with cross sectional area A_2. The volumetric flow in the smaller pipe would be the same as that leaving the larger pipe, i.e:

$$Q = \rho \cdot v_1 \cdot A_1 = \rho \cdot v_2 \cdot A_2 \tag{5.7}$$

However, because the smaller pipe has a smaller cross sectional area and less "space" for liquid to flow, the velocity through the smaller pipe would be greater than that in the larger pipe, i.e:

$$v_2 = v_1 \left(\frac{A_1}{A_2} \right) \tag{5.8}$$

The same concept applies to the different regions inside an airlift, which have different volumes, cross sectional areas and hold-ups. The fluid velocity in the riser is most often greater than the downcomer owing to the gas hold-up and energy imparted by the rising gas bubbles.

The *mean* circulation velocity $v_c$can be thought of as the average velocity for all regions that define a single circulation loop. This can be defined as follows:

$$v_c = \frac{L}{t_c} \tag{5.9}$$

Where L is the average fluid circulation path length and t_C is the average time for one complete recirculation of fluid. Liquid circulation time t_C is easily measured using the tracer response technique (pH or conductivity). This method is popular because of its simplicity and has been employed in numerous previous works on airlift reactors (Miron *et al.*, 2000; Freitas *et al.*, 1999; Korpijarvi *et al.*, 1999; Merchuk *et al.*, 1998b; Chisti *et al.*, 1988; Bello *et al.*, 1985). The responses are typically sinusoidal in shape, with the distance between adjacent peaks equal to circulation time.

Mean circulation velocity cannot be used directly for the compartmental model since values of the separate liquid velocities in the riser or downcomer section are required to determine the times spent in each of these sections. Before discussing modelling the riser and downcomer velocities separately, it is important to define the difference between linear and superficial velocity.

Consider the riser of an airlift reactor: the liquid occupies only a part of the flow channel, the rest being occupied by gas. Consider the total cross section of the riser to be A_r, then the area actually occupied by liquid flow A_{liquid} would be $A_r(1-\varepsilon_r)$. If we let the total volumetric flow of liquid be Q then the true *linear* velocity of liquid V_{Lr} would be:

$$V_{Lr} = \frac{Q}{A_{liquid}} = \frac{Q}{A_r(1-\varepsilon_r)} = \frac{U_{Lr}}{(1-\varepsilon_r)} \tag{5.10}$$

where U_{Lr} is the superficial liquid velocity, a value which is based on the *total* cross section of the riser, rather than on the true cross section area that is occupied by the liquid phase. Similarly, for the downcomer:

$$V_{Ld} = \frac{U_{Ld}}{(1-\varepsilon_d)} \tag{5.11}$$

The relationship between the superficial velocity in the riser and downcomer can be summarized by a mass balance balance between the riser and downcomer sections, referred to as the *continuity relationship* (Chisti *et al.*, 1988). i.e $Q = Q_r = Q_d$ (constant density assumed), which gives:

$$Q = U_{Lr}A_r = V_{Lr}A_r(1-\varepsilon_r) = V_{Ld}A_d(1-\varepsilon_d) = U_{Ld}A_d \tag{5.12}$$

Estimation of U_{Lr} and/or U_{Ld} requires a liquid circulation model. A wide variety of such models are available in literature, with clear discrepancies between their parameters and ability to predict data (Miron *et al.*, 2000). This is made more prevalent by the variability of the conditions under which each was developed and tested, such as different reactor dimensions, A_d/A_r ratios, range of U_{Gr} and fluids.

The most popular and widely used model for describing liquid circulation in airlift reactors is that of Chisti *et al.* (1988). The model is based on energy balances for the riser and downcomer and the application of continuity equations over a liquid circulation loop (derivation given Appendix F.1). Since its inception this model has been extensively used (Stephenson, 2009; Janssen, 2002; Fernandez *et al.*, 2001; Miron *et al.*, 2000) and validated by numerous independent authors. It has been shown

to apply to low viscosity, water-like fluids in external and internal loop airlift reactors over a broad range of scales and superficial gas velocities (Gumery *et al.*, 2009). The model, for internal loop airlift reactors, is given as follows:

$$U_{Lr} = \sqrt{\frac{2gh_D(\varepsilon_r - \varepsilon_d)}{K_B \left(\frac{A_r}{A_d}\right)^2 \frac{1}{(1-\varepsilon_d)^2}}} \tag{5.13}$$

where g is the gravitational acceleration (m.s^{-2}), h_D is the height of gas-liquid dispersion (m) and K_B is the frictional loss coefficient for the bottom of the reactor. In the case where the riser and downcomer gas hold-ups are not known *a priori*, Eq. 5.13 must be used in conjunction with a gas hold-up model, such as given in Equations 5.4 and 5.6. For internal loop reactors, K_B has been empirically related to the geometry at the bottom of the reactor according to Chisti *et al.* (1988) :

$$K_B = 11.4 \cdot \left(\frac{A_d}{A_b}\right)^{0.79} \tag{5.14}$$

Where A_b is the free area (beneath the draft tube) available for liquid flow between the downcomer and riser, as illustrated in Fig. 5.1.

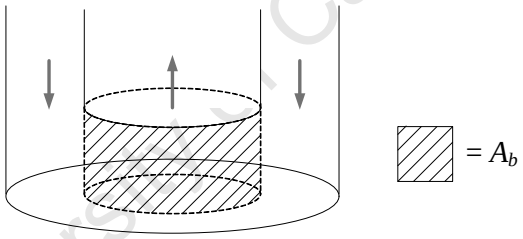

Figure 5.1 – Free area for liquid flow (A_b) between riser and downcomer for an internal loop airlift reactor. Image source: this author, after Chisti *et al.* (1988).

5.2 Hydrodynamic model development for the present work

The hydrodynamic model for the present work utilized the drift-flux model according to Miron *et al.* (2000) to model gas hold-up and the Chisti *et al.* (1988) model for liquid circulation. To summarize:

Gas holdup according to Miron *et al.* (2000):

$$\varepsilon_d \begin{cases} = 0 & for \quad \varepsilon_r \leq \frac{b}{a} \\ = a\varepsilon_r - b & for \quad \varepsilon_r \geq \frac{b}{a} \end{cases} \tag{5.15}$$

$$\varepsilon_r = \frac{U_{Gr}}{\sigma + \phi\,(U_{Gr} + U_{Lr})} \tag{5.16}$$

Liquid circulation according to Chisti *et al.* (1988):

$$U_{Lr} = \sqrt{\frac{2gh_D(\varepsilon_r - \varepsilon_d)}{K_B\left(\frac{A_r}{A_d}\right)^2 \frac{1}{(1-\varepsilon_d)^2}}} \tag{5.17}$$

The aim of this model was to obtain values for liquid circulation (U_{Lr}, U_{Ld}) and hold-ups ($\varepsilon_r, \varepsilon_d$) as a function of the superficial gas velocity U_{Gr} and reactor geometry (A_r, A_d, h_D). This would later form part of a sub-model for use the global airlift model.

Because ε_r in Eq. 5.16 is a function of U_{Lr} , and U_{Lr} in Eq. 5.17 is a function of ε_r in Eq. 5.16, a model solution was obtained iteratively. The method of solution is given in Appendix G.3. In order to obtain model parameters (a, b, σ, ϕ) that were applicable to the airlift reactors in our laboratory, experimental work was required to generate a data set on which the model parameters could be obtained (via regression). The standard practice for measuring U_{Lr} and U_{Ld} is by using the tracer response technique already mentioned, but with the use of two identical probes placed a known vertical distance apart in the downcomer of the airlift reactor (Miron *et al.*, 2000). U_{Ld} is obtained from the time data corresponding to the difference between peaks from the two different probes' signals (Chisti, 1989). U_{Lr} could then be inferred from the continuity expression (Eq. 5.12). However, t_C can be estimated directly from U_{Lr}, as shown in Eq. 5.18, which arises from the fact that the average time for one complete liquid circulation should be equal to the reactor fluid volume divided by the liquid volumetric flow rate Q:

$$t_C = \frac{V}{Q} = \frac{V}{U_{Lr}A_r(1-\varepsilon_r)} \tag{5.18}$$

This observation gives a relationship between t_C and U_{Lr}. The hydrodynamic model defined by Eq. 5.15 to 5.17 can therefore be used to predict t_C (once U_{Lr} is calculated). Thus, parameters for the hydrodynamic model could be obtained from the regression of model predicted t_C values versus experimentally observed t_C values, over a range of superficial gas velocities. Instead of the traditional method, utilizing two probes to generate a U_{Lr} dependency on U_{Gr} data, only a single probe was required to measure t_C and estimate model parameters.

5.3 Materials and experimental methods

5.3.1 Airlift reactor and fluid

The experiments were conducted on a concentric draft-tube airlift reactor as shown in Fig. 5.2. The reactor had an internal diameter of 0.09 m and height of 0.6 m. The draft tube was 0.45 m in length with an internal diameter of 0.045 m. When accounting for the thickness of the glass, this riser to downcomer ratio A_r/A_d was 0.36. The draft tube was set a distance of 0.002 m from the bottom of the reactor and the gas free liquid height was approximately 0.536 m in all cases. The total fluid volume V was 3.2 liters. All other significant geometric details are noted in Fig. 5.2.

The influence of cell concentration on fluid viscosity for *Scenedesmus* only becomes significant at very high concentrations (> 150 g.L^{-1}), this is supported by Fig. 6.7 in Section 6.1.4. Since the viscosity of the algal suspension remains close to that of water during typical ALR operation (< 5 g.L^{-1}), distilled water was used as the circulating fluid for the experiments.

Air was used as the gas phase and the superficial gas velocity (U_{Gr}) was based on the cross sectional area of the riser (draft tube). The gas inlet flow rates tested ranged from 100 ml·min^{-1} to 5 L·min^{-1}, which corresponded to a range of U_{Gr} from 0.001 m·s^{-1} to 0.052 m·s^{-1}. The air sparger pore size was 0.22 μm. All measurements were conducted at a temperature of 23 ±1°C.

5.3.2 Measuring liquid circulation time t_C

The liquid circulation time was measured by means of a tracer response over time. A single conductivity probe (86505-pH/ORP/Cond./TDS/Salinity, AZ Instruments) was placed at a fixed location at the top and center of the reactor , as shown in Fig. 5.2. Five mililitre of 6M NaOH was used as tracer and was injected via a syringe through a metal tube into the downcomer, also also shown in Fig. 5.2. The amount and concentration of the tracer was determined by trial and error and was chosen so as to allow for a fast injection and to give a sufficient increase in conductivity, enabling adequate detection by the probe. Before each test, the reactor was aerated for ± 2 min and the conductivity was allowed to reach a stable state. After tracer injection, the time-changing conductivity response (in mS) was logged to a computer. The test was stopped once the conductivity reached a new higher stable state.

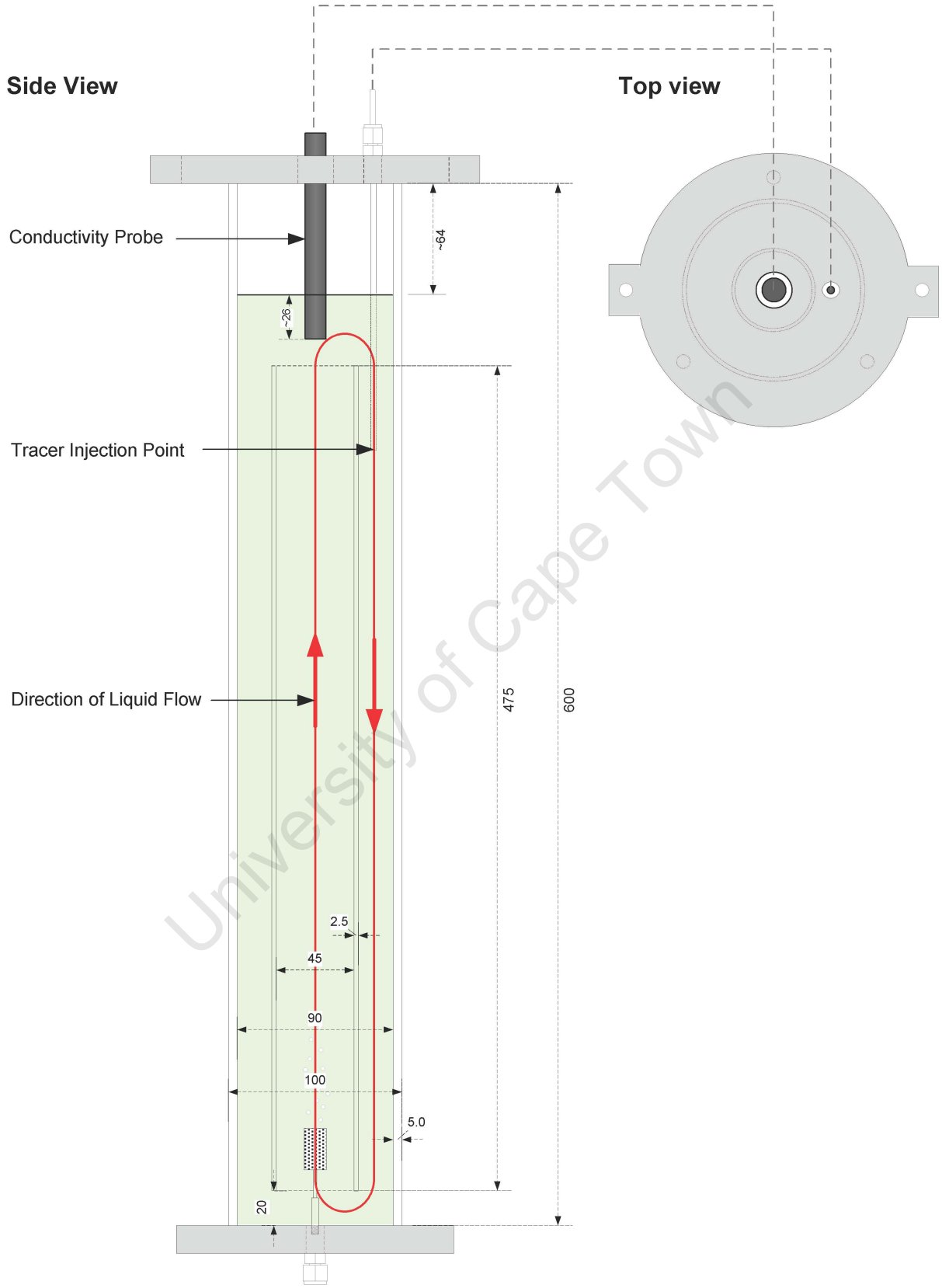

Figure 5.2 – Airlift reactor (internal loop) – All dimensions given in mm. Location of conductivity probe and tracer injection point shown. Image source: this author.

The response signals showed the typical damped oscillatory patterns characteristic of airlift reactors (Miron *et al.*, 2000; Chisti, 1989). An example of a typical from these experiments is shown in Fig. 5.3. Responses were normalized relative to the starting conductivity to give a dimensionless conductivity signal via the following calculation:

$$[C]_{t,normalized} = \frac{[C]_t - [C]_0}{[C]_\infty - [C]_0} \tag{5.19}$$

where $[C]_t$ is the instantaneous conductivity, and the subscripts 0 and ∞ denote the initial and final values respectively.

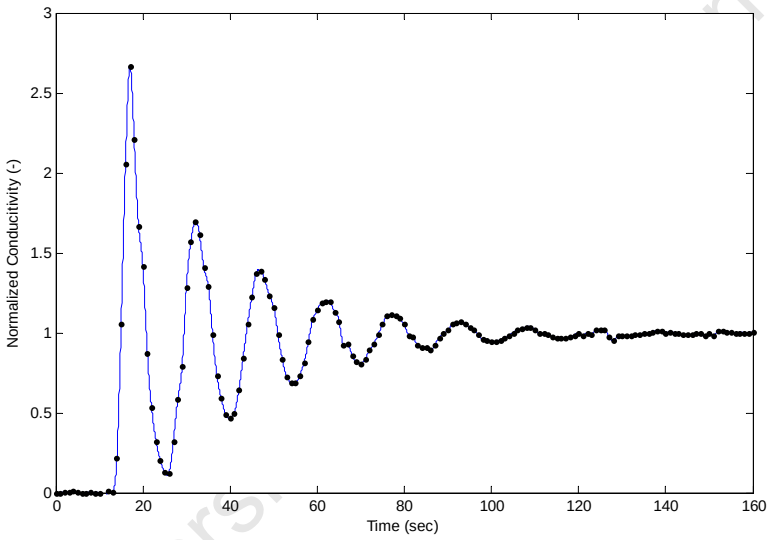

Figure 5.3 – Tracer response signal for Run 02, with $U_{Gr} = 2 \times 10^{-3}$ m·s^{-1}. Data relating to the calculation of all circulation times is given in Appendix H.5 with relevant error data.

The circulation time per loop t_C was calculated from the time interval between successive peaks. Since each run had between 3 and 7 peaks, a mean circulation time was obtained per run (Data given in Appendix H.5). The experiments were repeated between 3 and 7 times per gas flow rate to obtain quantification of the error in t_C values.

Note: After repeated additions of 6M NaOH, a reduction in bubble size was observed. Preliminary tests were done to determine the conductivity limit at which this occurred, which was found to be in the region of $[C] > 19$ mS , after which further additions of NaOH reduced the bubble size significantly. Changing bubble size has an effect on the gas hold-up and thus the hydrodynamic characteristics. Since the conductivity increased stepwise after each run (by approximately 2 mS per injection), care was taken to empty the reactor and replace the water when conductivity increased above this critical value.

5.4 Results and Discussion

5.4.1 Experimental results and model parameter fitting

The liquid circulation times determined in the experiments are shown in Fig. 5.4 and Table 5.2 as a function of gas flowrate and related superficial gas velocity. As expected, liquid circulation time decreases with increasing gas flow rate. At very high gas flow rates, further increases result in minimal decreases in liquid circulation time, which tended towards a saturation value.

Table 5.2 – Experimental results of average liquid circulation time t_C as a function of superficial gas velocity U_{gr}

F_{gas} (l.min^{-1})	U_{gr} (m.s^{-1})	t_C (s)	
0.1	0.00105	19.4	± 0.4
0.2	0.0021	15.9	± 1.9
0.4	0.0042	11.4	± 0.4
0.6	0.0063	9.5	± 0.3
0.8	0.0084	8.5	± 0.2
1.0	0.0105	7.9	± 0.4
1.2	0.0126	7.5	± 0.4
2.0	0.0210	6.6	± 0.2
3.0	0.0314	6.1	± 0.3
4.0	0.0419	5.6	± 0.1
5.0	0.0524	5.6	± 0.1

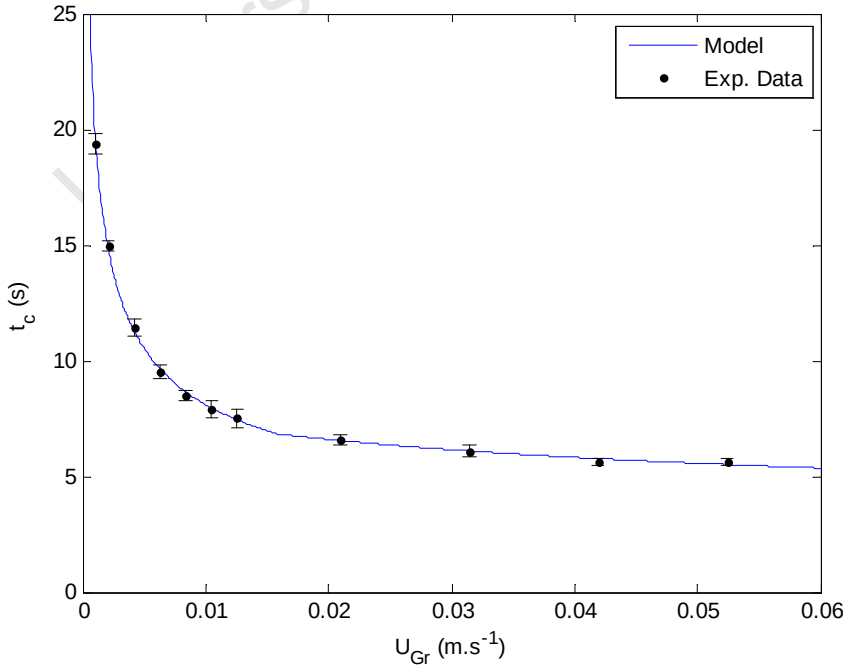

Figure 5.4 – Circulation time t_C as a function of superficial gas velocity U_{Gr}. Solid line shows model prediction.

The model was solved using MATLAB and the parameter regression was performed using a nonlinear least squares method. As explained in Section 5.2, all of the parameters were estimated from measurements of t_C data. A detailed solution algorithm is given in Appendix G.3. K_B had a value of 14.0 according to the geometry in Fig. 5.2. Table 5.3 shows the best-fit parameters obtained. The model predicts liquid circulation time in good accordance with the experimental data obtained, as shown by the model fit in Fig. 5.4.

Table 5.3 – Model parameters obtained by best-fit regression with 95% confidence intervals. Parameters for literature systems are shown for comparison.

Parameter	Value	95% Confidence	Literature	
σ	0.291	$\pm$0.141	0.24	Hills (1976)
ϕ	2.061	$\pm$0.948	1.35	Hills (1976)
a	0.633	$\pm$0.490	0.79	Bello *et al.* (1985)
b	0.011	$\pm$0.015	0.057	Bello *et al.* (1985)

Substituting the parameters obtained for the current system yields:

$$\varepsilon_r = \frac{U_{Gr}}{0.291 + 2.061\,(U_{Gr} + U_{Lr})} \tag{5.20}$$

and

$$\varepsilon_d = 0.633 \cdot \varepsilon_r - 0.011 \tag{5.21}$$

Values obtained from literature studies are presented in Table 5.3 to show that the parameters obtained are of a similar order of magnitude. Parameters obtained for these types of models are almost always unique to the system tested, such as the reactor dimensions (H and D_d etc) the properties of the fluids (water, seawater, biological media in other cases) which have different viscosities and the range of superficial gas velocities tested (up to $2\,\mathrm{m{\cdot}s^{-1}}$ in much larger airlift reactors).

5.4.2 Model simulation for negligible downcomer gas hold-up

Fig. 5.5 shows the model prediction of local gas hold-ups in the riser and downcomer regions. It is clear to see how ε_d remains zero until a critical ε_r of $\varepsilon_r = \frac{b}{a} = 0.174$. Without the necessary experimental means (manometers or tomography equipment) it was not possible to verify the models prediction of these hold-ups. The gas hold-up model of Popovic and Robinson (1984), given earlier in Eq. 5.3, is shown for comparison. The dashed line shows the model prediction, were the holdup in the downcomer assumed negligible ($\varepsilon_d = 0$) over the full range of superficial gas velocities. This is

a common assumption used when modelling hold-ups in airlift reactors (Contreras *et al.*, 1998) and one that was used by Wu & Merchuk (2004) in their global airlift model.

The assumption of negligible downcomer hold-up is illustrated further in Fig. 5.6 which shows a comparison of the the model's prediction of t_C with and without this assumption. The less accurate model prediction was performed by fitting new parameters[1] to the model with ε_d fixed at zero . The model predictions with $\varepsilon_d = 0$ are most inaccurate at high gas flow rates. At high gas flow rates, and concomitant high liquid circulation rates, there is sufficient hold-up in the downcomer to affect the liquid circulation. This arises when the liquid velocity is sufficiently fast to entrain bubbles from the riser into the downcomer, preventing their disengagement in the top section. Thus, the resultant increase in circulation velocity at high gas flow rates is less rapid than predicted with negligible hold-up (Fig. 5.6). The assumption of negligible gas hold-up is only valid at low gas flow rates. Above a critical velocity the trend deviates (Fig. 5.6). While this assumption of zero hold-up in the downcomer may approximate a laboratory-scale reactor, its extrapolation or use to simulate scale-up requires validation to prevent or estimate inaccuracies caused.

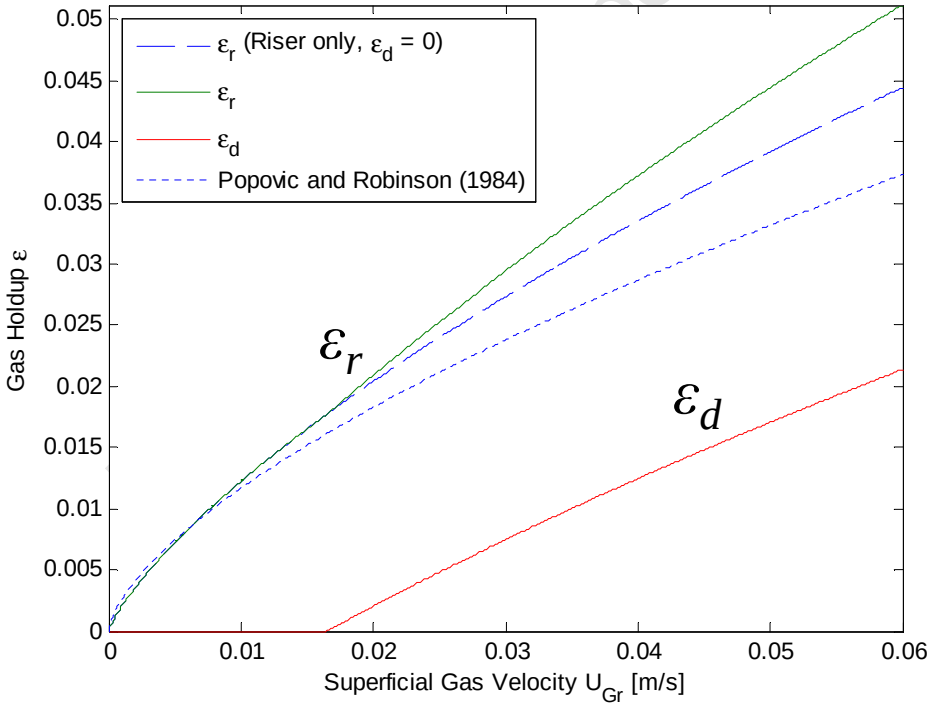

Figure 5.5 – Model prediction of local gas hold-ups, for riser ε_r and downcomer, ε_d. The dashed line shows the model prediction, were the holdup in the downcomer assumed negligible ($\varepsilon_d = 0$). The dotted line shows the Popovic and Robinson (1984) prediction and the remaining lines show the prediction from this model. The downcomer holdup in this model is zero until the critical point at which $\varepsilon_r \geq \frac{b}{a} \geq 0.174$.

[1]Fit with $\varepsilon_d = 0$ yielded $\sigma = 0.2067$, $\phi = 2.724$ and $a = 0.611$

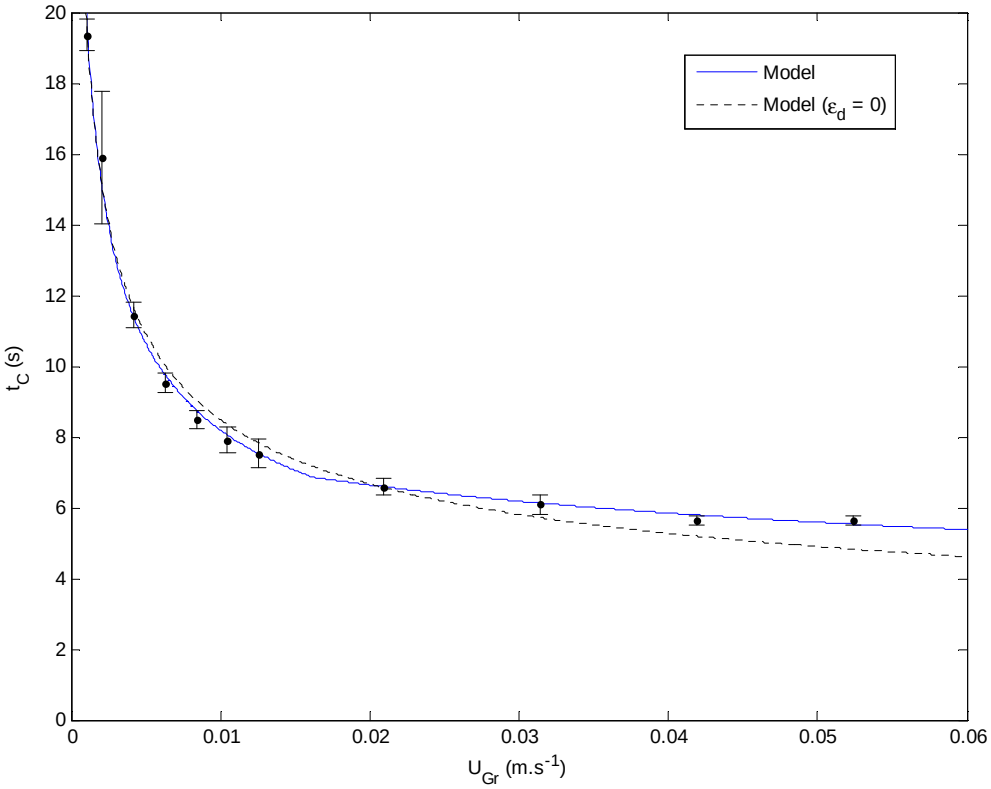

Figure 5.6 – Comparison between model prediction with and without downcomer hold-up. Dotted line is for $\varepsilon_d = 0$, generated by fitting new parameters to the model with ε_d fixed at zero.

5.4.3 Model simulation for varying A_r/A_d ratios

Control of light/dark cycles in an airlift reactor is most effectively achieved by adjusting the ratio of the downcomer to riser cross section areas, A_r/A_d. Since the system is bound by a volumetric flow balance (see Eq. 5.12), increasing the area available for flow in one region, say the riser, and consequently decreasing the area in the other (downcomer), causes a decrease in the velocity and in riser and a corresponding increase in the downcomer. These velocities directly affect the time spent by the cells in either the light or dark regions of the reactor and hence change the light/dark cycle characteristics.

To investigate these effects, the model simulated the cycle times that would result from a range of A_r/A_d ratios by varying the draft tube diameter, with the remaining reactor dimensions kept constant [2]. The light time t_l was calculated from reactor geometry according to:

$$t_l = \frac{H_d}{V_{Ld}} = \frac{H_d(1-\varepsilon_d)}{U_{Ld}} \tag{5.22}$$

where H_d was the draft tube length. Note: The relationship between light fraction and A_r/A_d is identical across all superficial gas velocities, since increasing the velocity increases the fluid velocity in the light (riser) and dark (downcomer) region equally. It is important to note that, for this simulation, one is assuming that the model parameters are NOT a function of A_r/A_d geometry.

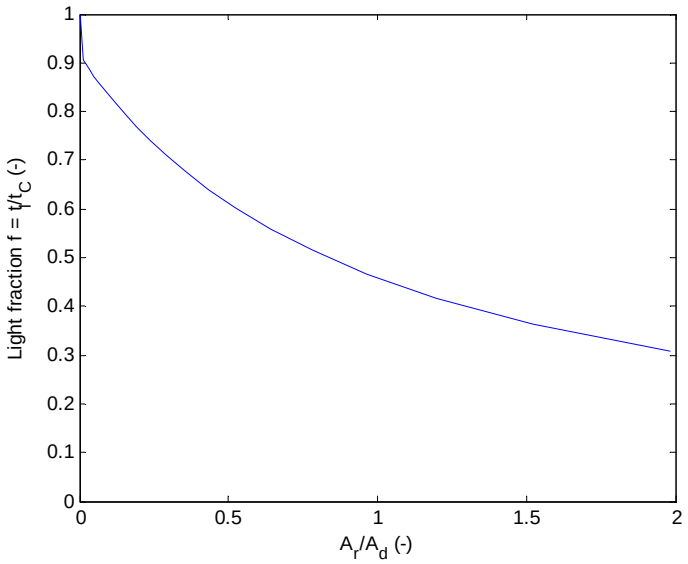

Figure 5.7 – The trend of $f = t_l/t_C$ as a function of A_r/A_d ratio for an airlift reactor of base dimensions: $D_c = 0.09$, $H_d = 0.475$, $H_0 = 0.6$ and $H_b = 0.02$ (m).

Fig. 5.7 gives the result of a typical trend for the assumed reactor dimensions. Note that $f \to 1$ as $A_r/A_d \to 0$, as expected. The model in its current formulation is undefined at A_r/A_d= 0, since no circulation would exist.

Using this result, one could design a reactor with a specific A_r/A_d ratio to operate at an exact light/dark ratio. The optimum light/dark fraction could be predetermined using the kinetic model and the optimum growth island simulation, as performed previously in Section 4.4.1. Subsequently, the optimum A_r/A_d ratio to achieve the optimum light/dark ration could be found via Fig. 5.7 rather than having to perform time consuming experiments..

[2] $D_{reactor} = 0.09$, $H_d = 0.475$, $H_r = 0.6$ and $H_b = 0.02$ (m)

5.5 Summary and conclusions for hydrodynamic model

- In order to generate light history and be able to integrate the kinetic model in a global airlift model, a description of a cell's movement inside an airlift reactor was needed. To achieve this, models for both gas hold-up and liquid circulation were required. The liquid circulation model of Chisti *et al.* (1988) and the gas hold-up model of Miron *et al.* (2000) were deemed applicable. The Chisti *et al.* (1988) approach is a superior approach to that used by Wu & Merchuk (2004) who used an outdated correlation of Popovic and Robinson (1984). The Gas-holdup model was improved to account for downcomer gas hold-up whereas Wu & Merchuk (2004) assumed this to be negligible.

- Measurements of circulation time (t_C) over a range of superficial gas velocities were used to enabled regression of best-fit model parameters (Fig. 5.4 and Table 5.3) as outlined in Section 5.4.1.

- Once defined, the model was analyzed with relevance to the common assumption of negligible downcomer gas hold-up (Fig. 5.6) to show the error in extrapolating this assumption to high gas flow rates. In addition, a simulation was performed to show how the model can be useful to aid in the design of photobioreactors with optimal A_r/A_d ratios to achieve optimum light/dark cycles (Fig. 5.7).

- This aim of developing this model is for later integration into a global model of an airlift reactor which incorporates both the light distribution and kinetic growth models. This development is done in Chapter 6.

Chapter 6

Global airlift model: development, results simulations and discussion

The methodology behind the development of the global airlift model was done according to Wu & Merchuk (2004) but with some modifications and improvements. The global model incorporated the three sub-models developed for light distribution (Chapter 3), algal growth kinetics as a function of light supply (Chapter 4) and hydrodynamics (Chapter 5). The light distribution and hydrodynamic models were completely different to those used by Wu & Merchuk (2004). Their choice was motivated by the limitations of the approaches used by Wu and Merchuk. The kinetic model employed (Chapter 4) used the form of the model of Eilers & Peeters (1988, 1993), later adapted by Wu & Merchuk (2001). New parameters were determined for *Scenedesmus* sp., based on its response to light provision, as outlined in Section 4.3.3

6.1 Global airlift model development

The compartmentalized approach according to Wu & Merchuk (2004) was used to integrate the kinetic model into the global airlift model. The fluid flows in a defined circulation pattern through regions defined by the geometry of the airlift (Fig. 6.1). Expressing the light histories of cells as they move through these regions requires a combination of the hydrodynamic model (Chapter 5) and light distribution model (Chapter 3). Sections 6.1.1 and 6.1.2 shows the development of the equations that define the light history of cells as they complete a cycle of the reactor, as illustrated schematically in Fig. 6.2. Section 6.1.3 deals with the integration of the kinetic model based on the light history to ultimately calculate growth rates. Section 6.1.4 concerns the issue of viscosity and shear stress.

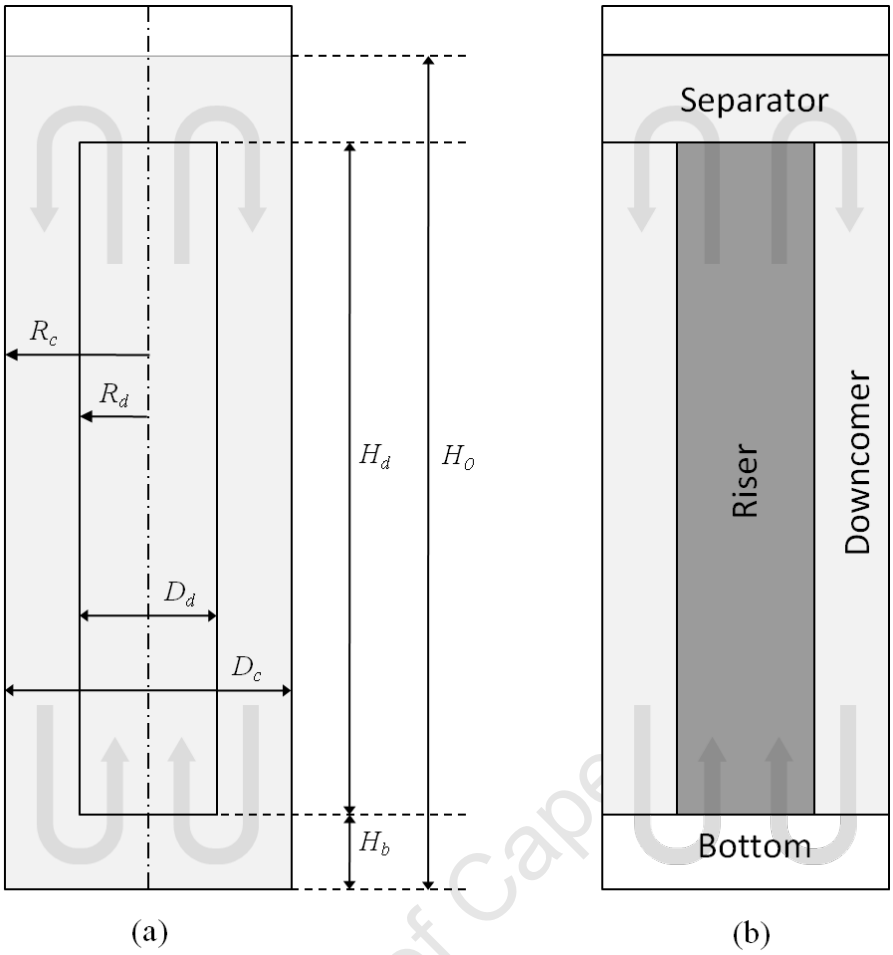

Figure 6.1 – Schematic of airlift giving dimension variables (a) and regions (b) defined by geometry. H_0 is gas-free liquid height, H_d is the draft tube height and H_b the bottom height, H_s the height of the separator. R_c and R_d are the radius of the outer column and draft tube, respectively, having diameters D_c and D_d.

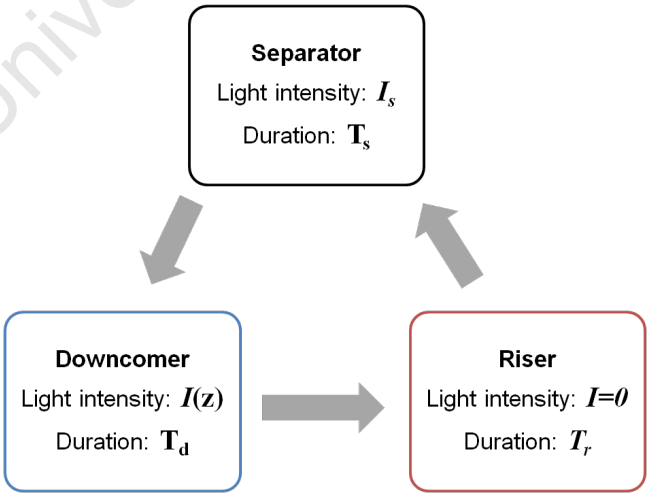

Figure 6.2 – Cyclic light history of cells in an airlift reactor, where T_s, T_d and $T_r$are the residence times per separator, downcomer and riser sections, respectively. Image source: this author, after Wu & Merchuk (2004).

6.1.1 Defining the times spent per reactor region

Firstly, the overall gas hold-up in the reactor is required to model the expansion of fluid volume from sparging. The overall holdup ε is calculated as a function of the hold-ups in the riser ε_r and downcomer ε_d (see Section 5.1.1):

$$\varepsilon = \frac{A_r\varepsilon_r + A_d\varepsilon_d}{A_r + A_d} \tag{6.1}$$

As a result of the fluid volume increasing during reactor operation, the height of the separator region, H_s, is variable and is calculated as a function of the gas-free liquid height, H_0, the airlift dimensions, H_d, H_b, and the overall gas hold-up, according to:

$$H_s = H_0(1+\varepsilon) - H_d - H_b \tag{6.2}$$

The residence times for the separator (T_s), downcomer (T_d) and riser (T_r) sections are calculated according to Equations 6.3, 6.4 and 6.5, respectively. The residence time in the bottom region was neglected since the time spent by a cell in passing between the downcomer and riser is negligibly small and assumed to be incorporated into T_d and T_r (Wu & Merchuk, 2004). The circulation time for one cycle is the sum of the three residence times, i.e. $t_C = T_s + T_r + T_d$.

$$T_s = \frac{H_s A(1-\varepsilon)}{Q_L} \tag{6.3}$$

$$T_d = \frac{H_d + H_b}{V_{Ld}} \tag{6.4}$$

$$T_r = \frac{H_d + H_b}{V_{Lr}} \tag{6.5}$$

where A is the cross sectional area of the outer column and ε is the overall gas hold-up, calculated from Eq. 6.1. V_{Ld} and V_{Lr} are the linear liquid velocities in the downcomer and riser, respectively. These are calculated from their respective superficial velocities according to:

$$V_{Ld} = \frac{U_{Ld}}{(1-\varepsilon_d)} \quad \text{and} \quad V_{Lr} = \frac{U_{Lr}}{(1-\varepsilon_r)} \tag{6.6}$$

Q_L in Eq. 6.3 is the liquid volumetric flow rate, calculated from the continuity balance:

$$Q_L = U_{Ld}A_d = V_{Lr}A_r(1-\varepsilon_r) = U_{Lr}A_d \tag{6.7}$$

The hydrodynamic model enables calculation of ε_r , ε_d ,U_{Ld} and U_{Lr} as a function of the superficial gas velocity U_{Gr}, according to Equations 6.8, 6.9 and 6.10, respectively. The hydrodynamic model development and method of solution is discussed in Chapter 5.

$$\varepsilon_r = \frac{U_{Gr}}{0.26 + 1.96\,(U_{Gr} + U_{Lr})^{0.93}} \tag{6.8}$$

$$\varepsilon_d = 0.64 \cdot \varepsilon_r - 0.011 \tag{6.9}$$

$$U_{Lr} = \sqrt{\frac{2gh_D(\varepsilon_r - \varepsilon_d)}{K_B \left(\frac{A_r}{A_d}\right)^2 \frac{1}{(1-\varepsilon_d)^2}}} \tag{6.10}$$

6.1.2 Defining the light distribution per reactor region

The light distribution in each region is calculated by incorporating the light distribution model developed in Chapter 3, which defines a light intensity (PFD) I at any position z from the airlift surface and any cell concentration C_x:

$$I(z, C_x) = \frac{2I_0}{\pi} \int_0^{\pi} exp\left[\frac{-K_{a,max} \cdot C_x \cdot s(z,\theta))}{(C_x + K_x)\,(s(z,\theta) + K_z)}\right] d\theta \tag{6.11}$$

Light profile in the downcomer using the concept of intervals

The continuous light distribution profile is simplified by using a step-shaped distribution (Wu & Merchuk, 2004). This is achieved by dividing the downcomer into intervals, each having a constant PFD determined from the light distribution model (Fig. 6.3). Because of the plug flow assumption, any individual cell that enters an interval at the top of the downcomer is assumed to stay in that interval and experience one PFD for its duration in the downcomer (T_d).

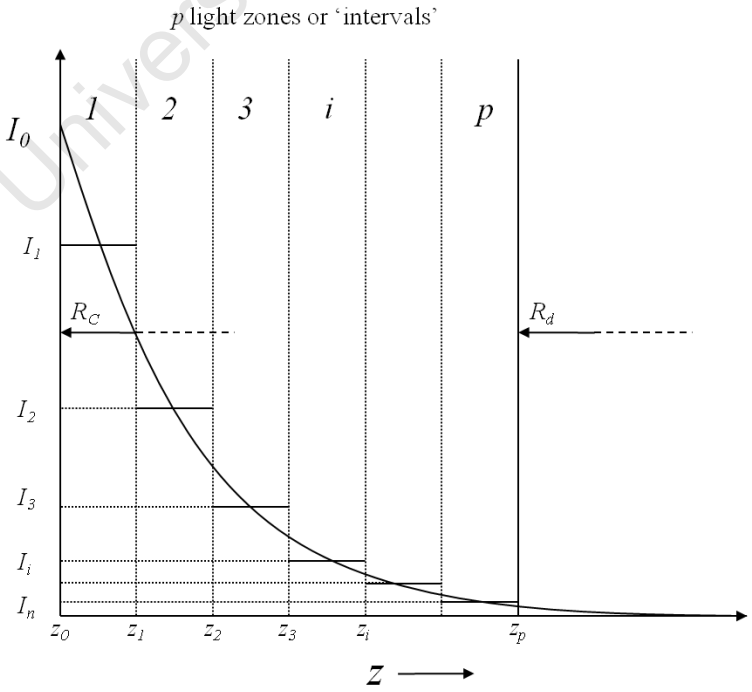

Figure 6.3 – Schematic showing step-wise light intervals of average PFD (I_i) for each light interval *i*.

A fixed number of intervals p are assumed, which start at $z_0 = 0$, the reactor outer surface, and end at $z_p = R_c - R_r$, the outer surface of the draft tube. A as $p \to \infty$ the step-shaped distribution approaches a continuous distribution and thus a larger value of p results in a higher model resolution. Fig. 6.4 shows a top view of for conceptualization

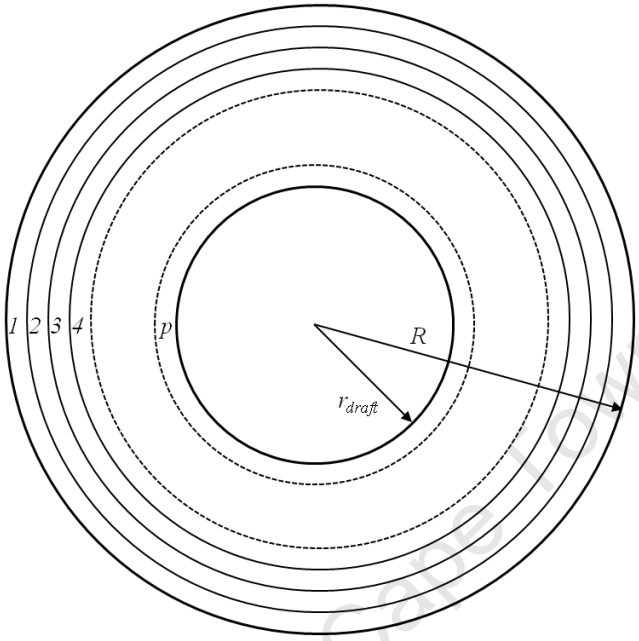

Figure 6.4 – Schematic showing top view of radial light zones in the airlift downcomer.

For each i^{th} light interval, an average PFD is calculated. The correct mathematical method of calculating this average is by using a true geometric mean, according to:

$$I_{ave,i} = \frac{2\int_{z_{i-1}}^{z_i}(R-z)I(z,C_x)dz}{(R-z_{i-1})^2-(R-z_i)^2} \quad (i = 1,2,...,p) \tag{6.12}$$

However, analytical integration of Eq. 6.12 is non-trivial[1] owing to the non-linear nature of the light distribution model $I(z,C_x)$ (Eq. 6.11). Numerical integration of Eq. 6.12 is trivial, but having to perform such an integration for every cycle would increase computational time considerably. This is because a single cycle is of order of magnitude 10 seconds, whereas the model simulates culture times of order of magnitude days, thus entailing ~90000 individual cycles. This issue can be overcome by realizing that the difference between the true geometric mean (Eq. 6.12) and an approximate trapezoidal mean is negligibly small. Fig. 6.5 illustrates how the trapezoidal rule approximates the light distribution function for each interval..

[1] Wu & Merchuk (2004) could obtain an analytical solution since they used linear Beer-Lambert law.

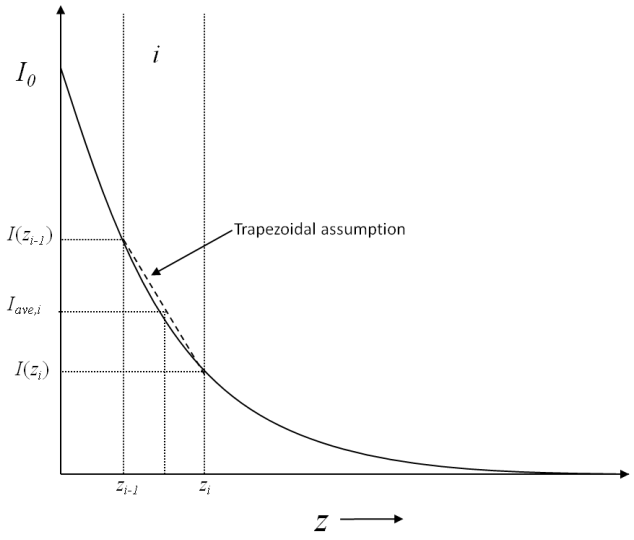

Figure 6.5 – Schematic showing how trapezoidal rule approximates the light distribution function across an interval.

The average PFD for the i^{th} light interval was thus approximated by applying the trapezoidal rule to Eq. 6.12, yielding:

$$\bar{I}_{d,i} = (z_i - z_{i-1}) \left[\frac{(R - z_{i-1}) \cdot I(z_{i-1}, C_x) + (R - z_i) \cdot I(z_i, C_x)}{(R - z_{i-1})^2 - (R - z_i)^2} \right] \quad (i = 1, 2, ..., p) \tag{6.13}$$

Derivation of Eq. 6.13 is given in Appendix F.3 along with an analysis to justify the negligible error between the two methods. The algal cells are assumed homogeneously distributed throughout the downcomer region (Wu & Merchuk, 2004) and thus, the fraction of cells $y(i)$ in each light interval i was calculated according to the relative area of each:

$$y(i) = \frac{(R_c - z_{i-1})^2 - (R_c - z_i)^2}{R_c^2 - R_d^2} \quad (i = 1, 2, ..., p) \tag{6.14}$$

As a side note, Wu & Merchuk (2004) varied the number of light zones p as the simulation progressed. At low biomass concentrations, and thus minimal light attenuation, a smaller number of light zones was used. As the biomass concentration increased, and the light decay increased to the point where the light intensity at the edge of the riser approached zero, the number of intervals increased, but not beyond a predetermined maximum p_{max}. The only conceivable reason for adopting this method was to reduce computational time, since less intervals required less calculations. Since computational power has advanced considerably since their publication, this author found this feature unnecessary. Instead, a fixed number of equally spaced intervals $p = 20$ was chosen.

Light profile in the riser:

The riser is assumed a dark zone (Wu & Merchuk, 2004). The analysis presented in the Light Model Chapter (Section 3.3.3) backs up this assumption by showing how rapidly light decays after just a few centimeters through an algal suspension. Thus, for the riser region:

$$I_{ave,r,i} = 0 \ \ (i = 1,2,...,p) \tag{6.15}$$

In this case the index i indicates that the cell originally came from interval i in the downcomer.

Light profile in the separator

The separator region is assumed perfectly mixed (Wu & Merchuk, 2004) such that all cells in the separator are exposed to an average PFD. This average can be calculated by integrating Eq. 6.11 over the full radius of the top section of the airlift:

$$\overline{I_s} = 2\int_0^{R_c} \frac{I(z,C_x)(R_c - z)dz}{R_c^2} \tag{6.16}$$

where R_c is the radius of the outer column. Wu & Merchuk (2004) obtained an analytical solution to Eq. 6.16 since they used simple Beer-Lambert law to model $I(z,C_x)$. Analytical integration of Eq. 6.11 using the dual asymptotic light distribution model for $I(z,C_x)$ is nontrivial and instead numerical means were used to evaluate the integral. Thus, for a homogeneous light intensity:

$$I_{s,i} = \overline{I_s} \ \ (i = 1,2,...,p) \tag{6.17}$$

6.1.3 Integrating the kinetic model

Sections 6.1.1 and 6.1.2 define the light history of cells travelling through any interval i between downcomer, riser and separator. The next step in simulating the global model is the integration of the kinetic model from Chapter 4.

The following development is based on that done by Wu & Merchuk (2004). A single cycle is defined by passage from the downcomer, to the riser to the separator and is denoted by index j. For each light interval i undergoing subsequent cycles j , the average growth rate per cycle is calculated via integration of the kinetic model. The number of cycles required for the simulation is defined by the length of each cycle (as a function of U_{Gr}) and the desired length of the simulation.

Values of PSF fractions x_1 and x_2 at the start of each cycle

The reader is referred to Section 4.1.1, in which the kinetic model equations are presented and a solution is given for integration over a single light/dark cycle, as well as successive cycles simulating cyclic steady-state. The integration of the model over cycles in an airlift reactor follows on from the same concepts. First, the values of the PSF fractions at the beginning of the first cycle for all intervals are:

$$x_{1,i}(0) = 1 \ \ (i = 1,2,...,p) \ \text{ at } j = 1 \tag{6.18}$$

$$x_{2,i}(0) = 0 \ \ (i = 1,2,...,p) \ \text{ at } j = 1 \tag{6.19}$$

Thereafter, the initial values of the PSF fractions at the beginning of a cycle are made equal to the average of all the fractions from the end point of the previous cycle, according to Equations 6.20 and 6.21. The reason for doing this is that the last region of a cycle is the separator, in which the suspension is assumed to be perfectly mixed, before moving back to the downcomer. Thus, cells of many different PSF values will find themselves distributed into various intervals in the downcomer for the next cycle. There is no way of knowing exactly how they are distributed and thus an average starting PSF fraction is assumed.

$$x_{1,i}(0) = x_1(0) = \overline{x_1} = \sum_{i=1}^{p} [y(i)x_{1,i}(T_s)] \tag{6.20}$$

$$x_{2,i}(0) = x_2(0) = \overline{x_2} = \sum_{i=1}^{p} [y(i)x_{2,i}(T_s)] \tag{6.21}$$

Integration for the downcomer region:

The method of deriving the model equations for a cycle have been given previously in Section 4.1. The variation between the expressions shown here and those shown previously involve the use of the index i to denote an equation applying to an interval i having average PFD $\bar{I}_{d,i}$. The profiles of x_1 and

x_2 for each light interval i in the downcomer are:

$$x_{1,d,i}(t) = \frac{c_i(\beta\bar{I}_{d,i}+\gamma) + b_i C_{1,i}(A_i+\beta\bar{I}_{d,i}+\gamma)e^{A_i t} + b_i C_{2,i}(B_i+\beta\bar{I}_{d,i}+\gamma)e^{B_i t}}{\alpha\bar{I}_{d,i}b_i} \tag{6.22}$$

$$x_{2,d,i}(t) = \frac{c_i}{b_i} + C_{1,i}e^{A_i t} + C_{2,i}e^{B_i t} \tag{6.23}$$

with $\bar{I}_{d,i}$ calculated from Eq. 6.13 and the constants a_i, b_i, c_i, A_i, B_i, $C_{1,i}$ and $C_{2,i}$ having unique values for each interval, according to:

$$a_i = \alpha\bar{I}_{d,i} + \beta\bar{I}_{d,i} + \gamma + \delta \tag{6.24}$$

$$b_i = \alpha\beta\bar{I}_{d,i}^2 + \delta\gamma + \alpha\bar{I}_{d,i}\delta + \beta\bar{I}_{d,i}I\delta \tag{6.25}$$

$$c_i = \alpha\bar{I}_{d,i}I\delta \tag{6.26}$$

$$B_i = -\frac{a_i - \sqrt{a_i^2 - 4b_i}}{2} \tag{6.27}$$

$$C_{1,i} = -\frac{B_i c_i - \alpha\bar{I}_{d,i}b_i x_1(0) + b_i x_2(0)(A_i+\beta\bar{I}_{d,i}+\gamma)}{b_i(A_i - B_i)} \tag{6.28}$$

$$C_{2,i} = -\frac{A_i c_i - \alpha\bar{I}_{d,i}Ib_i x_1(0) - b_i x_2(0)(A_i+\beta\bar{I}_{d,i}+\gamma)}{b_i(A_i - B_i)} \tag{6.29}$$

The values of x_1 and $x_2$at the end of the time in the downcomer are obtained by setting $t = T_d$ in Equations 6.22 and 6.23, respectively. The average growth rate in the i^{th}interval in the downcomer is given by:

$$\overline{\mu_{d,i}} = \frac{k\gamma}{T_d}\int_0^{T_d} x_{2,d,i}(t)dt - Me \tag{6.30}$$

Eq. 6.30 has the analytical solution according to Wu & Merchuk (2004):

$$\overline{\mu}_{d,i} = \frac{k\gamma}{T_d}\left[\frac{c_i}{b_i}T_d + \frac{C_{1,i}}{A_i}(e^{A_i T_d} - 1) + \frac{C_{2,i}}{B_i}(e^{BA_i T_d} - 1)\right] - Me \tag{6.31}$$

As a side note: Should a different kinetic model be used which has no analytical solution, such as the nonlinear form proposed by Rubio *et al.* (2003), Eq. 6.30 could be integrated numerically,

Integration for the riser region:

The riser is assumed a dark zone and thus $I = 0$. The profiles for x_1 and x_2 for each light interval i in the riser are obtained according to the method mentioned in Section 4.1.1:

$$x_{1,r,i}(t) = 1 - x_{2,i}(T_d)e^{-\gamma(t)} - (1 - x_{2,i}(T_d) - x_{1,i}(T_d))e^{-\delta(t)} \tag{6.32}$$

$$x_{2,r,i}(t) = x_{2,i}(T_d)e^{-\gamma(t)} \tag{6.33}$$

where $x_{1,i}(T_d)$ and $x_{2,i}(T_d)$ are the values of the PSFs at the end of the downcomer (i.e entering the riser). Here the index i denotes that the cells came from the i^{th} interval in the downcomer. The values

of x_1 and x_2 at the end of the time in the riser are obtained by setting $t = T_r$ in Equations 6.32 and 6.33, respectively. The average growth rate in the riser is:

$$\overline{\mu_{r,i}} = \frac{k\gamma}{T_r}\int_0^{T_r} x_{2,d,i}(t)dt - Me \tag{6.34}$$

which has the analytical solution according to Wu & Merchuk (2004):

$$\overline{\mu_{r,i}} = \frac{k\gamma}{T_r}x_{2,i}(T_d)\left(\frac{1-e^{-\gamma T_r}}{\gamma}\right) - Me \tag{6.35}$$

As mentioned previously for $\overline{\mu}_{d,i}$, Eq. 6.34 could be integrated numerically, should a non analytical method be used to obtain profiles for $x_{2,r}$.

Integration for the separator region:

The light intensity in the separator is assumed constant, $I = \overline{I_s}$ according to Eq. 6.16, thus it is assumed that all cells from all the intervals experience the same photosynthetic activity:

$$x_{1,s,i}(t) = \frac{c_i(\beta\overline{I_s}+\gamma) + b_iC_{1,i}(A_i+\beta\overline{I_s}+\gamma)e^{A_it} + b_iC_{2,i}(B_i+\beta\overline{I_s}+\gamma)e^{B_it}}{\alpha\overline{I_s}b_i} \tag{6.36}$$

$$x_{2,s,i}(t) = \frac{c_i}{b_i} + C_{1,i}e^{A_it} + C_{2,i}e^{B_it} \tag{6.37}$$

Again, the index i denotes cells having passed through interval i in the downcomer. For the separator region, the integration constants a_i, b_i, c_i, A_i, B_i, $C_{1,i}$ and $C_{2,i}$ are re-calculated according to Equations 6.24 to 6.29 by replacing $\overline{I}_{d,i}$ with $\overline{I_s}$ (from Eq. 6.16). The values of x_1 and x_2 at the end of the time in the separator are obtained by setting $t = T_s$ in Equations 6.36 and 6.37, respectively. The average growth rate in the separator is:

$$\overline{\mu_{s,i}} = \frac{k\gamma}{T_s}\int_0^{T_s} x_{2,s,i}(t)dt - Me \tag{6.38}$$

which has the analytical solution according to Wu & Merchuk (2004):

$$\overline{\mu}_{s,i} = \frac{k\gamma}{T_s}\left[\frac{c_i}{b_i}T_{sd} + \frac{C_{1,i}}{A_i}(e^{A_iT_s}-1) + \frac{C_{2,i}}{B_i}(e^{BA_iT_s}-1)\right] - Me \tag{6.39}$$

Biomass adjustment at the end of a cycle:

The biomass concentration C_x is assumed to remain constant over the duration of a cycle, and its value is adjusted at the end of each cycle. This can be justified by the fact that the circulation time for one cycle is of order of magnitude 6 seconds, whereas the doubling time of the algae *Scenedesmus* sp. is of order of magnitude hours[2]. The increase in biomass concentration for each region of a cycle can be calculated using the average growth rates and the fraction of cells per interval:

$$C_{x,T_d} = C_{x_j} \sum_{i=1}^{p} \left[e^{\overline{\mu_d} T_d} \cdot y(i) \right] \tag{6.40}$$

$$C_{x,T_r} = C_{x,T_d} \sum_{i=1}^{p} \left[e^{\overline{\mu_r} T_r} \cdot y(i) \right] \tag{6.41}$$

$$C_{x_{j+1}} = C_{x,T_r} \sum_{i=1}^{p} \left[e^{\overline{\mu_s} T_s} \cdot y(i) \right] \tag{6.42}$$

where $C_{x_{j+1}}$ and C_{x_j} are the biomass concentrations at the start and end of a complete cycle, and where C_{x,T_d} and C_{x,T_r} are the biomass concentrations at the end of the time in the downcomer and riser, respectively. Equations 6.40 to 6.42 can be combined to form one expression that adjusts the concentration per complete cycle:

$$C_{x_{j+1}} = C_{x_j} \sum_{i=1}^{p} \left[e^{\overline{\mu_d} T_d + \overline{\mu_r} T_r + \overline{\mu_s} T_s} \cdot y(i) \right] \tag{6.43}$$

The PSF values are then adjusted for the next cycle $(j+1)$, according to Equations 6.20 and 6.21. The updated biomass concentration $C_{x_{j+1}}$ is then used to define an updated light distribution profile. Each subsequent cycle then follows the same sequence of calculations until the sum of all the cycle times equals the simulation time. The model's entire process of calculations is summarized and represented schematically in Fig 6.6.

Assumption of constant biomass concentration across intervals

The model assumes a constant C_x *everywhere* in the bioreactor which is updated once per cycle. This constant C_x is used to define the light distribution function across *all* intervals. One might be concerned with the validity of this assumption, when considering that the intervals near the outside of the downcomer experience higher growth rates than the intervals near the center, since they experience more light. As a result, the biomass increases by different amounts for each interval leading to a radial concentration gradient. However, because the growth rates are of order of magnitude 0.01 to 0.06 hr^{-1}, and the actual time spent in the downcomer for each cycle is of order of magnitude seconds, this relative increase in the biomass is small and the concentration gradient is negligible.

[2]Doubling time = $\ln 2/\mu$, assuming the maximum growth rate obtained from the experiments (Table 4.9) of μ=0.143 h^{-1} gives a minimum doubling time of 4.8 hrs.

It is easier to illustrate this assumption using actual numbers. Table 6.1 shows growth rates for each interval for a single cycle during the model simulation[3]. All other conditions for this simulation are the same as those presented in Section 6.3. The starting concentrations for each interval are assumed to be equal (as a result of the perfectly mixed separator). The final concentration in each interval is calculated according to $C_{x,T_d,i} = C_{x0,i}e^{\mu_{d,i}T_d}$, where T_d is the time spent in the downcomer. There is clearly significant variation in the growth rates, with the intervals closer to the light source having the highest rates, however the data shows the relative change in the biomass to be negligible, since the duration of the time spent in the downcomer (T_d) is so relatively short (4.43 seconds).

Thus, for calculation of the light distribution function (which depends on C_x) the biomass can be assumed to have the same average value across *all* intervals in the downcomer. If the concentration gradients were found to be significant, then the light distribution function would have to be calculated based on local C_x values at each interval. It would also require that the model account for radial diffusion taking place across intervals. Luckily we can assume a constant C_x everywhere in the bioreactor and thus ignore both of these complications.

Table 6.1 – Typical data from the model to justify negligible C_x gradient. T_d = 4.43 seconds. $C_{x,T_d,i} = C_{x0,i}e^{\mu_{d,i}T_d}$

interval , i	$\mu_{d,i}$ (h^{-1})	$\mu_{d,i}$ (s^{-1})	$C_{x0,i}$	$C_{x,Td,i}$
1	0.0602	1.672E-05	0.1	0.1000074
2	0.0576	1.601E-05	0.1	0.1000071
3	0.0552	1.534E-05	0.1	0.1000068
4	0.0528	1.468E-05	0.1	0.1000065
5	0.0506	1.406E-05	0.1	0.1000062
6	0.0485	1.347E-05	0.1	0.1000060
7	0.0465	1.291E-05	0.1	0.1000057
8	0.0446	1.238E-05	0.1	0.1000055
9	0.0428	1.189E-05	0.1	0.1000053
10	0.0411	1.142E-05	0.1	0.1000051
11	0.0396	1.099E-05	0.1	0.1000049
12	0.0381	1.058E-05	0.1	0.1000047
13	0.0368	1.021E-05	0.1	0.1000045
14	0.0355	9.860E-06	0.1	0.1000044
15	0.0343	9.540E-06	0.1	0.1000042
16	0.0333	9.240E-06	0.1	0.1000041
17	0.0323	8.960E-06	0.1	0.1000040
18	0.0314	8.710E-06	0.1	0.1000039
19	0.0305	8.480E-06	0.1	0.1000038
20	0.0297	8.260E-06	0.1	0.1000037

[3]The maximum growth rates encountered across all cycles in the simulation were used.

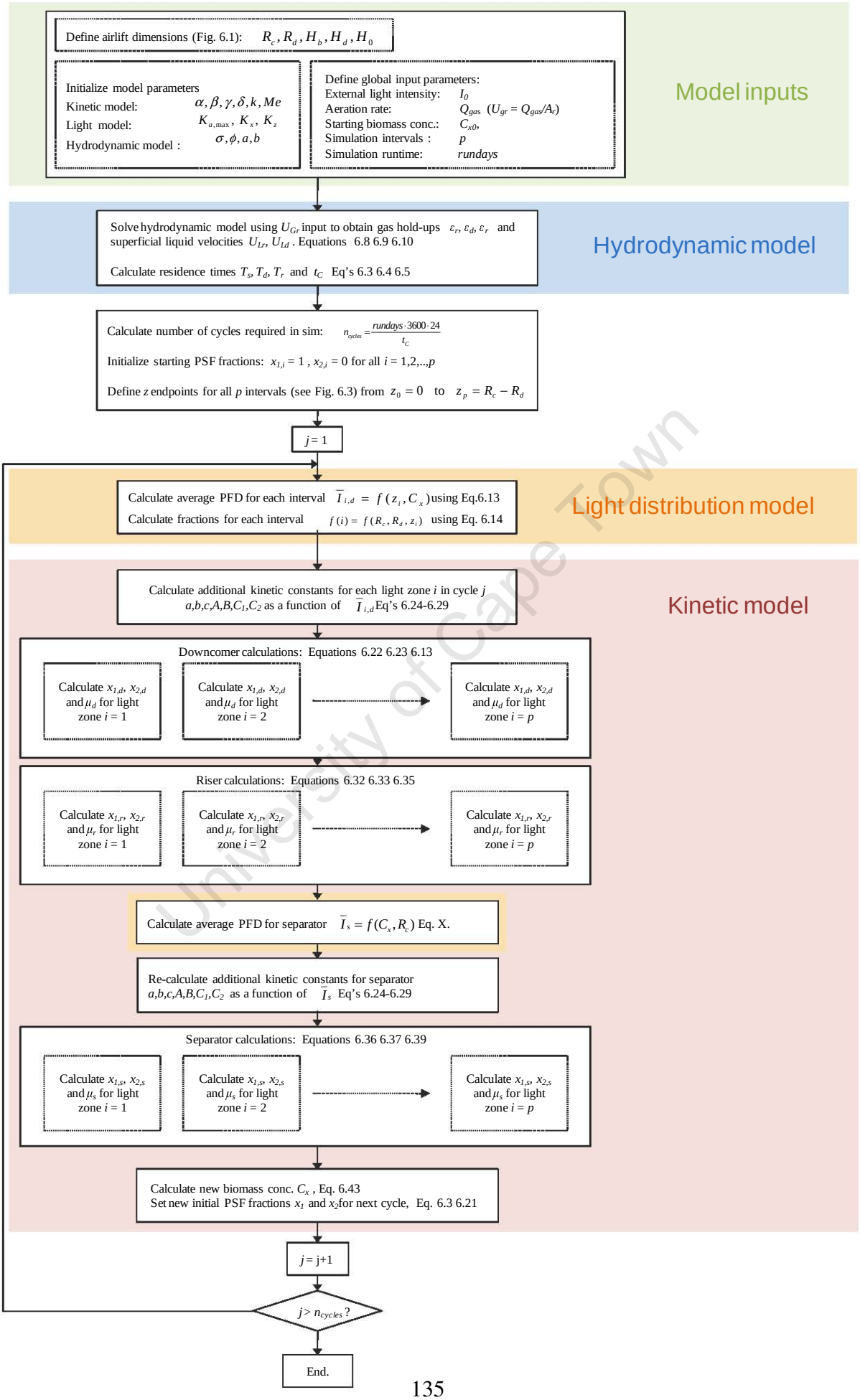

Figure 6.6 – Schematic summary of global airlift model calculations and method of solution.

6.1.4 The influence of viscosity and shear stress

Increase in biomass would have a small effect on fluid viscosity. Data obtained in our laboratory by Dicks (2010) showed the increase in viscosity for *Scenedesmus* to only become significant at very high cell concentrations (> 150 g.L^{-1}), as shown in Fig. 6.7. When considering the typical concentration that would be encountered in an ALR (< 5 g.L^{-1}) the viscosity could be assumed the same as water. Thus, any influence of slight changes in viscosity on the hydrodynamics were assumed negligible and ignored.

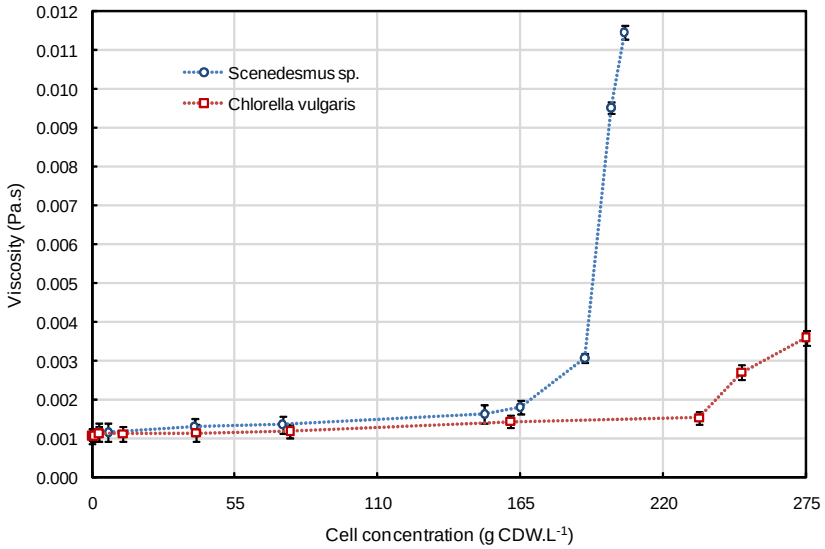

Figure 6.7 – Viscosity (Pa.s) as a function of cell concentration (g .L $^{-1}$) for *Scenedesmus* sp. and *Chlorella vulgaris*. Data source: Dicks (2010)

Algal cells can be damaged by shear stress caused by interactions with the reactor surfaces and fluid flow. The phenomenon is generally accepted to be as a result of two influences:

1. With increased aeration rate (increased superficial gas velocity), increased turbulence in the flow results in fluid micro eddy sizes approaching dimensions comparable to that of algal cells (Miron *et al.*, 1999). This has been found to occur at a critical aeration rate that is species and strain dependent.

2. Damage associated with the presence of bubbles (Eriksen, 2008; Barbosa *et al.*, 2003a; Miron *et al.*, 1999). It was traditionally thought that bubbles rising and bursting was responsible for cellular death, however Barbosa *et al.* (2004) showed that bubble formation at the sparger was the main effect contributing to shear damage.

It is difficult to decouple both these effects experimentally. Increasing aeration rates to produce different bubble dynamics effects micro eddy sizes. It is also beyond the scope of this project to attempt to model shear stress effects. The parameter in the developed kinetic model that allows simulation of

damage to cells (i.e negative growth) is the maintenance term Me. Thus, maintenance term was one of the adjusted parameters when fitting the global airlift model to experimental data since the shear environment in an airlift reactor would be notably different to that in thin tubular loop reactors.

6.2 Materials and methods

Experimental data from a 3.2 litre laboratory airlift was used to fit the global model

6.2.1 Airlift reactor and light environment

The glass and stainless steel internal loop airlift reactor used (Figures 6.8 and 6.9), was the same as that used for the experiment in Section 5.3.1 and had the same dimensions.

A 3% CO_2 and Air mixture was supplied at a volumetric flow of 2 L.min^{-1} controlled via a rotameters. This yielded a superficial gas velocity U_{Gr} of 0.021 m.s^{-1}. Light was supplied to the apparatus by 6 Osram 18 watt cool white fluorescent bulbs (Fig. 6.9) arranged in such a way as to provide light from all outer directions. 10 equally spaced measurements on the outer surface of the reactor using the spherical quantum sensor (see Section 3.2) gave an estimated average incident PFD (I_0) of 590 μmol$\cdot$m$^{-2}\cdot$s^{-1}.

All experiments were carried out in a room with a controlled temperature of 22$\pm$2 °C. A fan was used to maintain the temperature in the reactor at about 27°C.

6.2.2 Methods and sampling

The inoculum was cultivated according to the methods presented in Appendix B and the initial cell concentration was 0.051 g.L^{-1}. Samples were taken 2 to 3 times daily and measured in triplicate for optical density at 750 nm. Concentration (g.L^{-1}) was inferred from these readings via a calibration curve (Appendix C). The experimental run lasted ~ 9 days, by which time the culture had passed the stationary phase and cell concentration decreased.

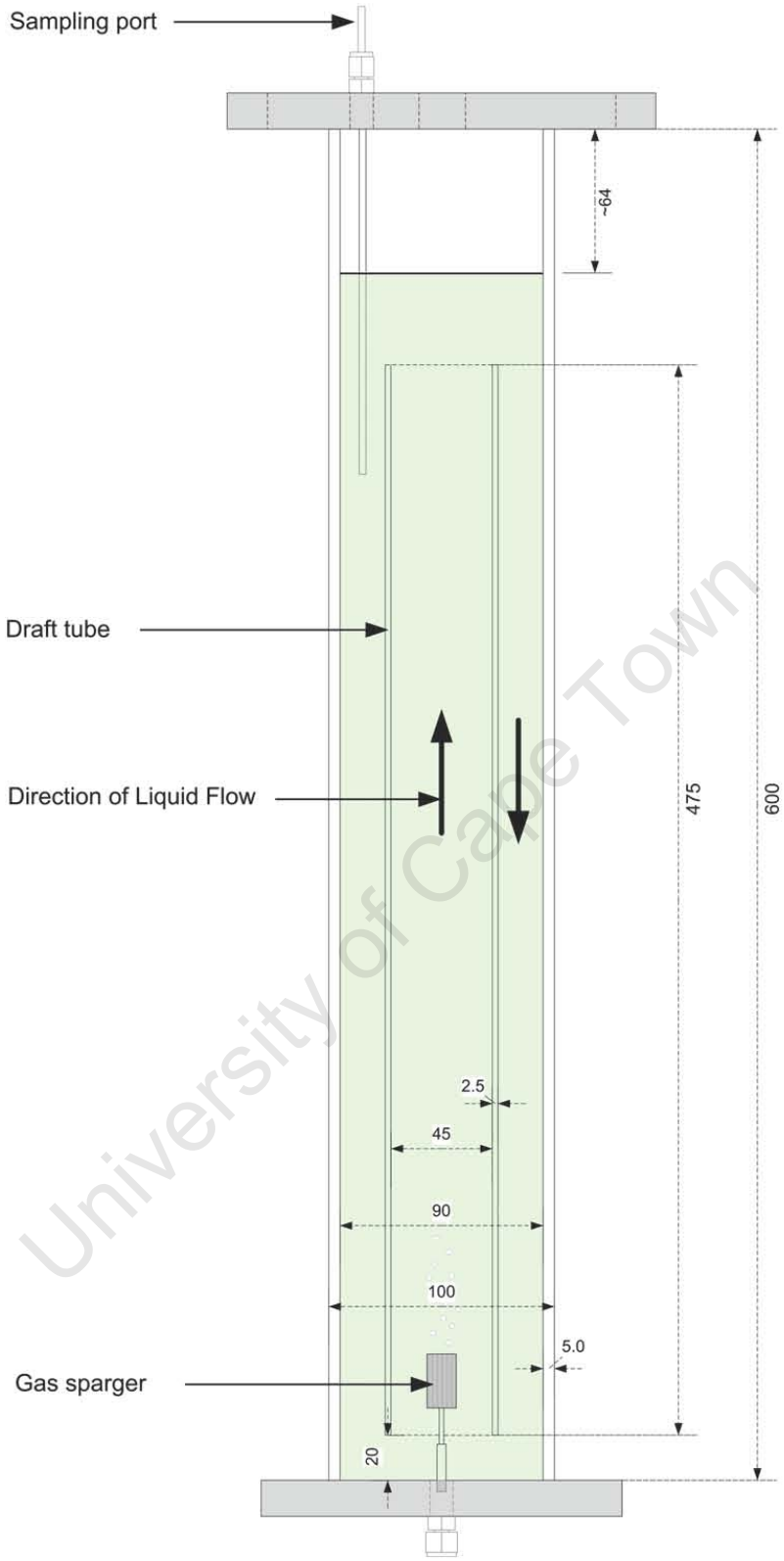

Figure 6.8 – Diagram of lab-scale 3.2 litre airlift reactor used for experiment.

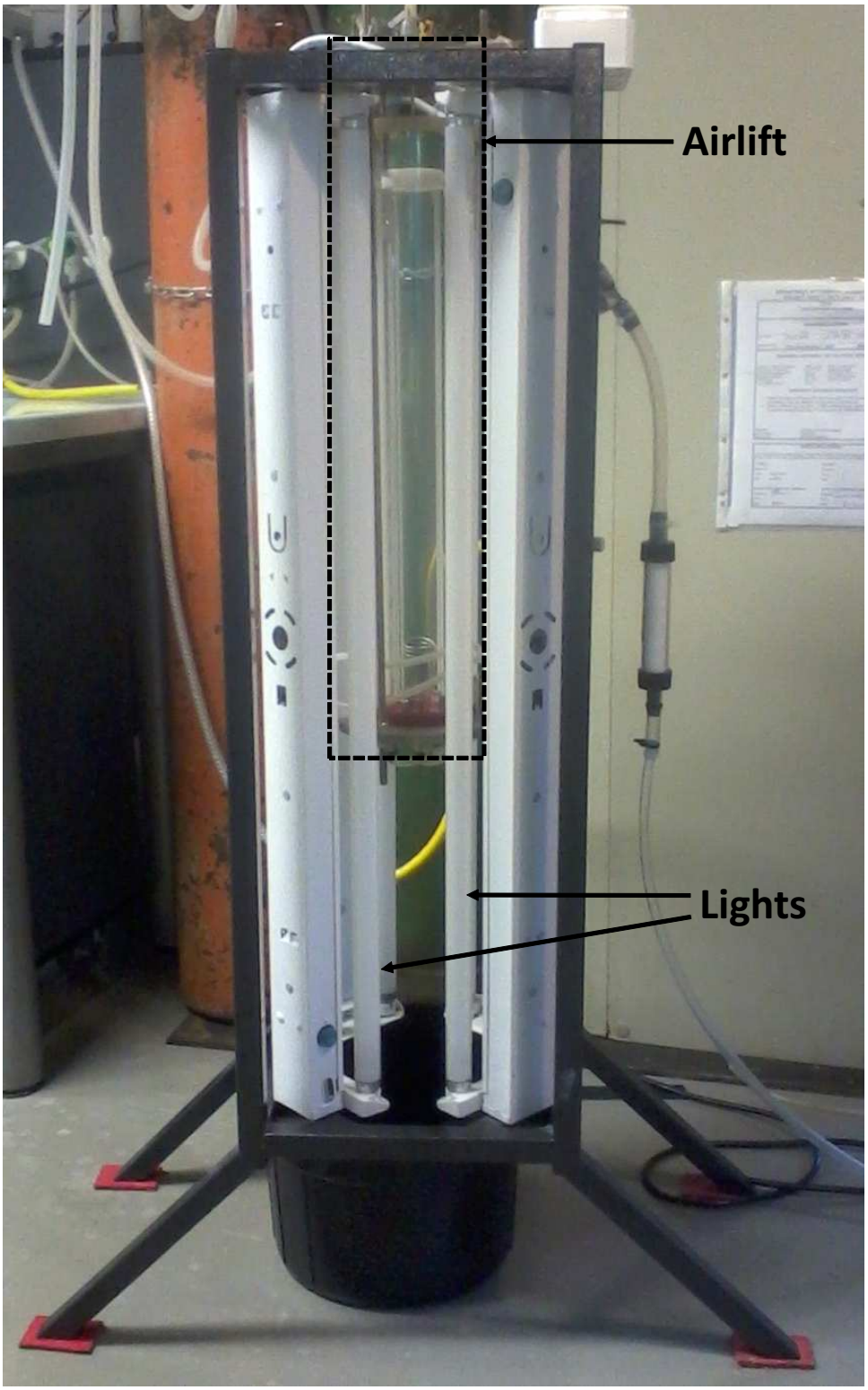

Figure 6.9 – Photograph of airlift reactor housed in light stand. Rectangular box shows location of airlift. For scale comparison, the box is 0.6 m in vertical length.

6.3 Results for global airlift model

6.3.1 Fitting model to experimental data

The model was simulated in MATLAB using the kinetic constants determined in Section 4.3.3 for the 21 second cycle time fit. In the experiment outlined in Section 5.3.1, the cycle time was 6.5 seconds (see Fig. 5.4). A 21 second cycle time could not be simulated in the laboratory airlift without the gas flow being too low to facilitate sufficient circulation and algal growth [4], as such the global model fit using the 21 second parameters was a proof of concept. Table 6.2 shows all additional model parameters and inputs used to emulate the real airlift used in the experiment (Section 5.3.1).

Table 6.2 – List of all input parameters for global airlift model simulation

Airlift Dimensions			
		Units	Description
R_c	0.090	m	Column diameter
R_d	0.045	m	Draft tube diameter
H_b	0.020	m	Bottom height
H_d	0.450	m	Draft tube height
H_0	0.536	m	Gas-free liquid height
Kinetic model parameters			
α	7.19E-04	$(\mu \text{mol. m}^{-2})^{-1}$	Kinetic rate constant of transfer $x_1 \rightarrow x_2$
β	1.40E-07	$(\mu \text{mol. m}^{-2})^{-1}$	Kinetic rate constant of transfer $x_2 \rightarrow x_3$
γ	0.097	s^{-1}	Kinetic rate constant of transfer $x_2 \rightarrow x_1$
δ	5.63E-03	s^{-1}	Kinetic rate constant of transfer $x_3 \rightarrow x_1$
Light model parameters			
$K_{a,max}$	83.9	(-)	Maximal absorption coefficent
K_x	7.51	g.L^{-1}	Constant for scattering from cells
K_z	9.53	cm	Constant for scattering from path length
Hydrodynamic model parameters			
σ	0.291	m.s^{-1}	Chisti liquid circulation model constant
Φ	2.061	(-)	Chisti liquid circulation model constant
a	0.633	(-)	Drift flux hold-up model constant
b	0.011	(-)	Drift flux hold-up model constant
Simulation inputs			
$C_{x,0}$	0.051	g.L^{-1}	Starting cell concentration
rundays	10	days	Simulation time
I_0	590	$\mu \text{mol. m}^{-2}\text{.s}^{-1}$	Incident light intenisity / PFD
Q_{gas}	2	L.min^{-1}	Aeration rate ($U_{gr} = Q_{gas}/A_r$)
p	20	(-)	Light intervals in downcomer

Two parameters were varied in order to fit the model to the experimental data: (i) the maintenance term Me, which simulates adjustments for shear stress; and the kinetic constant k, which relates the

[4] Consider Table 5.2. The maximum circulation time was 19.1 seconds for 0.1 L.min^{-1}.

rate of biomass production to the rate of PSF energy release (see Section 2.9.3). The regression was performed using the same nonlinear least squares method used for the regressions in Chapters 3,4 and 5. Table 6.3 shows the best-fit results for the two parameters and Fig. 6.10 shows the agreement between the model and the experimental data. The fitted model is successfully able to simulate the shape of the real growth curve.

Table 6.3 – Global model parameters obtained by best-fit regression with 95% confidence intervals.

Parameter	Value	95% Confidence
Me (h^{-1})	0.0407	±0.0050
k (-)	4.2502e-004	±3.9426e-005

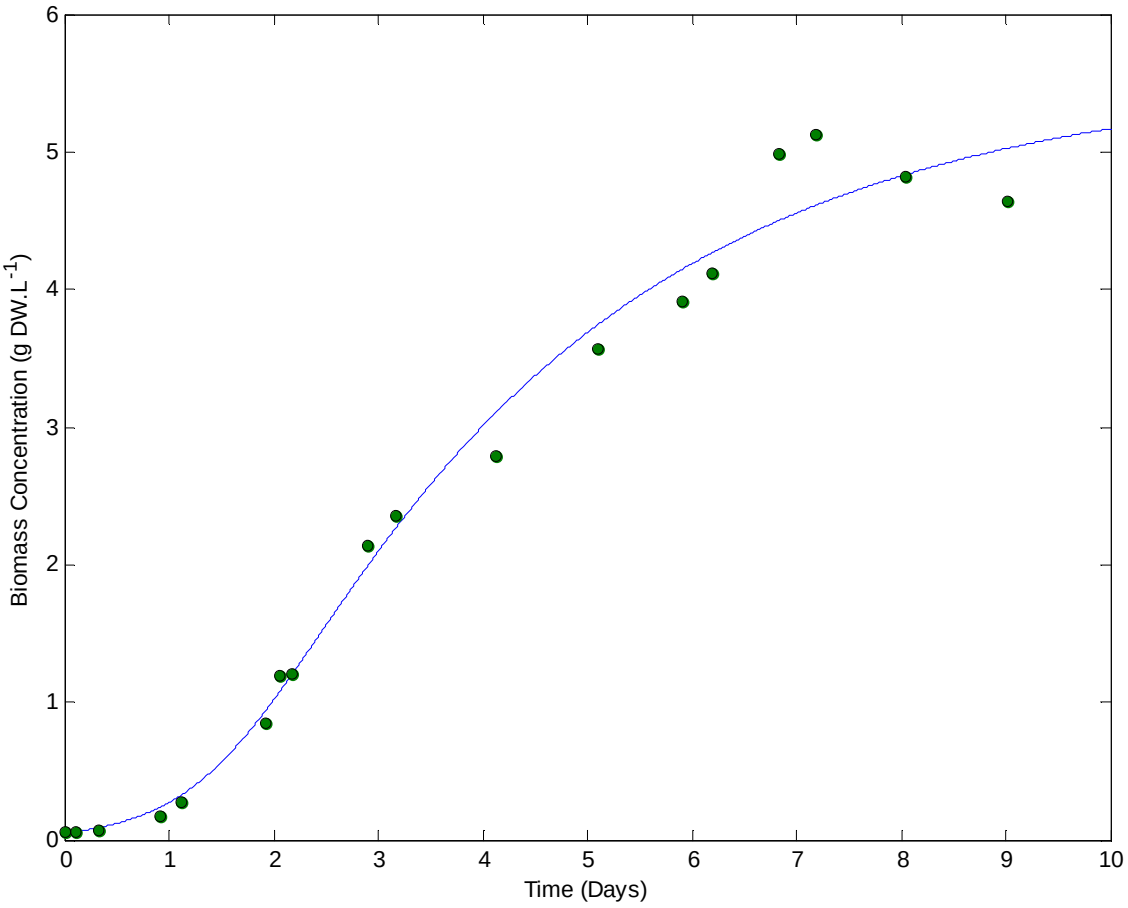

Figure 6.10 – Model simulation of biomass growth in an airlift photobioreactor (smooth line) with comparison to experimental data (dots). Raw data for growth points can be found in Appendix H.6.

6.3.2 Model sensitivity

Sensitivity to light input

The importance of an accurate and independently defined light distribution model was discussed in Chapter 3. The traditional Beer-Lambert law was shown to be inaccurate and a new dual asymptotic model was used and defined in an independent experiment.

The model was simulated for PFDs ranging from -20,-10,+10 and +20 % of the mean value of 590 μmol·m$^{-2}\cdot$s^{-1} to test the influence of the light distribution model on the overall growth curve. Fig. 6.11 shows the results and illustrates how changing the light environment in the reactor by as little as 10% has a significant effect on the overall result. Thus, an accurate light distribution model is extremely important in order to be confident in the global model's accuracy.

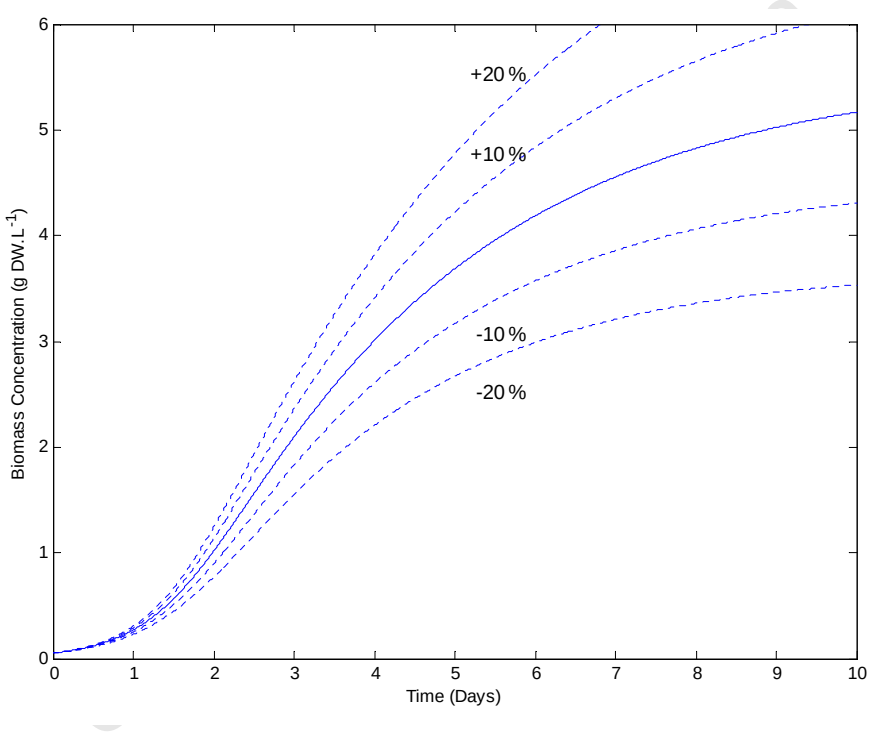

Figure 6.11 – Model simulation for increases and decreases in incident PFD from the base case of 590 μmol·m$^{-2}\cdot$s^{-1}

Sensitivity to fitted parameters

The model sensitivity to the two fitted parameters, k and Me, was investigated by testing these parameters at the boundary values defined by the 95% confidence intervals shown in Table 6.3. As expected, the larger k values and smaller Me values result a higher final biomass concentrations.

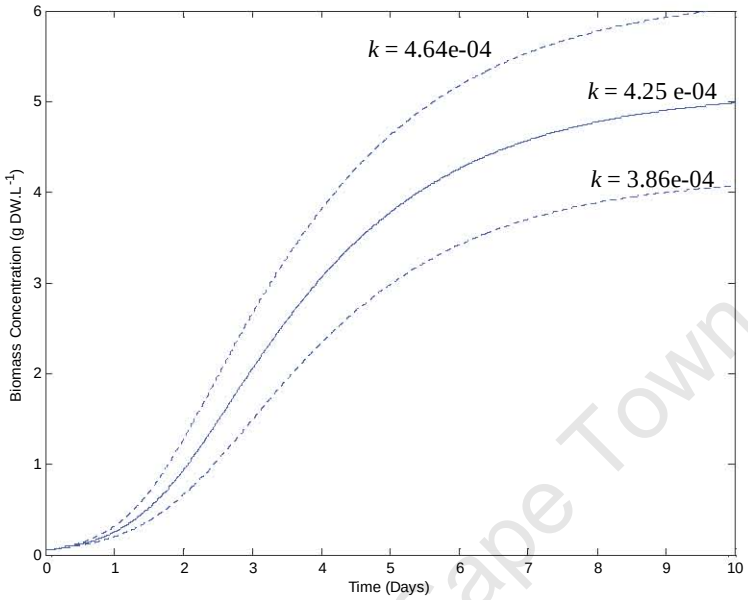

(a)

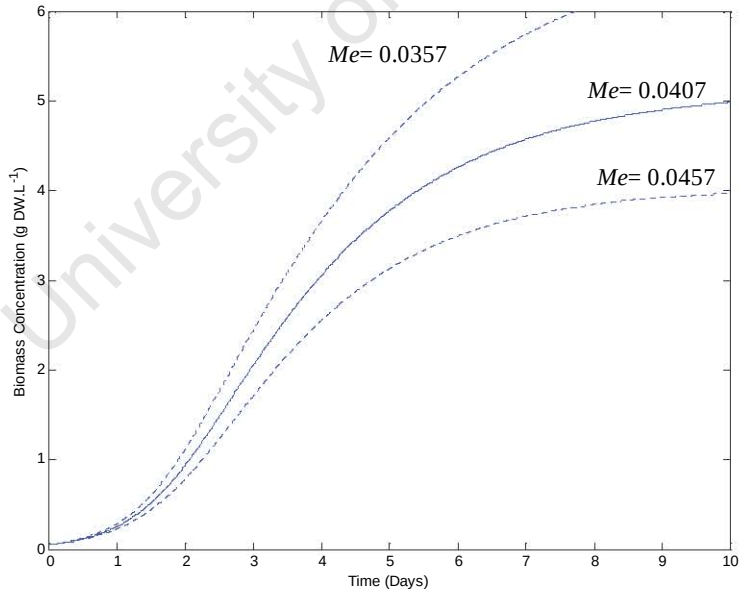

(b)

Figure 6.12 – Model sensitivity results for variations in k (6.12a) and Me (6.12b). Dotted lines represent the minimum and maximum values of the parameters defined by the 95% confidence intervals given in Table 6.3

6.4 Summary and conclusions for global airlift model

- Each of the models for (i) light distribution, (ii) kinetic growth and (iii) hydrodynamics from Chapters 3,4 and 5 were successfully integrated into a global model for an airlift reactor. This was achieved by using the compartmentalized approach of Wu & Merchuk (2004), which incorporated the concept of constant light intervals in the downcomer region.
- The model was fitted to experimental data via regression of two parameters (k and Me) and by making use of the kinetic parameters for the 21 second cycle time fit from Chapter 4 (Fig. 6.10).
- The influence of light input on the variation in results of the global model were analyzed (Fig. 6.11). As a result of the strong influence, the importance of an accurate light distribution model was stressed.

6.5 Recommendations

- Experimental data could be generated in airlift reactors for different incident PFDs (higher and lower than the PFD of 590 μmol·m$^{-2}\cdot$s^{-1}. tested) and the model's ability to simulate different growth curves analyzed. In addition, data could be generated at different input gas flow rates and compared to the model prediction. Furthermore, different sized airlift reactors could be constructed having different lengths or A_r/A_d ratios to generate more experimental data and build confidence in the model's predictions.
- In order for the global model to accurately predict algal growth and have good scalability to larger systems, it could incorporate a true Lagrangian description of cellular movement through the reactor. Such precise descriptions of cellular movement can either come from CFD modelling or from particle tracking data. A new student in our laboratory is starting a project that utilizes PEPT (Positron Emission Particle Tracking) to monitor the trajectories of algal cells in different photobioreactors. This presents a good opportunity for combining data with the existing light distribution model to generate accurate light histories using a similar approach to Luo & Al-Dahhan (2004). Subsequent combination with the PSF kinetic model could result in an improved global model of an airlift bioreactor. Since the PEPT data ca be obtained for any reactor type, the model could be applied to other reactor types by substitution of this data.

Chapter 7

Conclusions

This study has investigated the modelling of algal photobioreactors, with the airlift reactor as a case study. Three independent models for light distribution, kinetic growth and hydrodynamics have been developed, tested and analyzed. These three models were then successfully integrated into a global airlift model. The focus throughout has been on how the combination of light provision and fluid dynamics cause light/dark cycles which affect algal kinetic growth characteristics. The value of such a model it that enables the prediction of algal growth conditions as a function of changing model inputs and hence allows optima to be predicted.

The models developed build on the approach of Wu & Merchuk (2004), whereby exposure to light and light/dark cycling is accounted. The global model used a similar compartmentalized method of integrating the the three sub-models. In this work, the approach has been refined through selection of superior approaches to light distribution and hydrodynamics and expanded data and understanding on light/dark cycling and kinetic response.

In Chapter 3, the dual asymptotic empirical light model of Suh & Lee (2003) was adapted for this work and found to be successful at representing the light distribution profile for *Scenedesmus* sp. The failure of traditional Beer-Lambert law to predict this same profile was highlighted. The model results confirmed how scale-up of airlift reactors to larger diameters would be impractical owing to the increase in dark volumes, which would be unable to sustain photosynthetic growth. Instead, a number of smaller airlift reactors should be designed to satisfy a large volumetric production.

In Chapter 4, the PSF kinetic model of Wu & Merchuk (2001) was fitted to experimental data obtained from a light/dark cycle investigation. The reactor design was improved to study different cycle times. The data obtained illustrated key findings. Firstly, the growth trends across 21 and 33 cycle times (that of increasing growth with increasing light fraction) were in accordance with the results of Janssen (2002). Secondly, photoinhibition, was found to be influenced by cycle time. In the 45 second case, the longer light exposure time and insufficient dark recovery time resulted in inhibition whereas the shorter cycle times, having short light exposure time and frequent dark recovery, did not exhibit photoinhibition.

The model was fitted to data from each cycle time independently and to the combined data of 21 and 33 seconds, to produce a different set of parameters for each case. The model's description of the combined data of the 21 and 33 second cycle times was reasonable. However, the unrealistically small *Me* parameter from this fit suggested that further experimental investigation is required to test the model's applicability for variations in cycle time.

Simulations using the 21 second parameters set gave insight into extrapolated relationships between light fraction and PFD on growth. Most importantly, simulation of a positive growth island and constant growth contours showed how the model could be used as an effective tool for seeking the optimum PFD and light fraction in a photobioreactor to achieve light/dark cycles that optimized growth.

In Chapter 5, the hydrodynamic liquid circulation model of Chisti *et al.* (1988) and gas-holdup model from Miron *et al.* (2000) were fitted to experimental data obtained from tracer studies. The Chisti *et al.* (1988) approach is a model based on an energy balance, wheres the approach used by Wu & Merchuk (2004) incorporated an outdated correlation of Popovic and Robinson (1984). The gas hold-up model in this work used a better drift-flux approach and was also improved to account for downcomer gas hold-up, whereas Wu & Merchuk (2004) assumed this to be negligible. A good fit between the model prediction and the experimental data was found for the best-fit parameters (Section 5.4.1). Simulations of ignoring the gas hold-up in the downcomer showed inaccuracies when predicting circulation time at high superficial gas velocities (> 0.02 m.s^{-1}). This built confidence in the refined approach. The model was also used to represent the relationship between A_r/A_d ratio and light/dark fractions, to show how it could be used to aid in optimization of reactor design.

In Chapter 6, the three models were combined to develop a global airlift model, according to the approach used by Wu & Merchuk (2004). As a proof of concept, the model successfully represented laboratory airlift data by regression of two model parameters. The model was then analyzed for its sensitivity to light input and the high sensitivity found stressed the importance of an accurate light distribution model for photobioreactor modelling.

The three sub-models that were developed and tested in this work represent the three essential modelling components for any photobioreactor model. As such, the overall approach used in this study is relevant in that it contributes to the design and optimization of all algal photobioreactors. Specifically, it can contribute to the design of photobioreactors that are more light efficient, which is of critical importance to improving productivity, since light is the major limiting substrate. This is essential for making cost effective biodiesel and improving the feasibility of bioenergy processes.

Recommendations to be made for the integrated project as a whole involve testing the relevance of the kinetic model parameters across different algal species, with consideration to their light uptake rates and tolerance to photoinhibition. In addition, the model's overall approach could be extended to other reactor types by integration of a more general hydrodynamic model or combination with trajectory data (from PEPT or CFD). In this respect, the model could be used for more than just optimization but also to aid in appropriate reactor selection.

References

Aiba, S. 1982. Growth kinetics of photosynthetic micro-organisms. *Advances in Biochemical Engineering*, **23**, 85–156.

Barbosa, M. J., Albrecht, M., & Wijffels, R. H. 2003a. Hydrodynamic stress and lethal events in sparged microalgae cultures. *Biotechnology and Bioengineering*, **83**(1), 112–120.

Barbosa, M. J., Janssen, M., H., N., Tramper, J., & Wijffels, R. H. 2003b. Microalgae cultivation in air-lift reactors: Modeling biomass yield and growth rate as a function of mixing frequency. *Biotechnology and Bioengineering*, **82**(2), 170–179.

Barbosa, M. J., Hadiyanto, & Wijffels, R. H. 2004. Overcoming shear stress of microalgae cultures in sparged photobioreactors. *Biotechnology and Bioengineering*, **85**(1), 78–85.

Barsanti, Laura, & Gualtieri, Paolo. 2006. *Algae: Anatomy, Biochemistry, and Biotechnology*. CRC Press, Tayler & Francis Group.

Bello, R. A, Robinson, C. W., & Moo-Young, M. 1985. Prediction of the volumetric mass transfer coefficient in pneumatic contactors. *Chemical Engineering Science*, **40**(1), 53–58.

Berberoglu, H., Yin, J., & Pilon, L. 2007. Light transfer in bubble sparged photobioreactors for H2 production and CO2 mitigation. *International Journal of Hydrogen Energy*, **32**, 2273–2285.

Bruhn, A., Dahl, J., Nielsen, H. B., Nikolaisen, L., Rasmussen, M. B., Markager, S., Olesen, B., Arias, C., & Jensen, P. D. 2011. Bioenergy potential of Ulva lactuca: Biomass yield, methane production and combustion. *Bioresource Technology*, **102**, 2595–2604.

Camacho, F. Garcia, Gomez, A. Contreras, Fernandez, F. G. Acien, Sevilla, J. Fernandez, & Grima, E. Molina. 1999. Use of concentric-tube airlift photobioreactors for microalgal outdoor mass cultures. *Enzyme and Microbial Technology*, **24**, 164–172.

Carvalho, A. P., Meireles, L. A., & Malcata, F. X. 2006. Microalgal reactors: A review of enclosed system designs and performances. *Biotechnology Progress*, **22**, 1490–1506.

Chisti, M. Y., Halard, B., & Moo-Young, M. 1988. Liquid circulation in airlift reactors. *Chemical Engineering Science*, **43**(3), 451–457.

Chisti, Y. 1989. *Airlift Bioreactors*. Elsevier, London.

Chisti, Y. 2007. Biodiesel from microalgae. *Biotechnology Advances*, **25**, 294–306.

Chisti, Y. 2008. Biodiesel from microalgae beats bioethanol. *Trends in Biotechnology*, **26**(3), 126–131.

Chiu, S., Kao, C., Chen, C., Kuan, T., Ong, S., & Lin, C. 2008. Reduction of CO2 by a high-density culture of Chlorella sp. in a semicontinuous photobioreactor. *Bioresource Technology*, **99**(9), 3389–3396.

Contreras, A., Chisti, Y., & Molina, E. 1998. A reassesment of relationship between riser and downcomer gas holdups in airlift reactors. *Chemical Engineering Science*, **53**(24), 4151–4154.

Cornet, J.-F., Dussap, C. G., & Dubertret, G. 1992a. A structured model for simulation of cultures of the cyanobacterium *Spirulina platensis* in photobioreactors, I. Coupling between light transfer and growth kinetics. *Biotechnology and Bioengineering*, **40**, 817–825.

Cornet, J.-F., Dussap, C. G., Luzel, P. C., & Dubertret, G. 1992b. A structured model for simulation of cultures of the cyanobacterium *Spirulina platensis* in photobioreactors, II. Identification of kinetic parameters under light and mineral limitations. *Biotechnology and Bioengineering*, **40**, 826–834.

Cornet, J.-F., Dussap, C. G., & Gros, J. B. 1994. Conversion of radiant light energy in photobioreactors. *AIChE Journal*, **40**, 1055–1066.

Cornet, J.-F., Dussap, C. G., & Gros, J.-B. 1995. A simplified monodimensional approach to modeling coupling between radiant light transfer and growth kinetics in photobioreactors. *Chemical Engineering Science*, **50**(9), 1489–1500.

Csogor, Z., Herrenbauer, M., Perner, I., Schmidt, K., & Posten, C. 1999. Design of a photo-bioreactor for modeling purposes. *Chemical Engineering and Processing*, **38**, 517–523.

Danquaha, M. K., Gladman, B., Moheimani, N., & Fordea, G. M. 2009. Microalgal growth characteristics and subsequent influence on dewatering efficiency. *Chemical Engineering Journal*, **151**, 73–78.

Dicks, R. G. 2010. *Experimental data from CeBER Laboratory, Department of Chemical Engineering, University of Cape Town*. Unpublished.

Eilers, P. H. C., & Peeters, J. C. H. 1988. A model for the relationship between light intensity and the rate of photosynthesis in phytoplankton. *Ecological Modelling*, **42**, 199–215.

Eilers, P. H. C., & Peeters, J. C. H. 1993. Dynamic behaviour of a model for photosynthesis and photoinhibition. *Ecological Modelling*, **69**, 113–133.

Eriksen, N. T. 2008. The technology of microalgal culturing. *Biotechnology Letters*, **30**, 1525–1536.

Evers, E. G. 1991. A model for light-limited continuous cultures: Growth, Shading, and maintenance. *Biotechnology and Bioengineering*, **38**, 254–259.

Feng, W., Wen, J., Liu, C., Yuan, Q., Jia, X., & Sun, Y. 2007. Modeling of local dynamic behavior of phenol degradation in an internal loop airlift bioreactor by yeast *Candida tropicalis*. *Biotechnology and Bioengineering*, **97**(2), 251–264.

Fernandez, F. G. Acien, Camacho, F. Garcia, Perez, J. A. Sanchez, Sevilla, J. M. Fernandez, & Grima, E. Molina. 1997. A model for light distribution and average solar irradiance inside outdoor tubular photobioreactors for the microalgal mass culture. *Biotechnology and Bioengineering*, **55**(5), 701–714.

Fernandez, F. G. Acien, Sevilla, J. M. Fernandez, Perez, J. A. Sanchez, Grima, E. Molina, & Chisti, Y. 2001. Airlift-driven external-loop tubular photobioreactors for outdoor production of microalgae: assessment of design and performance. *Chemical Engineering Science*, **56**, 2721–2732.

Fleck-Schneider, P., Lehr, F., & Posten, C. 2007. Modelling of growth and product formation of *Porphyridium purpureum*. *Journal of Biotechnology*, **132**, 134–141.

Freitas, C., Fialova, M., Zahradnik, J., & Teixeira, J. A. 1999. Hydrodynamic model for three-phase internal and external-loop airlift reactors. *Chemical Engineering Science*, **54**, 5253–5258.

Garcin, C., Nicolls, F., Randall, B., Fraser, M., Griffiths, M., & Harrison, S. 2010. *Development of a low cost LED-photodiode based spectrophotometer for continuous on-line monitoring using optical flow cells*. WRC project K8/865.

Griffiths, M. J., & Harrison, S. T. L. 2009. Lipid productivity as a key characteristic for choosing algal species for biodiesel production. *Journal of Applied Phycology*, **21**, 492–507.

Griffiths, M. J., Garcina, C., van Hill, R. P., & Harrison, S.T.L. 2011a. Interference by pigment in the estimation of microalgal biomass concentration by optical density. *Journal of Microbiological Methods*, **Article in Press**.

Griffiths, M. J., L., S. T., & and, Rob. V. Hill. 2011b. Work and publication in progress.

Grima, E. Molina, Camacho, F. Garcia, Perez, J. A. Sanchez, Fernandez, F. G. Acien, & Sevilla, J. M. Fernandez. 1997. Evaluation of photosynthetic efficiency in microalgal cultures using averaged irradiance. *Enzyme and Microbial Technology*, **21**, 375–381.

Grima, E. Molina, Fernandez, F.G. Acien, Camacho, F. Garcia, & Chisti, Y. 1999. Photobioreactors: Light regime, mass transfer, and scaleup. *Journal of Biotechnology*, **70**, 231–247.

Grobbelaar, J. U. 1989. Do light/dark cycles of medium frequency enhance phytoplankton productivity? *Journal of Applied Phycology*, **1**, 333–340.

Grobbelaar, J. U. 1991. The influence of light/dark cycles in mixed algal cultures on their productivity. *Bioresource Technology*, **38**(2-3), 189–194.

Grobbelaar, J. U. 1994. Turbulence in mass algal cultures and the role of light/dark fluctuations. *Journal of Applied Phycology*, **6**, 331–335.

Grobbelaar, J. U. 2000. Physiological and technological considerations for optimising mass algal cultures. *Journal of Applied Phycology*, **12**, 201–206.

Gumery, F., Ein-Mozaffari, F., & Dahman, Y. 2009. Characteristics of local flow dynamics and macro-mixing in airlift column reactors for reliable design and scale-up. *International Journal of Chemical Reactor Engineering*, **7**, 1–47.

Han, B. 2001. Photosynthesis - Irradiance response at physiological level: a mechanistic model. *Journal of Theoretical Biology*, **213**, 121–127.

Han, B. 2002. A mechanistic model of algal photoinhibition induced by photodamage to photosystem-II. *Journal of Theoretical Biology*, **214**, 519–527.

Hills, J. H. 1976. The operation of a bubble column at high throughputs : I. Gas holdup measurements. *The Chemical Engineering Journal*, **12**(2), 89–99.

Iehana, M. 1983. Kinetic analysis of the growth of *Spirulina* sp. on continuous culture. *Journal of Fermentation Technology*, **61**, 457–466.

Jacob-Lopes, E., Scoparo, C. H. G., Lacerda, L. M. C. F., & Franco, T. T. 2009. Effect of light cycles (night/day) on CO2 fixation and biomass production by microalgae in photobioreactors. *Chemical Engineering and Processing*, **48**, 306–310.

Janssen, M., Kuijpers, T. Chris, Veldhoen, B., Ternbach, M. B., Tramper, J., Mur, L. R., & Wijffels, R. H. 1999. Specific growth rate of *Chlamydomonas reinhardtii* and *Chlorella sorokiniana* under medium duration light:dark cycles: 13 - 87 s. *Journal of Biotechnology*, **70**, 323–333.

Janssen, M., Tramper, J., Mur, L. R., & Wijffels, R. H. 2003. Enclosed outdoor photobioreactors: Light regime, photosynthetic efficiency, scale-up, and future prospects. *Biotechnology and Bioengineering*, **81**(2), 193–210.

Janssen, Marcel. 2002. *Cultivation of microalgae: effect of light/dark cycles on biomass yield*. Ph.D. thesis, Wageningen University, Wageningen, The Netherlands.

Jin, H., Yang, S., Wang, M., & Williams, R.A. 2007. Measurement of gas holdup profiles in a gas liquid co-current bubble column using electrical resistance tomography. *Flow Measurement and Instrumentation*, **18**, 191–196.

Kaewpintong, K., Shotipruk, A., Powtongsook, S., & Pavasant, P. 2007. Photoautotrophic high-density cultivation of vegetative cells of Haematococcus pluvialis in airlift bioreactor. *Bioresource Technology*, **98**, 288–295.

Korpijarvi, J., Oinas, P., & Reunanen, J. 1999. Hydrodynamics and mass transfer in an airlift reactor. *Chemical Engineering Science*, **54**(13-14), 2255–2262.

Kunjapur, A. M., & Eldridge, R. B. 2010. Photobioreactor design for commercial biofuel production from microalgae. *Industrial & Engineering Chemistry Research*, **49**, 3516–3526.

Lee, Y., & Pirt, S. J. 1981. Energetics of photosynthetic algal growth: influence of intermittent illumination in short (40 s) cycles. *Journal of General Microbiology*, **124**, 43–52.

Luo, H.-P., & Al-Dahhan, M. H. 2004. Analyzing and modeling of photobioreactors by combining first principles of physiology and hydrodynamics. *Biotechnology and Bioengineering*, **85**(4), 382–393.

Luo, H.-P., & Al-Dahhan, M. H. 2008a. Local characteristics of hydrodynamics in draft tube airlift bioreactor. *Chemical Engineering Science*, **63**, 3057–3068.

Luo, H.-P., & Al-Dahhan, M. H. 2008b. Macro-mixing in a draft-tube airlift bioreactor. *Chemical Engineering Science*, **63**, 1572–1585.

Luo, H.-P, & Al-Dahhan, M H. 2010. Local gas holdup in a draft tube airlift bioreactor. *Chemical EngineeringScience*, **65**(15), 4503–4510.

Luo, H.-P., Kemouna, A., Al-Dahhana, M. H., Sevilla, J. M. F., Sanchez, J. L. G., Camacho, F. G., & Grima, E. M. 2003. Analysis of photobioreactors for culturing high-value microalgae and cyanobacteria via an advanced diagnostic technique: CARPT. *Chemical Engineering Science*, **58**, 2519–2527.

Marshall, J.S., & Huang, Y. 2010. Simulation of light-limited algae growth in homogeneous turbulence. *Chemical Engineering Science*, **65**, 3865–3875.

Matsuura, T., & Smith, J. M. 1970. Light distribution in cylindrical photoreactors. *AIChE Journal*, **16**(2), 321–324.

Merchuk, J. C., Ronen, M., Giris, S., & Arad, S. 1998a. Light/dark cycles in the growth of the red microalga *Porphyridium sp. Biotechnology and Bioengineering*, **59**(6), 705–713.

Merchuk, J. C., Contreras, A., Garcia, F., & Molina, E. 1998b. Studies of mixing in a concentric tube airlift bioreactor with different spargers. *Chemical Engineering Science*, **53**(4), 709–719.

Merchuk, J. C., Garcia-Camacho, F., & Molina-Grima, E. 2007. Photobioreactor design and fluid dynamics. *Chemical and Biochemical Engineering Quarterly*, **21**(4), 345–355.

Merchuk, J.C, Gluz, M., & Mukmenev, I. 2000. Comparison of photobioreactors for cultivation of the red microalga *Porphyridium sp.* *Journal of Chemical Technology and Biotechnology*, **75**, 1119–1126.

Miron, A. Sanchez, Gomez, A. Contreras, Camacho, F. Garcia, Grima, E. Molina, & Chisti, Y. 1999. Comparative evaluation of compact photobioreactors for large-scale monoculture of microalgae. *Journal of Biotechnology*, **70**, 249–270.

Miron, A. Sanchez, Camacho, F. Garcia, Gomez, A. Contreras, Grima, E. Molina, & Chisti, Y. 2000. Bubble-column and airlift photobioreactors for algal Culture. *AIChE Journal*, **46**(9), 1872–1887.

Miron, A. Sanchez, Garcia, M. Ceron, Camacho, F. Garcia, Grima, E. Molina, & Chisti, Y. 2002. Growth and biochemical characterization of microalgal biomass produced in bubble column and airlift photobioreactors: Studies in fed-batch culture. *Enzyme and Microbial Technology*, **31**, 1015–1023.

Molina, E., Fernandez, J., Acien, F.G., & Chisti, Y. 2001. Tubular photobioreactor design for algal cultures. *Journal of Biotechnology*, **92**, 113–131.

Muller-Feuga, A., Guedes, R. Le, & Pruvost, J. 2003. Benefits and limitations of modeling for optimization of *Porphyridium cruentum* cultures in an annular photobioreactor. *Journal of Biotechnology*, **103**, 153–163.

Nedbal, L., Tichy, V., Xiong, F., & Grobbelaar, J. U. 1996. Microscopic green algae and cyanobacteria in high-frequency intermittent light. *Journal of Applied Phycology*, **8**, 325–333.

Park, K., & Lee, C. 2000. Optimization of algal photobioreactors using flashing lights. *Biotechnology and Bioprocess Engineering*, **5**, 186–190.

Park, K., & Lee, C. 2001. Effectiveness of flashing light for increasing photosynthetic efficiency of microalgal cultures over a critical cell density. *Biotechnology and Bioprocess Engineering*, **6**, 189–193.

Perner-Nochta, I., & Posten, C. 2007. Simulations of light intensity variation in photobioreactors. *Journal of Biotechnology*, **131**, 276–285.

Pottier, L., Pruvost, J., Deremetz, J., Cornet, J.-F., Legrand, J., & Dussap, C.G. 2005. A fully predictive model for one-dimensional light attenuation by *Chlamydomonas reinhardtii* in a torus photobioreactor. *Biotechnology and Bioengineering*, **91**(5), 569–582.

Pruvost, J., Legrand, J., & Legentilhomme, P. 2002. Simulation of microalgae growth in limiting light conditions: Flow effect. *AIChE Journal*, **48**(5), 1109–1120.

Pruvost, J., Cornet, J.-F., & Legrand, J. 2008. Hydrodynamics influence on light conversion in photobioreactors: An energetically consistent analysis. *Chemical Engineering Science*, **63**, 3679–3694.

Richmond, A. 2004. Principles for attaining maximal microalgal productivity in photobioreactors: an overview. *Hydrobiologia*, **512**, 33–37.

Richmond, A., & Cheng-Wu, Z. 2001. Optimization of a flat plate glass reactor for mass production of *Nannochloropsis* sp. outdoors. *Journal of Biotechnology*, **85**, 259–269.

Roger, M., & Villermaux, J. 1983. Modelling of light absoprtion in photoreactors Part II. Intensity profile and efficiency of light absorption in a cynlindrical reactor. Experimental comparison of five models. *The Chemical Engineering Journal*, **26**, 85–93.

Rubio, F. Camacho, Fernandez, F. G. Acien, Perez, J. A. Sanchez, Camacho, F. Garcia, & Grima, E. Molina. 1999. Prediction of dissolved oxygen and carbon dioxide concentration profiles in tubular photobioreactors for microalgal culture. *Biotechnology and Bioengineering*, **62**(1), 71–86.

Rubio, F. Camacho, Camacho, F. Garcia, Sevilla, J. M. Fernandez, Chisti, Y., & Grima, E. Molina. 2003. A mechanistic model of photosynthesis in microalgae. *Biotechnology and Bioengineering*, **81**, 459–473.

Sastre, R. R., Csogor, Z., Perner-Nochta, I., Fleck-Schneider, P., & Posten, C. 2007. Scale-down of microalgae cultivations in tubular photo-bioreactors - A conceptual approach. *Journal of Biotechnology*, **132**, 127–133.

Sato, T., Yamada, D., & Hirabayashi, S. 2010. Development of virtual photobioreactor for microalgae culture considering turbulent flow and flashing light effect. *Energy Conversion and Management*, **51**, 1196–1201.

Schamphelaire, L. De, & Verstraete, W. 2009. Revival of the Biological Sunlight-to-Biogas Energy Conversion System. *Biotechnology and Bioengineering*, **103**(2), 296–304.

Schuster, A. 1905. Radiation through a foggy atmosphere. *The Astrophysics Journal*, **21**, 1–22.

Sobczuk, T. Mazzuca, Camacho, F. Garcia, Rubio, F. Camacho, Fernandez, F. G. Acien, & Grima, E. Molina. 2000. Carbon dioxide uptake efficiency by outdoor microalgal cultures in tubular airlift photobioreactors. *Biotechnoly and Bioengineering*, **67**(4), 465–475.

Stephenson, Anna. 2009. *The sustainability of first- and second-generation biofuels using life cycle analysis*. Ph.D. thesis, Ph.D. Thesis Department of Chemical Engineering and Biotechnology, University of Cambridge.

Suh, I. Soo, & Lee, S. Bok. 2003. A light distribution model for an internally radiating photobioreactor. *Biotechnology and Bioengineering*, **82**(2), 180–189.

Talvy, S., Cock, A., & Line, A. 2005. Global modeling of a a gas-liquid solid airlift reactor. *Chemical Engineering Science*, **60**, 5991–6003.

Ugwu, C.U., Aoyagi, H., & Uchiyama, H. 2008. Photobioreactors for mass cultivation of algae. *Bioresource Technology*, **99**(10), 4021–4028.

Vonshak, A., Torzillo, G., & Tomaseli, L. 1994. Use of chlorophyll fluorescence to estimate the effect of photoinhibition in outdoor cultures of Spirulina platensis. *Journal of Applied Phycology*, **6**, 31–34.

Vunjak-Novakovic, G., Kim, Y., Wu, X., Berzin, I., & Merchuk, J. C. 2005. Air-lift bioreactors for algal growth on flue gas: Mathematical modeling and pilot-plant studies. *Industrial & Engineering Chemistry Research*, **44**, 6154–6163.

Walter, C., Steinau, T., Gerbsch, N., & Buchholz, R. 2003. Monoseptic cultivation of phototrophic microorganisms development and scale-up of a photobioreactor system with thermal sterilization. *Biomolecular Engineering*, **20**, 261–271.

Wu, X., & Merchuk, J. C. 2001. A model integrating fuid dynamics in photosynthesis and photoinhibition processes. *Chemical Engineering Science*, **56**, 3527–3538.

Wu, X., & Merchuk, J. C. 2002. Simulation of algae growth in a bench-scae bubble column reactor. *Biotechnology and Bioengineering*, **80**(2), 156–168.

Wu, X., & Merchuk, J. C. 2003. Measurement of fuid fow in the downcomer of an internal loop airlift reactor using an optical trajectory-tracking system. *Chemical Engineering Science*, **58**, 1599–1614.

Wu, X., & Merchuk, J. C. 2004. Simulation of algae growth in a bench scale internal loop airlift reactor. *Chemical Engineering Science*, **59**, 2899–2912.

Yokota, T., Yashima, K., Takigawa, T., & Takahashi, K. 1991. A new random walk model for assessment of light energy absorption by a photosynthetic microorganisms. *Journal of Chemical Engineering of Japan*, **24**, 558–562.

Yoshimoto, N., Sato, T., & Kondo, Y. 2005. Dynamic discrete model of flashing light effect in photosynthesis of microalgae. *Journal of Applied Phycology*, **17**, 207–214.

Yun, Y., & Park, J. M. 2003. Kinetic modeling of the light-dependent photosynthetic activity of the green microalga *Chlorella vulgaris*. *Biotechnology and Bioengineering*, **83**(3), 303–311.

Yun, Y. S., & Park, J. M. 2001. Attenuation of monochromatic and polychromatic lights in *Chlorella vulgaris* suspensions. *Applied Microbiology Biotechnology*, **55**, 765–770.

Appendices

Appendix A

Comparison between algae species for biofuels production

For biodiesel production, the oil or "lipid" content of the algae is optimized. After the oil-containing microalgae is grown and harvested, the lipid or triglycerdises present, often called "green crude" are transformed into biodiesel in a reaction known as transesterification (Fig. A.1). In this process, the triglycerides are converted to methyl esters (biodiesel) and glycerol, via the addition of an alcohol and a suitable catalyst (often NaOH). The product is cleaned to remove the glycerol, a valuable by-product, leaving algal biodiesel fuel.

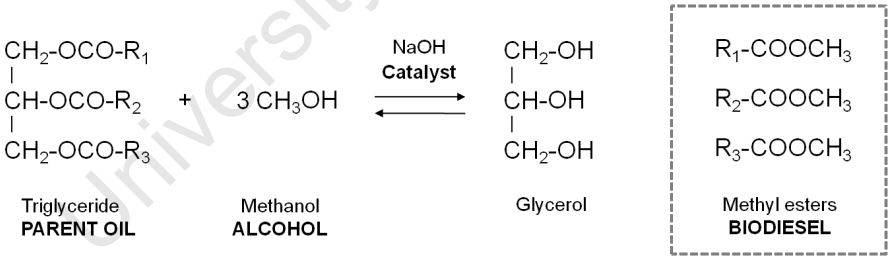

Figure A.1 – Oil to biodiesel via transesterification. Image source: this author, after Chisti (2007)

A high lipid productivity (mg $L^{-1}day^{-1}$) is a desirable characteristic when choosing a species to use for biodiesel production. Recognizing this, Griffiths & Harrison (2009) collated 50 algae species according to their lipid productivities using literature data. This has been extended to experimentation using 10 species (Griffiths *et al.*, 2011b).

Lipid productivity is not the sole desirable characteristic in an algae species for large scale culture. Other characteristics such as rapid growth rates, high final biomass concentration. and resistance to contamination, to name a few, play a role in determining an optimum species (Grobbelaar, 2000). This highlights the need for prioritization of the selection criteria as discussed by Griffiths & Harrison

(2009) and further considered in their experimental study. Extracts from these data found in (Griffiths *et al.*, 2011b), presented in Table A.1, compare various parameters across different species.

Table A.1 – Comparison between algae species for algal biofuels production, based on literature analysis Griffiths & Harrison (2009) and subsequent experimental refinement using a 3.2 litre airlift system (Griffiths *et al.*, 2011b)

Species		*Chlorella vulgaris*	***Scenedesmus***	*Neochloris oleoabundans*	*Ankistrodesmus falcatus*	*Spirulina platensis*	*Nannochloropsis*	*Tetraselmis suecica*	*Cylindrotheca fusiformis*	*Phaeodactylum tricornutum*	*Pavlova*	*Isochrysis C4*
Biomass												
μ_{max}	day^{-1}	1.34	**1.15**	1.56	0.99	0.43	0.76	1.20	0.72	0.68	0.60	1.32
Max Biomass Conc.	$g\ L^{-1}$	1.65	**2.74**	1.13	1.20	2.74	1.89	2.44	1.52	1.74	1.00	2.48
Max Productivity	$g\ L^{-1}day^{-1}$	0.28	**0.30**	0.29	0.25	0.29	0.24	0.49	0.35	0.34	0.17	1.23
Lipid												
Lipid content	%	18	**10**	13	12	4	26	9	27	20	15	7
Max Lipid Productivity	$mg\ L^{-1}day^{-1}$	27	**23**	32	29	10	29	31	39	28	15	40
Vol. Product yield	$mg\ L^{-1}$	231	**242**	27	96	84	413	124	199	308	105	37
Harvesting												
Settling recovery (24hrs)	%	25	**86**	23	54	95	59	80	96	42	40	15

From the work of Griffiths *et al.* (2011b) and shown in Table A.1, *Scenedesmus* showed a combined high biomass growth rate μ_{max}, biomass productivity, lipid productivity, volumetric product yield and % recovery from settling. As an attractive species for biofuels production, *Scenedesmus* was chosen as the algal species to be used for this thesis.

Appendix B

Algae culturing methods

The *Scenedesmus* sp. strain in our laboratory was isolated by Melinda Griffiths (a post graduate student here) from the Njodzi ponds in Upington, South Africa. Stock cultures were maintained at ambient temperature in 500 ml flasks, sparged with air and illuminated with fluorescent bulbs from one side to give a PFD of ~120 μmol.m^{-2}.s^{-1} at the surface. A general purpose freshwater media "Modified Bold 3N" (Table B.1) was used for culture maintenance and growth experiments.

Table B.1 – Bold 3N algal media composition

Substance	g.L^{-1}
$NaNO_3$	0.75
$CaCl_2.2H_2O$	0.025
$MgSO_4.7H_2O$	0.075
K_2HPO_4	0.075
KH_2PO	0.175
NaCl	0.025
P-IV Metal solution	6 ml.L^{-1}

P-IV Metal solution composition	g.L^{-1}
Na_2EDTA	0.75
$FeCl_3.6H_2O$	0.017
$MgCl_2.4H_2O$	0.041
$ZnCl_2$	0.005
$CoCl_2.6H_2O$	0.002
$Na_2MoO_4.2H_2O$	0.004

Appendix C

Calibration curves

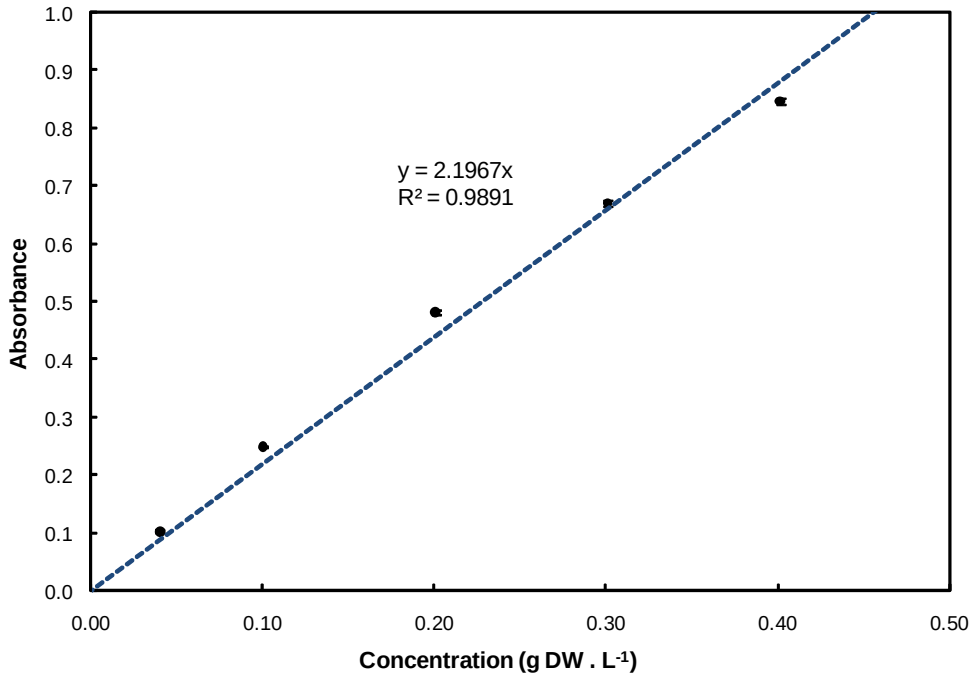

Figure C.1 – *Scenedesmus* sp. absorbance as a function of dry mass concentration, measured at 750 nm in a Helios spectrophotometer.

Appendix D

On-line spectrophotometer flow cell for continuous concentration measurements

A low cost LED-photodiode based spectrophotometer for continuous on-line monitoring using optical flow cells was being developed at UCT in a project headed by Clive Garcin and funded by the Water Research Commission (WRC) in South Africa. This author was involved in the project to the extent of testing the system for its use on algae systems as well as creating developing a LabVIEW programme to monitor and log concentration data to a PC.

The systems utilizes flow cells (Fig. D.2) that enable a sample from the experiment to be continuously sent through the device whilst having its real time concentration calculated and recorded. The clear advantage of using such a system was that concentration readings could be continuously logged; this avoided the need for intrusive (and at times tedious) manual sampling. In addition, the data captured allowed a greater accuracy for characterizing the exponential growth curve, since a reading could be recorded at and frequency desired (every 5 min for this work). The main disadvantage was found to be the phenomenon of algae accumulating on the walls of the flow cell after extensive use, which produced inaccurate readings. Since the flow cell project is still in development, its use in this work formed part of an ongoing investigation into redesigning and developing a system that could have practical real world applications.

D.1 Background and theory

The basis of light spectroscopy in analytical chemistry is the use of Beer-Lambert Law (see Section 2.8.1), in which absorbance is linearly proportional to light path length (l) and given by: $A = K_a \cdot C_x \cdot z$. In a photodetector, the light intensity detected is proportional to the voltage output signal. Thus, comparing the voltage output from an LED shining through pure water V_0 (i.e with $C_x = 0$) to that observed when shining through a dissolved species, is an equivalent measure of absorbance:

$$A = log(V_0/V) \tag{D.1}$$

By continuously measuring the equivalent absorbance, the concentration of the dissolved species can be calculated.. Higher concentration means higher absorbance. For accuracy, spectroscopic measurements are generally performed at < 1 absorbance unit, since above 1, less than 2% of the incident light is transmitted through the liquid, and thus accuracy and precision is lost and relative standard deviation becomes excessive. In the case of algae suspensions, this inaccuracy is only increased at higher absorbances (i.e higher concentrations), owing to the inability of the Beer-Lambert model to describe scattering effects at high algae concentrations (see Section 2.8.1).

The two standard method for overcoming these limitations in a conventional spectrophotometer are to either dilute the sample until A < 1 or use a cuvette with a much shorter path length (< 1cm standard). For on-line measurements in a flow cell, dilution is impractical, however, it is possible to use flow cells of varying path length i.e shorter path length for higher concentrations. Flow-through cells come in a range of path lengths, from 0.1 – 50 mm, and thus narrower flow cells can be chosen for high concentration work.

D.2 Materials and methods

The materials and methods outlined are according to Garcin *et al.*, 2010. The basic design of the system involved passing light from an LED through the flow cell to be detected on the other side by a photodetector (Fig. D.1). The voltage output from the photodetector is then sent via a data acquisition card (DAQ) to a computer and processed using LabVIEW software. Two such devices were used in this work, the first generation and the second generation prototype (Fig. D.3). Two were needed in order to be able to monitor the growth of two simultaneous experiments. A third generation version has since been developed that uses a printed circuit board.

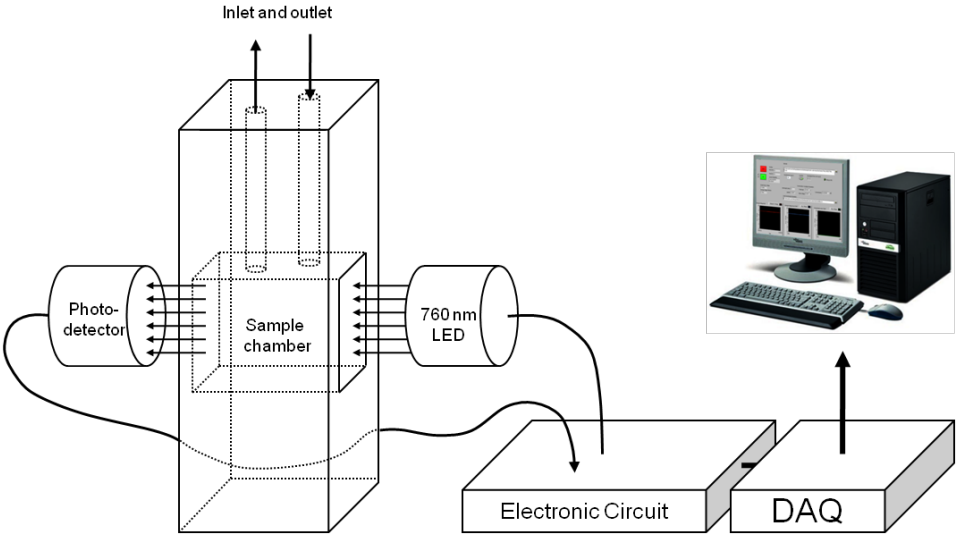

Figure D.1 – Schematic of the flow cell measurement system. Image source: this author.

Figure D.2 – The 10 mm flow cell used for the algae device (176.703-QS, Hellma)

The electrical circuit for powering the LED's and amplifying the photodetector output is shown in Fig. D.4. A constant current chip was used to supply the LED in order to maintain a stable light output irrespective of extraneous factors. Current supply to the LED was adjustable (up to 100 mA) by judicious selection of resistors. This allowed for an appropriate adjustment of light output as required. Similarly, the voltage output from the photodetector was adjustable via a variable resistor up to a maximum of 11 V. Power supply to the system was from a simple purpose-built transformer that converted 240 V AC mains supply to 12 V DC.

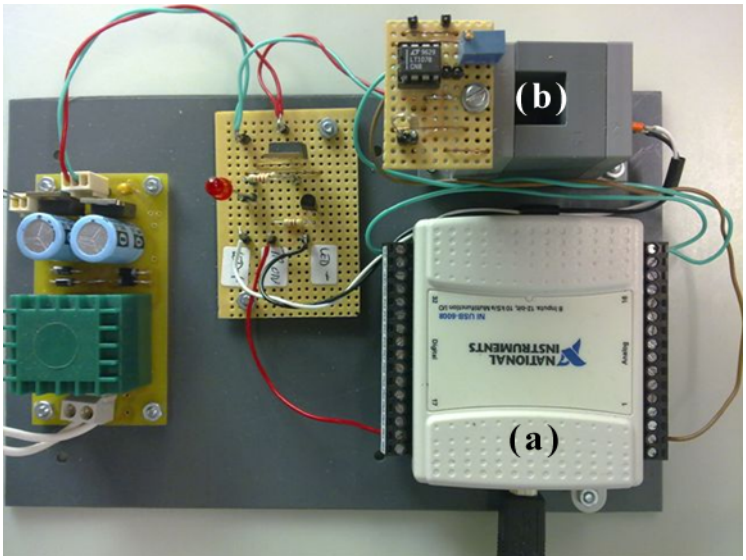

Figure D.3 – Second generation prototype of device. (a) LabVIEW USB-6008 DAQ Data Acquisition Card. (b) Flow cell holder. Image source: Garcin *et al.* (2010)

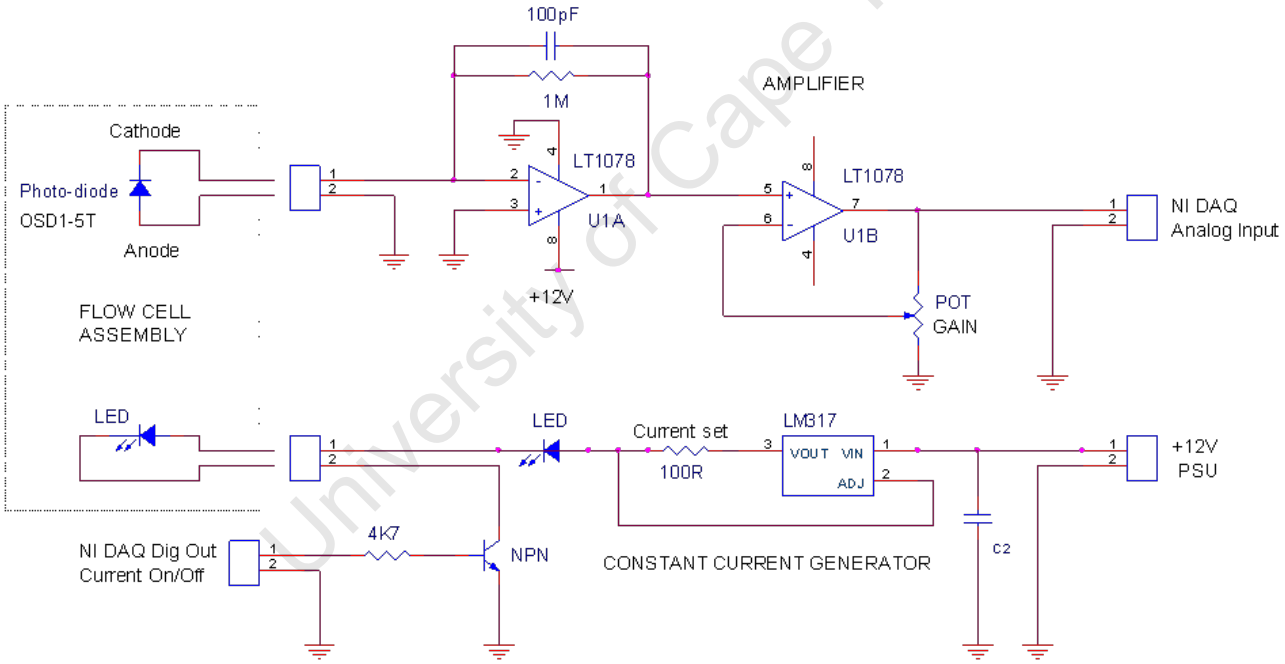

Figure D.4 – Electrical circuit for the device. Image source: Garcin *et al.* (2010)

A visible range LED of 760 nm was used for algae measurements. Visible range photodetectors were from Texas Instruments, supplied by RS components (Vorna Valley, South Africa). A USB-6008 data capture card (DAQ) was obtained from National Instruments (Midrand, South Africa). A 10 mm flow cell (176.703-QS) was from Hellma Müllheim, Germany. A microbore peristaltic pump (REGLO, Ismatec) was used for directing fluids through the flow cells at F ~ 5 ml.min^{-1} via 1.6 mm ID tubing (R3603, TYGON).

D.3 Data acquisition and processing

LabVIEW made it possible to digitally process the signal (for noise reduction and averaging), negating the need for a low pass filter in the electronic circuit. Fig. D.5 shows the LabVIEW graphic user interface developed whilst Fig. D.6 shows the back panel program developed to process the signal into a useful form. Once calibrated, the software automatically converted the voltage output from the photodetector directly into a concentration measurement using the calibration parameters and Beer-Lambert Law (for low concentrations) or a hyperbolic model (for high concentrations). Both data signals (voltage and concentration) could then be continuously logged to an MS Excel compatible file at a frequency set by the user.

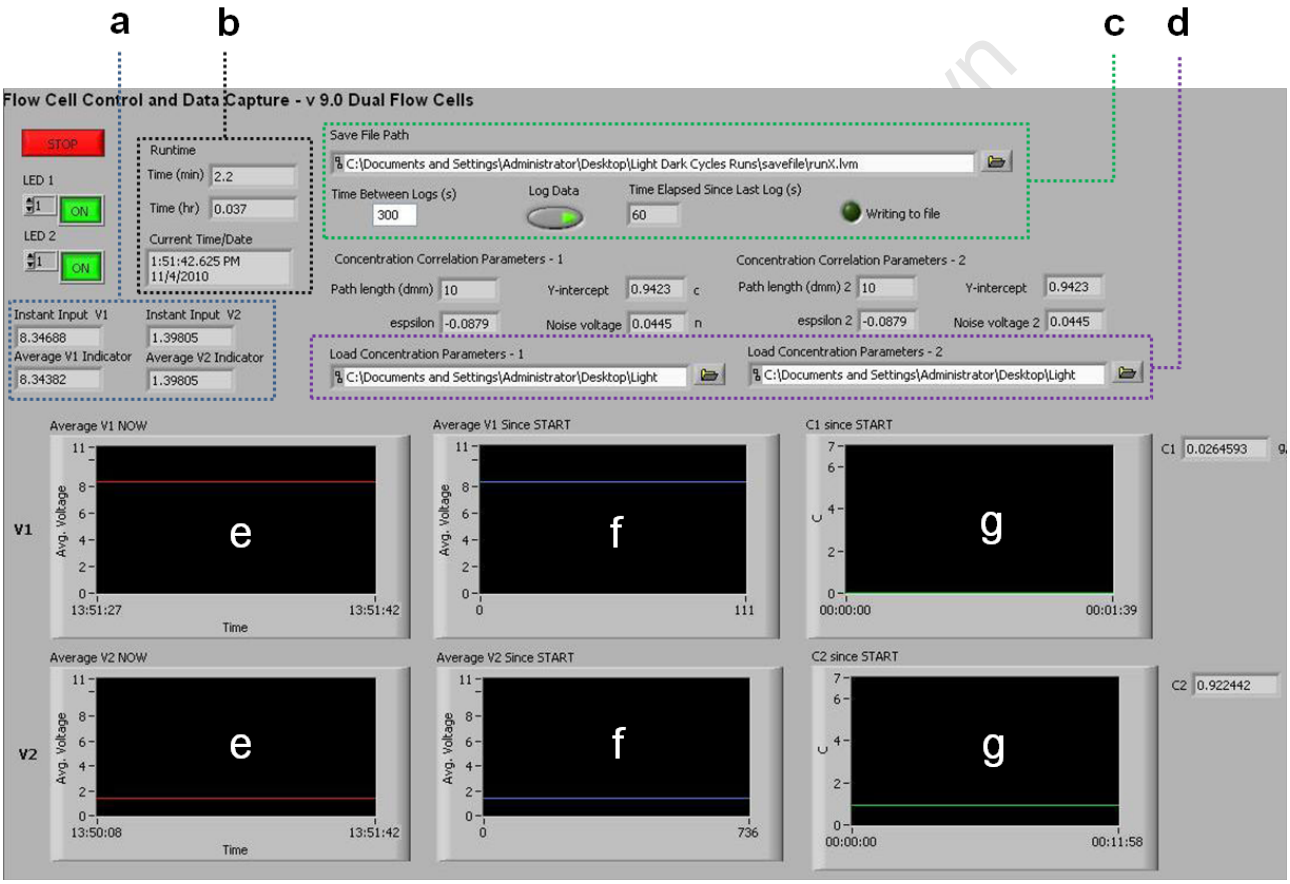

Figure D.5 – Screenshot from LabVIEW user interface. **(a)** Instant voltage indicators **(b)** Elapsed time **(c)** Control of data logging: File path and time between logs **(d)** Files that store calibration parameters **(e)** Average instant voltage for each device **(f)** Average voltage since $t = 0$ **(g)** Concentration graphs. Image source: this author

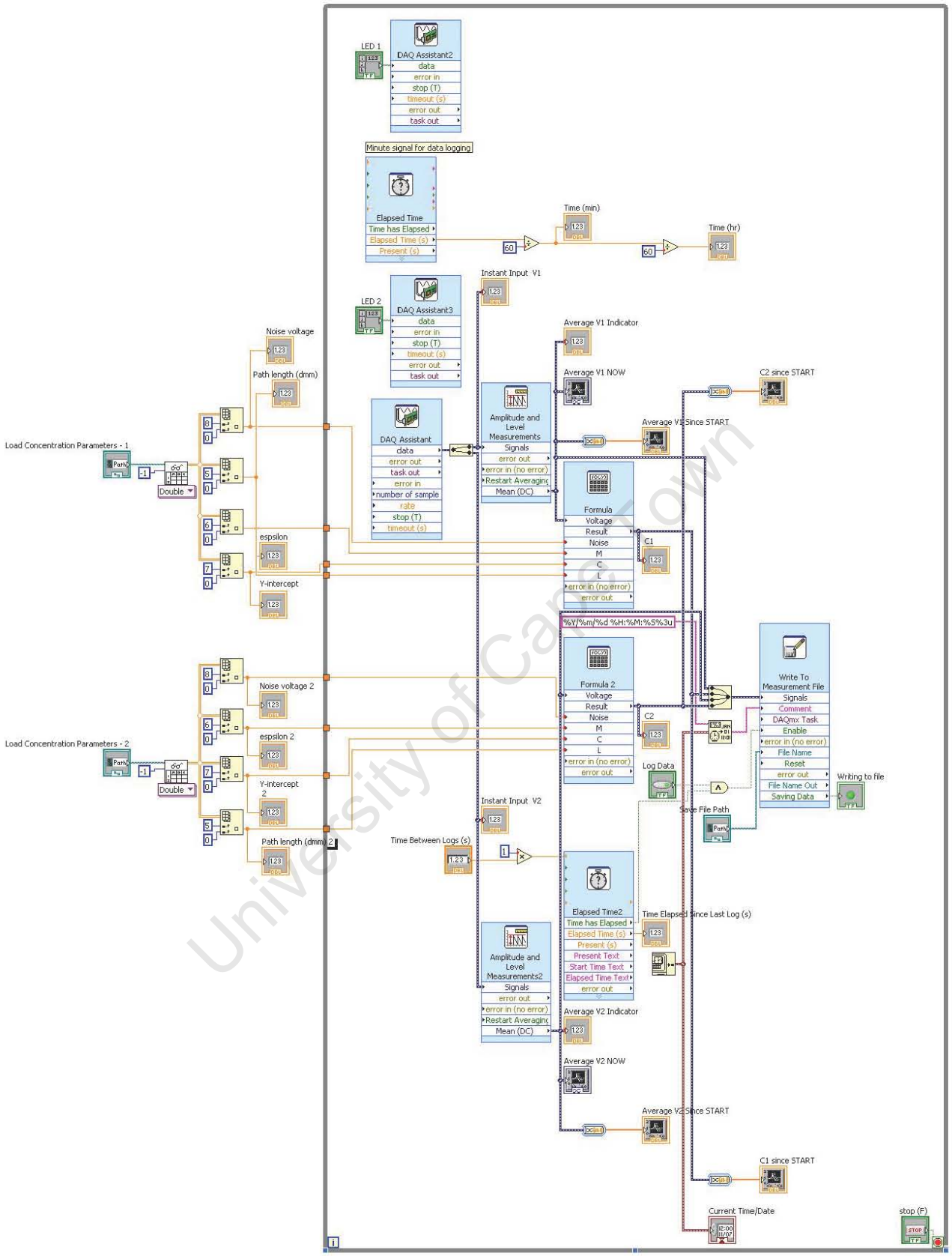

Figure D.6 – LabVIEW back panel programme. Image source: this author

D.4 System calibration

D.4.1 Calibration method

First and foremost, the device parameters were adjusted (LED output, photodetector gain, and light path length) such that at zero concentration (e.g. pure water) the processed output signal had a baseline maximum of around 10 V without saturating the component (zero concentration = maximum light intensity, thus maximum voltage output for the system), while at high concentration (high optical density i.e. low light transmission) the photodetector was near its minimum output (between 0 and 1 V). Parameter adjustments were performed by trial and error and, once suitable, their values remained fixed for the duration of the devices use.

Once these criteria were met, a serial dilution of an algae sample (*Scenedesmus* sp.) was made up in duplicate, and corresponding voltage outputs were measured for the different concentrations. Cell density was determined by filtration, drying and weighing; the same cell density was then serially diluted and used for the calibration of the system. Each sample was then sent through the flow cell and the voltage logged for a period of ~2 seconds at (logging at 0.1 second intervals). The mean value of the voltage over this time interval was used at the corresponding voltage for that concentration.

A plot of $log\left(\frac{V_0-V_n}{V-V_n}\right)$ versus concentration C_x would then be generated from this data (Fig. D.7), which formed the basis for the calibration. Where, V is the voltage output at a specific concentration value C_x. V_0 is the voltage of pure water (i.e $C_x = 0$) and V_n is the noise voltage of the device, which is the voltage reading present with the LED switched off.

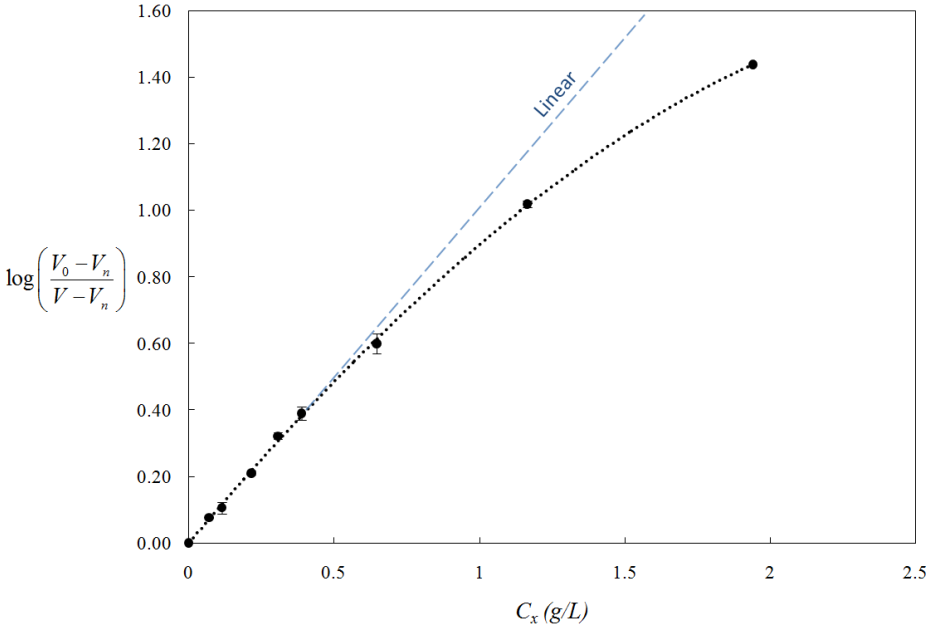

Figure D.7 – Calibration plot. Absorbance versus concentration. (Flow Cell: 2, Device: Left)

From Fig. D.7, it is clear to see the deviations from linear Beer-Lambert law at high concentrations

(C_x > 1 g.L^{-1}). A more detailed discussion of Beer-Lambert law's assumptions and limitations is presented in the literature review (Section 2.8.1). Owing to the non-linear nature of the relationship between absorbance and concentration, two different calibrations were performed, one that would be applicable at low concentrations and the other over the full concentration range.

D.4.2 Calibration results

Since two different devices were used in parallel[1] to accommodate two simultaneous run on the rig (requiring a double set of concentration data), two flow cells were used and each was calibrated separately for a respective device. The two different devices were denoted as *Left* and *Right* and the flow cells used were allocated numbers '1' and '2'. The same calibration parameters could not be used for both flow cells since they exhibited slightly different optical properties and needed to be calibrated separately. Examples of calibration data are presented. The parameters from all the calibrations performed are summarized Table D.2 .

D.4.2.1 Low concentration linear calibration (Beer-Lambert)

At low concentrations, Beer-Lambert law is sufficient to predicts the linear relationship between voltage and concentration according to equation X.

$$log\left(\frac{V_0 - V_n}{V - V_n}\right) = K_a \cdot z \cdot C_x \tag{D.2}$$

By linear regression through the data for C_x < 1 g/L, one is able to obtain a best fit value for the absorption coefficient. Figure D.8 shows the plot of the average data (error bars shown) and the corresponding linear regression. For experiments performed at low concentration rage, a linear calibration would suffice. Error in the calibration comes from the combination of many sources, human and instrument based. Ideally, the calibration should be repeated many times to generate sufficient data points to account for this error and simulate a more accurate mean values.

[1] Data from both devices could be processed using a single LabVIEW programme (Fig D.5)

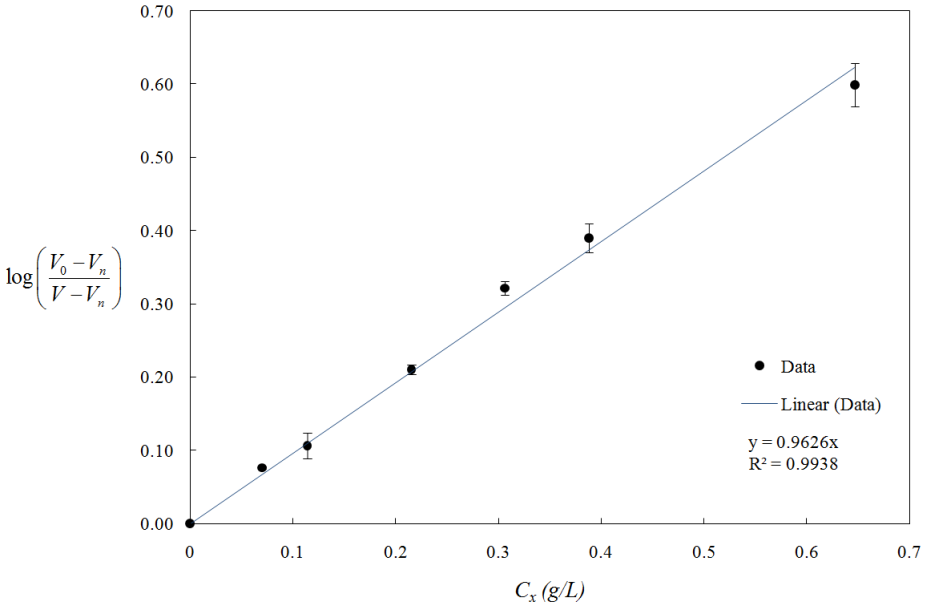

Figure D.8 – Low concentration (<1 g/L) linear regression. Flow cell: **2**, Device: **Left.** From the slope of the graph: Slope = $K_a \cdot l$, with l = 10 cm and K_a= 0.0963 g.L^{-1}

D.4.2.2 Full concentration range calibration (Hyperbolic)

At higher algae concentrations, scattering effects are significant and thus deviations from Beer-Lambert linearity occur. An empirical method of accounting for this deviation is to fit a hyperbolic absorption model to the data, with scattering coefficient. This model follows the hyperbolic models used to predict light distribution in real photobioreactors (see Section 2.8.3):

$$log\left(\frac{V_0 - V_n}{V - V_n}\right) = \frac{K_{a,max} \cdot z \cdot C_x}{C_x + K_x} \tag{D.3}$$

where, $K_{a,max}$ is the maximal absorption co-efficient and K_x is the scattering coefficient. Figure D.9 shows the hyperbolic absorption curve fitted over the full concentration range with a comparison to linear Beer-Lambert law prediction. For experiments over a large concentration range, the hyperbolic model would be required to predict concentration with any accuracy.

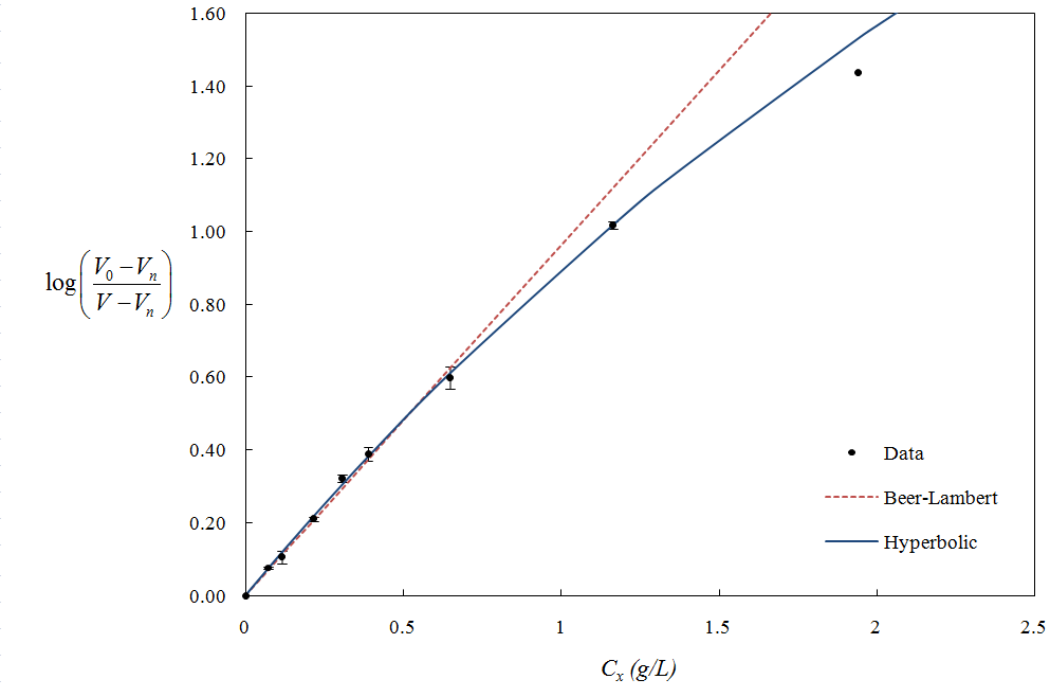

(a) Flow cell: **2**, Device: **Left**. Regression of the model parameters gave $K_{a,max}$ = 0.626 L.(g.mm)$^{-1}$and K_x = 5.990 g.L^{-1}

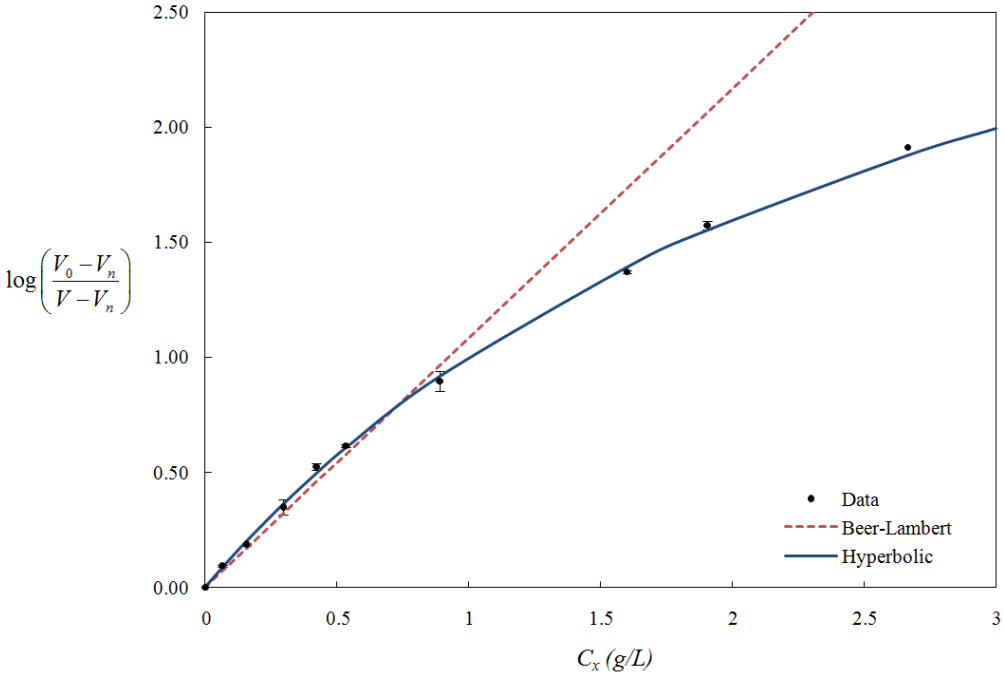

(b) Flow cell: **1**, Device: **Right**. Regression of the model parameters gave $K_{a,max}$ = 0.395 L.(g.mm)$^{-1}$ and K_x = 2.949 g.L^{-1}

Figure D.9 – High concentration, hyperbolic calibration regression.

D.4.2.3 Calibration summary

Table D.2 shows the determined calibration parameters. Flow cell: 2 was never used on the *Right* device and hence was not calibrated for it.

Table D.1 – Calibration parameters for *Scenedesmus* sp.

Flow Cell	Device	Conc. Range	V_0(V)	V_n(V)	K_a	$K_{a,max}$	K_x
		g.L^{-1}	Volts	Volts	L.(g.mm)$^{-1}$	L.(g.mm)$^{-1}$	g.L^{-1}
1	L	0.067-3.33	8,280	0.0445	0.0801	0.324	3.196
	R	0.065-2.667	10.22	0.0436	0.1084	0.395	2.949
2	L	0.070-1.940	8.894	0.0445	0.0963	0.626	5.990

Once calibrated, the model parameters could be loaded into the LabVIEW application which calculated, displayed and enabled logging of algae concentration over time. Table D.2 shows the two models and the corresponding equations used calculate C_x for each time point in the experiment.

Table D.2 – Summary of calibrations and models

Concentration range	Model	Calculation of C_x
< 1 g/L	$A = K_a \cdot l \cdot C_x$	$C_x = \frac{A}{K_a \cdot l}$
0 - 4 g/L	$A = \frac{K_{a,max} \cdot l \cdot C_x}{C_x + K_x}$	$C_x = \frac{A \cdot K_x}{K_{a,max} \cdot l - A}$
	where, $A = log\left(\frac{V_0 - V_n}{V - V_n}\right)$	

D.5 System performance

The success of the current system to accurately monitor algae concentration over an extended period was questionable. Accumulation of algae agglomerates to the clear surface of the flow cell was found to be the major problem. It is thought that extracellular polysaccharide (EPS) were the cause of the the agglomeration (Garcin *et al.*, 2010). This substance is responsible for the formation of most biofilms. Once there is a layer of it on the glass, the algae tends to stick. A build up of solids on the clear "window" of the flow cell blocks some of the light that passes through the cell and thus an overestimation of the actual absorbance occurs (Fig. D.10). Because of this phenomenon, the confidence in the concentration data obtained from flow cell data was low. For this reason, the author resorted to manual sampling (with corresponding OD readings to calculate concentrations) as a backup for all experiments.

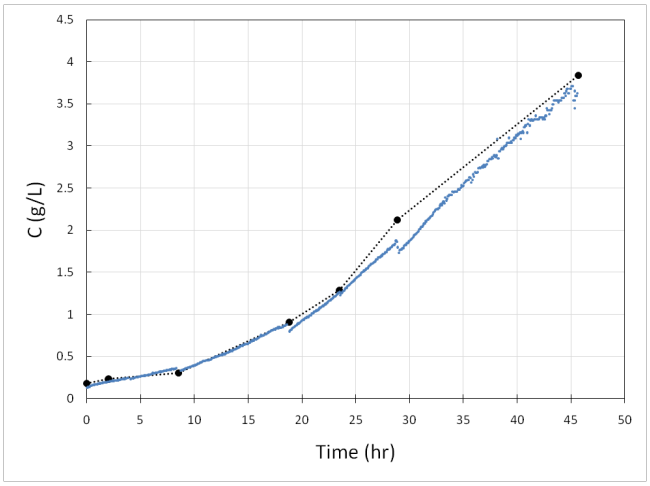

(a) Run 14

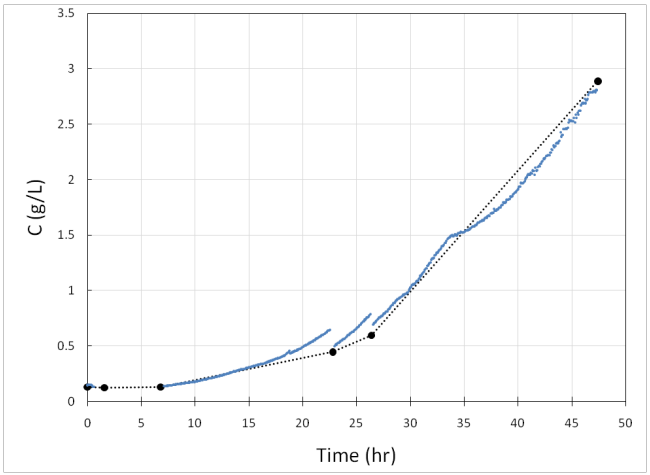

(b) Run 3

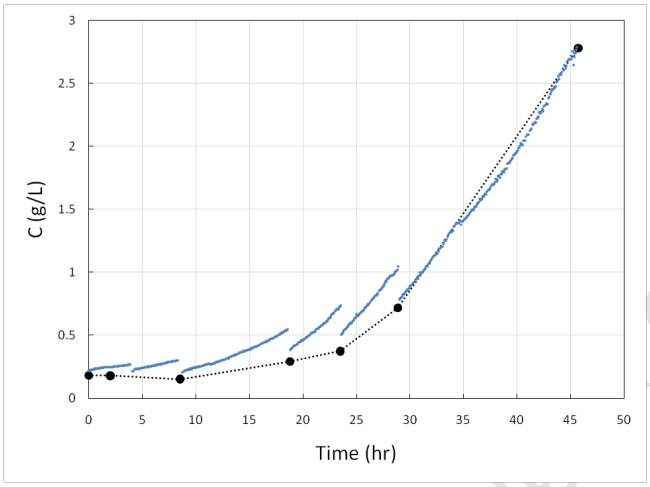

(c) Run 12

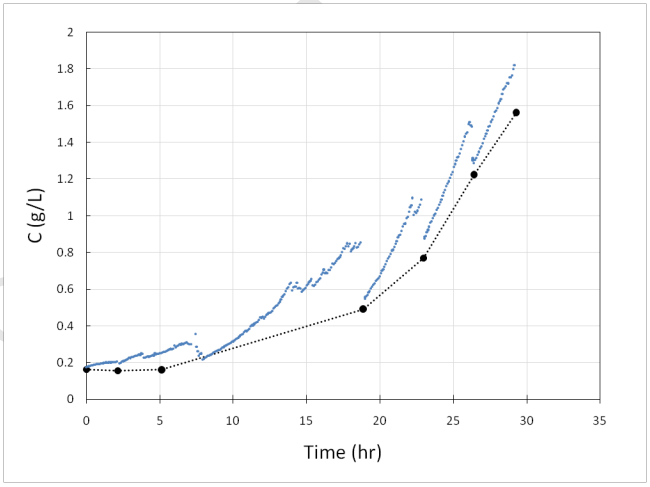

(d) Run 18

Figure D.10 – Extracts from flow cell data: Concentration versus time.. Reasonable predictions (a & b) vs. Poor predictions (c & d). Black circles are discrete points obtained from manual OD readings. Run numbers correspond to experimental runs performed for the kinetic model experiment (see Section 4.2.2).

Strategies were taken to try and counter the agglomeration issue:

- *Increasing the rate at which algae passed through the cell* - It was thought that the faster the algae traveled through the cell (i.e shorter residence time) the less likely it would be for cells to stick to the wall. This was achieved in two ways: (i) By using the maximum pump flow rate (5 $ml.min^{-1}$) and (ii) by swapping from using a 1500 μl cell (174-QS, Hellma) to the 176.703-QS with a much smaller volume of 160 μl . A smaller smaller volume resulted in a much shorter residence time.

- *Flow cell cleaning to ensure clean surfaces* - Intermittent cleaning of the cells during the runs was performed as a temporary solution to the problem. This was done via fast injection of demineralized water from 5 ml pipettes, which managed to remove most of the build up. The cleaning was done when taking manual samples and it is clear to see the effects of it in Fig. D.10

c & d. As soon as the cell was cleaned of build-up, the concentration calculated was closer to the real value, but soon after the build-up increased and the concentration deviated from the real profile. Thorough cleaning of the flow cells between runs was also performed; A basic wash for 1 hour (2 M NaOH) followed by an acid wash (2 M HCl) followed by demineralized water. Ultrasonication cleaning was also investigated but not found to be any more effective than the acid/base washes.

Although these factor did *reduce* the effects, none enabled running the system with enough confidence to rely purely on flow cell data for calculating growth rates. Thus, in almost all cases, data from manual sampling was used to calculate exponential growth rates. The system definitely has potential and this author has proposed some redesigns were it to be developed further:

- A flow cell design should be used that allows the algae to flow straight through and past the "window" without changing direction. In the current cell, the algae flows down through a channel, into a small chamber and then back up out of the cell through another channel in the opposite direction. This change of direction could be creating small eddies in the flow which allows cells the time to agglomerate and stick to the walls.
- To design a control system which pumps samples intermittently, when a reading is required, and which washes the cell with water on each side of that sample. i.e every five minute a valve changes and the system pumps algae into the cell for a few seconds, during which time it takes a reading. After the reading, the valve to the source is closed and switched to pump water through the system and the cell, effectively flushing out any algae present. This would make the chances of algae sticking to the walls much less likely. In the current case, algae is flowing through the cell continuously for 2-3 days.

Appendix E

Tubular loop reactor design

E.1 Reactor specifications

Table E.1 gives dimensions that were common to all three the tubular reactors used. Additional specification sheets which list dimensions unique to each reactor are given in Tables E.2, E.3 and E.4. Detailed to-scales diagrams are given for each system in Figures E.1, E.3 and E.3.

Table E.1 – Dimensions common to all three tubular reactors

Downcomer					
Tube inside diameter	$D_{d,i}$	7	mm	0.0070	m
Tube outside diameter	$D_{d,o}$	10	mm	0.0100	m
Tube cross sectional Area	A_d	38.48451	mm^2	3.85E-05	m^2
Standard length	L_t	56	cm	0.56	m
Bottom piece length*	L_{bot}	59	cm	0.59	m
Angle of tubes	θ_t	5	°		
Bends					
Bend length	L_{bend}	12.725	cm	0.12725	m
Bend radius	R_{bend}	2.5	cm	0.025	m
Straight lengths on bend	$L_{s,bend}$	5	cm	0.05	m
Top cup					
Inside diameter	D_{cup}	4.5	cm	0.045	m
Height of piece	H_{cup}	15	cm	0.15	m

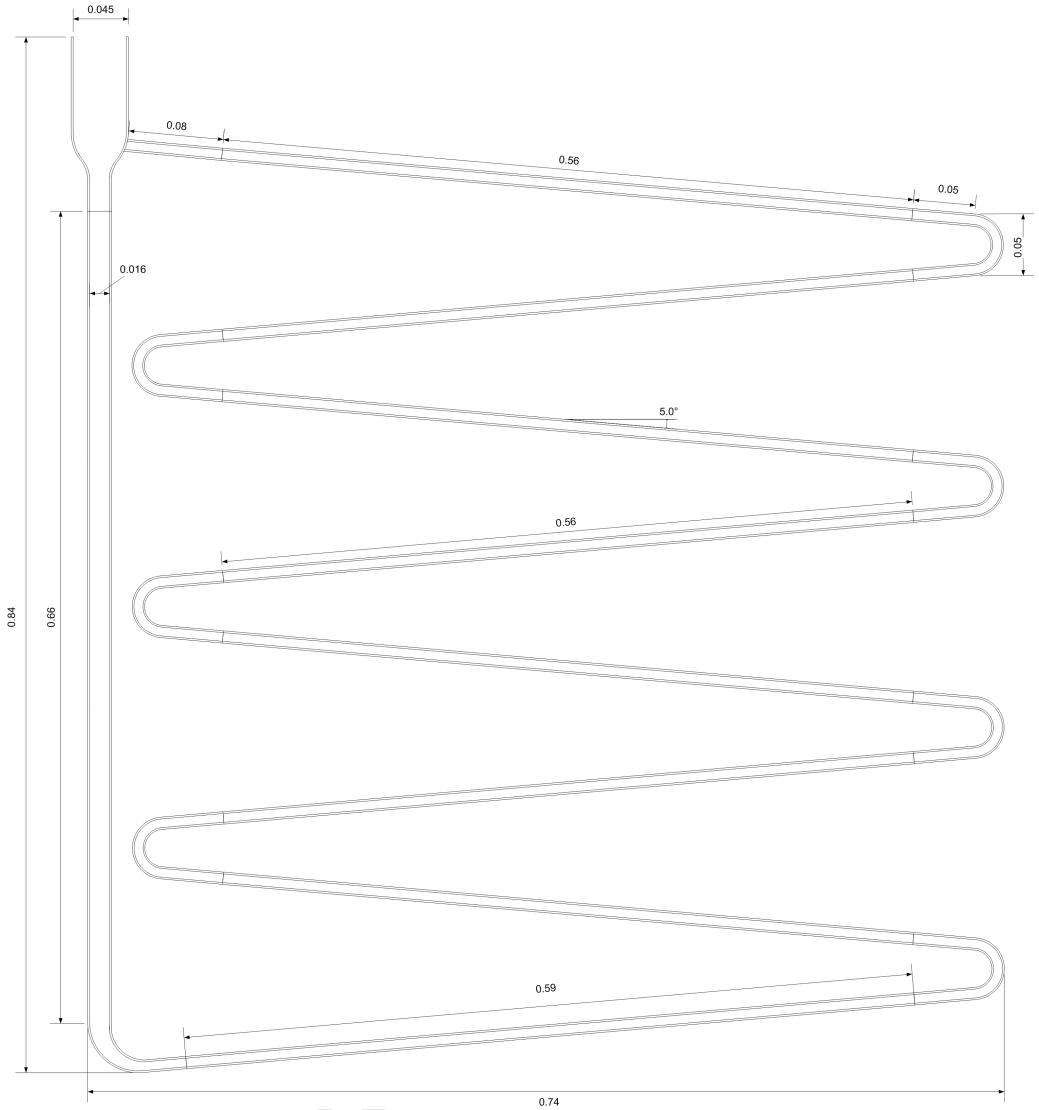

Figure E.1 – To-scale diagram of 8-tube tubular reactor. Dimensions given in meters.

Table E.2 – 8-tube tubular reactor specifications

Downcomer				
No. Standard tubes	N_t	7	#	*Measured*
No. Bends	N_{bend}	7	#	*Measured*
Bottom piece	N_{bot}	1	#	*Measured*
Total tubing length incl. bends	L_1	5.40	m	$N_t*L_t+N_{bend}*L_{bend}+N_{bot}*L_{bot}$
Length to top of riser	L_{top}	0.155	m	*Measured*
Length to bottom of riser	L_{bot}	0.08	m	*Measured*
Downcomer length	L_d	5.64	m	$L_1+L_{top}+L_{bot}$
Downcomer volume	V_d	2.17E-04	m^3	A_d*L_d
Riser				
Riser length	L_r	0.66	m	*Measured*
Riser inside diameter	D_r	0.16	m	*Measured*
Riser cross sectional area	A_r	0.020106193	m^2	*Measured*
Riser volume	V_r	2.33E-04	m^3	$V-V_d$
Reactor				
Reactor total fluid volume	V	4.50E-04	m^3	*Measured*
Total height	H	0.84	m	*Measured*
Total width	W	0.74	m	*Measured*

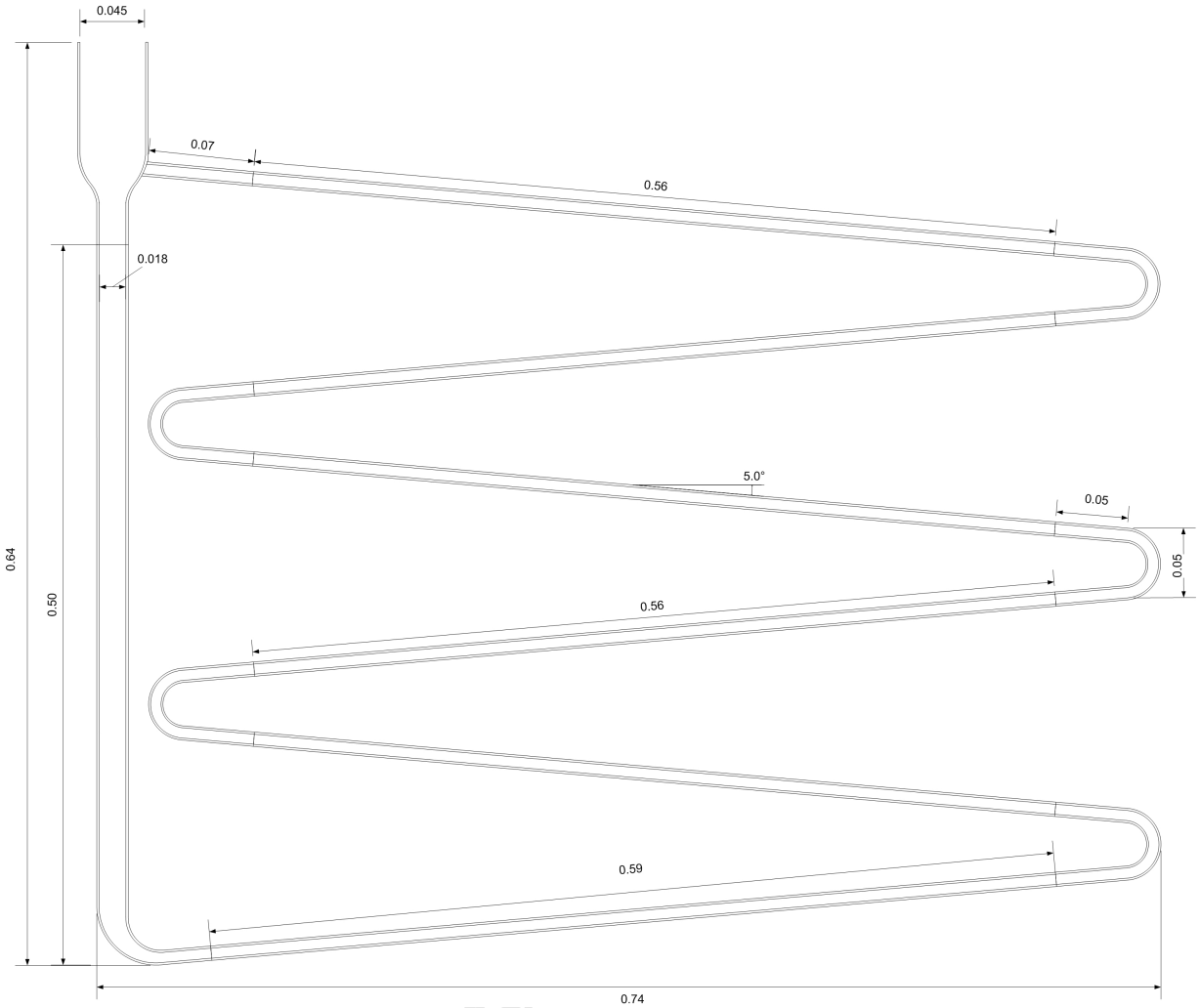

Figure E.2 – To-scale diagram of 6-tube tubular reactor. Dimensions given in meters.

Table E.3 – 6-tube tubular reactor specifications

Downcomer				
No. Standard tubes	N_t	5	#	*Measured*
No. Bends	N_{bend}	5	#	*Measured*
Bottom piece	N_{bot}	1	#	*Measured*
Total tubing length incl. bends	L_1	4.03	m	$N_t*L_t+N_{bend}*L_{bend}+N_{bot}*L_{bot}$
Length to top of riser	L_{top}	0.137	m	*Measured*
Length to bottom of riser	L_{bot}	0.08	m	*Measured*
Downcomer length	L_d	4.24	m	$L_1+L_{top}+L_{bot}$
Downcomer volume	V_d	1.63E-04	m^3	A_d*L_d
Riser				
Riser length	L_r	0.5	m	*Measured*
Riser inside diameter	D_r	0.18	m	*Measured*
Riser cross sectional area	A_r	0.0254469	m^2	*Measured*
Riser volume	V_r	1.67E-04	m^3	$V-V_d$
Reactor				
Reactor total fluid volume	V	3.30E-04	m^3	*Measured*
Total height	H	0.64	m	*Measured*
Total width	W	0.74	m	*Measured*

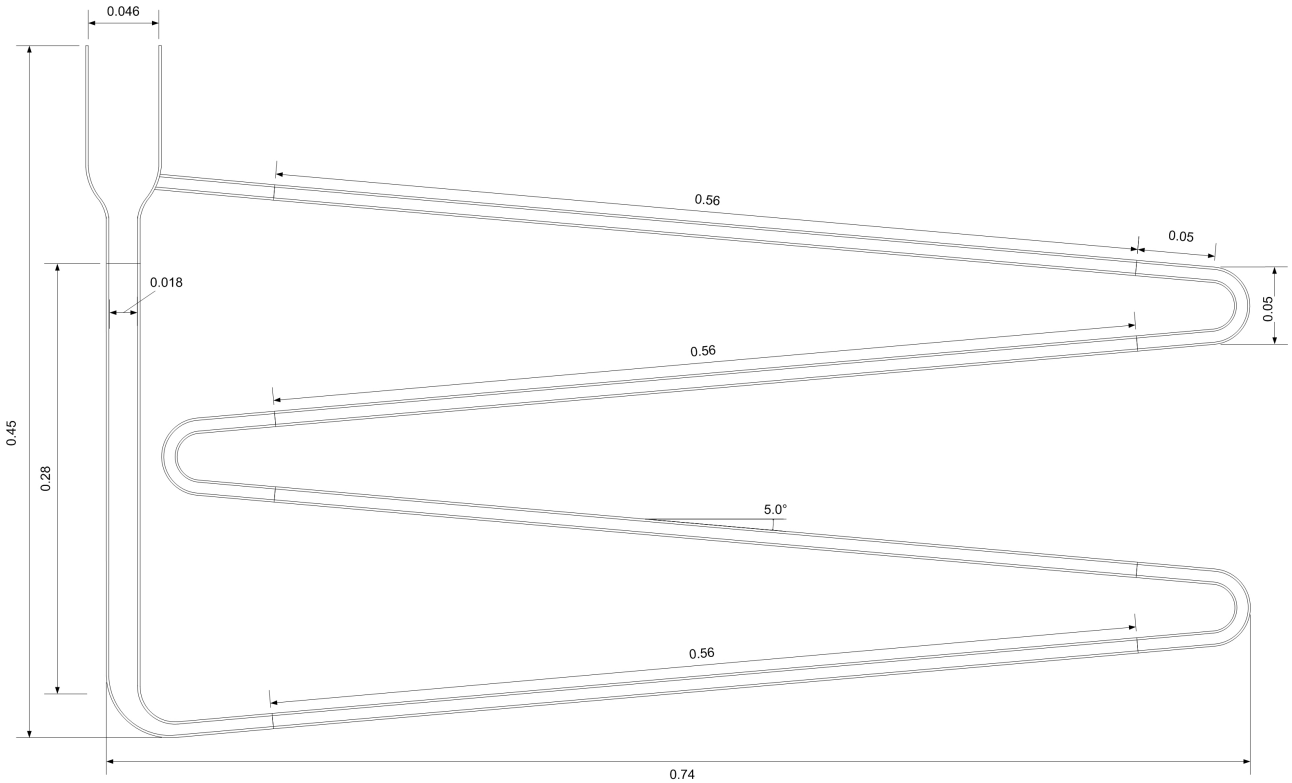

Figure E.3 – To-scale diagram of 4-tube tubular reactor. Dimensions given in meters.

Table E.4 – 4-tube tubular reactor specifications

Downcomer				
No. Standard tubes	N_t	4	#	*Measured*
No. Bends	N_{bend}	3	#	*Measured*
Bottom piece	N_{bot}	0	#	*Measured*
Total tubing length incl. bends	L_1	2.62	m	$N_t*L_t+N_{bend}*L_{bend}+N_{bot}*L_{bot}$
Length to top of riser	L_{top}	0.137	m	*Measured*
Length to bottom of riser	L_{bot}	0.105	m	*Measured*
Downcomer length	L_d	2.86	m	$L_1+L_{top}+L_{bot}$
Downcomer volume	V_d	1.10E-04	m^3	A_d*L_d
Riser				
Riser length	L_r	0.28	m	*Measured*
Riser inside diameter	D_r	0.18	m	*Measured*
Riser cross sectional area	A_r	0.0254469	m^2	*Measured*
Riser volume	V_r	9.88E-05	m^3	$V-V_d$
Reactor				
Reactor total fluid volume	V	2.09E-04	m^3	*Measured*
Total height	H	0.45	m	*Measured*
Total width	W	0.74	m	*Measured*

E.2 Calibration of gas flow rate to cycle time for each tubular reactor

Cycle time calibrations were performed for each reactor by varying the gas flow rate and measuring the time taken for small particles to travel known distance in the downcomer tubes. Cycle times were estimated for each downcomer velocity some via mathematical manipulation. A full sample calculation is presented for the 8-tube calibration and the data from the 6 and 4-tube versions is also shown.

E.2.1 8-tube cycle time calibration and calculation in full detail

The 8-tube reactor downcomer section comprised 7 straight tubes of 56 cm length, a bottom tube of 59 cm length and 7 bends of ~12.725 cm length. Additional lengths accounted for were the small sections that joined to the bottom of the riser and to the top of the top-cup, totaling approximately 23.5 cm. Thus, the length of the downcomer section L_d was calculated according to:

$$L_d = 7 \times (0.56 + 0.12725) + 0.59 + 0.235 = 5.64\,\text{m} \tag{E.1}$$

Knowing the downcomer tubes inside diameter D_d , and thus the cross section area A_d, allows the volume of the downcomer section to be calculated according to $V_d = A_d \cdot L_d$. The riser length L_r was measured to be 0.66 m and the total fluid volume V_{reactor} was measured directly as 0.45 liters. Table E.5 shows the process of calculating the volumes for riser and downcomer sections, denoted V_r and V_d, respectively.

Table E.5 – Calculation of riser and downcomer volumes for 8-tube reactor, utilizing the estimated downcomer length L_d. Refer to Table E.1 for relevant specifications such as tube diameters used in the calculation.

Description	Symbol	formula	Units	Value
Downcomer Area	A_d	$\pi*0.25*D_d{}^2$	m^2	3.85E-05
Riser Area	A_r	$\pi*0.25*D_r{}^2$	m^2	2.01E-04
Reactor Volume	V	measured	dm^3	0.450
Downcomer Volume	V_d	A_d*L_d	dm^3	0.217
Riser Volume	V_r	$V - V_d$	dm^3	0.233

Tissue paper rolled into small ~2 mm balls were used as particles to approximate fluid flow in the downcomer tubes. Table E.6 shows the data obtained for tracking the time taken by these small particles to travel between two points 4.85 m apart in the downcomer of the 8-tube reactor system. The range of gas flow F ranged from 100 to 600 $ml.min^{-1}$. The average time t_{ave} for each F was then

used to calculate an average velocity in the tubes, according to: $v = \frac{4.85}{t_{ave}}$. Other values inferred from this data are also shown; such as, the velocity v (m.s^{-1}), volumetric flow Q (m^3.s^{-1}) and Reynolds number Re (-).

Table E.6 – Calibration data for 8-tube reactor system: Time taken for tracer particles to travel 4.85 m in downcomer, repeated for gas flow rates F.

F (ml.min^{-1})	$t_{measured}$ (sec)							t_{ave} (sec)	std. deviation in t_{ave}	% error	v (m.s^{-1})	Q (m^3.s^{-1})	Re
100	37.81	37.94						37.88	0.09	0.24	0.13	4.93E-06	897
200	27.31	29.3	29					28.54	1.07	3.76	0.17	6.54E-06	1190
400	13.84	15.06	16.6	16.11	15.16	15.31	16.57	15.52	0.99	6.35	0.31	1.20E-05	2188
500	14.62	13.62	14.5	13.72				14.12	0.52	3.67	0.34	1.32E-05	2406
600	13.2	13.03	12.97	13.19	13.16			13.11	0.10	0.79	0.37	1.42E-05	2590

It was not possible to physically measure a cycle time via the tracer particles undergoing a complete circulation of the loop. The bubbles in the riser section caused the particles to travel through the riser region far too slowly when compared to the actual fluid movement. For this reason, mathematical manipulation was required to be able to estimate a complete circulation time for the full loop (which includes the riser section).

The method required the gas holdup in the riser section to be known for each F. This was achieved by manually measuring the increase in fluid height $\triangle h$ for each F, and then calculating the hold-ups by the volume expansion method, i.e:

$$\varepsilon_r = \frac{\triangle V}{V + \triangle V} \tag{E.2}$$

Where $\triangle V$ is the increase in fluid volume as a result of gas bubbles, calculated from $\triangle V = \triangle h \cdot D_{tc}$ and D_{tc} is the diameter of the top cup (0.045 m). Table E.7 shows the results for estimated gas hold-ups for the 8-tube calibration.

Table E.7 – Calculated gas hold ups for the 8-tube reactor calibration using the volume expansion method.

F (ml/min)	Δh (cm)	Δh (m)	ΔV (m^3)	ε_r est.
100	0.40	0.004	6.36E-06	0.027
200	0.75	0.008	1.19E-05	0.049
400	1.50	0.015	2.39E-05	0.093
500	1.75	0.018	2.78E-05	0.107
600	2.00	0.020	3.18E-05	0.120

With the flow in the downcomer fully defined according to Table E.6, and the gas holdups known according to Table E.7, the flow in the riser could be defined using the continuity equation, which essentially a volumetric balance between the two regions.

$$v_r = \frac{Q}{A_r(1 - \varepsilon_r)} \tag{E.3}$$

Where Q is the volumetric flow rate (m^3.s^{-1}), A_r the area of the riser (m^2), and ε_r the estimated gas holdup in the riser (Table E.7). Thus, separate residence times for the downcomer tubes and riser

sections could be calculated separately, according to:

$$t_d = \frac{L_d}{v_d} \tag{E.4}$$

$$t_r = \frac{L_r}{v_r} \tag{E.5}$$

Where L_d and L_r are the total downcomer and riser lengths, respectively; v_d and v_r are the different velocities in the downcomer and riser regions. The full circulation time was then estimated to be the sum of these times, $t_c = t_d + t_r$. Table E.8 shows a summary of these calculations for all gas flow rates F tested.

Table E.8 – Calculation of circulation time t_C calibration for 8-tube reactor.

F (ml.min^{-1})	t_d (sec)	Q (m^3.s^{-1})	v_r (m.s^{-1})	t_r (sec)	t_c (sec)
100	44.00	4.93E-06	0.025	26.21	70.21
200	33.15	6.54E-06	0.034	19.30	52.45
400	18.03	1.20E-05	0.066	10.01	28.04
500	16.40	1.32E-05	0.074	8.96	25.36
600	15.23	1.42E-05	0.080	8.20	23.43

In this manner, a calibration curve of cycle time (t_c) as a function of gas flow rate was obtained for each reactor type, according to Fig. E.4.

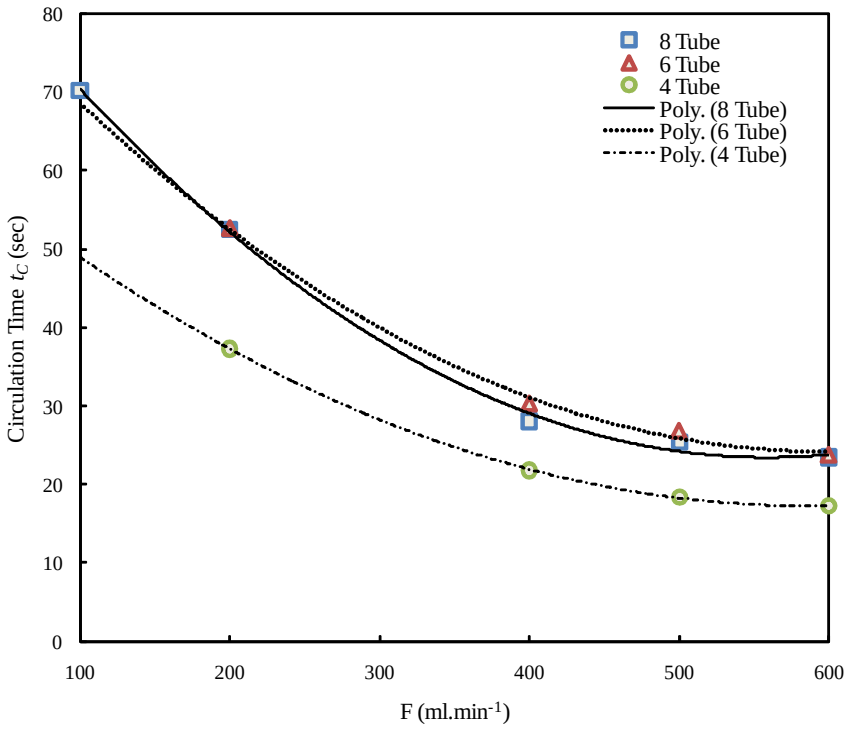

Figure E.4 – Calibration curves for cycle time t_C as a function of F for each tubular reactor system.

E.2.2 6 and 4-tube reactors cycle time calibration summary

6-tube system

Table E.9 – Calculation of riser and downcomer volumes for 6-tube reactor, utilizing the estimated downcomer length of $L_d = 4.24$ m ($L_r = 0.5$ m).

Description	Symbol	Formula	Units	Value
Downcomer Area	A_d	$\pi*0.25*D_d^2$	m^2	3.85E-05
Riser Area	A_r	$\pi*0.25*D_r^2$	m^2	2.54E-04
Reactor Volume	V	measured	dm^3	0.330
Downcomer Volume	V_d	A_d*L_d	dm^3	0.163
Riser Volume	V_r	$V - V_d$	dm^3	0.167

Table E.10 – Calibration data for 6-tube reactor system: Time taken for tracer particles to travel 3.48 m in downcomer, repeated for gas flow rates F.

F ($ml.min^{-1}$)	$t_{measured}$ (sec)				t_{ave} (sec)	std. deviation in t_{ave}	% error	v ($m.s^{-1}$)	Q ($m^3.s^{-1}$)	Re
100	x	x	x	x	x	x	x	x	x	x
200	26.53	26.68	23.8	23.44	25.11	1.50	5.97	0.14	5.33E-06	9.69E+02
400	15.31	14.72	14.75	14.56	14.84	0.28	1.91	0.23	9.02E-06	1.64E+03
500	13.25	13.1	13.34	13.06	13.19	0.11	0.86	0.26	1.01E-05	1.85E+03
600	11.65	11.62	11.75	11.7	11.68	0.05	0.42	0.30	1.15E-05	2.08E+03

Table E.11 – Calculated gas hold ups for the 6-tube reactor calibration using the volume expansion method.

F (ml/min)	Δh (cm)	Δh (m)	ΔV (m^3)	ε_r est.
100	0.60	0.006	9.54E-06	0.054
200	0.90	0.009	1.43E-05	0.079
400	1.60	0.016	2.54E-05	0.132
500	1.70	0.017	2.70E-05	0.140
600	1.70	0.017	2.70E-05	0.140

Table E.12 – Calculation of circulation time t_C calibration for 6-tube reactor.

F ($ml.min^{-1}$)	t_d (sec)	Q ($m^3.s^{-1}$)	v_r ($m.s^{-1}$)	t_r (sec)	t_c (sec)
100	x	x	x	x	
200	30.65	5.33E-06	0.023	21.99	52.65
400	18.11	9.02E-06	0.041	12.24	30.35
500	16.10	1.01E-05	0.046	10.79	26.89
600	14.26	1.15E-05	0.052	9.56	23.82

4-tube system

Table E.13 – Calculation of riser and downcomer volumes for 4-tube reactor, utilizing the estimated downcomer length of $L_d = 2.86$ m ($L_r = 0.28$ m).

Description	Symbol	Formula	Units	Value
Downcomer Area	A_d	$\pi*0.25*D_d^2$	m^2	3.85E-05
Riser Area	A_r	$\pi*0.25*D_r^2$	m^2	2.54E-04
Reactor Volume	V	measured	dm^3	0.209
Downcomer Volume	V_d	A_d*L_d	dm^3	0.110
Riser Volume	V_r	$V - V_d$	dm^3	0.099

Table E.14 – Calibration data for 4-tube reactor system: Time taken for tracer particles to travel 2.1 m in downcomer, repeated for gas flow rates F.

F (ml.min^{-1})	$t_{measured}$ (sec)						t_{ave} (sec)	std. deviation in t_{ave}	% error	v (m.s^{-1})	Q (m^3.s^{-1})	Re
100	31.84	31.06	30.94	too slow			x	x	x	x	x	x
200	16.66	17.22	17.5	17.3	17.13		14.35	0.31	2.17	0.15	5.64E-06	1.02E+03
400	10.19	10.06	10.07	10.06			8.09	0.06	0.79	0.26	1.00E-05	1.82E+03
500	8.53	8.47	8.62	8.62			6.86	0.07	1.07	0.31	1.18E-05	2.14E+03
600	7.94	7.84	7.87	8.15	8.15	8.03	6.87	0.14	1.97	0.31	1.18E-05	2.14E+03

Table E.15 – Calculated gas hold ups for the 4-tube reactor calibration using the volume expansion method.

F (ml/min)	Δh (cm)	Δh (m)	ΔV (m^3)	ε_r est.
100	0.30	0.003	4.77E-06	0.046
200	0.55	0.006	8.75E-06	0.081
400	0.67	0.007	1.07E-05	0.097
500	0.70	0.007	1.11E-05	0.101
600	0.70	0.007	1.11E-05	0.101

Table E.16 – Calculation of circulation time t_C calibration for 4-tube reactor.

F (ml.min^{-1})	t_d (sec)	Q (m^3.s^{-1})	v_r (m.s^{-1})	t_r (sec)	t_c (sec)
100	x	x	x	x	
200	19.56	5.64E-06	0.024	11.62	31.17
400	11.02	1.00E-05	0.044	6.43	17.45
500	9.35	1.18E-05	0.052	5.43	14.78
600	9.37	1.18E-05	0.051	5.44	14.81

E.3 Model to test for CO_2 limitations

A simple CO_2 mass transfer model was used to test for CO_2 limitations in the downcomer tubes during the design phase. In the riser section, CO_2 is supplied by mass transfer and consumed via biomass formation:

$$\frac{dC}{dt} = k_L a(C_{sat} - C) - \mu_{max} C_x Y \tag{E.6}$$

where $k_L a$ is an assumed mass transfer coefficient (s^{-1}), C_{sat} the saturation solubility of CO_2 at 25°C in g.L^{-1}, C the concentration of dissolved CO_2in g.L^{-1}, $\mu_{max}$the maximum specific growth rate (s^{-1}), C_x the biomass concentration (g.L^{-1}) and Y an assumed yield coefficient for the mass of CO_2 utilized per mass of biomass formed (g.g^{-1}).

In the downcomer section ,CO_2 was assumed to only be consumed by biomass formation, thus:

$$\frac{dC}{dt} = -\mu_{max} C_x Y \tag{E.7}$$

The rate of biomass formation was modeled as exponential growth for both the riser and downcomer sections:

$$\frac{dC_x}{dt} = -\mu_{max} C_x \tag{E.8}$$

The model was solved as follows:

1. A percentage concentration of CO_2 in the gas feed was defined. This %CO_2 was first converted to partial pressure P_{CO_2} to estimate the saturation solubility in the liquid C_{sat} via Henry's Law:

$$C_{sat} = k \cdot P_{CO_2} \tag{E.9}$$

Where $P_{CO_2} = \frac{\%CO_2}{100}$ and k = 0.034 mol.l^{-1}.atm^{-1}, Henry's Law constant at 25 °C.

2. A maximum growth rate μ_{max} was assumed during the design phase. Since all the experiments have been completed, one might as well use the maximum growth rate encountered over all runs, thus, $\mu_{max} = 0.143\,\mathrm{h}^{-1} = 3.97 \times 10^{-5}\mathrm{s}^{-1}$.

2. A circulation time was assumed (e.g $t_C = 45$ sec) and the residence times for both the riser and downcomer regions calculated. During preliminary design, these had to be estimated by assuming reactor dimensions and performing iterative calculations using the continuity equation and basic correlations for gas-holdup. After calibrations were performed (Section E.2), it was found that the riser time was on average 37% of the total circulation time. This enabled the linear velocity in the riser V_{Lr} and downcomer V_{Ld} to be estimated.

3. A superficial gas velocity U_{Gr} was estimated from the linear liquid velocity in the riser V_{Lr} by using the correlation of Bello et al (1985), cited in Wu & Merchuk (2004):

$$U_{Gr} = \left(\frac{V_{Lr}}{0.66}\right)^{\frac{1}{0.33}} \tag{E.10}$$

4. Knowing U_{Gr} enabled k_La to be estimated from the correlation of Miron *et al.* (2000) for bubble columns:

$$k_La = \frac{0.874}{U_G^{-0.979} - 1} \tag{E.11}$$

5. The biomass yield on CO_2 Y was estimated from the general chemical formula of algae biomass (which assumed 44.6% carbon) and by assuming all of the CO_2 was converted to biomass, this gave $Y = 1.6357$ g.g^{-1}.

6. With everything defined, Equations E.6 to E.8 were integrated over the assumed cycle until the system reached steady state. The result gave the steady state concentration profile of CO_2 in the liquid and predicted a concentration at the end of the downcomer region. If this value was negative then it implied that more than the available $CO_2$was consumed in the downcomer, i.e CO_2 limitations existed. Thus, the CO_2concentration in the gas feed could be varied to find the critical limit at which the downcomer would not be CO_2 limited.

Example of model results

Fig. E.5 shows an example of the model result for assuming $t_C = 45$seconds (with 37% of that time spend in the riser). A conservative *worst case* mass transfer coefficient of 0.0001 s^{-1}was assumed. The lowest value encountered by Miron *et al.* (2000) for an airlift reactor was k_La = 0.0025 s^{-1} at U_{Gr} of 0.05 m.s^{-1}. The results show profiles for two different assumed % CO_2in the feed. The time points and $t = 0$ and $t = 45$ seconds represent the end of the downcomer and start of the riser. For 0.1 % CO_2 the model predicts limitations whereas for 0.2 % CO_2 limitations are avoided. Both are far below the 3% CO_2 used in this work. Even though the model is simplistic and based on assumptions, it is a fairly safe bet to assume that at 3% CO_2, limitations are completely avoided.

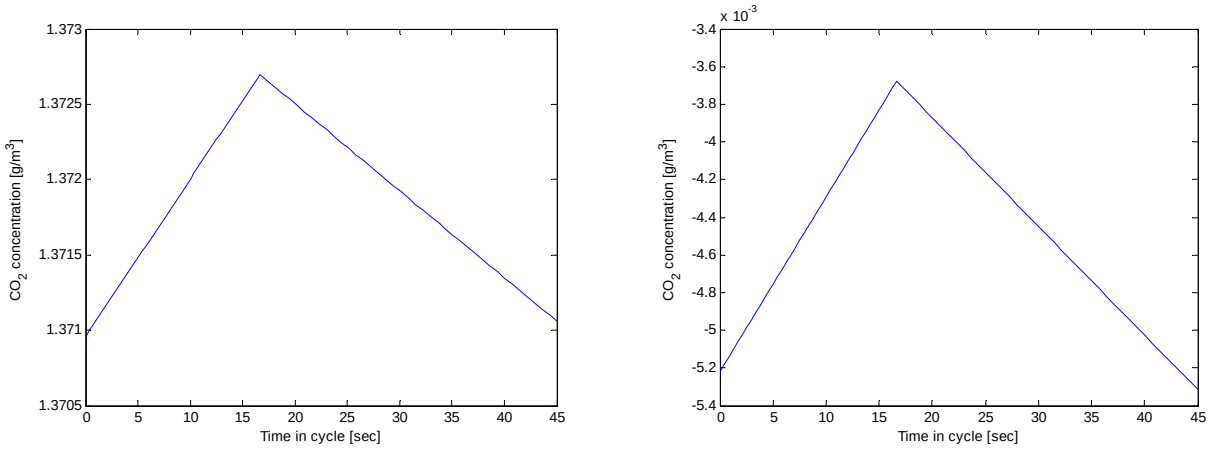

(a) 0.2 % CO_2 **(b)** 0.1 % CO_2

Figure E.5 – Model results for different % CO_2feeds.

Appendix F

Mathematical derivations and solutions

F.1 Derivation of Chisti (1989) liquid circulation model

The derivation of the expression that relates the superficial liquid velocity in an airlift reactor to the reactor height and gas hold-up's is presented from Chisti *et al.* (1988) .

First an energy balanced is performed over an airlift loop:

$$E_i = E_R + E_D + E_B + E_T + E_F \tag{F.1}$$

where, E_i is the energy input due to isothermal gas expansion, E_R is energy dissipation due to wakes behind bubbles in the riser, E_D is energy lost due to stagnant gas in the downcomer, E_B and E_T is energy lost due to friction and fluid turn-around at the bottom and top of the reactor, and E_F is energy lost due to friction in the riser and downcomer. When considering Newtonian, low viscosity flows, E_F in an air-lift vessel is negligible compared to dissipation due to the other terms in Eq. F.1, and therefore it is ignored. E_R can be determined by performing an energy balance on the riser, using the riser liquid as the control volume:

$$E_i = E_R - \rho_L g h_D (1-\varepsilon_r) U_{Lr} A_r + \rho_L g h_D U_{Lr} A_r \tag{F.2}$$

Hence,

$$E_R = E_i - \rho_L g h_D U_{Lr} A_r \varepsilon_r \tag{F.3}$$

E_D can be determined by performing an energy balance on the downcomer, using the downcomer liquid as the control volume:

$$0 = E_D + \rho_L g h_D (1-\varepsilon_d) U_{Ld} A_d - \rho_L g h_D U_{Ld} A_d \tag{F.4}$$

Re-arranging:

$$E_D = \rho_L g h_D U_{Ld} A_d \varepsilon_d \tag{F.5}$$

The energy losses in the top and bottom sections of the air-lift reactor can be determined as for pipe flow:

$$E_B + E_T = \frac{1}{2}\rho_L \left[V_{Lr}^3 K_T A_r (1-\varepsilon_r) + V_{Ld}^3 K_B A_d (1-\varepsilon_d)\right] \tag{F.6}$$

Where, $K_T$and K_B are the friction loss coefficients for the top and bottom connecting sections. Here V_{Lr} and V_{Ld} are the true linear liquid velocities in the riser and downcomer, respectfully. V_{Lr} and can be written as a function of superficial liquid velocities U_{Lr} according to:

$$V_{Lr} = \frac{U_{Lr}}{(1-\varepsilon_d)} \tag{F.7}$$

Furthermore, the continuity equation relates the liquid flow between the downcomer and riser as the following:

$$V_{Lr} A_r (1-\varepsilon_r) = V_{Ld} A_d (1-\varepsilon_d) \tag{F.8}$$

Thus, Equations F.6, F.8 and F.7 can be combined to obtain:

$$E_B + E_T = \frac{1}{2}\rho_L U_{Lr}^3 A_r \left[\frac{K_T}{(1-\varepsilon_r)^2} + K_B \left(\frac{A_r}{A_d}\right)^2 \frac{1}{(1-\varepsilon_d)^2}\right] \tag{F.9}$$

Finally, by substitution of F.9, F.5and F.3 into F.1 , the following expression is obtained:

$$E_i = E_i - \rho_L g h_D U_{Lr} A_r \varepsilon_r + \rho_L g h_D U_{Ld} A_d \varepsilon_d + \frac{1}{2}\rho_L U_{Lr}^3 A_r \left[\frac{K_T}{(1-\varepsilon_r)^2} + K_B \left(\frac{A_r}{A_d}\right)^2 \frac{1}{(1-\varepsilon_d)^2}\right] \tag{F.10}$$

which, can be re-written explicitly in terms of U_{Lr} :

$$U_{Lr} = \sqrt{\frac{2 g h_D (\varepsilon_r - \varepsilon_d)}{\frac{K_T}{(1-\varepsilon_r)^2} + K_B \left(\frac{A_r}{A_d}\right)^2 \frac{1}{(1-\varepsilon_d)^2}}} \tag{F.11}$$

Equation F.11 can be simplified for internal-loop airlift reactors. The energy loss in the top will be minimal compared to that in the bottom since the top head-space can be likened to an open channel as apposed to a constricted flow path (Chisti *et al.*, 1988). Thus, the K_T term can be ignored, giving:

$$U_{Lr} = \sqrt{\frac{2 g h_D (\varepsilon_r - \varepsilon_d)}{K_B \left(\frac{A_r}{A_d}\right)^2 \frac{1}{(1-\varepsilon_d)^2}}} \tag{F.12}$$

F.2 Methods of integrating kinetic model equations

The two additional methods for integrating the kinetic model are presented here: (i) the eigen vector method and (ii) the numerical 4^{th} order Runge-Kutta method. Section 4.1 presents a detailed solution for the analytical method. A built-in MATLAB numerical integrator was also tested (ode45, a common non-stiff solver). Numerical methods were investigated to account for the possibility of a non-linear kinetic model, for which a purely analytical solution would be non-trivial. The computational efficiency of these methods was briefly analyzed and is presented at the end of this section.

F.2.1 Eigen vector method for solving kinetic model

The set of model ODEs (Equations 4.1 to 4.3) can be represented in matrix form as:

$$\dot{X} = AX \tag{F.13}$$

$$\text{where, } A = \begin{bmatrix} -\alpha I & \gamma & \delta \\ \alpha I & -(\gamma+\beta I) & 0 \\ 0 & \beta I & -\delta \end{bmatrix} \text{ and } X = \begin{bmatrix} x_1 \\ x_2 \\ x_3 \end{bmatrix} \text{ and } \dot{X} = \begin{bmatrix} \frac{dx_1}{dt} \\ \frac{dx_2}{dt} \\ \frac{dx_3}{dt} \end{bmatrix}$$

We make the substitution $X = PY$, where $Y = \begin{bmatrix} y_1 \\ y_2 \\ y_3 \end{bmatrix}$. Since X is a function of t, so is Y and $\dot{X} = P \cdot \dot{Y}$. P is a 3x3 matrix whose columns are the corresponding eigen vectors so that $AP = PD$, with D a diagonal matrix of eigen values.

Substituting:

$$P\dot{Y} = AX = A(PY) \tag{F.14}$$

Thus:

$$\dot{Y} = (P^{-1}AP)Y = DY = \begin{bmatrix} \lambda_1 & 0 & 0 \\ 0 & \lambda_2 & 0 \\ 0 & 0 & \lambda_3 \end{bmatrix} Y \tag{F.15}$$

Hence:

$$\frac{dy_1}{dt} = \lambda_1 y_1 \text{ , } \frac{dy_2}{dt} = \lambda_2 y_2 \text{ and } \frac{dy_3}{dt} = \lambda_3 y_3.$$

These differential equations are well known and have simple solutions:

$$y_1 = y_{10}e^{\lambda_1 t}\ ,\ y_2 = y_{20}e^{\lambda_2 t} \text{ and } y_3 = y_{30}e^{\lambda_3 t}$$

where y_{10}, y_{20}, y_{30} are the values when $t = 0$. These are easily obtained by:

$$\begin{bmatrix} y_{10} \\ y_{20} \\ y_{30} \end{bmatrix} = Y_0 = P^{-1}X_0 = P^{-1}\begin{bmatrix} x_{10} \\ x_{20} \\ x_{30} \end{bmatrix} \tag{F.16}$$

Thus in full matrix form:

$$Y = Y_0 e^{Dt} \tag{F.17}$$

and this is transform back to the solution for X as an explicit function of t:

$$X = \begin{bmatrix} x_1(t) \\ x_2(t) \\ x_3(t) \end{bmatrix} = PY_0e^{Dt} \tag{F.18}$$

In this manner, functions of $x_1(t), x_2(t)$ and $x_2(t)$ can be obtained explicitly for any given set of parameters and light intensity, which define A, and P and D can be calculated using a built in MATLAB function: $[P,D] = \text{eig}(A)$.

To utilize this solution for the dark period, the initial conditions at the start of the dark period are defined according to the final conditions of the light period using Eq. F.16. Since $I = 0$ for the dark period, A is redefined as:

$$A = \begin{bmatrix} 0 & \gamma & \delta \\ 0 & -\gamma & 0 \\ 0 & 0 & -\delta \end{bmatrix} \tag{F.19}$$

D is recalculated using this new A and the final solution for the dark period is of the same form as Eq. F.18.

F.2.2 4th order Runge-Kutta numerical method for solving kinetic model

The most common Runge-Kutta method is of order 4. To integrate a set of ODEs over an interval $[a,b]$, one first defines a step-size h according to $h = \frac{b-a}{N}$, with N being the chosen the number of mesh points over the interval. The time at every mesh point i is:

$$t_i = a + ih \quad i = 0,1,2,...,N \tag{F.20}$$

To integrate over a cycle, say $[0\,, t_C]$, the initial conditions are $w_0 = [x_{10}, x_{20}]$ and $t_0 = 0$, where w denotes the approximation to $[x_1(t), x_2(t)]$.

We define $\left[\frac{dx_1}{dt}, \frac{dx_2}{dt}\right] = f(t,x)$, where:

$$\frac{dx_1}{dt} = -\alpha I x_1 + \gamma x_2 + \delta(1 - x_1 - x_2) \tag{F.21}$$

$$\frac{dx_2}{dt} = \alpha I x_1 - \gamma x_2 - \beta I x_2 \tag{F.22}$$

To implement the Runge-Kutta method, for $i = 0, 1, 2, ..., N$ we calculate:

$$\begin{aligned} k_1 &= h \cdot f(t_i, w_i) \\ k_2 &= h \cdot f(t_i + \frac{h}{2}, w_i + \frac{1}{2}k_1) \\ k_3 &= h \cdot f(t_i + \frac{h}{2}, w_i + \frac{1}{2}k_2) \\ k_4 &= h \cdot f(t_{i+1}, w_i + k_3) \\ w_{i+1} &= w_i + \frac{1}{6}[k_1 + 2k_2 + 2k_3 + k_4] \end{aligned} \tag{F.23}$$

The result is w, which approximates the solution $[x_1(t), x_2(t)]$ at every i. To integrate over the dark period, the process is repeated for new initial values w_0, defined via the final values at the end of the light period. In addition, $I = 0$ in Equations F.21 and F.22.

F.2.3 Comparison of computational efficiency between integration methods

Because the global airlift model requires the kinetic model to be integrated many times during the simulation, it is worth analyzing the efficiency of each method with consideration to overall computational time. To do this, each was used integrate a single light cycle of $t_C = 20$ sec and I = 100 μmol·m^{-2}·s^{-1}. The time taken to perform the integration in MATLAB was compared, as well as the final calculated value of the PSF fraction x_2. Table F.1 shows the results and Fig. F.1 shows the PSF profiles calculated using each method.

The eigen vector method was the fasted. The Runge-Kutta method (using 10 steps) and the analytical method had hardly a difference between them and the built-in MATLAB ode45 integrator was extremely slow by comparison. Since the global model solution was based on the development by Wu & Merchuk (2004), the analytical method was used for the global model in this work. However, this analysis shows that the Eigen vector method may be more efficient. The eigen vector method is of course limited to linear systems, thus, should a non-linear kinetic model be incorporated, the numerical Runge-Kutta method could be used, with very similar computational times to that of the analytical method

Table F.1 – Computational times for each method as well as final x_2 value. Runge-Kutta method (Section F.2.2) simulated with 10 steps.

Method	Time (sec)	Final x_2
Analytical	0.005597	0.56895
Eigen Vector	0.000381	0.56895
Runge-Kutta (numerical)	0.004023	0.56894
ode45 (numerical)	0.307213	0.56895

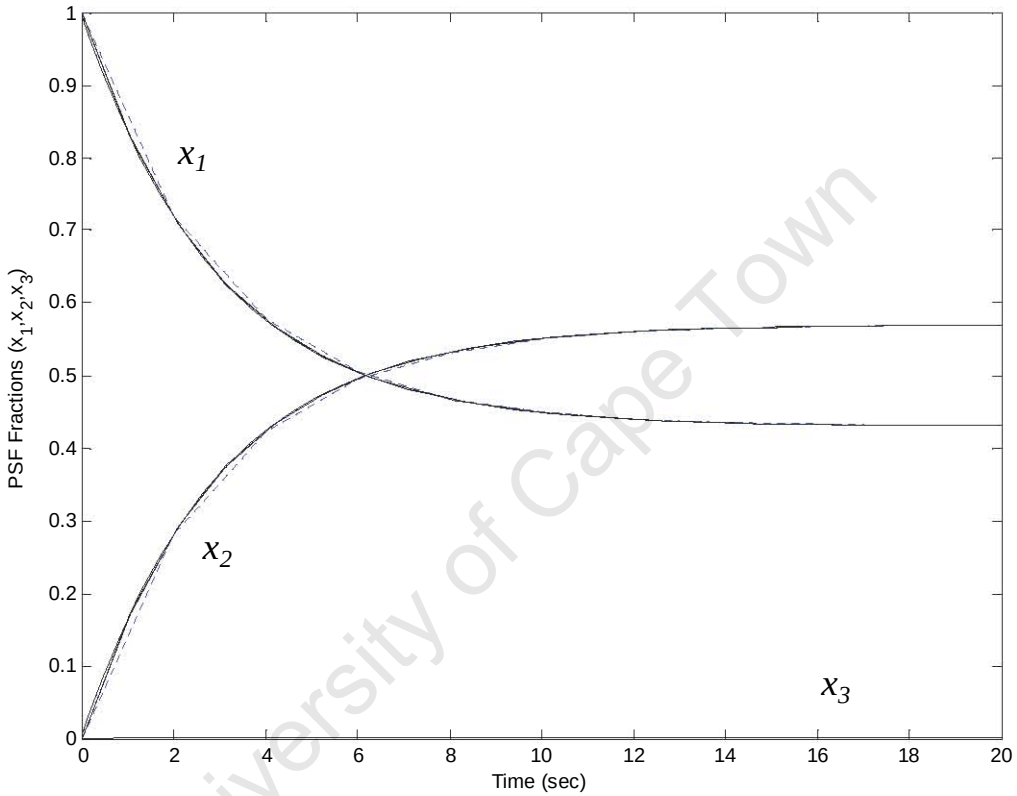

Figure F.1 – Simulation of PSF profiles using the different integration methods. The solid dark lines show the profiles of the analytical, eigen and ode45 method; which are almost indistinguishable. The dotted line shows the Runge-Kutta profile. The smoothness of the Runge-Kutta profile can be improved by increasing the number of steps (i.e decreasing step-size) but this increases its computational time. However, such an improvement is unnecessary since the final value of x_2 with 10 steps is almost identical to the analytical solution (see Table F.1).

F.3 Linear versus geometric mean comparison

The true geometric mean for the light distribution function for any i^{th} interval is given by:

$$I_{ave,i} = \frac{2\int_{z_{i-1}}^{z_i}(R-z)I(z,C_x)dz}{(R-z_{i-1})^2-(R-z_i)^2} \quad (i=1,2,...,p) \tag{F.24}$$

The trapezoidal rule is an approximate technique for calculating a definite integral, given by:

$$\int_a^b f(x)dx \approx (b-a)\frac{f(a)+f(b)}{2} \tag{F.25}$$

Applying this rule to Eq. F.24 yields an approximate trapezoidal method for calculating the integral in Eq. F.24:

$$\bar{I}_{d,i} = (z_i - z_{i-1})\left[\frac{(R-z_{i-1})\cdot I(z_{i-1},C_x)+(R-z_i)\cdot I(z_i,C_x)}{(R-z_{i-1})^2-(R-z_i)^2}\right] \quad (i=1,2,...,p) \tag{F.26}$$

For calculation of average light intensities over an interval, a simple simulation enabled the error to be compared between the trapezoidal mean (Eq. F.26) and true geometric mean (Eq. F.24) . A 2 cm column diameter was assumed. The total number of intervals was varied from 2 to 24 and the cell concentration varied from 1 to 5 g.L $^{-1}$. *i.e* for 3 intervals, each interval has a width 2/3 cm, for 25 intervals the width is 0.08 cm. For each scenario, the maximum error between the two calculated values of I/I_0encountered over *all* intervals was reported. Table **??** shows the results for each scenario and Fig. F.2 gives a graphical comparison between the cases of 3 and 20 intervals. As the number of intervals increases the error between the two values decreases considerably. The error decreases to a lesser degree for higher cell concentrations, owing to the more rapid decay in the light distribution function. Importantly, the error over all other intervals is equal to or less than that reported in Table **??**, Fig. F.2 illustrates this. For sufficient intervals, the overall error between the two methods is very small and thus the trapezoidal method of calculation is sufficient when considering increased computational time for integration of Eq. F.24.

Table F.2 – Maximum error (%) encountered over all intervals between the geometric and trapezoidal method for calculating the average PFD.

p	C_x (g.L^{-1})				
	1	2	3	4	5
2	28.73	53.72	75.21	93.67	109.60
3	17.87	32.95	45.73	56.63	66.02
4	12.96	23.72	32.76	40.42	47.00
5	10.16	18.52	25.49	31.39	36.43
6	8.36	15.19	20.86	25.64	29.72
7	7.10	12.87	17.65	21.66	25.08
8	6.17	11.16	15.29	18.75	21.70
9	5.45	9.86	13.49	16.53	19.11
10	4.89	8.83	12.07	14.78	17.08
11	4.43	7.99	10.91	13.36	15.44
12	4.05	7.30	9.96	12.19	14.08
13	3.73	6.71	9.17	11.21	12.94
14	3.45	6.22	8.49	10.38	11.97
15	3.22	5.79	7.90	9.66	11.14
16	3.01	5.42	7.39	9.03	10.42
17	2.83	5.09	6.94	8.48	9.78
18	2.67	4.80	6.54	7.99	9.22
19	2.53	4.54	6.19	7.56	8.72
20	2.40	4.31	5.87	7.17	8.27
21	2.28	4.10	5.58	6.82	7.86
22	2.17	3.91	5.32	6.50	7.49
23	2.08	3.74	5.09	6.21	7.16
24	1.99	3.58	4.87	5.94	6.85

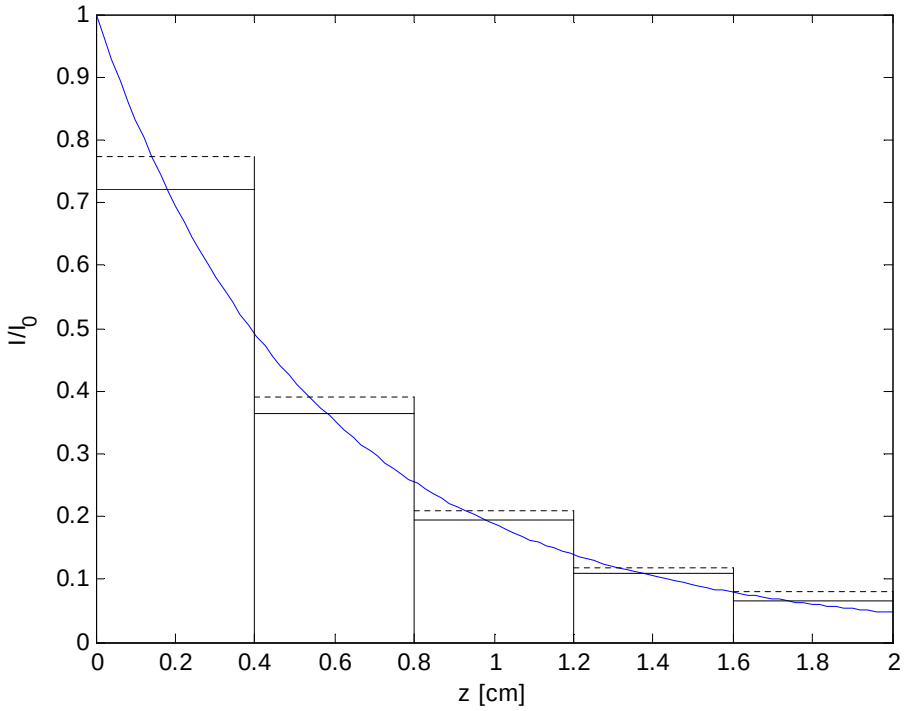

(a) 5 intervals.

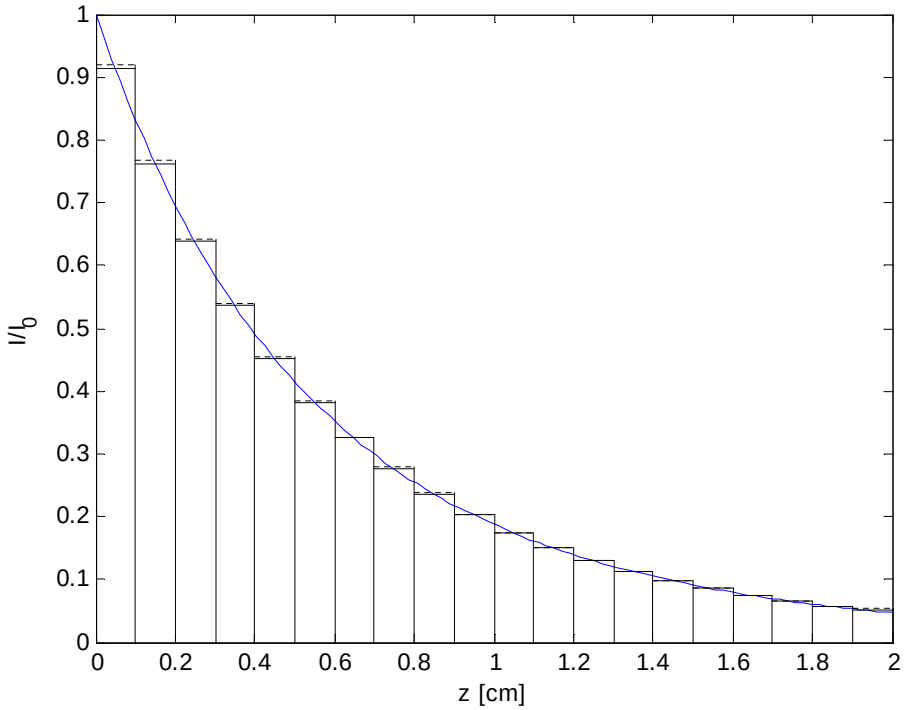

(b) 20 intervals.

Figure F.2 – Comparison between true geometric mean and linear mean for calculating average light intensity over each interval. Dotted line shows the linear mean value. For simulation: $C_x = 2$ g.L^{-1}.

Appendix G

Methods of solution and algorithms

Model regressions were coded in MATLAB utilizing a non-linear solver called *lsqcurvefit.* The solver performs least square regression and uses a trust-region-reflective algorithm. For more information about this solver, the reader is referred to: http://www.mathworks.com/help/toolbox/optim/ug/lsqcurvefit.html

The solver produced outputs for each regression performed, as shown by the example given in Fig. G.1

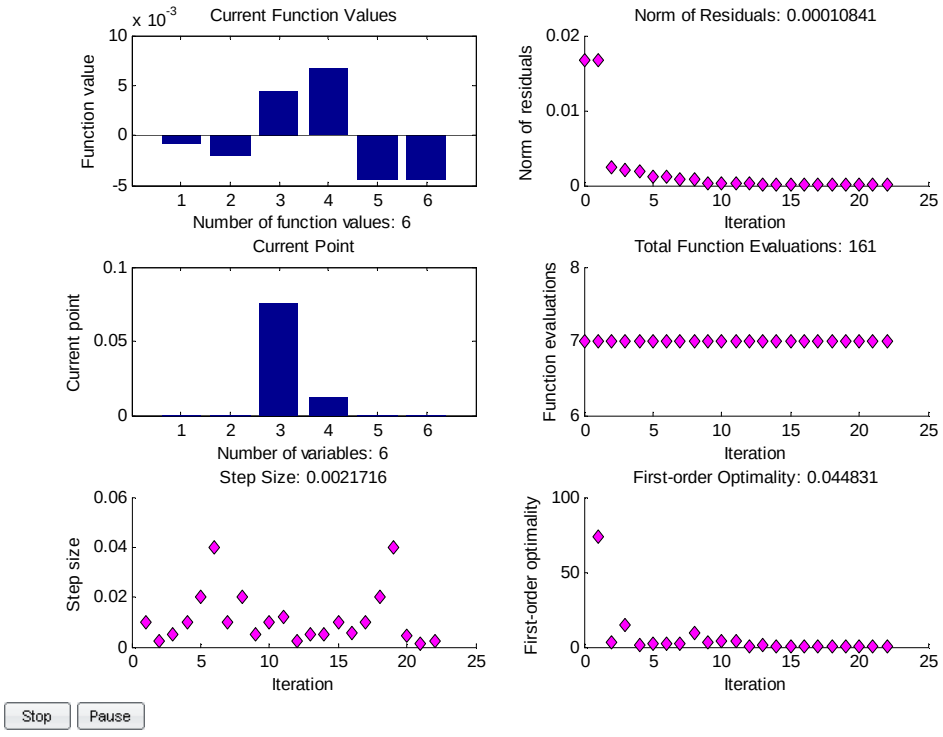

Figure G.1 – Typical solver output for kinetic model regression. Specifically for fitting to $t_C = 21$sec data.

G.1 Algorithm for obtaining light model parameters

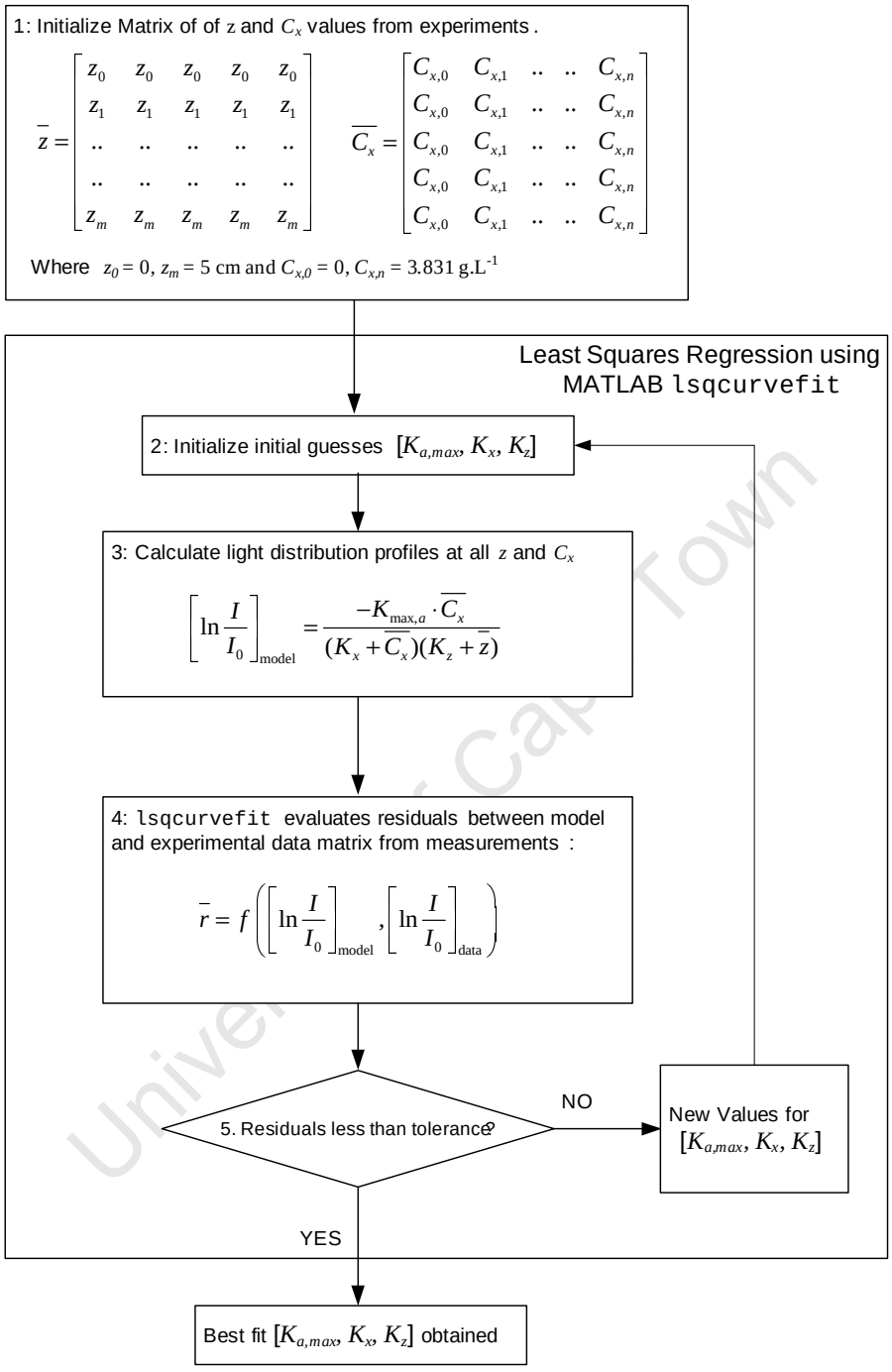

Figure G.2 – Algorithm for obtaining best-fit light model parameters.

G.2 Algorithm for obtaining kinetic model parameters

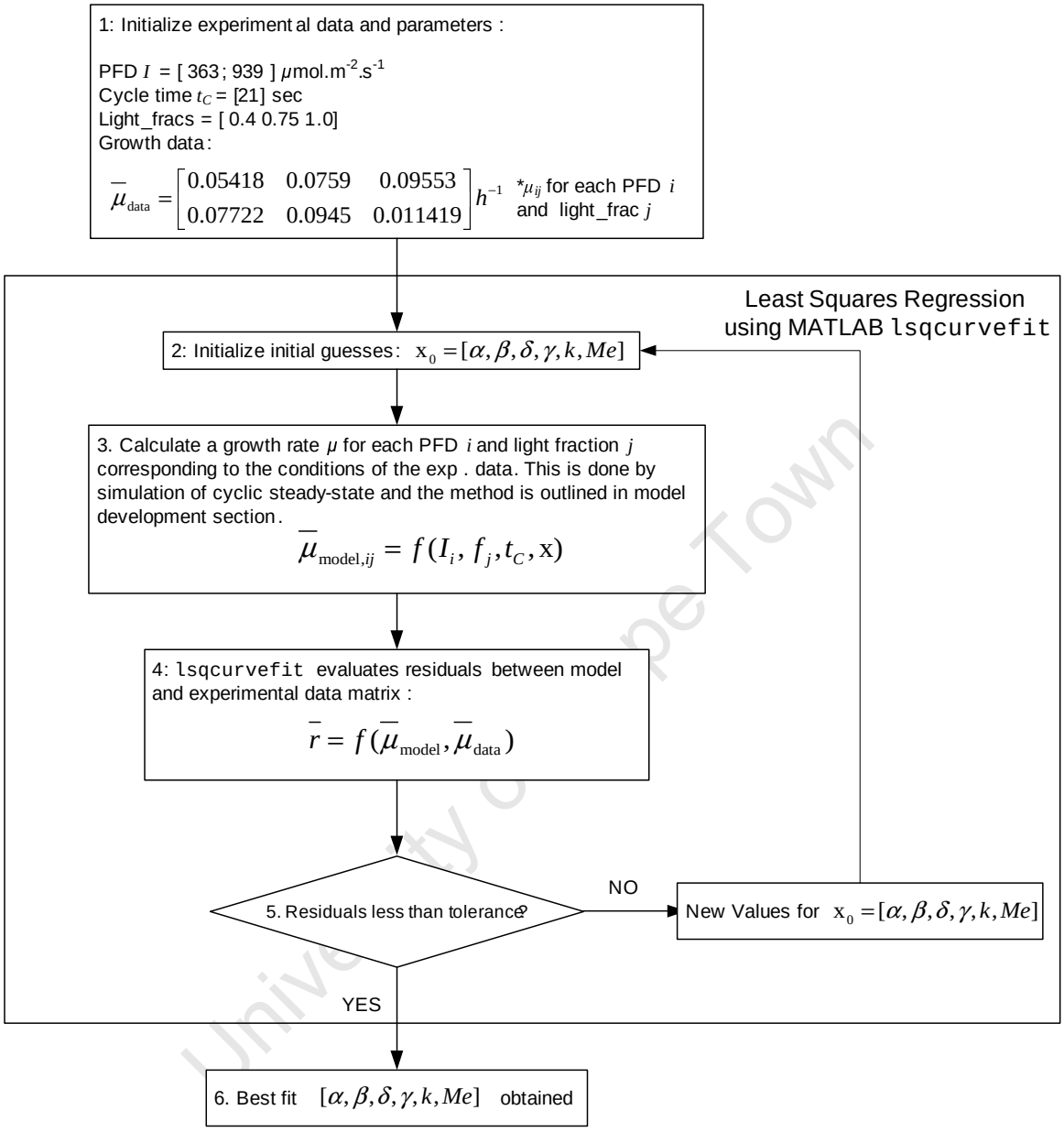

Figure G.3 – Algorithm for obtaining best-fit kinetic model parameters. Example gives numeric values for fitting $t_C = 21$ sec data specifically. For the other fits mentioned in Section 4.3.3, the values of t_C and $\bar{\mu}_{\text{data}}$ were different.

G.3 Algorithm for solving hydrodynamic model and obtaining model parameters

The grey box in Fig. G.4 illustrates the iterative method of solving for U_{Lr} as a function of U_{Gr}.

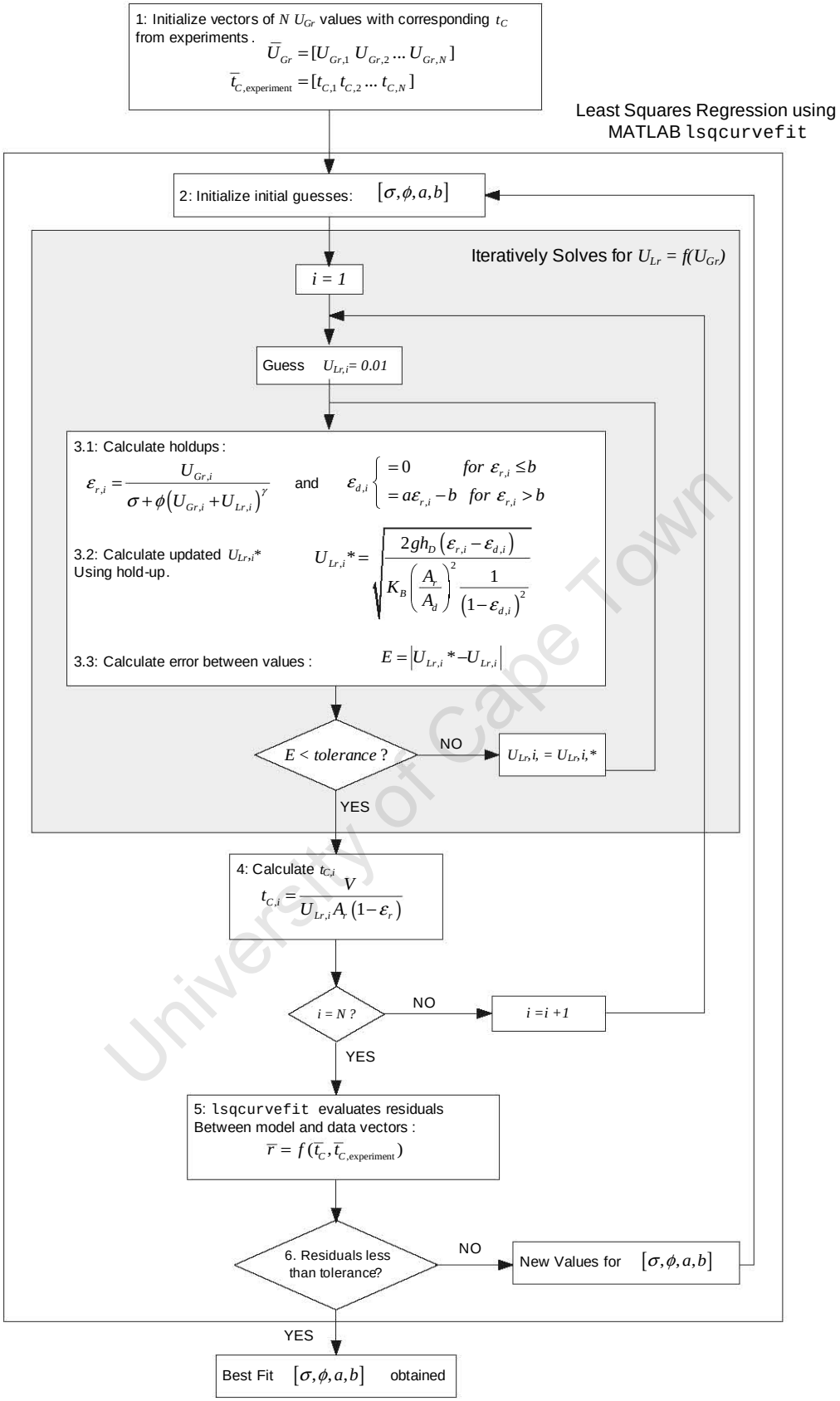

Figure G.4 – Algorithm for obtaining best-fit hydrodynamic model parameters.

Appendix H

Experimental Data

H.1 Data for absorbance spectra and Beer-Lambert law parameters

Absorbance data for *Scenedesmus* over the PAR range (400 - 700 nm) was obtained using using standard 1 cm cuvettes in a spectrophotometer (Helios Gamma UV-Vis, Thermo Scientific). Concentrations were varied from 0.227 to 2.270 g.L^{-1} to produce the data given in Table H.2 and shown graphically in Fig. 3.8. Beer-Lambert law absorption coefficients $K_a(\lambda)$ were calculated for each λ by linear regression of $A'(C_x,\lambda) = K_a(\lambda)\cdot C_x$. This was only performed for $C_x < 1$ g.L^{-1}, since the relationship between absorbance $A'(C_x,\lambda)$ and C_x was non-linear (i.e did not obey Beer-Lambert law) at any greater concentrations.

A sample of this calculation is summarized in Table H.1 for calculating $K_a(\lambda = 400)$. For each concentration, an absorbance was estimated from $A'_{est}(C_x,\lambda) = K_a(\lambda)\cdot C_x$ based on an assumed $K_a(\lambda)$. The error between the estimated absorbance and the actual absorbance at each concentration is calculated according to:

$$\text{error} = \left[A'_{est}(C_x,\lambda) - A'(C_x,\lambda)\right]^2 \tag{H.1}$$

The sum of the errors was then minimized by varying $K_a(\lambda)$, with the best fit $K_a(\lambda)$ yielding the lowest error. In this manner the $K_a(\lambda)'s$ in Table H.2 were calculated for every wavelength. The average K_a was then calculated according to Eq. 2.10, yielding K_a= 2.30 L.g^{-1}.cm^{-1}.

Table H.1 – Sample of linear regression for calculating $K_a(\lambda = 400)$.

C_x (g.L^{-1})	0.227	0.454	0.681	0.908
Abs. actual	0.676	1.289	1.777	2.271
Abs. est.	0.591	1.181	1.772	2.363
error	0.0074	0.0118	0.0001	0.0067
error sum	0.026			

Table H.2 – Absorbance values $A'(C_x, \lambda)$ at integer wavelengths in the PAR range, measured at various *Scenedesmus* concentrations. $K_a(\lambda)$ values were calculated from linear regression of $A'(C_x, \lambda) = K_a(\lambda) \cdot C_x$ at every λ.

	Concentration ($g.L^{-1}$)						K_a (λ)
λ	0.227	0.454	0.681	0.908	1.135	2.270	($L.g^{-1}.cm^{-1}$)
400	0.676	1.289	1.777	2.271	2.633	3.564	2.595
401	0.677	1.290	1.780	2.280	2.649	3.545	2.602
402	0.677	1.292	1.783	2.285	2.661	3.558	2.606
403	0.678	1.294	1.788	2.295	2.660	3.575	2.616
404	0.678	1.296	1.793	2.298	2.672	3.613	2.620
405	0.679	1.298	1.797	2.304	2.692	3.660	2.626
406	0.680	1.302	1.804	2.317	2.708	3.686	2.638
407	0.681	1.304	1.808	2.323	2.716	3.602	2.644
408	0.681	1.306	1.815	2.332	2.734	3.686	2.653
409	0.681	1.309	1.818	2.341	2.750	3.666	2.661
410	0.682	1.311	1.824	2.351	2.759	3.701	2.670
411	0.683	1.312	1.828	2.356	2.769	3.674	2.675
412	0.683	1.314	1.833	2.363	2.782	3.731	2.681
413	0.684	1.314	1.837	2.372	2.785	3.682	2.689
414	0.684	1.317	1.840	2.376	2.801	3.762	2.693
415	0.685	1.318	1.845	2.384	2.805	3.796	2.701
416	0.686	1.320	1.847	2.389	2.809	3.740	2.705
417	0.686	1.322	1.851	2.391	2.827	3.686	2.709
418	0.685	1.323	1.853	2.397	2.828	3.726	2.713
419	0.686	1.324	1.855	2.400	2.833	3.851	2.716
420	0.686	1.325	1.857	2.402	2.837	3.724	2.719
421	0.685	1.326	1.858	2.404	2.840	3.765	2.721
422	0.682	1.323	1.858	2.401	2.829	3.735	2.717
423	0.683	1.324	1.859	2.406	2.835	3.818	2.721
424	0.683	1.324	1.862	2.412	2.840	3.757	2.726
425	0.683	1.326	1.864	2.416	2.852	3.760	2.730
426	0.684	1.326	1.867	2.420	2.855	3.788	2.734
427	0.685	1.329	1.871	2.426	2.867	3.780	2.740
428	0.685	1.331	1.874	2.432	2.869	3.830	2.746
429	0.685	1.333	1.878	2.437	2.881	3.815	2.751
430	0.686	1.334	1.881	2.443	2.886	3.799	2.756
431	0.686	1.336	1.884	2.449	2.899	3.821	2.762
432	0.686	1.337	1.887	2.454	2.905	3.815	2.766
433	0.687	1.338	1.889	2.457	2.909	3.801	2.769
434	0.687	1.339	1.890	2.461	2.907	3.788	2.772
435	0.687	1.340	1.891	2.463	2.914	3.815	2.774
436	0.687	1.340	1.891	2.463	2.913	3.788	2.774
437	0.687	1.340	1.891	2.464	2.914	3.839	2.775
438	0.687	1.341	1.891	2.461	2.909	3.799	2.773
439	0.686	1.340	1.889	2.460	2.903	3.810	2.771
440	0.686	1.339	1.885	2.454	2.897	3.833	2.765
441	0.686	1.338	1.883	2.450	2.893	3.836	2.762
442	0.685	1.336	1.879	2.443	2.887	3.839	2.755
443	0.685	1.334	1.873	2.433	2.868	3.810	2.746
444	0.684	1.332	1.868	2.425	2.859	3.836	2.738
445	0.683	1.328	1.862	2.415	2.843	3.801	2.729
446	0.682	1.324	1.854	2.402	2.824	3.830	2.717
447	0.680	1.320	1.846	2.390	2.807	3.818	2.705
448	0.679	1.316	1.839	2.379	2.795	3.818	2.693
449	0.678	1.312	1.830	2.366	2.773	3.824	2.681
450	0.677	1.307	1.821	2.351	2.752	3.824	2.666

	Concentration ($g.L^{-1}$)						K_a (λ)
λ	0.227	0.454	0.681	0.908	1.135	2.270	($L.g^{-1}.cm^{-1}$)
501	0.652	1.205	1.629	2.039	2.315	3.431	2.365
502	0.651	1.200	1.618	2.021	2.290	3.390	2.347
503	0.649	1.193	1.605	1.999	2.260	3.333	2.327
504	0.647	1.187	1.593	1.978	2.234	3.280	2.307
505	0.645	1.180	1.579	1.955	2.202	3.226	2.285
506	0.643	1.175	1.569	1.938	2.181	3.179	2.269
507	0.641	1.166	1.553	1.912	2.146	3.109	2.244
508	0.639	1.161	1.544	1.897	2.126	3.070	2.230
509	0.637	1.155	1.533	1.878	2.101	3.016	2.211
510	0.635	1.151	1.524	1.865	2.083	2.980	2.198
511	0.633	1.145	1.514	1.848	2.061	2.935	2.182
512	0.632	1.141	1.506	1.834	2.043	2.896	2.168
513	0.630	1.136	1.496	1.818	2.022	2.850	2.153
514	0.629	1.131	1.486	1.804	2.003	2.812	2.139
515	0.627	1.127	1.479	1.791	1.987	2.778	2.127
516	0.626	1.122	1.470	1.779	1.970	2.740	2.114
517	0.624	1.118	1.462	1.765	1.953	2.705	2.101
518	0.623	1.115	1.456	1.756	1.941	2.678	2.092
519	0.623	1.111	1.450	1.746	1.928	2.649	2.082
520	0.622	1.107	1.443	1.736	1.915	2.621	2.072
521	0.621	1.104	1.438	1.727	1.904	2.598	2.063
522	0.620	1.101	1.433	1.720	1.894	2.577	2.056
523	0.619	1.098	1.428	1.713	1.885	2.559	2.049
524	0.618	1.095	1.423	1.705	1.874	2.535	2.040
525	0.617	1.093	1.418	1.698	1.866	2.517	2.033
526	0.616	1.091	1.415	1.693	1.860	2.505	2.028
527	0.616	1.088	1.411	1.688	1.854	2.491	2.023
528	0.615	1.087	1.408	1.684	1.849	2.482	2.019
529	0.614	1.085	1.405	1.679	1.843	2.469	2.014
530	0.614	1.083	1.402	1.675	1.838	2.460	2.010
531	0.613	1.082	1.401	1.673	1.835	2.454	2.007
532	0.613	1.081	1.398	1.670	1.831	2.446	2.004
533	0.613	1.080	1.397	1.667	1.829	2.441	2.002
534	0.613	1.079	1.394	1.664	1.825	2.434	1.999
535	0.612	1.078	1.393	1.662	1.823	2.429	1.997
536	0.612	1.077	1.392	1.660	1.820	2.425	1.994
537	0.612	1.076	1.390	1.658	1.818	2.420	1.992
538	0.612	1.075	1.389	1.656	1.816	2.417	1.990
539	0.611	1.074	1.387	1.655	1.813	2.413	1.988
540	0.611	1.073	1.386	1.653	1.811	2.409	1.986
541	0.611	1.073	1.385	1.652	1.810	2.407	1.985
542	0.610	1.072	1.383	1.650	1.809	2.404	1.983
543	0.610	1.071	1.382	1.649	1.807	2.401	1.982
544	0.610	1.071	1.381	1.648	1.805	2.399	1.980
545	0.609	1.070	1.380	1.646	1.804	2.397	1.979
546	0.609	1.069	1.379	1.645	1.802	2.394	1.977
547	0.609	1.069	1.378	1.644	1.801	2.392	1.976
548	0.608	1.068	1.377	1.643	1.800	2.391	1.974
549	0.608	1.067	1.375	1.642	1.799	2.389	1.973
550	0.608	1.066	1.374	1.641	1.798	2.388	1.971
551	0.608	1.066	1.374	1.640	1.796	2.387	1.971

Concentration ($g.L^{-1}$)						K_a (λ)
0.227	0.454	0.681	0.908	1.135	2.270	($L.g^{-1}.cm^{-1}$)
0.676	1.302	1.813	2.338	2.732	3.810	2.654
0.675	1.298	1.804	2.324	2.713	3.839	2.640
0.675	1.294	1.798	2.313	2.695	3.772	2.629
0.674	1.290	1.791	2.303	2.681	3.810	2.619
0.674	1.287	1.785	2.295	2.670	3.775	2.611
0.673	1.284	1.781	2.287	2.657	3.783	2.603
0.673	1.283	1.777	2.281	2.651	3.770	2.598
0.673	1.280	1.774	2.275	2.642	3.757	2.593
0.673	1.279	1.770	2.271	2.636	3.775	2.588
0.673	1.276	1.767	2.266	2.628	3.810	2.583
0.674	1.275	1.764	2.259	2.623	3.765	2.577
0.674	1.274	1.762	2.259	2.616	3.770	2.576
0.674	1.273	1.759	2.255	2.614	3.783	2.572
0.674	1.272	1.759	2.252	2.607	3.767	2.570
0.674	1.271	1.755	2.249	2.604	3.767	2.566
0.673	1.270	1.753	2.246	2.601	3.760	2.563
0.673	1.270	1.753	2.244	2.595	3.788	2.562
0.672	1.268	1.751	2.242	2.593	3.752	2.559
0.671	1.268	1.750	2.240	2.591	3.762	2.558
0.670	1.267	1.749	2.240	2.588	3.752	2.556
0.669	1.266	1.748	2.238	2.586	3.780	2.555
0.669	1.265	1.747	2.238	2.584	3.770	2.554
0.668	1.264	1.745	2.237	2.582	3.762	2.552
0.669	1.264	1.745	2.235	2.583	3.752	2.551
0.668	1.263	1.744	2.234	2.581	3.755	2.550
0.668	1.262	1.743	2.234	2.581	3.747	2.549
0.668	1.262	1.743	2.234	2.580	3.757	2.549
0.668	1.262	1.743	2.233	2.579	3.765	2.548
0.668	1.262	1.743	2.234	2.580	3.752	2.549
0.668	1.262	1.743	2.235	2.581	3.747	2.549
0.668	1.262	1.744	2.235	2.583	3.777	2.550
0.668	1.262	1.744	2.237	2.583	3.735	2.550
0.668	1.262	1.744	2.235	2.582	3.767	2.550
0.668	1.262	1.744	2.236	2.583	3.757	2.550
0.669	1.261	1.742	2.234	2.580	3.745	2.548
0.669	1.260	1.740	2.231	2.574	3.752	2.545
0.669	1.259	1.738	2.226	2.569	3.760	2.541
0.669	1.258	1.735	2.221	2.562	3.745	2.536
0.669	1.256	1.731	2.214	2.553	3.742	2.530
0.669	1.254	1.727	2.206	2.542	3.733	2.523
0.667	1.251	1.722	2.197	2.530	3.706	2.515
0.667	1.248	1.715	2.186	2.514	3.695	2.504
0.665	1.245	1.708	2.174	2.497	3.668	2.492
0.664	1.241	1.700	2.161	2.480	3.666	2.480
0.662	1.236	1.691	2.144	2.457	3.633	2.464
0.661	1.233	1.685	2.132	2.441	3.613	2.453
0.660	1.227	1.672	2.112	2.414	3.582	2.435
0.658	1.222	1.663	2.096	2.393	3.550	2.419
0.657	1.217	1.653	2.078	2.368	3.517	2.402
0.655	1.212	1.644	2.063	2.346	3.476	2.388

	Concentration ($g.L^{-1}$)						K_a (λ)
λ	0.227	0.454	0.681	0.908	1.135	2.270	($L.g^{-1}.cm^{-1}$)
552	0.608	1.065	1.373	1.639	1.796	2.386	1.970
553	0.608	1.065	1.372	1.639	1.795	2.386	1.969
554	0.607	1.064	1.371	1.638	1.795	2.385	1.968
555	0.607	1.064	1.371	1.637	1.794	2.386	1.967
556	0.607	1.063	1.370	1.637	1.794	2.387	1.967
557	0.607	1.063	1.369	1.637	1.794	2.388	1.966
558	0.607	1.063	1.369	1.637	1.794	2.390	1.966
559	0.607	1.063	1.369	1.638	1.795	2.393	1.966
560	0.607	1.063	1.369	1.639	1.796	2.397	1.967
561	0.606	1.063	1.369	1.639	1.797	2.399	1.967
562	0.606	1.063	1.370	1.640	1.799	2.405	1.968
563	0.606	1.063	1.370	1.642	1.801	2.409	1.969
564	0.606	1.063	1.371	1.643	1.803	2.415	1.970
565	0.606	1.064	1.372	1.644	1.805	2.424	1.972
566	0.606	1.065	1.373	1.647	1.808	2.431	1.974
567	0.607	1.066	1.374	1.650	1.813	2.443	1.977
568	0.607	1.067	1.376	1.652	1.816	2.451	1.979
569	0.607	1.067	1.377	1.655	1.820	2.462	1.981
570	0.607	1.069	1.378	1.658	1.823	2.469	1.984
571	0.607	1.069	1.380	1.661	1.828	2.484	1.987
572	0.607	1.071	1.382	1.664	1.832	2.492	1.989
573	0.607	1.072	1.383	1.666	1.836	2.501	1.992
574	0.607	1.073	1.385	1.670	1.840	2.512	1.995
575	0.607	1.074	1.386	1.672	1.843	2.521	1.997
576	0.607	1.075	1.388	1.674	1.847	2.529	1.999
577	0.607	1.076	1.389	1.677	1.851	2.538	2.002
578	0.607	1.076	1.390	1.679	1.854	2.546	2.004
579	0.606	1.077	1.391	1.682	1.857	2.555	2.006
580	0.607	1.078	1.392	1.683	1.858	2.554	2.007
581	0.607	1.079	1.392	1.685	1.860	2.562	2.009
582	0.607	1.080	1.394	1.687	1.863	2.568	2.011
583	0.607	1.080	1.395	1.689	1.865	2.574	2.013
584	0.608	1.081	1.395	1.690	1.868	2.580	2.014
585	0.608	1.081	1.396	1.692	1.870	2.585	2.015
586	0.608	1.082	1.397	1.693	1.872	2.592	2.017
587	0.609	1.082	1.398	1.695	1.874	2.595	2.018
588	0.609	1.083	1.399	1.697	1.876	2.602	2.020
589	0.608	1.084	1.400	1.698	1.878	2.607	2.022
590	0.609	1.084	1.400	1.699	1.879	2.610	2.022
591	0.608	1.085	1.400	1.700	1.880	2.613	2.023
592	0.609	1.085	1.400	1.701	1.882	2.617	2.024
593	0.609	1.085	1.401	1.702	1.882	2.620	2.025
594	0.609	1.085	1.401	1.702	1.883	2.623	2.025
595	0.609	1.086	1.401	1.703	1.884	2.625	2.026
596	0.609	1.086	1.401	1.704	1.885	2.628	2.026
597	0.609	1.086	1.402	1.704	1.886	2.631	2.027
598	0.609	1.086	1.402	1.705	1.887	2.634	2.028
599	0.609	1.087	1.403	1.707	1.889	2.640	2.029
600	0.610	1.087	1.403	1.708	1.891	2.644	2.030
601	0.610	1.088	1.404	1.710	1.893	2.650	2.032

	Concentration ($g.L^{-1}$)						K_a (λ)
λ	0.227	0.454	0.681	0.908	1.135	2.270	($L.g^{-1}.cm^{-1}$)
602	0.610	1.088	1.405	1.712	1.896	2.655	2.033
603	0.610	1.088	1.406	1.714	1.899	2.663	2.035
604	0.610	1.088	1.408	1.716	1.902	2.670	2.037
605	0.611	1.089	1.409	1.719	1.906	2.679	2.040
606	0.611	1.089	1.411	1.722	1.910	2.689	2.042
607	0.611	1.090	1.412	1.725	1.913	2.697	2.045
608	0.611	1.091	1.415	1.729	1.919	2.710	2.049
609	0.611	1.092	1.416	1.732	1.923	2.721	2.052
610	0.612	1.093	1.419	1.737	1.929	2.732	2.056
611	0.612	1.093	1.420	1.739	1.932	2.742	2.058
612	0.612	1.094	1.423	1.744	1.938	2.755	2.063
613	0.613	1.095	1.425	1.747	1.942	2.764	2.065
614	0.613	1.096	1.427	1.751	1.947	2.776	2.069
615	0.613	1.097	1.429	1.754	1.951	2.784	2.072
616	0.613	1.098	1.430	1.757	1.955	2.792	2.074
617	0.614	1.099	1.432	1.760	1.959	2.799	2.077
618	0.615	1.100	1.434	1.763	1.963	2.809	2.080
619	0.615	1.101	1.435	1.765	1.966	2.816	2.083
620	0.615	1.102	1.436	1.768	1.969	2.822	2.085
621	0.615	1.102	1.437	1.770	1.971	2.827	2.086
622	0.615	1.102	1.438	1.771	1.973	2.830	2.088
623	0.616	1.103	1.438	1.772	1.974	2.834	2.088
624	0.616	1.103	1.438	1.772	1.975	2.836	2.089
625	0.615	1.103	1.438	1.772	1.975	2.837	2.089
626	0.615	1.103	1.438	1.773	1.975	2.837	2.089
627	0.615	1.103	1.439	1.773	1.975	2.836	2.089
628	0.616	1.102	1.438	1.772	1.975	2.835	2.088
629	0.615	1.102	1.437	1.771	1.973	2.835	2.087
630	0.614	1.101	1.436	1.771	1.972	2.832	2.086
631	0.614	1.100	1.435	1.770	1.971	2.829	2.085
632	0.614	1.100	1.434	1.769	1.970	2.827	2.084
633	0.613	1.099	1.433	1.768	1.969	2.827	2.082
634	0.613	1.098	1.432	1.767	1.968	2.827	2.081
635	0.613	1.098	1.432	1.767	1.968	2.828	2.081
636	0.612	1.098	1.432	1.768	1.969	2.830	2.082
637	0.613	1.098	1.433	1.770	1.972	2.837	2.083
638	0.613	1.098	1.434	1.772	1.975	2.845	2.085
639	0.613	1.100	1.436	1.777	1.982	2.857	2.089
640	0.613	1.101	1.439	1.783	1.989	2.876	2.094
641	0.613	1.102	1.443	1.789	1.998	2.895	2.100
642	0.613	1.105	1.448	1.798	2.010	2.921	2.109
643	0.614	1.108	1.453	1.808	2.023	2.947	2.118
644	0.615	1.111	1.460	1.817	2.036	2.973	2.127
645	0.616	1.114	1.466	1.829	2.052	3.004	2.138
646	0.617	1.117	1.473	1.840	2.066	3.032	2.149
647	0.618	1.121	1.481	1.853	2.082	3.063	2.161
648	0.620	1.126	1.489	1.867	2.099	3.093	2.174
649	0.621	1.129	1.496	1.879	2.115	3.121	2.186
650	0.622	1.133	1.504	1.890	2.130	3.148	2.197

	Concentration ($g.L^{-1}$)						K_a (λ)
λ	0.227	0.454	0.681	0.908	1.135	2.270	($L.g^{-1}.cm^{-1}$)
651	0.623	1.136	1.509	1.900	2.143	3.171	2.206
652	0.624	1.138	1.513	1.906	2.151	3.184	2.212
653	0.625	1.142	1.520	1.917	2.165	3.206	2.223
654	0.626	1.144	1.525	1.926	2.175	3.225	2.230
655	0.626	1.146	1.530	1.935	2.187	3.240	2.239
656	0.627	1.150	1.536	1.945	2.201	3.263	2.249
657	0.628	1.154	1.545	1.959	2.218	3.288	2.263
658	0.629	1.159	1.553	1.973	2.235	3.313	2.276
659	0.631	1.164	1.564	1.991	2.259	3.352	2.293
660	0.633	1.171	1.577	2.012	2.286	3.380	2.314
661	0.635	1.178	1.589	2.031	2.311	3.409	2.333
662	0.638	1.186	1.604	2.055	2.340	3.443	2.355
663	0.640	1.194	1.617	2.076	2.367	3.462	2.376
664	0.643	1.201	1.630	2.095	2.391	3.478	2.396
665	0.646	1.208	1.643	2.117	2.416	3.507	2.417
666	0.648	1.216	1.656	2.135	2.440	3.522	2.436
667	0.652	1.224	1.669	2.155	2.463	3.541	2.456
668	0.654	1.230	1.679	2.169	2.480	3.548	2.471
669	0.656	1.236	1.689	2.182	2.495	3.556	2.485
670	0.660	1.242	1.698	2.197	2.512	3.562	2.500
671	0.662	1.246	1.704	2.203	2.519	3.564	2.508
672	0.664	1.250	1.709	2.209	2.526	3.570	2.515
673	0.665	1.252	1.712	2.213	2.529	3.569	2.519
674	0.667	1.256	1.716	2.217	2.533	3.567	2.525
675	0.669	1.257	1.718	2.218	2.534	3.575	2.527
676	0.669	1.259	1.719	2.220	2.534	3.569	2.529
677	0.671	1.261	1.721	2.222	2.535	3.574	2.532
678	0.672	1.263	1.723	2.223	2.537	3.572	2.534
679	0.673	1.265	1.725	2.225	2.538	3.572	2.538
680	0.675	1.267	1.727	2.227	2.539	3.570	2.540
681	0.676	1.269	1.728	2.226	2.536	3.567	2.540
682	0.677	1.269	1.726	2.220	2.527	3.559	2.537
683	0.678	1.268	1.722	2.213	2.516	3.553	2.530
684	0.678	1.265	1.714	2.198	2.497	3.539	2.518
685	0.678	1.261	1.703	2.179	2.472	3.516	2.500
686	0.677	1.254	1.689	2.155	2.439	3.498	2.477
687	0.676	1.247	1.673	2.126	2.404	3.461	2.451
688	0.674	1.239	1.657	2.100	2.370	3.423	2.426
689	0.671	1.229	1.638	2.069	2.329	3.375	2.396
690	0.669	1.218	1.615	2.032	2.281	3.315	2.361
691	0.667	1.209	1.599	2.004	2.246	3.261	2.334
692	0.664	1.200	1.582	1.976	2.211	3.205	2.308
693	0.662	1.193	1.568	1.954	2.182	3.157	2.286
694	0.659	1.182	1.546	1.918	2.137	3.076	2.252
695	0.656	1.174	1.531	1.894	2.105	3.018	2.228
696	0.654	1.166	1.516	1.870	2.075	2.960	2.205
697	0.651	1.157	1.499	1.842	2.040	2.891	2.178
698	0.649	1.149	1.484	1.820	2.011	2.831	2.155
699	0.646	1.140	1.467	1.792	1.976	2.761	2.129
700	0.643	1.131	1.450	1.765	1.941	2.688	2.102

H.2 Data for light model experiment

Tables H.3 shows the data obtained from the experiment outlined in Section 5.3, the results of which are presented in Section 3.3.2, Chapter 3. Table H.4 shows the same data normalized to I/I_0.

Table H.3 – PFD reported in $\mu\text{mol} \cdot \text{m}^{-2}\text{s}^{-1}$ measured at distances z (cm) from the illuminated surface. Repeated over a range of cell concentrations (g.L^{-1}).

	Concentration (g.L^{-1})													
z (cm)	0.102	0.160	0.266	0.380	0.543	0.776	1.109	1.584	2.262	2.514	2.793	3.103	3.448	3.831
0.00	180	180	180	180	208.8	215	218	210	208.5	210	212.3	210.5	211.7	214.1
0.50	173.3	172.5	174.2	163.8	159.9	144.1	116	96.7	61.2	58.1	48.7	47	41.7	32.4
1.00	162.7	160.69	156.1	141.72	133.3	111.3	86.3	59	30.2	25.08	21.2	19	16.75	11.9
1.50	158	150.22	139.4	125.13	113.6	81	56.6	31.3	18.8	13.5	10.11	6.4	5.9	4.1
2.00	149.7	139.2	121.3	103.75	89.4	62.9	42.5	18.8	7.5	9.8	4.2	2.82	2.5	1.23
2.50	142	127.5	107.7	88.5	74.8	48.6	24.3	11.03	4.46	3.58	2.28	1.19	0.9	0.43
3.00	133.16	115.7	95.79	74.36	58.13	34.2	19.5	6.4	2.04	1.8	0.74	0.53	0.39	0.18
3.50	125	107.4	83.9	62.08	46.5	25.87	12.4	4.2	1.2	0.99	0.53	0.27	0.19	0.1
4.00	114.89	95.73	73.6	53.52	37.5	22.7	8.2	2.77	0.99	0.35	0.2	0.16	0.1	0.06
4.50	108	88.7	63.22	45.98	30.01	15.45	5.14	1.61	0.35	0.23	0.14	0.08	0.07	0.02
5.00	97.5	78.49	55.74	37.5	25.4	11.85	4.22	1.01	0.23	0.11	0.1	0.07	0.03	0.01

Table H.4 – Normalized PFD I/I_0 from Table H.3 at distances z (cm) from the illuminated surface. Repeated over a range of cell concentrations (g.L^{-1}).

	Concentration (g.L^{-1})													
z (cm)	0.102	0.160	0.266	0.380	0.543	0.776	1.109	1.584	2.262	2.514	2.793	3.103	3.448	3.831
0.00	1	1	1	1	1	1	1	1	1	1	1	1	1	1
0.50	0.963	0.958	0.968	0.910	0.766	0.670	0.532	0.460	0.294	0.277	0.229	0.223	0.197	0.151
1.00	0.904	0.893	0.867	0.787	0.638	0.518	0.396	0.281	0.145	0.119	0.100	0.090	0.079	0.056
1.50	0.878	0.835	0.774	0.695	0.544	0.377	0.260	0.149	0.090	0.064	0.048	0.030	0.028	0.019
2.00	0.832	0.773	0.674	0.576	0.428	0.293	0.195	0.090	0.036	0.047	0.020	0.013	0.012	0.006
2.50	0.789	0.708	0.598	0.492	0.358	0.226	0.111	0.053	0.021	0.017	0.011	0.006	0.004	0.002
3.00	0.740	0.643	0.532	0.413	0.278	0.159	0.089	0.030	0.010	0.009	0.003	0.003	0.002	0.001
3.50	0.694	0.597	0.466	0.345	0.223	0.120	0.057	0.020	0.006	0.005	0.002	0.001	0.001	4.67E-04
4.00	0.638	0.532	0.409	0.297	0.180	0.106	0.038	0.013	0.005	0.002	0.001	0.001	4.72E-04	2.80E-04
4.50	0.600	0.493	0.351	0.255	0.144	0.072	0.024	0.008	0.002	0.001	0.001	3.80E-04	3.31E-04	9.34E-05
5.00	0.542	0.436	0.310	0.208	0.122	0.055	0.019	0.005	0.001	5.24E-04	4.71E-04	3.33E-04	1.42E-04	4.67E-05

H.3 Data for calculation of average light intensities (I_1 and I_2)

The data in Table H.5 was used to calculate an average PFD for each light scenario, as presented in Section 4.2.5, Chapter 4. Combining this data with the (x,y) location of each measurement point, according to Fig. H.1, enabled the light maps given in Fig 4.11 to be generated using MATLAB.

Table H.5 – PFD in $\mu\text{mol} \cdot \text{m}^{-2}\text{s}^{-1}$ measured for a single light bank (I_1) and for both banks (I_2) at each numbered point corresponding to the grid in Fig. H.1

#	I_1	I_2	#	I_1	I_2	#	I_1	I_2
1	188.3	444.7	31	398.4	1198.6	61	346.7	930.6
2	316.8	641.7	32	335.5	969.9	62	335.7	937.6
3	338.8	692.2	33	391.2	1022.2	63	324.1	954.6
4	344.1	668.5	34	459.3	1240.7	64	215.8	476.0
5	266.4	516.1	35	445.1	1246.0	65	343.4	830.0
6	366.5	700.9	36	408.4	1091.0	66	329.2	872.0
7	399.9	812.2	37	314.3	892.0	67	346.5	821.0
8	402.9	849.8	38	390.2	1165.0	68	301.2	672.0
9	384.4	746.5	39	412.4	1249.0	I_{ave}	362.5	939.1
10	290.5	705.5	40	389.8	1201.4			
11	387.9	924.5	41	323.9	1003.0			
12	405.5	1008.2	42	387.4	1008.1			
13	384.9	1002.0	43	426.2	1178.4			
14	318.2	758.3	44	433.4	1195.4			
15	402.1	894.7	45	395.6	1052.7			
16	435.0	1080.6	46	279.7	736.8			
17	432.9	1069.5	47	376.8	1080.2			
18	399.5	978.3	48	394.6	1168.5			
19	287.0	643.0	49	371.5	1113.2			
20	399.5	1059.4	50	315.5	973.2			
21	395.8	1171.8	51	344.5	939.7			
22	392.6	1130.0	52	407.1	1092.1			
23	344.6	939.7	53	396.1	1100.5			
24	403.2	964.0	54	329.2	896.7			
25	430.8	1082.2	55	247.5	548.0			
26	444.9	1192.0	56	361.4	863.4			
27	416.6	1076.0	57	380.1	983.2			
28	282.4	621.7	58	339.5	862.1			
29	399.8	1170.4	59	288.5	701.1			
30	398.7	1262.6	60	305.9	785.0			

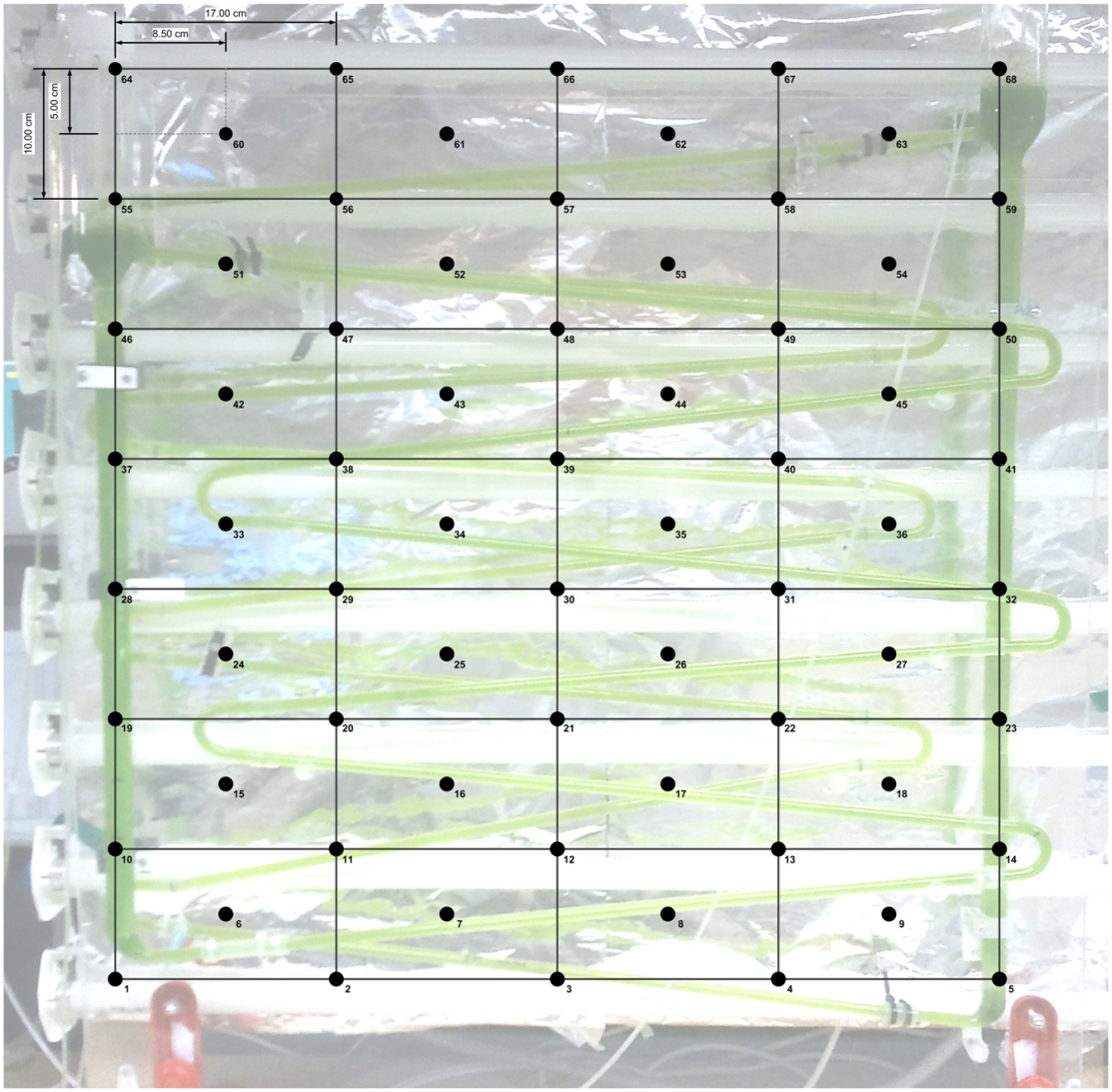

Figure H.1 – Grid diagram of points at which light intensity was measured.

H.4 Data for kinetic model experiment

The data refers to the kinetic model experimental results in Section 4.3, Chapter 4.

Table H.6 – Data for all experimental runs: Concentration ($g.L^{-1}$) as a function of time (hrs). Data for runs 2 and 5 not shown since these were from flow cell data and contain hundreds of time points (See Section D). However, linear plots for Runs 2 and 5 from flow cell data are shown in Fig. H.2.

Run 1		Run 3		Run 4		Run 6		Run 7	
Time(hrs)	ave C_x ($g.L^{-1}$)	Time(hrs)	ave C_x ($g.L^{-1}$)	Time(hrs)	ave C_x ($g.L^{-1}$)	Time(hrs)	ave C_x ($g.L^{-1}$)	Time(hrs)	ave C_x ($g.L^{-1}$)
0.0	0.131	0.0	0.128	0.0	0.128	0.0	0.107	0.0	0.095
17.3	0.140	1.6	0.122	17.0	0.216	22.0	0.659	18.3	0.179
21.3	0.180	6.8	0.129	22.9	0.341	25.1	1.025	23.7	0.200
25.8	0.233	22.8	0.445	41.4	1.357	30.1	1.498	45.1	1.546
42.9	0.568	26.4	0.594	45.5	1.916	45.1	3.803	48.1	1.756
49.5	0.653	47.4	2.888	66.3	2.871			67.7	3.175
66.8	1.740								
91.2	3.399								

Run 8		Run 9		Run 10		Run 11		Run 12	
Time(hrs)	ave C_x ($g.L^{-1}$)	Time(hrs)	ave C_x ($g.L^{-1}$)	Time(hrs)	ave C_x ($g.L^{-1}$)	Time(hrs)	ave C_x ($g.L^{-1}$)	Time(hrs)	ave C_x ($g.L^{-1}$)
0.0	0.068	0.0	0.119	0.0	0.182	0.0	0.223	0.0	0.181
3.3	0.097	17.3	0.236	2.7	0.205	3.9	0.206	2.0	0.180
5.4	0.122	21.3	0.472	5.5	0.185	20.1	0.378	8.5	0.152
10.8	0.177	25.8	0.777	22.5	0.644	24.9	0.513	18.8	0.294
22.5	0.520	42.9	3.429	25.2	0.841	31.1	0.819	23.5	0.375
26.2	0.803	49.5	3.540	27.4	1.022	46.0	1.860	28.9	0.718
29.2	1.002			31.2	1.238			45.7	2.780
33.5	1.226			48.5	1.382				

Run 13		Run 14		Run 15		Run 16		Run 17	
Time(hrs)	ave C_x ($g.L^{-1}$)	Time(hrs)	ave C_x ($g.L^{-1}$)	Time(hrs)	ave C_x ($g.L^{-1}$)	Time(hrs)	ave C_x ($g.L^{-1}$)	Time(hrs)	ave C_x ($g.L^{-1}$)
0.0	0.202	0.0	0.182	0.0	0.161	0.0	0.298	0.0	0.147
10.0	0.262	2.0	0.232	3.9	0.169	2.8	0.419	2.1	0.153
12.6	0.317	8.5	0.304	20.1	0.469	6.8	0.652	5.1	0.167
16.8	0.434	18.8	0.906	24.9	0.734	9.2	0.757	18.9	0.524
20.9	0.568	23.5	1.288	31.1	1.407	26.6	3.624	23.0	0.794
34.2	2.354	28.9	2.124	46.0	3.678			26.4	1.240
		45.7	3.841					29.3	1.518

Run 18		Run 19		Run 20		Run 21		Run 22	
Time(hrs)	ave C_x ($g.L^{-1}$)	Time(hrs)	ave C_x ($g.L^{-1}$)	Time(hrs)	ave C_x ($g.L^{-1}$)	Time(hrs)	ave C_x ($g.L^{-1}$)	Time(hrs)	ave C_x ($g.L^{-1}$)
0.0	0.164	0.0	0.082	0.0	0.100	0.0	0.138	0.0	0.128
2.1	0.156	3.3	0.103	4.1	0.190	12.2	0.201	1.6	0.131
5.1	0.162	5.4	0.130	8.1	0.293	17.0	0.615	6.8	0.127
18.9	0.492	10.8	0.183	12.1	0.520	21.0	0.788	22.8	0.330
23.0	0.770	22.5	0.568	21.5	1.544	25.0	1.074	26.4	0.411
26.4	1.224	26.2	0.871	26.7	2.572	34.4	1.708	47.4	1.807
29.3	1.562	29.2	1.084						
		33.5	1.363						

Run 23		Run 24	
Time(hrs)	ave C_x ($g.L^{-1}$)	Time(hrs)	ave C_x ($g.L^{-1}$)
0.0	0.271	0.0	0.359
10.0	0.268	2.8	0.532
12.6	0.306	6.8	0.856
16.8	0.405	9.2	1.018
20.9	0.541	26.6	3.737
34.2	2.237		

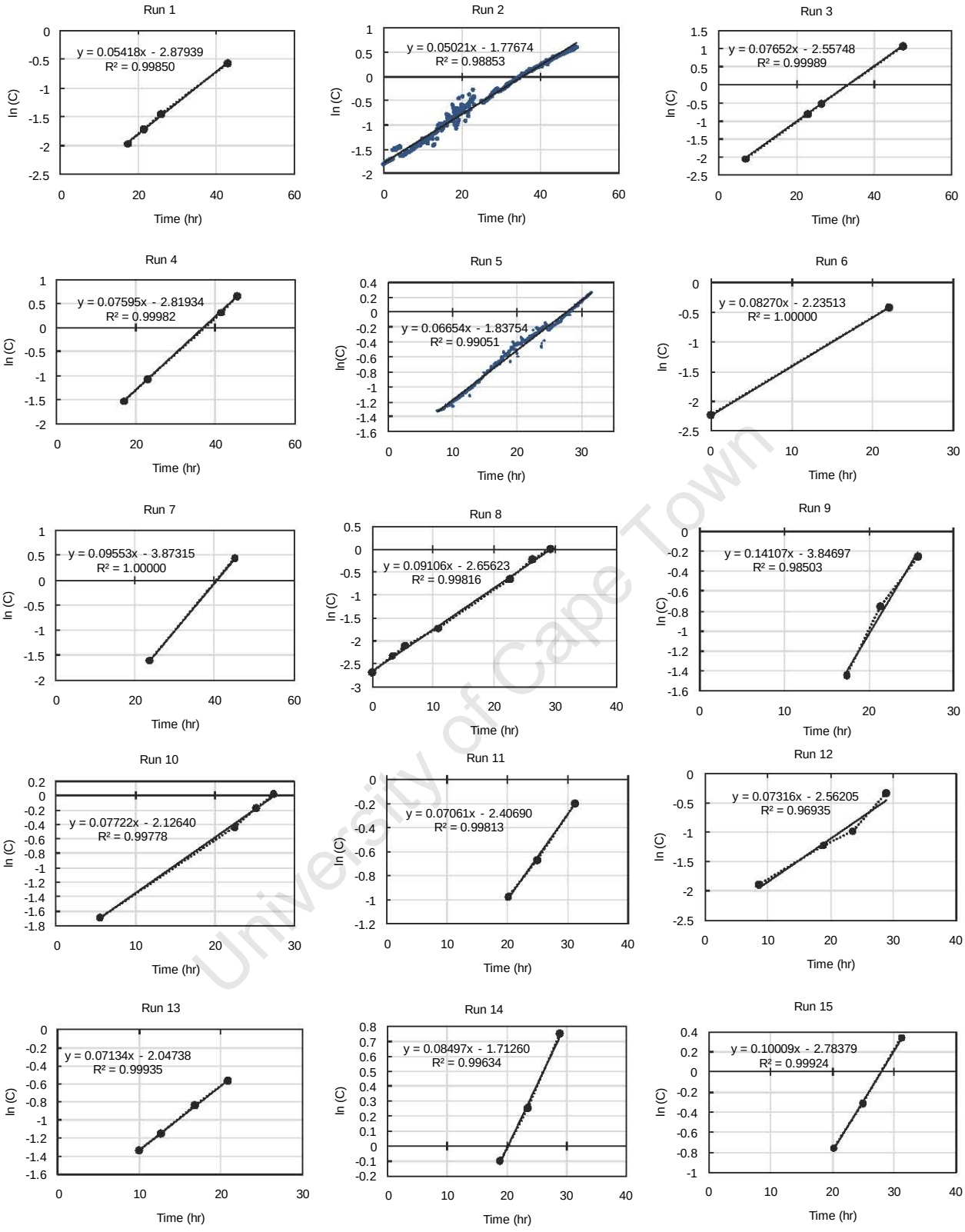

Figure H.2 – Linear plots of ln(C_x) as a function of time for calculation of exponential growth rates. Runs 1 to 15.

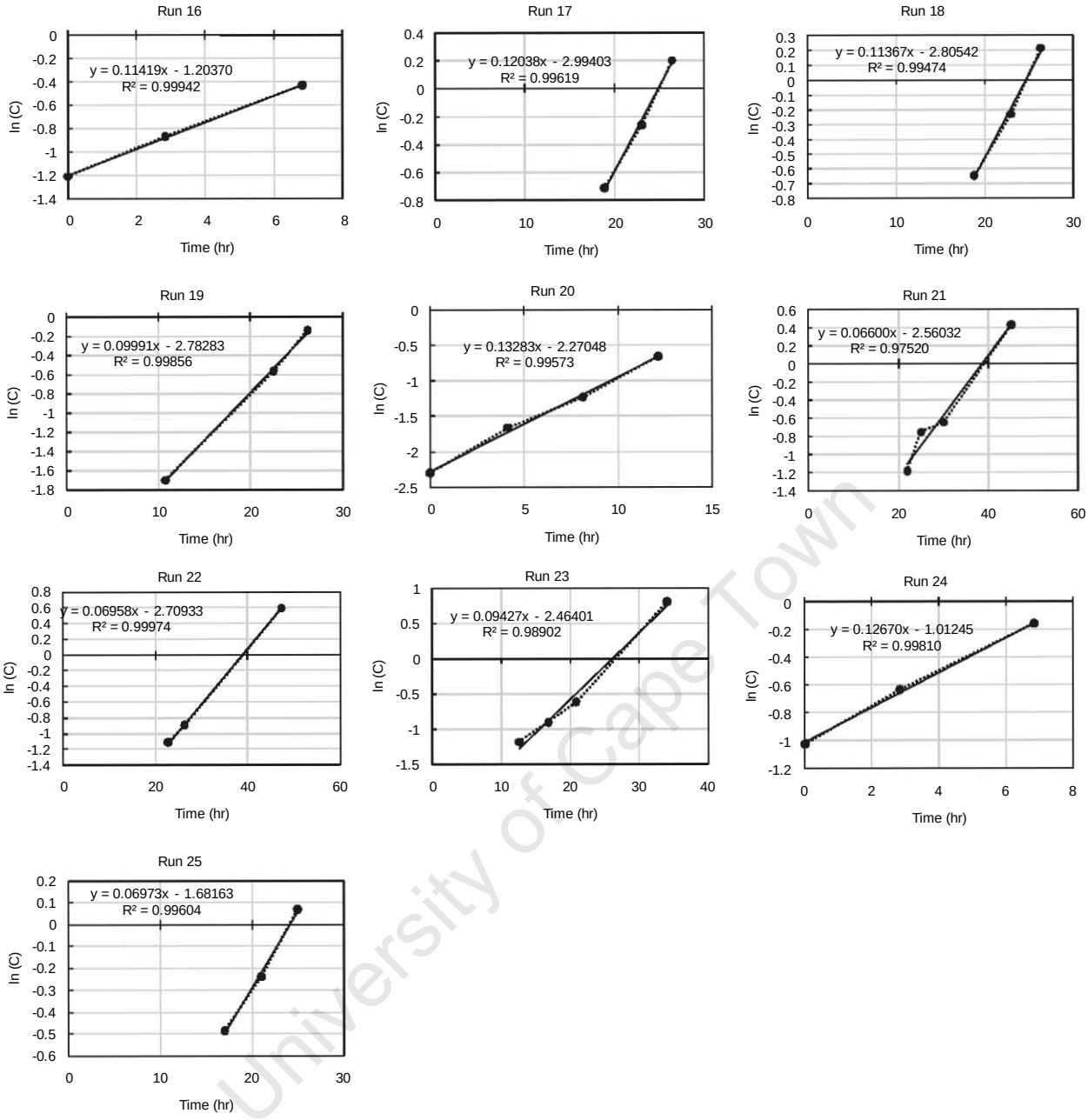

Figure H.3 – Linear plots of $\ln(C_x)$ as a function of time for calculation of exponential growth rates. Runs 16 to 25.

H.5 Data for hydrodynamic model experiment

The raw data here refers to the hydrodynamic model experimental results in Section 5.4, Chapter 5. It would be to tedious to present all the conductivity data from the tracer experiments. There were 48 runs performed and some had over 200 data points. Fig. H.4 shows a typical normalized conductivity response, taken from Run 4 (see Table H.7). Table H.7 shows how the data was processed using the times identified for each observed. The peak times were auto-calculated using a MATLAB programme written by this author. The programme fitted a cubic spline to the normalized conductivity response and then estimated the time points of the peaks using a built in MATLAB function (*findpeaks*). Fig. H.4 shows how these peaks were located visually. As a result of noise in the data, the programme would determine peaks that were not real maxima, as can be seen in Fig. H.4. Thus, thus the correct peaks were selected from those found by the programme using visual observation.

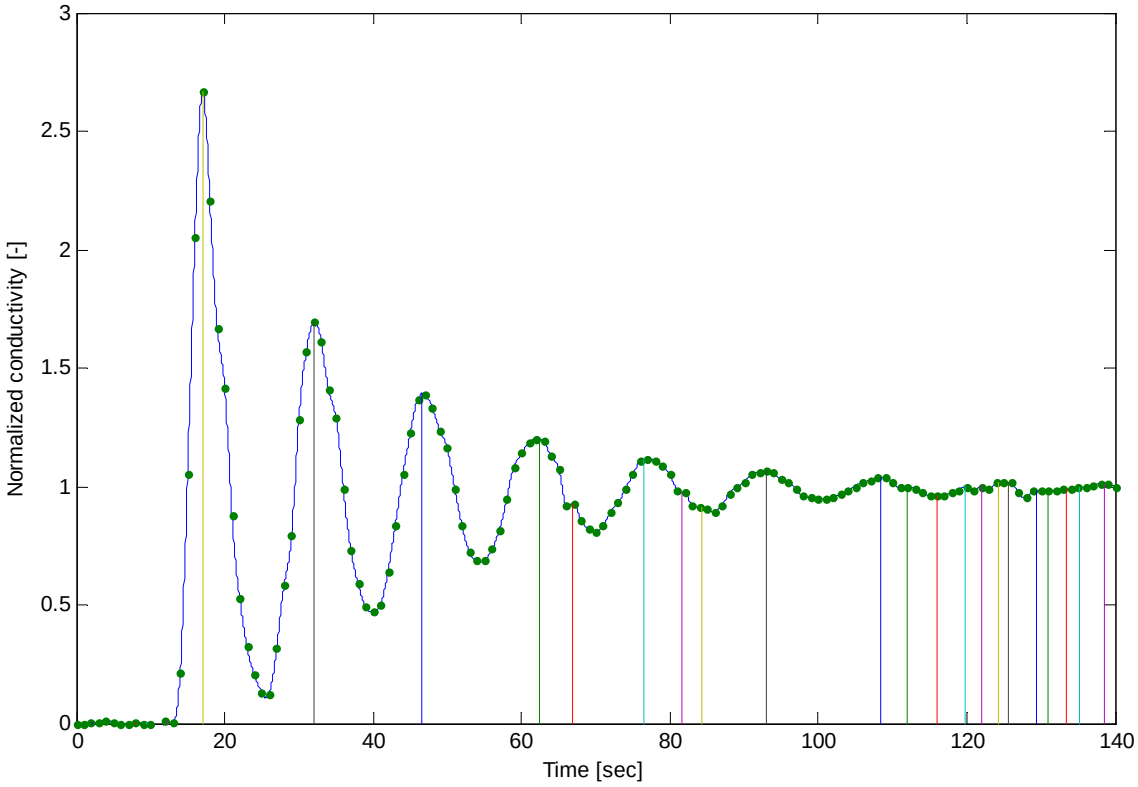

Figure H.4 – Normalized tracer conductivity curve for Run 4 in Table H.7 showing peaks. Lines represent the time points at which the programme identified peaks.

Table H.7 – Tracer experimental data processed to calculate mean circulation times for each superficial gas velocity U_{Gr}. First an estimate circulation time (t_C est.) is calculated from each run from the average time between successive peaks. The mean circulation time is then estimated from the average of all the t_C est. values corresponding to each U_{Gr}.

Run	F (l.min^{-1})	U_{Gr} (m.s^{-1})	Time at peak nth peak (s)							t_C(s) = difference between peak time points						y_i t_C est.	stdev in t_C est.	t_C mean	error as stdev in t_C mean
			1	2	3	4	5	6	7	t_{C1}	t_{C2}	t_{C3}	t_{C4}	t_{C5}	t_{C6}				
1	0.1	0.00105	21.13	41.15	59.9					20.02	18.75					19.385	0.898		
2	0.1	0.00105	20.72	38.72	58.59	77.83	97.08	115.2		18	19.87	19.24	19.25	18.12		18.896	0.806	19.355	0.444
3	0.1	0.00105	31.21	51.4	71.59	90.56				20.19	20.19	18.97				19.783	0.704		
4	0.2	0.00210	17.02	32.15	46.58	62.5	76.53	93		15.13	14.43	15.92	14.03	16.47		15.196	1.012		
5	0.2	0.00210	51.21	66.15	80.87	95.3	110.2			14.94	14.72	14.43	14.9			14.748	0.232	15.912	1.870
6	0.2	0.00210	34.89	49.84	65.51	95.51	109.7			14.95	15.67	30	14.19			18.703	7.556		
7	0.2	0.00210	16.85	30.53	46.85					13.68	16.32					15.000	1.867		
8	0.4	0.00419	21.89	32.47	44.7	55.2	66.95	77.96	90.03	10.58	12.23	10.5	11.75	11.01	12.07	11.357	0.759		
9	0.4	0.00419	45.02	55.75	66.77	78.14				10.73	11.02	11.37				11.040	0.320	11.446	0.351
10	0.4	0.00419	28.3	39.65	51.05	62.67	74.31			11.35	11.4	11.62	11.64			11.503	0.149		
11	0.4	0.00419	32.18	43.67	55.95					11.49	12.28					11.885	0.559		
12	0.6	0.00629	16.62	25.65	35.35	45.19				9.03	9.7	9.84				9.523	0.433		
13	0.6	0.00629	22.14	32.1	42.09	51.81				9.96	9.99	9.72				9.890	0.148		
14	0.6	0.00629	19.17	28.38	37.67	47.37	55.97			9.21	9.29	9.7	8.6			9.200	0.454	9.529	0.272
15	0.6	0.00629	43.63	53.27	63					9.64	9.73					9.685	0.064		
16	0.6	0.00629	35	43.9	53.66	62.99	72.56	81.74		8.9	9.76	9.33	9.57	9.18		9.348	0.335		
17	0.8	0.00838	18.49	26.85	35.3	44.8				8.36	8.45	9.5				8.770	0.634		
18	0.8	0.00838	14.63	23.41	32.1					8.78	8.69					8.735	0.064		
19	0.8	0.00838	15.95	23.77	31.95	40.52	48.19			7.82	8.18	8.57	7.67			8.060	0.402		
20	0.8	0.00838	12.82	20.99	30.07	37.68				8.17	9.08	7.61				8.287	0.742	8.485	0.248
21	0.8	0.00838	31.75	39.99	48.81	57.19	66.01			8.24	8.82	8.38	8.82			8.565	0.300		
22	0.8	0.00838	35.07	43.29	52.09	60.51				8.22	8.8	8.42				8.480	0.295		
23	0.8	0.00838	32.27	40.67	49.07	57.94	66.26			8.4	8.4	8.87	8.32			8.498	0.251		
24	1	0.01048	31.09	39.4	46.93	54.86				8.31	7.53	7.93				7.923	0.390		
25	1	0.01048	20.22	28.59	37.3	46.41				8.37	8.71	9.11				8.730	0.370		
26	1	0.01048	24.22	31.27	40.195	48.46				7.05	8.925	8.265				8.080	0.951		
27	1	0.01048	17.29	24.82	32					7.53	7.18					7.355	0.247		
28	1	0.01048	6.631	14.12	22.32	30.7				7.489	8.2	8.38				8.023	0.471	7.907	0.369
29	1	0.01048	17.1	25.54	32.97					8.44	7.43					7.935	0.714		
30	1	0.01048	38.22	45.49	53.09	61.25				7.27	7.6	8.16				7.677	0.450		
31	1	0.01048	38.09	45.94	53.95	61.5	69.93	77.6	85.63	7.85	8.01	7.55	8.43	7.67	8.03	7.923	0.311		
32	1	0.01048	48.71	56.3	64.42	72.36	80.32			7.59	8.12	7.94	7.96			7.903	0.223		
33	1	0.01048	14.13	21.2	28.73	36.7				7.07	7.53	7.97				7.523	0.450		
34	1.2	0.01258	40.96	48.49	56.38					7.53	7.89					7.710	0.255		
35	1.2	0.01258	12.09	20.22	28.58					8.13	8.36					8.245	0.163		
36	1.2	0.01258	16.15	23.62	31.61	39				7.47	7.99	7.39				7.617	0.326		
37	1.2	0.01258	9.398	16.32						6.922	7.01					6.966	0.062	7.518	0.399
38	1.2	0.01258	13.09	20.7	27.92	35.3				7.61	7.22	7.38				7.403	0.196		
39	1.2	0.01258	27.89	35.4	43	49.97				7.51	7.6	6.97				7.360	0.341		
40	1.2	0.01258	27.72	35.16	42.42	49.69				7.44	7.26	7.27				7.323	0.101		
41	2	0.02096	25.03	31.31	37.78	45.01	51.05			6.28	6.47	7.23	6.04			6.505	0.514		
42	2	0.02096	30.89	36.94	43.46	50.06				6.05	6.52	6.6				6.390	0.297	6.582	0.239
43	2	0.02096	42.2	49.01	55.9					6.81	6.89					6.850	0.057		
44	3	0.03144	34.13	40.29	46.73	52.17	59.24			6.16	6.44	5.44	7.07			6.278	0.676	6.090	0.265
45	3	0.03144	18.02	23.9	29.83	35.73				5.88	5.93	5.9				5.903	0.025		
46	4	0.04192	31.02	36.32	42	48.17				5.3	5.68	6.17				5.717	0.436	5.626	0.128
47	4	0.04192	31.12	37	42.19					5.88	5.19					5.535	0.488		
48	5	0.05240	31.99	37	43.25					5.01	6.25					5.630	0.877	5.630	0.000

H.6 Data for airlift experiment

The data here refers to the experimental results for the airlift model experiment in Section 6.3, Chapter 6.

Table H.8 – Concentration as a function of time for airlift reactor experiment. 3% CO_2 in Air at 2 l.min^{-1} with average PFD of ~590 μmol.m^{-2}s^{-1}. Optical density converted to concentration via calibration curve given in Fig. C.1.

Date / Time	Hours	Days	Dilution (D)	3 x Optical Density (OD) at 750 nm			$_{ave}$OD/D	C_x (g.L^{-1})
01/11 12:34	0.00	0.00	1	0.109	0.113	0.116	0.11	0.051
01/11 15:05	2.52	0.10	1	0.119	0.109	0.114	0.11	0.052
01/11 20:30	7.93	0.33	1	0.156	0.157	0.141	0.15	0.069
01/12 10:45	22.18	0.92	1	0.368	0.375	0.371	0.37	0.169
01/12 15:33	26.98	1.12	1	0.603	0.606	0.609	0.61	0.276
01/13 10:35	46.02	1.92	0.5	0.938	0.931	0.923	1.86	0.847
01/13 14:00	49.43	2.06	0.25	0.652	0.651	0.655	2.61	1.188
01/13 16:47	52.22	2.18	0.25	0.664	0.668	0.665	2.66	1.212
01/14 10:00	69.43	2.89	0.1	0.468	0.473	0.468	4.70	2.138
01/14 16:25	75.85	3.16	0.1	0.504	0.521	0.529	5.18	2.358
01/15 15:42	99.13	4.13	0.1	0.611	0.611	0.618	6.13	2.792
01/16 15:00	122.43	5.10	0.1	0.783	0.798	0.774	7.85	3.574
01/17 10:30	141.93	5.91	0.1	0.854	0.856	0.867	8.59	3.910
01/17 17:12	148.63	6.19	0.1	0.886	0.905	0.919	9.03	4.112
01/18 08:30	163.93	6.83	0.05	0.552	0.548	0.544	10.96	4.989
01/18 16:52	172.30	7.18	0.05	0.56	0.559	0.568	11.25	5.120
01/19 13:39	193.08	8.05	0.05	0.539	0.521	0.529	10.59	4.822
01/20 13:00	216.43	9.02	0.05	0.5	0.52	0.511	10.21	4.646